Ultrafast Laser Fabricated Nanoparticles and Nanostructures: Characterization, Spectroscopy and Applications

A Thesis Submitted for the Award of the Degree of

Doctor of Philosophy

in Physics

By

Syed Hamad

School of Physics

University of Hyderabad

Hyderabad-500046, India.

December 2014

DECLARATION

I, ***Syed Hamad,*** declare that the work presented in this thesis entitled "***Ultrafast Laser Fabricated Nanoparticles and Nanostructures: Characterization, Spectroscopy and Applications***" has been carried out by me under the supervision of **Dr. Ashok Vudayagiri,** Assistant Professor, School of Physics and **Dr. S. Venugopal Rao**, Associate Professor, ACRHEM, University of Hyderabad, as per the Ph.D. ordinances of the university, which is also plagiarism free. I declare, to the best of my knowledge, that no part of this thesis has been submitted for the award of a research degree or diploma of any other university. I hereby agree that my thesis can be deposited in Shodhganga/ INFLIBNET.

Date:

Syed Hamad

Reg. No: 09PHPH09

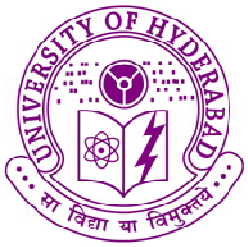

CERTIFICATE

This is to certify that the thesis entitled "**Ultrafast Laser Fabricated Nanoparticles and Nanostructures: Characterization, Spectroscopy and Applications"** *being submitted to the University of Hyderabad by* ***Syed Hamad*** *(Reg. No: 09PHPH09), for the award of the degree of* ***Doctor of Philosophy in Physics****, is a record of bonafide work carried out by him under my supervision and is free of plagiarism.*

The matter embodied in this report has not been submitted to any other university or institution for the award of any degree or diploma.

Dr. Ashok Vudayagiri

Thesis Supervisor
School of Physics, University of Hyderbad

Dr. S. Venugopal Rao

Thesis Supervisor
ACRHEM, University of Hyderabad.

Dean

School of Physics

Dedicated to...

Almighty God, My Ammi and Abba

Acknowledgements

Foremost I would like to thank Almighty God for offering me knowledge, wisdom, health and patience to finish this project. I thank my Ammi and Abba for their unlimited love which made me start the way to research and I owe everything to them.

Regarding Ph.D., I would like to first express my sincere appreciation and thanks to my supervisors, Dr. Ashok Vudayagiri and Dr. S. Venugopal Rao. To Dr. Ashok for his support, help during Ph.D, especially at the end of my Ph.D period. I have benefited a lot from the advice and direction received from him and my heartful thanks to him for being always pleasant and friendly. To Dr. S. Venugopal Rao, for his support, encouragement and his constant guidance during the period of Ph.D, which have helped me learn technical abilities and achieve excellent results. Also, I am grateful to get the opportunity to do research work in his group and produce a good contribution to science. He granted me enormous freedom to do research in my field of interest and offered the right guidance. He was also available for any sort of personal help.

I would like to thank my former supervisor Prof. Surya P. Tewari his inspiring guidance and constant encouragement throughout the course of this research work. I have been able to learn a great deal in this fascinating field of research through his inspiring and thought provoking discussions and I consider my association with him a rewarding experience.

I thank Prof. Chaturvedi, Dean, School of Physics, former Deans Prof. Bansal and Prof. Surya P. Tewari and School of Physics faculty for their co-operation in providing facilities of the School. My heartful thanks to Prof. A.K. Kapoor for his encouragement. I sincerely thank my doctoral committee members, Prof. M. Ghanashyam Krishna and Dr. S.V.S. Nageswara Rao, for their guidance and valuable suggestions during my research and thesis work. My special thanks to Prof. A.P. Patak for his invaluable suggestions.

I am grateful to express my thanks to the present director Dr. K. Venkateswara Rao, ACRHEM for his encouragement in providing experimental facilities to do work in the ACRHEM. I would like to thank ACRHEM faculty, especially Dr. G. Manoj

Kumar and Dr. P. Prem Kiran for their invaluable suggestions regarding to my research. I also thank Dr. G. Vitheeswaran and Dr. A.K. Chaudhary for their support.

My heartfelt thanks to Y. Balaji who inspired and guided me to join Ph.D in HCU. My heartful thanks to my lab mate G. Krishna Podgatlapalli and Dr. M. Ahamad Mohiddon (my friends, brothers, and well wishers) for their support and encouragement. They made my time in and out of the university greatly enjoyable and enriched my life. I deeply thank my senior Mr. S. Sreedhar for his help in doing experiments, advices and comments about optics skills and lab methods during the beginning days of my research.

I would like extend my gratitude to all my friends and colleagues, M. Venkatesh, M. Ashwin Kumar, Sk. Umar Pasha, Ch. Leela, S. Rama Kanth, S. Appala Kondaih, S. Sreeja (CUSAT), T. Shuvan Prasanth (NUS, Singapore), B. Sita Lakshmi, Dr. Debasis Swain, Mrs. Vijaya Lakshmi, Abdul Kalam, E. Manhikanta, Anil Kumar, E. Nageswara Rao, A. Siva Kumar, P.T. Anusha, , Mounika, B. Chandu V. Rakesh, P. Venkateswarlu, Vinod Kumar, Sai Shiva, Dr. Fahem Yahya, K. Srinivasa Rao, Ramesh Babu, Sudha Nirmala, Bheema Lingam, N. Yedukonalu, Narasimha, and all present and past laser group colleagues for their great cooperation in laser labs for their support in various stages of my thesis work. I acknowledge Lakshmi Narayana for assisting me in FESEM analysis and I also acknowledge Mr. M. D. Prasad, for assisting me in TEM analysis. I also thank my batchmates or friends, seniors and juniors in school of Physics, Vijay Kumar, Thirupathi, Azeem, Lakshun, Ananthaiah, Lakshmi, Srinu, Narasimha Raju, Narasimappa, Geo, Dr. Rajesh, Sree Ramulu, Suman Kalyan, Sanjeev, Alu boda, Surath, Dr. Shankar, Pidisetty Shankar, Ravi, Raju, Ramesh, all present and past colleagues for their great encouragement. I feel it a pleasant duty to express my regards to Mr. Abraham and non-teaching staff, School of Physics, IGM Library and University of Hyderabad administration.

I thank University of Hyderabad for providing Boarding / Boarding-cum-Lodging (BBL) Allowance for the period Aug 2009 – Jul 2012. I also thank to UGC-BSR (Basic scientific research) for providing JRF fellowship during the period Aug. 2012 – Mar. 2013. I acknowledge the funding agency Council of Scientific and Industrial Research (CSIR) India for sponsoring SRF fellowship during the period

Apr 2013 – Dec 2014 and also acknowledge ACRHEM for providing excellent laser laboratories, through which this work was possible.

It's my pleasure to thanks my teachers, Shaheda teacher (Prakasam Convent) Janaki Ram Sir (A.R.C & G.V.R Govt. high school, Singaraya Konda), Prasad Sir (A.R.C&G.V.R Govt. Jr. College, Singaraya Konda), Mujeer Sir (Inter mediate tution), Umamaheshwara Sir, Balaji Sir, Ramu Sir and Vamsilatha Madam (Sri Gayathri Degree & P.G. College, Kandukuru) from whom I gained knowledge and wisdom to reach HCU.

Finally, I would like to thank my brothers and best friends out of the university, brothers - Rameez, Amzad and Hashmath, friends - Arif, Khajavali, Rafi, Naresh, Venkatrao, Tahaseen, Kalpana, Shazad, Haneef, and Hari Babu, for their love, affection and constant support during my growing up years.

(Syed Hamad)

Table of contents

Nomenclature

Abbreviations	Description
ANTA	5 Amino, 3-nitro,1,3,5-nitrozole
BBO	β-Barium Borate
CARS	Coherent anti-Stokes Raman scattering
CB	Cavitation Bubble
CL-20	2,4,6,8,10,12-Hexanitro-2,4,6,8,10,12-hexaazaisowurtzitane
DFWM	Degenerate four wave mixing
EF	Enhancement Factor
FOX-7	1,1-diamino-2,2-dinitroethene
Fs	Femtosecond
HAZ	Heat affected zone
HEM	High energy materials
HMX	Cyclotetramethylene-tetranitramine
LIPSS	Laser induced periodic surface structures
NMs	Nano materials
NPs	Nanoparticles
NSs	Nanostructures
PSP	Propagating surface plasmons
Ps	Picosecond
RDX	1,3,5-Trinitroperhydro-1,3,5-triazine
SERS	Surface enhanced Raman scattering
SHG	Second harmonic generation
SNR	Signal to noise ratio
SPR	Surface plasmon resonances
THG	Third harmonic generation
TNT	Trinitrotoluene
ULAL	Ultrafast laser ablation in liquids
LSPR	Localized surface plasmon resonance
SPP	Surface plasmon polaritons
SEM	Scanning electronic microscopy
TEM	Transmission electron microscopy

1

Introduction and Outline of the Thesis

1.1. Motivation

In the current world scenario, obligatory problems of human beings are the lack of security (e.g. challenges from terrorist activates) and incompetence of existing diagnostic tools to obliterate health hazards (e.g. early detection of cancer, trace level of bacteria).[1-3] One of the simple possible solutions for the above described problems is the development of explosive detection techniques and improvisation of diagnostic limits through incorporating advanced technologies. There many techniques to accomplish both tasks of explosive detection and health diagnostics individually. Amongst them Raman effect based spectroscopic techniques are efficient and practical which are compatible to work simultaneously for explosives detection and for health diagnostics.[4] Raman spectroscopy is a versatile technique which works in near field and standoff[5] modes of explosive detection. Raman spectroscopy[6] is a simple spectroscopic method for detecting molecular materials among recently studied detection techniques. However, trace level detection of molecules using Raman process is extremely difficult since it is weak process with extremely smaller scattering cross-sections (typically ~10^{-31} cm^2) results in poor signal to noise ratio.[6] Improvements in the Raman scattering cross-sections can be achieved by incorporating a few simple methods. First possibility is the elevation by nonlinear optical effects (through the coherent excitation) in the molecular media using high power pulsed lasers, and second one is the utilization of surface engineered plasmonic materials (plasmonic nanoparticles and nanostructures). Examples of the former are coherent anti-Stokes Raman scattering (CARS),[7] Stimulated Raman scattering, Hyper Raman scattering etc. while for latter is surface enhanced Raman scattering (SERS). Among the diverse versions of Raman scattering, SERS is a simplest experimental tool that provides enormous signal strength through the excitation of surface plasmon resonances (SPR).[8] SERS technique requires the fabrication of materials facilitating plasmon excitations. Plasmonic metal nanoparticles (NPs) and nanostructures (NSs) are the platforms to provide SPR excitations. Fabrication of these NPs and NS is of great interest in scientific community due to their wide range applications.

1.2. Nanomaterials

The various properties of solid materials such as optical, electronic, mechanical and magnetic are influenced by the energy difference in between the

valence band and conduction band.[9,10] This energy difference can be effectively changed by the alteration of crystal structure, lattice reduction, modification of the surface and strain induction.[9] Nevertheless, a significant change can also be observed into the energy gap of the material when the solid material comes to nano size, which also affects the physical and chemical properties of the material. The energy gap of nanosized material is extensively different from bulk material. Especially, the size of the NP (<10 nm) significantly affects the properties of metals and semiconductors.[9] In the case of metal NPs, tight binding model and electron shell models describe band gap and various possibilities of transitions.[11, 12] Particularly, the size of plasmonic NPs demands a strong change in the band gap.[9, 12] In the case of semiconductor NPs, the band gap is significantly influenced by the effective mass of the material.[13] Over the last two decades potential applications of metal NPs encompassed broad areas of biotechnology, and photonics.[14-16] Particularly, The plasmonic NPs such as gold (Au), silver (Ag), copper (Cu) are fascinating due to their exceptional optical, electronic, mechanical properties mediated by the excitation of surface Plasmons. The size and shape of NPs play a significant role in providing SPRs. Additionally, plasmonic metal nanomaterials (NMs) [NPs and NSs] such Au, Ag and Cu, were predominantly studied and have found several applications[17-23] in biochemical sensors, SERS, carriers of drug delivery, nano-photonics devices, in biology, bio-sensing in-vivo and vitro diagnostics, solar cells, opto-electronic devices, cooling systems, antibacterial agents, in cancer treatment, catalysis etc.

1.3. Interaction of metal nanomaterials with EM fields

When a particle is illuminated an electromagnetic field it exerts a force on conduction electrons displace them towards the surface of NP. Due to this displacement negative charge will be accumulated on one side and positive charge in the opposite, act as an electric dipole. Electric field inside the NP is opposite to that of the field of incident one. Field generated in the NP force the displaced electrons to equilibrium. Larger electron displacements lead to stronger the electric dipole and consequently strong restoring force[24-26] which supports the electron system to oscillate with respect to positive ion cores of NP. These oscillations are described as localized surface plasmon resonance (LSPR). Frequency of these oscillations is called as plasmon frequency. This plasmon frequency (ω_p) depends on dielectric constant (ϵ) of the bulk metal.[24] Dielectric constant of the material is retrieved by solving the

Maxwell's equations those subjecting to appropriate boundary conditions inside and outside of the NP. The resultant equation of the electric field is described as[24, 27-28]

$$E_{out}(x,y,z) = E_0\hat{z} - E_{SP}\left(\frac{\hat{z}}{r^3} - \frac{3z}{r^5}(x\hat{x} + y\hat{y} + z\hat{z})\right) \quad (1.1)$$

Where E_0 is amplitude of incident electric field, r is the distance from outside of particle to center, α refers to atomic polarizability and $\hat{x}, \hat{y}\ \hat{z}$ are unit vectors. The term $E_{SP}=\alpha E_0$ is the induced dipole moment which is generated through the excitation of surface Plasmons.

Here $$\alpha = \frac{\epsilon_{in}-\epsilon_{out}}{\epsilon_{in}+2\epsilon_{out}}a^3 \quad (1.2)$$

Where 'a' is radius of the particle, ϵ_{in} and ϵ_{out} are the dielectric constants of the sphere for in and outside, respectively. Substituting equation (1.2) in equation (1.1) under the condition of quasi static approximation and the modified equation can be given as

$$E_{out}(x,y,z) = E_0\hat{z} - \left(\frac{\epsilon_{in}-\epsilon_{out}}{\epsilon_{in}+2\epsilon_{out}}\right) \times a^3 E_0\left(\frac{\hat{z}}{r^3} - \frac{3z}{r^5}(x\hat{x} + y\hat{y} + z\hat{z})\right) \quad (1.3)$$

Generally the output electric field depends on the inner surface dielectric function[24] of the particle which is significantly affected by the excitation wavelength. When the ϵ_{in} reaches to -2 ϵ_{out}, the denominator tends to minimal consequently E_{out} get enhanced which will be more than E_0 (incident field). Particularly Ag and Au NMs are compatible to produce surface Plasmons in the visible region those resonant with excitation wavelength from visible spectrum and this phenomena supports the EM field enhancement in SERS.[27]

It is important to express the dielectric constants of materials that invoke the surface plasmon resonances. The complex dielectric function can be described as

$$\epsilon_{in} = \epsilon_1 + i\,\epsilon_2 \quad (1.4)$$

where ϵ_1 and ϵ_2 refer to the real and imaginary parts of complex dielectric functions, respectively and the relation between the plasma frequency and dielectric functions has been derived earlier from the Lorentz-Drude model.[29] Thus described SPR play a crucial role in providing local field intensity enhancements in SERS experiments.

1.4. Surface enhanced Raman scattering

1.4.1 Introduction

Raman signal enhancement can be obtained when the analyte in trace amount gets in contact with the nanosized plasmonic metal surface through the excitation of surface Plasmons. The oscillations of surface Plasmons generate local field intensity enhancements under the influence of which an analyte molecule radiates more. If the excitation wavelength is closer to plasmonic absorption of metal nanomaterial resonantly enhances the Raman scattering.

The SERS effect was first observed by M. Fleishmann in 1974 for pyridine molecules adsorbed on silver electrodes. Albrecht and Creighton[30] proposed that the resonance Raman transitions from the electronic states of molecules those broadened due to the interaction of metal surface target might be responsible for Raman enhancements.[31] Single molecular (SM) detection was carried out by different groups Kneipp et al.,[32] Nie et al.[33] and Emory et al.[34] Researchers have reported[35-37] that the colloidal Ag and Au NPs have demonstrated enhancement factors (E.F.s) upto 10^7. Xu et al.[38] increased the E.F. up to 10^{11} in the presence of sharper edge of disintegrated spherical NPs and also recognized that the space between the Ag NPs demonstrated huge enhancement. Moreover, the plasmonic NSs such as Ag, Au and Cu, have been comprehensively used as active platforms for SERS[39-44] for trace level detection of various analytes. Similarly the plasmonic plating of silicon (Si) NMs substrates also demonstrated the SERS activity.[45-48] SERS is the proficient technique for the identification bio-molecules,[49-50] bacterial detection[16, 51-52] and explosive molecules in the trace level. [53-55]

1.4.2 Formulation for enhancement factor

In the later years people have demonstrated the SERS enhancement of the analytes through adsorption in colloidal Ag and Au NPs and they confirmed that the enhancement occurred under the effect of nanostructure and it is not because of surface effect.[56] The theoretical explanation of enhancement phenomena in SERS provides the better understanding of it.[57]

The power of the normal Raman signal (P_{NR}) scattered from the analyte depends on the scattering cross-section (σ_{NR}) and number of molecules (N_{NR}) involved which can be explained by the following equation

$$P_{NR} = N_{NR}\sigma_{NR}I_L \tag{1.5}$$

Here I_L is the excitation intensity of the Raman laser.

To formulate scattering power generated from the analyte molecule for SERS, we need to estimate the total field experienced by the molecule.

When the laser light interacts with molecule adsorbs on the NPs at distance of 'd', the molecule experiences two forces. One is incident field and other one is induced electromagnetic field (E_{SP}) which is generated by the excitation of surface Plasmons. The total electromagnetic field (E) can be described as

$$E = E_0 + E_{SP} \tag{1.6}$$

$$E = E_0 + E_0 \frac{\epsilon_{in}-\epsilon_{out}}{\epsilon_{in}+2\epsilon_{out}} a^3 \frac{1}{(a+d)^3} \tag{1.7}$$

There are two possible mechanisms responsible for the Raman signature enhancement in SERS process. First, number of molecules (cross-section) participating in Raman is more when these molecules are in close contact with metal NSs enables charge transfer between the NS and analyte molecule. This is known as chemical enhancement. Second, enhancement of Raman signal takes place due to local field produced through the surface Plasmons excitations which is known as electromagnetic enhancement.

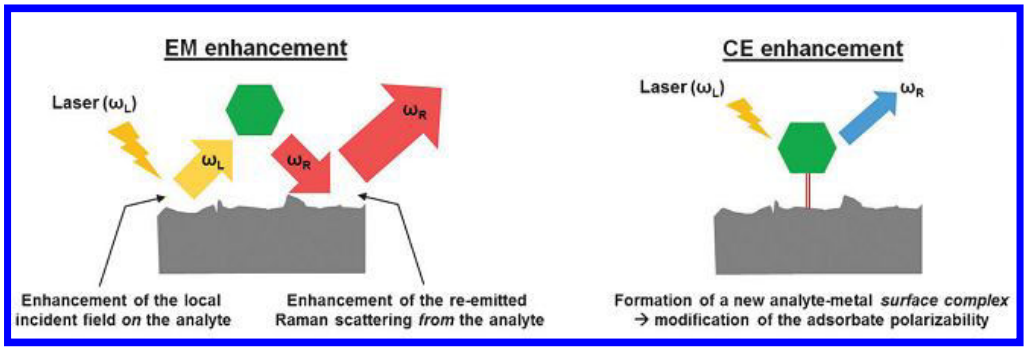

Figure1.1 Schematic of electromagnetic enhancement and chemical enhancement in SERS studies (adopted from ref. 55)

The scattering power of enhanced Raman signal is described as

$$P_{SERS} = N_{SERS}\sigma_{SERS}|A_L|^2|A_S|^2 I_L \quad (1.8)$$

Here, N_{SERS} is the number of molecules participated in recording to the SERS and σ_{SERS} cross-section of molecules adsorbed on NSs. A_L and A_S are laser and Raman signal enhancement factors, respectively.

The electromagnetic enhancement (A_S) for SERS signal is defined as the ratio of molecule experiences local field generated by NM and incident field

$$A_S = \frac{E}{E_0} \approx \frac{\epsilon_{in}-\epsilon_{out}}{\epsilon_{in}+2\epsilon_{out}}\left(\frac{a}{a+d}\right)^3 \quad (1.9)$$

When the real part of the dielectric function (ϵ_1) ≈ -2 ϵ_{out} and the imaginary part (ϵ_2) is small, resulting the huge electromagnetic enhancement for SERS.

The resultant electromagnetic enhancement factor is obtained when the excitation laser field is resonant with the condition of surface Plasmons, is given as[57]

$$G_{EM} = |A_L|^2|A_S|^2 \approx \left|\frac{\epsilon_{inL}-\epsilon_{out}}{\epsilon_{inL}+2\epsilon_{out}}\right|^2 \left|\frac{\epsilon_{in}-\epsilon_{out}}{\epsilon_{in}+2\epsilon_{out}}\right|^2 \left(\frac{a}{a+d}\right)^{12} \quad (1.10)$$

The above equation confirms that SERS enhancement factor depends on fourth power of local electromagnetic field produced by oscillations of surface Plasmons at resonance condition. The fabrication of NMs those possesses plasmonic behavior is a fast growing field to generate NMs with different dimensions and shapes. Many chemical methods are established to achieve NMs of required characteristics. Laser ablation of metal targets in liquid media is an efficient technique to produce NPs and NSs in single experiments.

1.5. Basic features of LAL

Many physical and chemical methods[58] have been studied/reported over the last decade for synthesizing metal/semiconductor NPs such as photochemical reduction, photo-reduction, electrochemical reduction, chemical reduction, solvothermal, electrolysis, green method, microwave-induced, sonoelctrochemical,

aerosol flow reactor, flame metal combustion, chemical fluid deposition, spray pyrolysis, and spark discharge, arc discharge, vapor deposition, electrochemical deposition, or ball milling, and laser ablation.

Laser ablation in liquid media[59-60] is a rapid and simple technique to fabricate NPs because of inhibited multistep chemical synthesis, long reaction times, and high bulk temperatures. Ultrafast laser ablation (ULA) of metallic target in liquid[61] guarantees extremely stable NPs without using chemical precursors with a highest degree of safety since fabricated NPs are in colloidal form rather than powders (hence, free of inhalation accidents). In the process of laser ablation, when a laser light is incident on material target, valence band electrons absorb visible/IR wavelengths and transitions occur from valance band to conduction band through different ionization processes such as tunneling process, multi-photon ionization process, combined effects of both process, Avalanche ionization etc. Some of these processes depend on the Keldysh parameter (γ)[62] which is the combination of ionization potential and gain energy (ponderomotive energy).

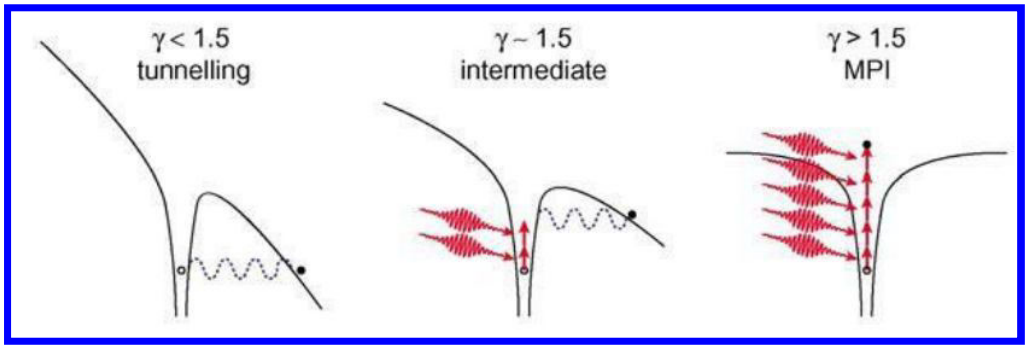

Figure 1.2 Schematics of Photo ionization process depending on the Keldysh parameter (γ) [adapted from ref. 64]. Red arrow - photons, black circles – electrons, open circles – holes and curvy lines-potential wells

Generally, Keldysh parameter plays a significant role in the ionization process[62-64] of the dielectric and semiconductor materials. For example when $\gamma < 0.5$, the system follows tunneling process to create free electrons. On the other hand, multi-photon ionization process leads to generation of free carriers where $\gamma > 1$. Nevertheless, we can also observe free electrons in the conduction band due to the dominant effect of combination of tunneling and multi-photon ionization processes when the condition $0.5 < \gamma > 1$ is fulfilled. These processes are illustrated in figure1.2. In general, the occurrence of free electrons in metals is attributed to the avalanche

ionization process which is the combination of free carrier absorption and impact ionization. This avalanche ionization process [illustrated in figure 1.3] occurs when the excited free electron impacts bound state electron resulting in production of two free electrons and this process repeats many times.

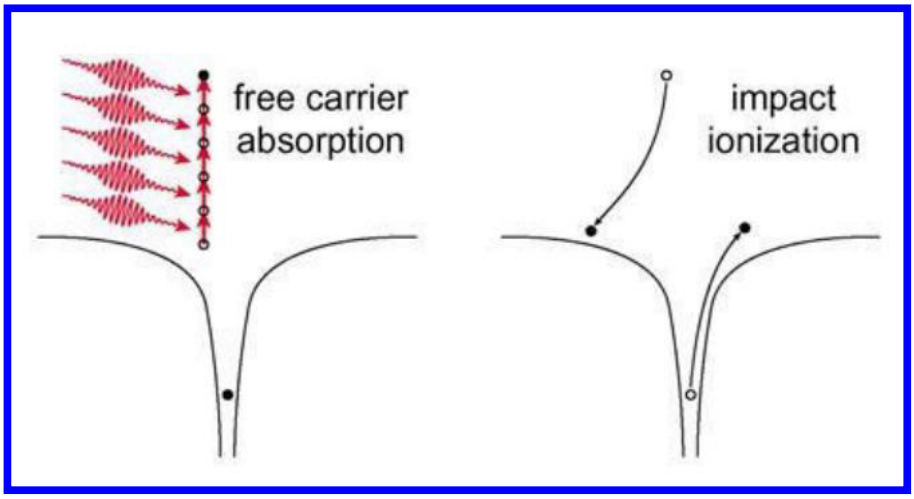

Figure 1.3 Schematics of Avalanche ionization process depending on the Keldysh parameter (γ) [adapted from ref. 64] Red arrow - photons, black circles – electrons, open circles – holes and curvy lines – potential wells.

1.5.1 Mechanism of Nanosecond Ablation

The repeated process of electron-electron collisions takes place by the above mentioned ionization processes for the specific material which absorbs nanosecond (ns) laser pulses (at t=0) and generates free carrier density. When the free carrier density is close to ~10^{22} cm^{-3}, the material generates electron plasma and shock wave which is typically on the time scale of ~10 ps – 100 ps.[65] This plasma oscillates with laser frequency which traps the incoming pulse energy and reflects back. Inside the plasma, collision between electron and lattice leads to higher temperatures at laser focused regions and moves toward the thermal energy distributions following the Fermi-Dirac distribution (carriers)[66-67] and Bose-Einstein distribution (lattice)[67] and reaches to thermal equilibrium quickly.[68] After that plasma expands in the form of plume and it gets quenched in the time scale of 0.1 ns – 100 ns which leads to the generation of cavitation bubble. The bubble starts to expand and finally collapses due to the large pressure differences inside the bubble in typically 1 μs – 100 μs time.[65] Consequently, material transits to a super critical fluid state and vaporization occurs which interacts with surrounding liquid media creating multifaceted structure of NMs

and possibility of agglomeration of NMs which takes more than 100 μs time.[65, 69] The timing diagram of laser ablation in liquids with ns pulses is illustrated in figure 1.4.

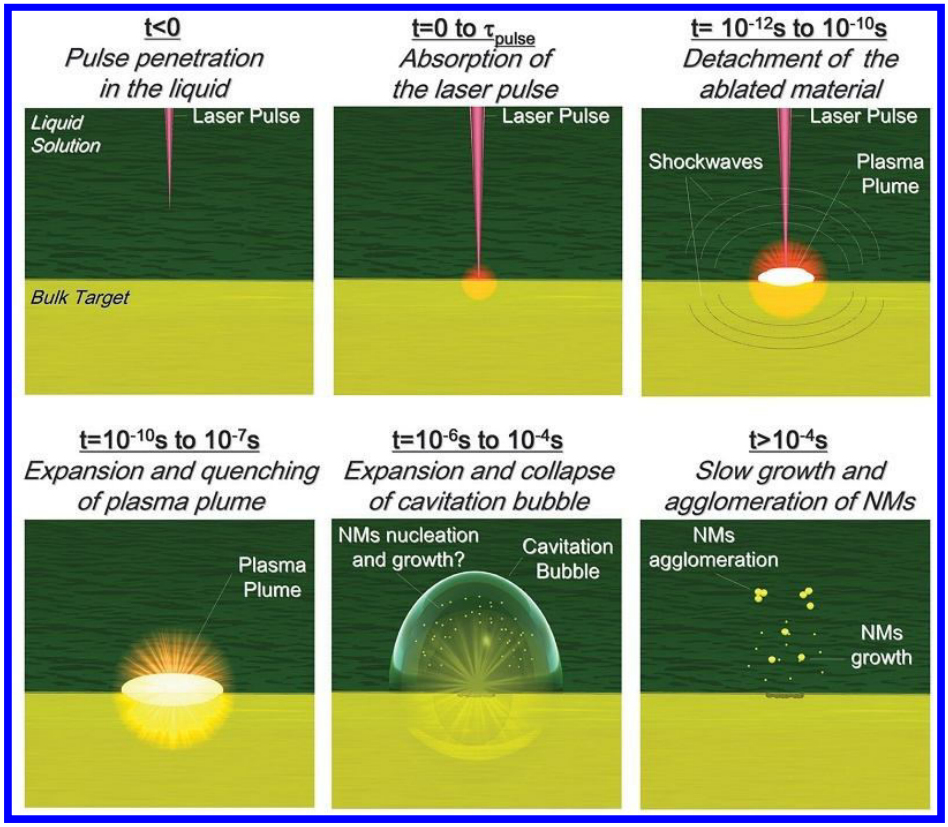

Figure 1.4 Typical timing diagram of ns laser ablation at different stages [adopted from ref. 65]

Some of the other possibilities of ns ablation have been proposed earlier by the other groups. The resolution of generated characteristics in ablation with ns pulses is that absorption of the laser pulse by material surface which can allow thermal vaporization and non thermal ablation.[70] This can be explained by heat diffusion length $l = (K \tau)^{1/2}$ where K is the thermal diffusivity of the material and τ is the laser pulse duration.[71] In general, the formation of micro/nano structures on metals will be inaccurate with ns pulses since the machining with ns pulses is connected to heat affected zone[70, 71] where the material experiences melting state at higher temperatures, followed by plasma formation which is created by lead part of the pulse. Since pulse width is large, plasma shielding occurs which absorbs the tail part of the pulse and releases some amount of pulse energy in the time scale of ~20 ns.[70] After that plasma detention takes place which allows generation of shock wave in ~1 μs time and plasma plume condensation and particle ejection in ~1 ms time.[70] Additionally,

invariable damage can occur on the material with longer pulses[70, 71] which causes the permanent change of optical property of material such as refractive index.

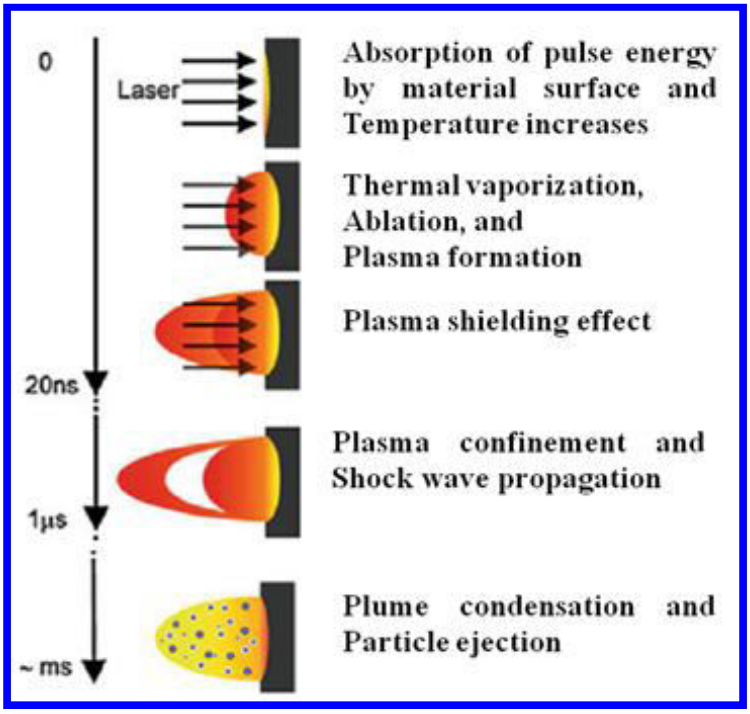

Figure 1.5 Nanosecond laser ablation of various processes with different time scales [adopted from ref. 70]

1.5.2. Mechanisms of Ultrashort Pulse Ablation

ULAL is a unique material processing technique[61] that provides distinct advantages in fabricating the NMs (NPs and NSs) in controlled geometry and size over the nanosecond and continuous wave (cw) laser ablation. In addition, ultrashort laser pulses allow less thermal damage and a nearly melt free ablation, if carried out close to ablation threshold. After the manufacturing of femtosecond (fs) and picosecond laser (ps) (<5 ps) with high peak intensity ~10^{12} W/cm^2 in the focal region, the absorbed laser energy can be heavily induced into the target at focal point resulting in high efficiency of material ablation. In the process of absorption and relaxations with excitation of fs pulses, various scattering effects can be observed in different time scales. When the fs pulses interact with materials, material absorbs the energy by inverse bremsstrahlung[70,72] and following the aforementioned ionization process in the time of ~10-100 fs. The excited electrons collide with each other (or) bounded electron resulting the production of high conductivity. This phenomenon is

described as electron-electron scattering (or coulomb explosion) which occurs in ~1ps time scale.[68,73] After that electrons transfer their energy to lattice through electron-lattice coupling and the corresponding characteristic time is up to ~10 ps.[68, 73]

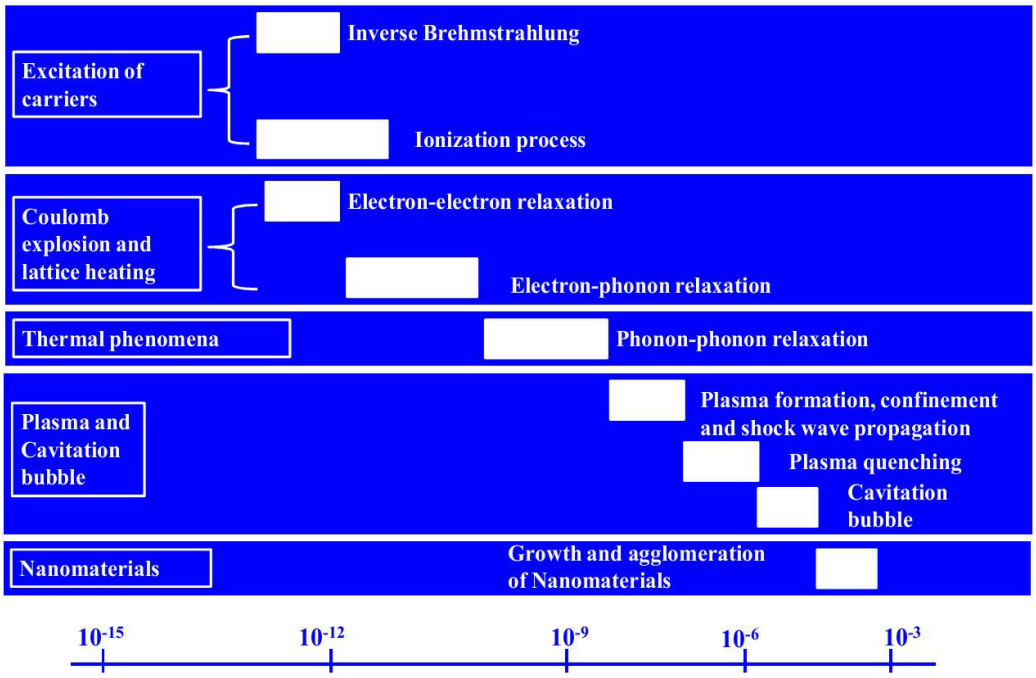

Figure 1.6 Typical timing diagram of fs laser ablation for various stages.

Consequently, thermal diffusion will take place inside the lattice via phonon-phonon scattering which could be after 10 ps and upto ~1 ns time. The electron-electron, electron-phonon and phonon-phonon relaxations can be explained by two temperature model.[67, 72] Further stages are followed by plasma formation[70] and plume quenching (~100 ns – 1 μs), formation and collapse of cavitation bubble (1 μs – 200 μs) [74] and NMs formation in liquid media (~1 ms).[70] The details dynamics of ablation in ultrashort pulse regime was demonstrated in figure 1.5.

1.5.3. Two temperature model

Thermalization takes place inside the system through the absorption of ultrashort pulses by metals/semiconductors following the electron-electron scattering and electron-phonon scattering process. The scattering processes can be characterized by two temperature model (TTM)[72, 75]

$$C_e \frac{\partial T_e}{\partial t} = -\frac{\partial}{\partial z}\left(k_e \frac{\partial T_e}{\partial z}\right) - g(T_e - T_l) + S(z,t) \qquad (1.11)$$

$$C_l \frac{\partial T_l}{\partial t} = g(T_e - T_l) \tag{1.12}$$

$$S(z,t) = I(t) A \alpha \exp(-\alpha z) \tag{1.13}$$

where, C_e, and T_e, C_l and T_l describe the specific heats and temperatures of electron and lattice, respectively, whereas k_e and g are conductivity of electron and electron-phonon coupling constant, respectively, S is the laser energy term which consists of laser intensity I (t). 'A' and 'α' are surface absorptivity and absorption coefficient, respectively.

Some authors have simulated the above equations since these cannot be solved analytically. Chichkov et al.[72] have solved aforementioned TTM equations by assuming some initial conditions. In the case of ultrafast laser pulses (<5 ps), there are three types of relaxations times that have been predicted such as electron-electron relaxation time (τ_e), electron-phonon coupling time (τ_l) and phonon-phonon relaxation time. To solve the equation (1.1) and (1.2), we assume that first, the pulse duration (τ) is much less than electron-phonon coupling time, i.e. $\tau << \tau_l$ which allows to neglect the term g (T_e - T_l) from equation (1.1). Second, $T_e >> T_l$ for the initial few ps time since no diffusion could take place in to the lattice, which may ignore diffusion (temperature gradient) term (or) first term from equation (1.1). Consequently, equation (1.1) is modified which can be described as

$$C_e \frac{\partial T_e}{\partial t} = I(t) A \alpha \exp(-\alpha z) \tag{1.14}$$

Here, $C_e = CT_e$ where C is constant and I (t) is assumed to be constant I_0. Substitute both C_e and I_0 in equation (1.4) and the resultant equation is illustrated as

$$C \frac{\partial T_e^2}{\partial t} = 2 I_0 A \alpha \exp(-\alpha z) \tag{1.15}$$

The analytical solution of the equation (1.5) is

$$T_e(z,t) = \left(\frac{2 I_0 A \alpha}{C} t \exp(-\alpha z) + Constant\right)^{1/2} \tag{1.16}$$

For getting the constant and final equation to consider the initial condition t=0, $T_e(z,t) = T_0$ (room temperature).

$$T_e(z,t) = \left(T_0^2 + \frac{2I_0 A\,\alpha}{C} t \exp(-\alpha z)\right)^{1/2} \quad (1.17)$$

After the complete of entire pulse length t=τ, the equation is modified as

$$T_e(z) = \left(\frac{2F_0 A\,\alpha}{C} \exp(-\alpha z)\right)^{1/2} \quad (1.18)$$

where, $F_0 = I_0\tau$ and $T_e >> T_0$

The lattice heating starts when the electrons begins to deposit energy into the lattice through electron-phonon coupling which would be owing to the fast cooling of electron system and it is very small. The time dependent lattice temperature can be determined from the equation (1.2) by assuming the initial temperature of lattice is ignored. The obtained equation is described as

$$T_l(z,t) \approx T_e(z)\ {}^{t}/_{\tau_i} \quad (1.19)$$

where $\tau_l = C_l/\gamma$

The feasible lattice temperature is derived by considering the average electron relaxation time which is half of the electron relaxation time[72] at the end of the pulse and it is expressed as

$$\tau_e = {}^{C_e}/_{\gamma}\,, \qquad \tau_e^a = {}^{CT_e(z)}/_{2\gamma} \quad (1.20)$$

The resultant equation of the lattice temperature can be obtained by substituting equation (1.10) in equation (1.9) and it is given by

$$T_l(z) \approx \frac{F_0 A\,\alpha}{C_l} \exp(-\alpha z) \quad (1.21)$$

Based on this model when the material interacts with ultrashort pulses, the energy is absorbed by electron system through multi-photon absorption at $T_e = T_l = T_0$ and they get heated upto maximum temperature. At $T_e >> T_l$, electron system starts to cool and transfer its energy to lattice system within tens of ps.[68,73] After few tens of ps, lattice temperature reaches maximum which will be greater than electron temperature ($T_i >> T_e$) and generates plasma (ionic state) and heat gets diffused in the material

(which is neglected in our case).[72] This TTM model is diagrammatically explained in figure 1.6.

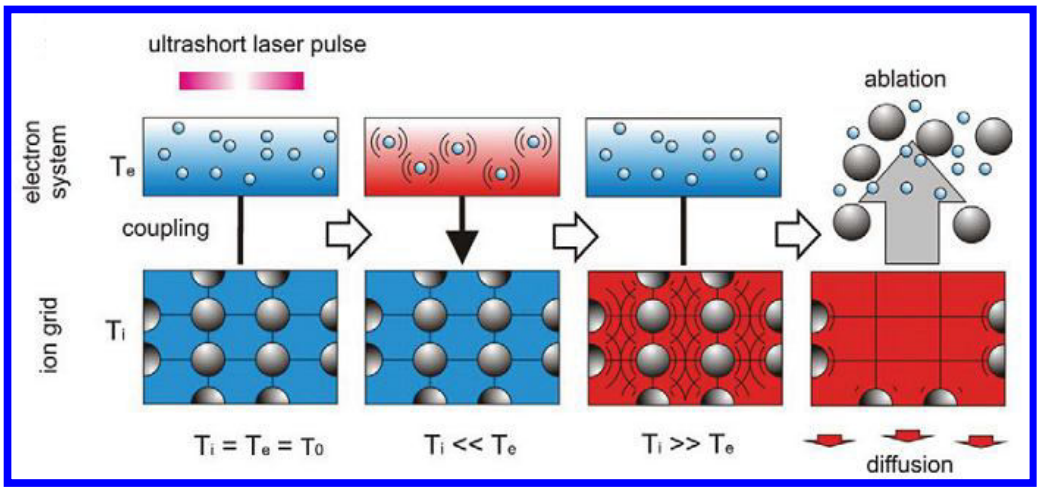

Figure 1.6 Sketch of two temperature model in ULA [adopted from ref. 76]

In the last two decades, several researchers have investigated the electron transient dynamics under influence of ultrashort pulses for metals and reported that the electron cooling time could be below 10 ps.[68,73] The product $C_l\, T_l$ will provide the information about solid-vaporization effect which could be greater than heat evaporation product $(\rho\Omega)$ when large evaporation takes place. The above mentioned equation (1.11) can be written as

$$C_l T_l(z) \approx F_0 A\, \alpha \exp(-\alpha z)$$

Since $C_l T_l(z) \geq \rho\Omega$,[72] $\qquad \rho\Omega \leq F_0 A\, \alpha \exp(-\alpha z)$

$$F_{th} \leq F_0 A \exp(-\alpha z) \tag{1.12}$$

Where $F_{th} = \frac{\rho\Omega}{\alpha}$, ρ = density of material and Ω = heat of evaporation

The modified equation of applied fluence is given as

$$F_0 \approx F_{th} A \exp(\alpha z) \tag{1.13}$$

The ablation depth (L) is defined from equation (1.13) when z=L, given by

$$L \approx \frac{1}{\alpha} \log\left(\frac{F_0}{F_{th}}\right) \tag{1.14}$$

According to TTM ablated mass of the material,[76] can be determined under the effect of ultrashort pulse ablation by considering the ablation depth which is described as

$$M = N \rho A \left[\frac{1}{\alpha} \log\left(\frac{F_0}{F_{th}}\right) \right] \quad (1.15)$$

Here, N refers to number of pulses.

1.6. Mechanism of metal ablation in liquids

Formation of NPs or NSs is the resultant of a complicated interaction between generated plasma plume and liquid media adjacent to it. This interface dynamics lead to diverse mechanisms such as (a) spallation (b) spinodal decomposition (c) phase explosion and (d) fragmentation and vaporization. These processes are followed by (e) plasma ablation and (f) coulomb explosion.

1.6.1. Spallation

Spallation is the fragmentation of the material under the influence of stresses developed due to the impact of laser pulse. Spallation occurs due to the propagation of tensile stress wave through a material which produces defects in the material. These defects enhance the probability of fragmentation. The removal of large metallic fragments under the influence of photomechanical effects[77] those driven by afore-described laser-induced stresses. The amount of laser induced mechanical stress prevails due to confinement of stress.[78] This stress confinement is predominant when the pulse duration is shorter compared to mechanical equilibration time of absorbing focal volume. Spallation occurs in solid phase of the material when the laser pulse energy is equal to the ablation threshold[79] of the material. Likelihood of spallation is higher when solid target immersed in liquid media.[80]

1.6.2. Spinodal decomposition

When a laser beam at higher fluence incident on a solid target, absorption of laser energy rises the temperature of the target locally (at the laser impact). Phase of the material can be described on the basis of the attained temperature whether it is below or above the critical temperature of the material. The molecular dynamics simulations [81] describe these mechanisms using two temperature model that the initial homogeneous phase become a mixture of gas and liquid droplets below the critical

point. Later, the liquid droplets combined to form big clusters. At higher fluences, the surface temperature of the clusters rises beyond the critical temperature. If the target surface layer is heated below the critical temperature [but above the melting temperature (T_m)] the material vaporizes. Material maintains in the vapor state upto attaining the saturation pressure (typical time scales ~1–10 ns),[81] later vaporized material re-solidifies due to thermal conductivity,

1.6.3. Phase explosion (Explosive boiling)

Nadezhda et al.,[82] Miotello et al., Kelly et al.[83] confirmed that phase explosion is very important mechanism in the ultrashort pulse ablation process which remove the molten droplets of the metal in short time. Phase explosion initiates with bubble nucleation below the critical temperature. In the case of ULAL, there many possibilities to the formation of bubbles in the focal region: Explosive boiling prevails when the heating process of metal melt and liquid interface is fast enough. Due to this molten drop behaves as a super saturated liquid. Explosion of this super saturated molten drop produces the NPs.

1.6.4 Fragmentation

Additionally, phase-explosion, fragmentation[68,84] may also take place within the interface of liquid-target. Below the critical temperature, the expansion of super heated volume at focal region produces expandable energy in super critical fluid[68] at liquid-target interface. This expandable energy facilitates the fragmentation[74] of the material.

1.6.5 Plasma ablation and coulomb explosion

Earlier reports[70] demonstrated the utility of emission spectroscopy, which describes the information of plasma plume [comprising electrons, atomic species, and ionic species those generated by direct ionization, sublimation and electron emission (typically in ps time scale)]. When the input fluence is above the threshold fluence of plasma formation, a straight forward phase transition occurs from solid state to plasma state. After that the plasma plume expands and generates a shock wave. In the case of ablation of metal in liquid media, the combined plasma is generated at interface of liquid-target. At focal point the expansion of plasma plume is confined strongly in solution. Confinement of plasma affects the thermodynamic, kinetic

properties of plasma plume and products. The localized thermal properties such as temperature, pressure are higher during the expansion of plasma plume. At this stage confined plasma removes the fragments from the target surface. At extreme electron temperature (T_e), coulomb explosion is another way of inducing the fragmentation to generate the nano-entities.[68, 70]

1.7. Cavitation bubble dynamics

During ULAL, plasma generation will occur at a particular stage and it starts to expand which generates the shock wave. In the development of shock wave, the expansion of plasma in the plume form moves into the surrounding liquid media and it gets quenched within the time scale of 100 ns[65] resulting in the formation of a bubble. This bubble is known as the cavitation bubble (CB). The bubble takes an action in the form of radial motion due to driving pressure in the form of a sinusoidal.[85] When the rarefaction part of the pressure field interacts with medium, the size of the bubble is enlarged which is owing to increase of pressure inside the bubble and this pressure will be more than surrounding pressure.[85,86] As in the case of compression part, the size of bubble slightly decreases due to pressure rise inside bubble is slow. The time evolution of cavitation bubble schematic is demonstrated in figure 1.7.[87]

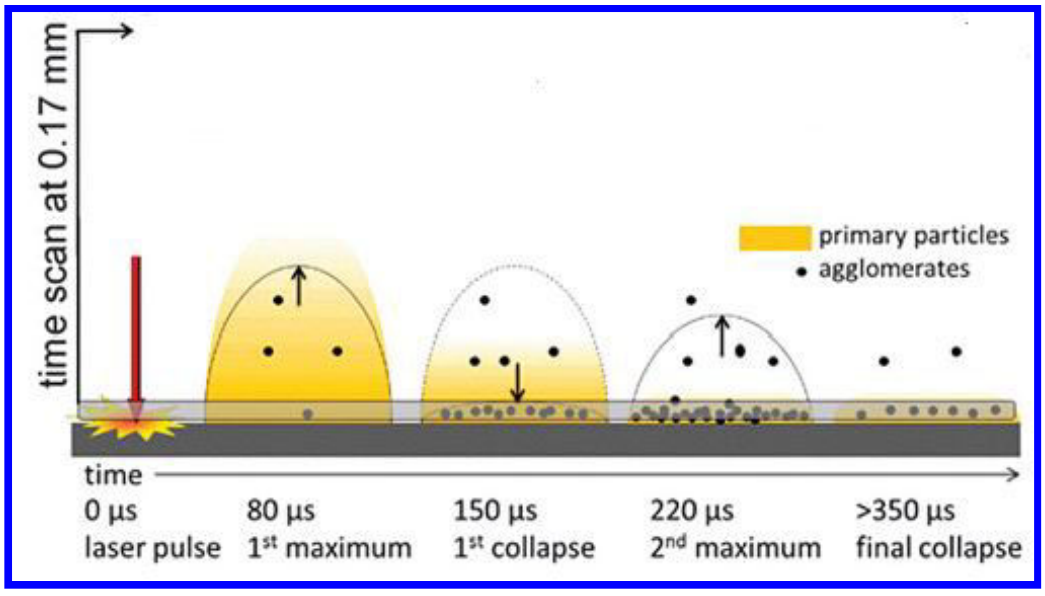

Figure 1.7 General schematic of Cavitation bubble dynamics in laser ablation for growth and agglomerated NPs [adopted from ref. 87]

After few μs the continuous growth of cavitation bubble occurs although in the form of compression and rare factions. During the bubble growth, bubble contains nano-sized ablated material.[65, 74, 87] However, the rapid growth of the bubble followed by collapse typically occurs in the time scale of 10 μs – 300 μs. During the expansion of CB into surrounding liquid media exerts pressure on metallic plume. This recoil pressure splashes the metal plume into nanoparticles. [87] Transient dynamics of the plasma can prompt composite material fabrication due to it's interaction with the liquid medium surrounding it.[88] Subsequently, the vaporized material fragments re-solidify (generation of NPs) over a timescale[88] of few hundred of μs. During the process of (CB's) expansion, temperature gradient in the inner and outer surfaces of CB leads to condensation, growth of NPs. The detailed discussion and numerical calculation on the liquid influenced cavitation bubble generation is presented in chapter 3. The production of nano-entities are influenced by liquid parameters such as surface tension, viscosity, density, refractive index etc

1.8. Effects of the laser parameters on the generation of Nanomaterials

The fabrication of nano-entities is not only effected by the liquid properties and also influenced by the laser parameters for example wavelength, pulse energy (or) fluence, pulse number, pulse width etc.

1.8.1. Effect of input wavelength

Ablation depth of the material depends on the wavelength of incident laser (wavelength determines the skin depth of a material). The photons with higher energies (shorter wavelengths) ionizes/breaks the bonds in an easier manner compared to photons with lower energies (longer wavelengths). Several works have demonstrated the effect of ultraviolet (UV) wavelengths on ablation in which UV photons stimulated inter-band transitions. The uniform absorbance of UV photons by the target material provides fine structures on the surface. In the case of near infrared radiation, random surface structures prevailed due to the absorption of NIR photons by the defects/impurities present in the material. In the ablation experiments, one has to take care in selecting input wavelength to avoid unwanted absorption of incident laser energy by the generated NPs in liquid. The wavelength below the SPR (of the

NPs under interest) should be chosen as working wavelength. This kind of absorption leads to an unpredictable modification of NPs[89].

Mortazavi et al.[89] documented the differences in size distribution of Palladium (Pd) NPs in de-ionized water at excitation wavelengths 1064 nm (Nd: YAG) and 193 nm (pulse duration ~6 ns). They observed an aggregation of NPs (case of 1064 nm) due to thermal effects induced by the confined plasma and hence larger sizes. In the case of ablation with shorter wavelengths, obtained average sizes were less. Schwenkeet et al.[89] also obtained better yields at 1064 nm ablation compared to 532 nm ablation. Moreover, excitation wavelength in ablation determines, cross-section of inverse Brehmstrahlung (CSIB) which strongly affects the cascade ionization since CSIB directly varies with the second power wavelength.[90, 91]

1.8.2. Pulse duration effects

Ablation dynamics strongly determined by the duration of the incident laser pulse. For longer pulses thermal effects determine the fabrication of NPs, NSs where as for shorter pulses non-thermal processes prevail. In the case of ablation with laser pulses at longer duration (μs to ns), thermal processes such as explosive boiling[92] and evaporation succeeds the electron-lattice collisions. Due to longer interaction times of laser pulses, heat diffuses to lattice in a very short period of time compared to its duration (μs or ns). Due to the generation of enormous heat energy materials transits to super heated liquid state (locally). Subsequently, super heated metallic melt evaporates and finally condensates. This condensation result in the fabrication of NPs.

In the case of ablation with longer pulses (μs or ns pulses) thermal effects influence the ablation and provide longer HAZ where as non-thermal ablation results in minimal HAZ [92]. Craters with different depths and morphology were observed in case of Al target ablation in water ~7 ns, and ~40 fs laser pulses.[92] In the case of ablation with longer pulses prolonged heating results in the highest degree of corrugation (HAZ). Moreover, plasma shielding,[92] in which trailing part of the pulse interacts with the generated plasma (by the leading part), results in unpredictable modification of the nanomaterials. Niu et al.[92] experimental studies elucidated the influence of longer pulses (ms) on surface reactions of metal droplets fabricating hollow spheres, core-shell nano-spheres, hetero structures, nano-cubes and nano-

wires. Ablation with ns pulses has been explored extensively and huge amount of experimental work is reported in the last two decades.[92] Only few reports[93] have explicitly been described the ultrafast dynamics of ULAL.

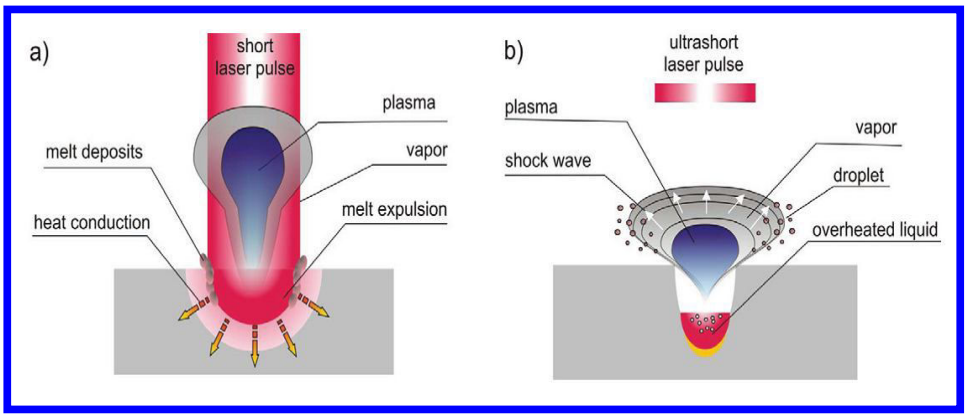

Figure 1.8 Major differences obtained in the laser ablation with (a) longer pulses and (b) ultrashort pulses (adopted from ref. 76)

Ultrafast ablation dynamics are mediated by multi-photon induced absorption and cascaded photo-ionization (avalanche). Ultrashort ablation avoids the residual interaction of the pulses with the generated plasma plume. Ultrafast ablation can be treated as an isochoric process in which target surface gets local modification while the remaining volume of the material maintains at lower temperature. This is due the extreme short time of the pulse in the medium. Acceleration of the ionized entities in the ultrafast ablation leads the development of higher pressures, temperatures at the point of laser impact. In this case continuous evaporation of material cannot be possible due to very short time of interaction. Consequently, material transforms to an overheated liquid state. Condensation of overheated molten drops result in the fabrication of NPs and NSs (with minimal HAZ) in ultrafast ablation.[93]

Barmina et al.[93] fabricated Tantalum (Ta_2O_5) NPs with laser pulses of duration 350 ps, 5 ps and 180 fs at ~1064 nm, 248 nm, and 800 nm respectively. They described the direct dependence of pulse duration than wavelength on nano-structuring of Tantalum. More over periodic structures were obtained in the case of ~180fs while it was not observed in the case of ablation with ~350 ps, ~ 5ps pulses. Similarly differences between longer and short pulse ablation was documented by Barcikowski et al. [93], Leitz et al.[93]. They found that fs ablation in water was 20% more proficient than ps laser ablation but due to higher power ps laser (higher

repetition rate), the productivity of NPs three fold enhancement for ps ablation. Their study demonstrated that fs (120 fs, 5 kHz) ablation was prominent to generate 2 μg of NPs/Joule where as it was 1.5 μg for ps (10 ps, 50 kHz) pulses. Additionally, rate of generation in the case of ps ablation (34 mg/h) was higher compared to fs ablation (6 mg/h). Recently, Riabinina et al.[93]observed that optimal yield of Au NPs were obtained in the case of ablation with 2 ps (5 mJ energy). Barmina et al.[94] studied NPs of Titanium (Ti), Nickel (Ni), Molybdenum and (Mb) in water by using Ti: Sapphire laser (180 fs, 1 kHz 355 nm). The average size of NPs was estimated to be 50nm, 100 nm, 220 nm for Ni, Ti, Mb respectively. Sylvestre et al.[95] examined gold NPs in different aqueous media namely water, KCL, NaCl, NaOH, and Propylamyne with Ti: Sapphire laser pulses (120 fs) and operating at 1 kHz rep rate. Gold NPs of different sizes 1-250 nm (Water), 1-12 nm (NaCl), 1-15 nm (KCl), 1-18 nm (NaOH) were reported in different media. The study elucidated that NPs of different sizes were formed on changing the medium. Boulais et al. studied plasma generation via the synthesis of gold in water by using Ti: Sapphire (800 nm, 45 fs, 1 kHz) pulses.[96] Barchanski et.al discussed the bi-conjugation of gold nano particles in double distilled water using Ti: Sapphire laser operating at 800 nm with pulse width of 120 fs.[97] Moreover, ultrafast ablation of gold nano NPs have been reported extensively by other groups.[98,99] Besner et al, investigated post fragmentation size of NPs and reported as 5-20 nm (15 mint.) 11±5 nm (30 mint).[100] The Besner group inspected the abundance of large nanoparticles in polymer solution with Ti :Sapphire (800 nm ,110 fs, 1 k Hz) and reported that the abundancy decreased as the dextran concentration increased from 0.01 to 1 g/L.[100] Tan et.al, studied Zirconia properties in water with Ti-sapphire laser of 120fs pulse width and Raman data was discussed.[101] A. Menendez-Manjon et al.[102] studied Ag NPs in de-ionized water and stated that variation of hydrodynamic size of the particles changes during the prolonged ablation and reaches a more stable level. Stratakis et al.[103] generated NPs of Al in ethanol by employing Ti: Sapphire laser (800 nm, 200 fs, 1 k Hz; 30 ps or 150 ps) and average size of NPs was 10-60 nm. Our group examined the effect of polarity of the liquid medium on the generation of Al nano particles in CCl_4 and $CHCl_3$ with 40 fs pulses and 1 k Hz repetition rate.[104] Additionally, we have investigated Cu NMs, Ag NMs and Si NMs under the effect in different liquid media, pulse numbers and pulse energy, respectively.[104]

1.8.3. Effects of energy per pulse, spot size, and fluence

Fragmentation of a material is determined from the energy of incident pulse. ULAL affected by the generated primary, secondary, ballistic electrons those produced due to the absorption of pulse energy by the quasi-free conduction electrons in the surface of the material. Density of the aforementioned electrons influences the plasma dynamics and hence the fabrication of NPs, NSs. Simulation studies of Zhigilei et al.[105] revealed the effect of laser parameters on the ablation productivity of NPs. They found that the productivity of NPs directly varies with the incident pulse energy. Higher input energies supports the generation of large melt reservoirs and hence higher yields of NPs.

Similarly, effective spot diameter at the focus affects the ablation products. At the central part of the beam waist mechanism of fragmentation dominates while at the edges thermal mechanisms occur. This is due to the absorbed energy density per unit time by the material at the focal plane is determined by the gradient of the Poynting vector.[105] At tight focusing conditions, entire energy may increase the productivity of the NPs but simultaneously result in poor structuring with sharp boundaries since tight focusing leads to an inhomogeneous gradient of temperature and pressure. In the case of a moderately focused laser beam, the gradient of the pressure and temperature are smoother leads to fine ablation of the target surface.

Beam waist at the focus and energy per pulse both determines the laser fluence and this combined effect influences the material ablation in a different way. Elsayed et al.[105] also investigated the fabrication of gold NPs in water at different fluences (10 ns pulses) and discussed increment and decrement of sizes and yields (gold NPs) at certain fluence. Kabashin et al.[105] investigated the effect of fluence (110 fs) in the fabrication Au NPs in water. Their observation demonstrated that the yield of Au NPs were good at higher laser fluences (1000 J/cm^2) than at lower fluences (60 J/cm^2). Moreover, distribution of NPs was observed to be good at the lower fluences than higher fluences. Intermediate fluences were providing both smaller and larger NPs. Barsch et al. reported[105] the fabrication of Ag, Cu, Mg and ZrO_2NPs with ps laser pulses. They attempted to fabricate the above mentioned metal and ceramic NPs at different fluences and focal positions.

1.8.4. Effect of number of pulses

Other promising parameter is the number of laser pulses per spot which strongly affect yield, size distribution of the NPs. Additionally, pulse number affect the structure of the ablated metal surfaces. In the case of multi-shot ablation Beer Lambert's relation do not hold good since the reflectivity diminishes during the first few pulses.[106] Multi-shot ablation is due to the interaction of N pulses at same place resulting change of optical properties of the ablated volume.[106] This is also known as incubation effect. The incubation effect dramatically decreases the threshold fluence required to damage a material to a great extent. Many authors documented incubation effects experimentally on different materials in fs, ps and ns domains.[106] In the fs ablation incubation influences micro and nanostructure formation. Jee et al.[107]suggested a model proposed according to which the deposited laser energy introduce plastic strain within the material through thermal effects. In this model they explained the modification of Cu target under the influence of incubation. Many thermal effects (causes induced plastic strain, re-crystallization, amorphization, oxidization) have been proposed to elucidate incubation mechanism for metals.[106]

This pulse accumulation process was described by thermal stress-strain induced on the target. However, for metals and semiconductors irradiated by ps/sub-ps pulses the incubation is determined by laser-induced defects. Effect of incubation can be understood from the following equation[108]

$$F_{Nth} = F_{1th} N^{S-1} \qquad (1.16)$$

where $F_{N\,th}$ is the fluence threshold at N number of shots, F_{1th} is the fluence threshold at single shot, N is pulse number and S is the incubation factor. In this model incubation is explained by cumulative ablation. S<1 denotes the presence of incubation. When S=1 the ablation threshold does not depend on the superposition of incident pulses and for S>1, the material becomes more resistant to ablation.[107, 108] There are some other models which described the incubation mechanisms in dielectric materials,[106-108] by an exponential decay accumulation model.[106-108] The exponential decay model can be written in the following equation

$$F_{Nth} = F_{\infty th} + (F_{1th} - F_{\infty th}) \exp\left[-S\,(N-1)\right] \qquad (1.17)$$

where $F_{\infty th}$ is the fluence threshold at infinite number of shots. In earlier studies, the ablation threshold was calculated from the damaged volume (due to incubation) in metal, semiconductor and dielectric as a function of the laser fluence at different pulse number. Incubation can be studied from overwriting of the line structures [determined from pulse to pulse spacing (d), separation between the line structures]. In this case effective pulse number (N) can be obtained from w_z/d which enables the investigation of incubation effect in nano-grating formation.[108] The efficiency of the input energy coupling with the surface structures through the established surface Plasmons also increases and thereby induce losses in reflectivity of the input beam.[106]Leitz et al.[93] discussed the effect of number laser pulses in the crater formation for microsecond, ns, ps and fs pulses and diameter of the holes formed were increased to a greater extant and blurred in the case of micro (1000 pulses) and ns (250 pulses) ablation, to a smaller extent in the case of ps (500000 pulses), fs (5000 pulses).

1.9. Outline of the thesis

The thesis is organized as follows

Chapter 1 In this chapter, the basic physics of laser–matter interaction and the dynamics of ultrashort pulse laser ablation in liquids are described. Some of the important models for ULAL such as two temperature model in comparison with one temperature model used for describing ns ablation along with different aspects of cavitation bubble are included. A brief survey of metal/semiconductor NMs fabrication via ULAL is comprehended. Furthermore, review on the applications of metal/semiconductor NPs/NSs in SERS, surface enhanced fluorescence (SEF), anti-microbial activity, photonics is presented. The relevance of excited state dynamics studies in NPs is explained. The motivation for the present work is also provided in this chapter.

Chapter 2 This chapter contains detailed information of experiments and equipment utilized for various studies carried out in this thesis. These include fs Ti:sapphire oscillator (MICRA), ps and fs Ti:sapphire amplifiers. Pulse characterization methods such as intensity auto-correlation and bandwidth measurements are explained. Experimental details of ULAL of metal/semiconductors along with critical parameters of the experiment are extensively discussed. Additionally, characterization

techniques such as Transmission electron microscopy (TEM) and high resolution TEM, selected area electron diffraction (SAED), energy dispersive X-ray analysis (EDAX), field emission scanning electron microscopy (FESEM), UV-Vis absorption spectroscopy, Raman spectroscopy and photoluminescence methods are briefly described. Discussion on the experiments of (a) SERS (b) SEF (c) NLO properties by Z-scan and degenerative four wave mixing, and (e) degenerate pump-probe experiment are included in chapter 2.

Chapter 3 In this chapter, we present results from extensive investigations on (a) the effect of different liquid media including the fabrication of Cu NPs and NSs of different morphologies on the Cu surface in acetone, dichloromethane (DCM), acetonitrile (ACN) and chloroform by ps ablation of multiple/single line ablation (b) influence of laser pulse energy (25-400 μJ) on the fabrication of CuO NPs and Cu surface structures when ablation was carried out in acetonitrile (ACN) with ~2 ps pulses at 800 nm. Effects of liquid properties influencing the ablation are discussed. The influence of liquid media led to generation of Cu, CuCl, CuO and $CuCl_2$ NPs. The ablation products were NPs/NSs of different nature, sizes and yield depending on the properties of chosen liquid media and pulse energy. The influence of liquid medium on generation of cavitation bubbles with different dynamics is explained. A simple numerical study of the dynamics of cavitation bubble was also carried out. From the results obtained we could estimate the periodic growth, collapse time of the bubble and maximum radius for different organic liquids (c) effect of pulse numbers on the fabrication of fabrication of Cu HSFL/LSFL structures in methanol and random NSs in acetone with ~2 ps pulses and ~40 fs pulses, respectively were carried out at 800 nm. The mechanisms involved on the production of LFSL/HFSL of periodicity ~λ/3 - 2λ/3 on Cu surface with ~2 ps pulses and Cu NSs with different morphologies with ~40 fs pulses was explained in detailed.

Chapter 4 In this chapter the following experimental results are discussed: (1) effect of liquid media on generation of Si NPs of different morphologies and LIPSS of Si in acetone, DCM, water and chloroform with ~2 ps pulses at 800 nm. (2) Effect of input pulse energy (10-500 μJ) on fabricated Si NPs with diverse morphologies and LIPSS formation under double/multiple line ablation acetone with ~40 fs pulses at 800 nm. The obtained results are explained using the effective fluence at the target surface by estimating the beam waist on the target. In addition, cavitation bubble dynamics with

respect to the input pulse energy and their dynamics such as oscillation and collapse which majorly influence the size of NPs are also explained (3) Si HSFL/LSFL structures in acetone with the effect of pulse number with ~2 ps pulses and at 800 nm. In this study the input laser beam passed through a hard edge circular aperture and utilizing diverse scanning speeds (modulation of pulses per spot on target) we studied the ablation mechanism. Complete details on the production of LFSL/HFSL of periodicity ~λ/2-λ/8 on Si substrates obtained due to the effect of scanning speeds (25-600 μm/sec) are discussed. The experimentally measured periodicity of LFSL/HFSL was agreed with theory.

Chapter 5 In this chapter, applications of Cu nanomaterials for SERS and SEF are included. Particularly, in SERS studies (a) detection of explosives such as ANTA from Cu NSs fabricated using ultrafast multiple/single line ablation of Cu target in acetone, DCM, ACN, and chloroform (b) multiple utility of SERS active Cu nanostructured targets followed by a simple cleaning procedure for detecting TNT and R6G molecules (c) detection of 1,1-diamino-2,2-dinitroethene (FOX-7), CL-20 and ANTA from the Cu NSs fabricated using different pulse energies in ACN, (d) the identification of FOX-7 and R6G molecules from the Cu NSs fabricated with effect of pulses number in acetone (e) Ag metal plating on Si NSs were also utilized for SERS activity to the detection of ANTA molecule of 1 μM concentration. Furthermore, (f) for CuCl NPs in chloroform SEF studies were carried out by mixing them with tritolyl corrole (TTC) and triphenyl corrole (TPC). Large enhancement factors (10^5-10^7) were obtained in these studies and the clear details are provided in this chapter.

Chapter 6 This chapter includes results from the studies of NLO properties of Cu/CuCl/CuO/$CuCl_2$ NPs and corrole conjugated Cu NPs performed with Z-scan technique using ~2 ps pulses and DFWM technique with ~40 fs laser pulses. NLO properties of Si/Si-C/SiO_2 NPs using fs Z-scan technique at 800 nm are also included in the chapter. The sign and magnitude of nonlinear refractive indices were derived from the closed aperture Z-scan data. Third order NLO susceptibilities [$\chi^{(3)}$] were obtained in ps Z-scan data and fs data from the DFWM data. We could observe intensity dependent saturable and reverse saturable absorption at the excitation wavelength of 800 nm. Our studies in the ps domain provide sufficient evidence that these molecules possess superior nonlinear coefficients required for applications in

optical switching. Additionally, preliminary results from the excited state dynamics of Cu/CuCl/CuO/$CuCl_2$ NPs and Si/Si-C/SiO_2 NPs, investigated using degenerate pump-probe technique using ~70 fs pulses at 600 nm are also included in this chapter.

Chapter 7 This chapter summarizes conclusions drawn from the work presented in this thesis and presents some of the future prospects of these techniques and materials.

References

1. G. Ross, Ecotoxicology and Environmental Safety **59**, 275 (2004).
2. Y. Ohtsubo, T. Kudo, M. Tsuda, et al. Appl. Microbio. Biotech. **65**, 250 (2004)
3. D. V. Cicchetti, A. S. Kaufman, S. S. Sparrow. Psychology in the Schools **41**, 589 (2004).
4. J. E. Hong, H. Pyo, S. J. Park, et al. Anal. Chem. Acta, **531**, 249 (2005)
5. Committee on the Review of Existing and Potential Stand-off Explosives Techniques, National Research Council, Existing and Potential Stand-off Explosives Detection Techniques, National Academies Press, Washington, DC, 2004.
6. C. V. Raman, and K. S. Krishnan, Nature **121**, 501 (1928); G. Landsberg, and L. Mandelstam, Naturwiss.**16**, 5577 (1928); H. M. Lee, S. M. Jin, H. M. Kim, Y. D. Suh, Phys. Chem. Chem. Phys. **15**, 5276 (2013).
7. P. D. Maker, R. W. Terhune, Phys. Rev. A **137,** 801 (1965); A.C. Eckbreth, Laser Diagnostics for Combustion Temperature and Species, Cambridge, MA: Abacus Press, 1988; S. Roy, J. R. Gord, A. K. Patnaik, Pro. Ene. Comb. Sci., **36**, 280. (2010)
8. M. Fleischman, P. J. Hendra and A. McQuillan, J. Chem. Phys. Lett. **26,** 163 (1974); A. Crookell, M. Fleischmann, M. Hanniet, P.J. Hendra, Chem. Phys. Lett. **149**, 123 (1988); D. B. Chase, B. A. Parkinson, Appl. Spectrosc.**42,** 1186 (1988), S. M. Angel, L. F. Katz, D. D. Archibald, D. E. Hongis, Appl. Spectrosc.**43,** 367 (1989).
9. Handbook of Thin Films Materials, edited by H.S. Nalwa Volume 5: Nanomaterials and Magnetic Thin Films 2002.
10. S. Link, A. M. El-Syed. Annu. Rev. Phys. Chem. **54**, 331 (2003).
11. V. Makinen, P. Koskinen, and H. Hakkinen, Eur. Phys. J. D **67**, 38 (2013)
12. W.A. de Heer, Rev. Mod. Phys. **65**, 611 (1993)
13. N. O. Farrell, A. Houlton, and B. R. Horrocks, Int. J. Nanomedicine **1**, 451 (2006).
14. H. Sekhar and D. Narayana Rao, J. Nanopart. Res. **14**, 976 (2012).
15. N. Faraji, W. M. M. Younus, A. Kharazmi, E. Saion, M. Shahmiri and N. Tamchek J. Europ. Opt. Soc. Rap. Public. **7**, 12040 (2012).
16. X. Dou, PY. Chung, P. Jiang and J. Dai, Appl. Phys. Lett. **100,** 063702 (2012)**.**
17. X. Huang, M. A. El-Sayed, J. Adv. Res. **1,** 13 (2010)
18. A. V. Kabshin, M. Meunier, C. Kingston and J. T. Luong, J. Phys. Chem. B **107,** 4527 (2003)
19. H. Cui, P. Liu, G. W. Yang, Appl. Phys. Lett. **89,** 153124 (2006); M. Arruebo, R. F. Pacheco, M. R. Ibarra, J. Santamaria, Nano today **2,** 22 (2007); J. Prikulis, F. Svedberg, M. Kall, Nano. Lett. **4,** 115 (2004)

20. J. L. Elechiguerra, J. L. Burt, J. R. Moranes, A. C. Bragado, X. Gavo, H.H. Lara, M. J. Yacaman, J. Nano. Biotechn. **3**, 1 (2005); S. Petersen, J. Jakobi, S. Barcikowski, App. Surf. Sci. **255,** 5435 (2009); S. W. Tong, C. F. Zhang, C. Y. Jiang, G. Liu, Q. D. Ling and E. T. Kan, Chem. Phys. Lett. **453,** 73 (2008)
21. A. I. Maaroof, G. B. Smith, Thin. Sol. Films. **485,** 198 (2005); M. Mishra, H. Kumar, K. Tripathi, Dig. J. Nanomat. Biostruc. **3,** 49 (2008); S.K. Das, S. U. Choi, W. Yu and T. Pradeep, Nano fluids-science and technology, John Wiley & Sons, INC. Publication (2007)
22. M. Raffi, F. Hussain, T. M. Bhatti, J. I. Akhter, A. Hameed and M. M. Hasan, J. Mater. Sci. Technol. **24,** 192 (2008); P. Jain, I. El-Sayed, M. El-Sayed, Nano Today **2,** 18 (2007); D. B. Sanchez, The surface Plasmon resonance of supported noble metal nanoparticles: Characterization, Laser tailoring, and SERS application, PhD thesis, Madrid University (2007)
23. P. K. Jain, X. Huang, I. H. El-Sayed, M. El-Sayed, Acc. Chem. Res. **41,** 1578 (2008); M. Shao, L. Lu, H. Wang, S. Luo, D. D. Ma, Microchim. Acta. **164,** 157 (2009); I. Rianasari, L. Walder, M. Burchardt, I. Zawisza and G. Wittstock, Langmuir **24,** 9110 (2008).
24. K. L. Kelly, E. Coronado, L. L. Zhao, and G. C. Schatz. J. Phys. Chem. B **107**, 668 (2003).
25. K. L. Kelly, T. R. Jensen, A. A. Lazarides, and G. C. Schatz, Modeling metal nanoparticles optical properties. Metal Nanoparticles: Synthesis, Characterization, and Applications. pp 88–118. New York: Marcel Dekker, Inc (2002)
26. R. P. Feynman, R. B. Leighton, and M. Sands, The Feynman Lectures on Physics. Reading, MA: Addison-Wesley (1964).
27. G. H. Chan, J. Zhao, G. C. Schatz, and R. P. Van Duyne. J. Phys. Chem. C **112**, 13958 (2008)
28. Nanostructures and Surface-Enhanced Raman Spectroscopy, K. M. Kosuda, J. M. Bingham, K. L. Wustholz, and R. P. Van Duyne, Northwestern University, Evanston, IL, USA
29. C. F. Bohren and D. R. Huffman Absorption and Scattering of Light by Small Particles. New York: Wiley (1983).
30. A. Campion, P. Kambhampati, Chem. Soc. Rev. **27**, 241 (1998).
31. M. G. Albrecht and J. A. Creighton, J. Am. Chem. Soc., **99**, 5215 (1977).
32. K. Kneipp. Y. Wang, H. Kneipp, L. T. Perelman, I. Itzkan, R. R. Dasari , M. Feld, Phys. Rev. Lett., **78,** 1667 (1997)
33. S. Nie, S. R. Emory, Science, **275,** 1102 (1997)
34. S. R. Emory, S. Nie, Anal. Chem. **69,** 2631 (1997)
35. M. Kerker, O. Siiman, L. A. Bumm and D. S. Wang, Appl. Opt.193253 (1980)
36. D. S. Wang and M. Kerker, Phys. Rev.B241777 (1981)
37. E. J. Zeman and G. C. Schatz, J. Phys. Chem. **91**, 634 (1987)
38. H. X. Xu, J. Aizpurua, M. Kall and P. Apell, Phys. Rev. E **62**, 4318 (2000)
39. K. Fukami, M. L. Chourou, R. Miyagawa, Á.M. Noval, T. Sakka, M. Manso-Silván, R. J. Martín-Palma, Y. H. Ogata, Materials **4,** 791 (2011).
40. Z. Dai, X. Xiao, L. Liao, J. Zheng, F. Mei, W. Wu, J. Ying, F. Ren, and C. Jiang, Appl. Phys. Lett. **103**, 041903 (2013).
41. B. Sharma, R. R. Frontiera, A. I. Henry, E. Ringe, R. P. Van Duyne, Mater. Today **15,** 16 (2012).
42. X.-M. Lin, Y. Cui, Y.-H. Xu, B. Ren, Z.-Q. Tian, Anal. Bioanal. Chem. **394,** 1729 (2009).
43. S. Schlucker, Angew. Chem. Int. Ed. **53,** 4756 (2014).

44. G. McNay, D. Eustace, W.E. Smith, K. Faulds, D. Graham, Appl. Spec. **65,** 825 (2011).
45. H. H. Lin, J. Mock, D. Smith, T. Gao, M. J. Sailor, J. Phys. Chem. B **108**, 11654 (2004)
46. S. Chan, S. Kwon, T.W. Koo, L.P. Lee, A.A. Berlin, Adv. Mater. **15**, 1595 (2003).
47. R. Miyagawa, K. Fukami, M. L. Chourou, T. Sakka,. Y. H. Ogata, ECS Trans., **33**, 109 (2011)
48. J. Yang, J. Li, Z. Du, Q. Gong, J. Teng, and M. Hong, Scientific Reports **4**, 6657 (2014); M. S. Schmidt, J. Hubner, and A. Boisen, Adv. Mater. **24**, OP11–OP18 (2012)
49. T. M. Cotton, Surface and Interfacial Aspects of Biomedical Polymersed J Andrade (New York: Plenum), p 161 (1985); E. Koglin and J. M. Sequaris, Top. Curr. Chem.**134**, 1 (1986); T. M. Cotton, Spectroscopy of Surfaces ed R. J. H. Clark and R. E. Hester (New York: Wiley) p 91 (1988); R. F. Paisley and M D Morris, Prog. Anal. Spectrosc.**11**, 111 (1988); T. M. Cotton, K. Jae-Ho and G. D. Chumanov, J. Raman Spectrosc.22, 729 (1991); K. Sokolov, P. Khodorchenko, A. Petukhov, I. Nabiev, G. Chumanov and T. M. Cotton, Appl. Spectrosc.**47**, 515 (1993)
50. Y. Wei, C. Cao, R. C. Jin and C. A. Mirkin, Science **297**, 1536 (2002); Y. Fang, N. H. Seong and D. D. Dlott, Science **321**, 388 (2008); D. Graham, G. Thompson, W. E. Smith and K. Faulds, Nat. Nanotechnol. **3** ,548 (2008); J. F. Li, Y. F. Huang, Y. Ding, Z. L. Yang, S. B. Li, X. S. Zhou, F. R. Fan, W. Zhang, Z. Y. Zhou, D. Y. Wu, B. Ren, Z. L. Wang, Z. Q. Tian, Nature **464**, 392 (2010); H. S. Cho, B. R. Baker, S. W. Hogiu, C. V. Pagba, T. A. Laurence, S. M. Lane, L. P. Lee and J. B. H. Tok, Nano Lett. **8**, 4386 (2008); X. Jiang, Z. Jiang, T. Xu, S. Su, Y. Zhong, F. Peng, Y. Su, and Y. He, Anal. Chem., **85**, 2809 (2013); Y. S. Huh, A. J. Chung, B. Cordovez and D. Erickson, Lab Chip, **9**, 433 (2009)
51. S. Efrima and B. V. Bronk. J. Phys. Chem. B **102**, 5947 (1998); G. D. Sockalingum, H. Lamfarraj, A. Beljebbar, P. Pina, M. Delavenne, F. Witthun, P. Allouch and M. Manfait Proc. SPIE **185**, 3608 (1999).
52. H. Zhou, D. Yang, N. P. Ivleva, N. E. Mircescu, R. Niessner, and C. Haisch, Anal. Chem. **86**, 1525 (2014); K. Gracie, E. Correa, S. Mabbott, J. A. Dougan, D. Graham, R. Goodacre and K. Faulds, Chem. Sci. **5**, 1030 (2014); H. W. Cheng , W.Q. Luo , G. L. Wen , S. Y. Huan, G. L. Shen and R. Q. Yu , Analyst. **135**, 2993 (2010).
53. I. Talian and J. Huebner, J. Raman Spectrosc. **44**, 536 (2013); I. Malka, A. Petrushansky, S. Rosenwaks and I. Bar, Appl. Phys. B **DOI 10.1007/s00340-013-5500-8**; S. Botti, S. Almaviva, L. Cantarini, A. Palucci, A. Puiu and A. Rufolon, J. Raman Spectrosc. **44**, 463 (2013),
54. F. T. Docherty, P. B. Monaghan, C. J. McHugh, D. Graham, W. E. Smith and M. J. Cooper, IEEE Sensors Journal, **5**, 632 (2005); S. Liu and Z. Tang, J. Mater. Chem., **20**, 24 (2010); O. M. Primera-Pedrozo, J. I. Jerez-Rozo, E. D. L. Cruz-Montoya, T. Luna-Pineda, L. C. Pacheco-Londoño, and S. P. Hernández-Rivera, IEEE Sensors Journal **8**, 963 (2008); C. L. Haynes, A. D. McFarland and R. P. Van Duyne, Anal. Chem. September **1**, pp. 338A-346A (2005).
55. L. Guerrini and D. Graham, Chem. Soc. Rev. **41**, 7085 (2012).
56. M. Moskovits J. Chem. Phys. **69,** 1459 (1978)
57. K. Kneipp, H. Kneipp, I. Itzkan, R. R. Dasari and M. S. Feld, J. Phys. Condens. Matter **14,** R597 (2002).

58. H. Jia, J. Zeng, W. Song, J. An, and B. Zhao, Thin Solid Films, **496**, 28 (2006); P. Y. Lim, R. S. Liu, P. L. She, C. F. Hung, H. C. Shih, Chem. Phys. Lett. **420**, 304 (2006); M. J. Rosemary and T. Pradeep, J. Colloids Inter. Sci. **268**, 81 (2003); M. S. Chargot, A. Gruszecka, A. Smolira, J. Cytawa, L. Michalak, Vacuum **82**, 1088 (2008); H. Huang, X. Yang, Carbohyd. Res. **339**, 2627 (2004); J. Gu, W. Fan, A. Shimojima, T. Okubo, J. Solid State Chem. **181**, 957 (2008); Y. Liu, L. Liu, W. Chiu, J. Phys. Chem. B **108**, 19237 (2004); H. Eerikainen, E. Kauppinen, Int. J. Pharma. **263,** 69 (2003); K. L. McGilvray, M. R. Decan, D. Wang and J. Scaiano, J. Amer. Chem. Soc. **128**, 15980 (2006); M. Duocastella, J. M. Fernandez-Pradas, J. Dominguez, P. Serra, J. L. Morenza, Appl. Phys. A **93,** 941 (2008); S. Y. Yang and S. G. Kim, Powder Technol. **146**, 185 (2004); N. S. Tabrizi, M. Ullmann, V. A. Vons, U. Lafont and A. Schmidt-Ott, J. Nanopart. Res. **11**, 315 (2009); S.L. Stoll, E.G. Gillan, A.R. Barron, Chem. Vap. Deposition **2**, 182 (1996); S. Banerjee, S. Roy, J. W. Chen and D. Chakravorthy, J. Magn. Magn. Mater. **45**, 219 (2000); W. Abdul-Razzaq and M.S. Seehra, Phys. Stat. Solid. A **94**, 193 (2002); K. Sturm, S. Fahler and H.-U. Krebs, Appl. Surf. Sci. **462**, 154 (2000); S. Eliezer, N. Eliaz and E. Grossman, Phys. Rev. B **69,** 144119 (2004),
59. P. Wagener, S. Ibrahimkutty, M. Andreas, P. Anton and S. Barcikowski Phys. Chem. Chem. Phys. **15**, 3068 (2013); R. M. Tilaki, A. Irajizad and S. M. Madhavi Appl. Phys. A **88**, 415 (2007); G.W. Yang, Progress in Materials Science **52**, 648 (2007); M. Fumitaka, J. Kohno, Y. Takeda and T. Kondow J. Phys. Chem. B **105**, 5114 (2001); F. Bozon-Verduraz, R. Brayner, V. V. Voronov, N. A. Kirichenko, A. V. Simakin and G. A. Shafeev Quantum Electron **33**, 714 (2003); N. V. Tarasenko, A. V. Butsen and E. A. Nevar. Appl. Surf. Sci. **247**, 418 (2005); F. Brayner R, V. Valerii Voronov, N. A. Kirichenko, Aleksandr V. Simakin and A. Georgii, *Quantum. Electron.* **33,** 714 (2003); H. L. Aye, S. Choopun and T. Chairuangsri, Adv. Mate. Res. **93**, 83 (2010); K. Leonard, J. Kurawaki, K. Hayakawa, M. Thein Tun and Y. Kusumoto, Colloid Polym. Sci. **287**, 773 (2009); M. Saito, K. Yasukawa, T. Umeda and Y. Aoi Opt. Mat. **30**, 1201 (2008).

60. G. Malyavantham, D.T. O'Brien, M. F. Becker, J.W. Keto and D. Kovar, J. Nanopar. Res. **6,** 661 (2004); P. V. Kazakevich, V.V. Voronov, A.V. Simakin and G. A. Shafeev, Quantum Electron. **34,** 951 (2004); V. S. Burakov, N. V. Tarasenko, A. V. Butsen, V. A. Rozantsev and N.I. Nedelko, Eur. Phys. J. Appl. Phys. **30**, 107 (2005).
61. V. Amendola, S. Polizzi and M. Meneghetti, Langmuir **23,** 6766 (2007); V. Amendola and M. Meneghetti, Phys. Chem. Chem. Phys **11**, 3805 (2009); V. Amendola, M. B. Osman and F. Stellacci, Plasmonic*s* **5,** 85 (2010); C. Giuseppe, A. S. Alessandro and P. Orazio, *Phys. Chem.* **4,** 2787 (2002); G. Emilia, M. Muniz-Miranda, P. Marsili, D. Scarpellini and F. Giammanco J. Nanopart Res **14**, 648 (2012); P. Boyer, D. Menard and M. Meunier, J. Phys. Chem. C **114,** 13497 (2010); J. M. J. Santillán, F. A. Videla, M. B. Fernández Van Raap, D. C. Schinca and L. B. Scaffardi, J. Appl. Phys. **112**, 054319 (2012).
62. L. V. Keldysh, Soviet Physics JETP **20**, 1307 (1965).
63. B. C. Stuart, M. D. Feit, S. Herman, A. M. Rubenchik, B. W. Shore, and M. D.Perry, Phys. Rev. B **53**, 1749 (1996); A. C. Tien, S. Backus, H. kapteyn, M. Murnane, and G. Mourou, Phys. Rev. Lett. **82**, 3883 (1999); N. Sanner, O. Uteza, B. Chimier, M. Sentis, P. Lassonde, F. Legare, and J. C. Kieffer, Appl. Phys. Lett. **96**, 071111 (2010).

64. M. D. Parrish, A Thesis Presented for the Master of Science Degree The University of Tennessee, Knoxville, 2009
65. V. Amendola and M. Meneghetti, Phys. Chem. Chem. Phys. **15**, 3027(2013)
66. G.C. Messina, "In Liquid" Laser Processes for Nanoparticles Synthesis and Manipulation Thesis Presented for the Doctoral degree in Scienza dei Materiali, 2009.
67. J. Hohlfeld, S. -S. Wellershoff, J. Gudde, U. Conrad, V. Jahnke and E. Matthias, Chem. Phys. **251**, 237 (2000)
68. D. Perez and L. J. Lewis, Phys. Rev. B **67**, 184102 (2003); D. Perez, L. K. Beland, D. Deryng, L. J. Lewis and M. Meunier, Phys. Rev. B **77**, 014108 (2008).
69. V. Amendola, S. Polizzi and M. Meneghetti, J. Phys. Chem. B **110**, 7232 (2006).
70. S. S. Harilal, J. R. Freeman, P. K. Diwakar and A. Hassanein, S. Musazzi and U. Perini (eds.),Laser-Induced Breakdown Spectroscopy, Springer Series in Optical Sciences 182, DOI: 10.1007/978-3-642-45085-3_6.
71. M. S. Brown and C. B. Arnold and K. Sugioka et al. (eds.),Laser Precision Micro-fabrication, Springer Series in Materials Science 135, DOI 10.1007/978-3-642-10523-4__4
72. B.N. Chichkov, C. Momma, S. Nolte, F. vonAlvensleben and A. Tunnermann, Appl. Phys. A Mater. Sci. Process.**63**, 109 (1996)
73. C. Momma, B. N. Chichkov, S. Nolte, F. von Alvensleben, A. Tu¨nnermann, H. Welling and B. Wellegehausen, Opt. Commun. **129**, 134 (1996).
74. A. D. Bonis, M. Sansone, L. D. Alessio, A. Galasso, A. Santagata and R. Teghil, J. Appl. Phys. **46,** 445301 (2013).
75. M. I. Kaganov, I. M. Lifshitz and L. V. Tanatarov, Sov. Phys.-JETP **4**, 173 (1957); S.I. Anisimov, B.L. Kapeliovich and T.L. Perel'man, Sov. Phys. -JETP **39**, 375 (1974).
76. K.H. Leitz, B. Redlingshöfer, Y. Reg, A. Otto and M. Schmidt, Physics Procedia **12**, 230 (2011).
77. L. V. Zhigilei and B. J. Garrison, J. Appl. Phys. **88**, 1281 (2000).
78. G. Paltauf and P. E. Dyer, Chem. Rev. **103**, 487 (2003).
79. V. L. Zhigilei, S. D. Ivanov, and E. Leveugle, In High-Power Laser Ablation, V. Claude R. Phipps, Editor, Proc. SPIE **5448**, 5448L (2004).
80. L. V. Zhigilei, Appl. Phys. Mater. Sci. Process. A **76**, 339 (2003).
81. K. Sokolowski-Tinten et al., Phys. Rev. Lett. **81**, 224 (1998); D.V. Makhov and L. J. Lewis, Phys. Rev. B **67**, 153202 (2003); P. Lorazo, L. J. Lewis and M. Meunier, Phys. Rev. lett. **91**, 225502 (2003).
82. N. M. Bulgakova and I. M. Bourakov, Appl. Surf. Sci. **197**, 41 (2002); N. M. Bulgakova and A.V. Bulgakov, Appl. Phys. A **73**, 199 (2001)
83. A. Miotello and R. Kelly: Appl. Phys. Lett. **67**, 3535 (1995); R. Kelly and A. Miotello, Nucl. Instrum. Methods. B **122**, 374 (1997); A. Miotello and R. Kelly: Appl. Phys. A 69, S67 (1999)
84. D. Perez and L. J. Lewis, Phys. Rev. Lett. **89**, 255504 (2002).
85. K. S. Suslick, and D. J. Flannigan, Annu, Rev. Phys. Chem.**59,** 659 (2008).
86. F. R. Young, Cavitation. London: Imperial Coll. Press (1999); C. E. Brennen, Cavitation and Bubble Dynamics. New York: Oxford Univ. Press (1995).
87. P. Wagener, S. Ibrahimkutty, A. Menzel, A. Plech and S. Barcikowski, Phys. Chem. **15**, 3068 (2013).
88. A. D. Giacomo, M. D. Aglio, O. D. Pascale and M. Capitelli, Spectrochimica. Acta B **62**, 721 (2007); T. Tsuji, D. Thang, Y. Okazaki, M. Nakanishi, Y. Tsuboi and M. Tsuji, Appl. Surf. Sci. **254**, 5224 (2008); A. D. Giacomo, A. D. Bonis, M.

D. Aglio, O. D. Pascale, R. Gaudiuso, S. Orlando, A. Santagata, G. Senesi, F. Taccogna and R. Teghil, J. Phys. Chem. C **115**, 5123 (2011); L. Bethe, R. Fabro, P. Peyre, L. Tollier and E. Bartnicki, J. Appl. Phys. **82**, 2826 (1997); L. Bethe, A. Sollier, P. Peyre, R. Fabro, L. Tollier and E. Bartnicki, J. Phys. D: Appl. Phys. **33**, 2142 (2000); M. S. El-Shall, S. Li, T. Turkki , D. Graiver , U. C. Pernisz and M. I. Baraton J. Phys. Chem. **99**, 1780 (1995); S. I. Dolgaev, A. V. Simakin, V. V. Voronov, G. A. Shafeev and F. Bozon-Verduraj, App. Surf. Sci. **186**, 546 (2002); S. B. Wen, X. L. Mao, R. Grief and R. E. Russo, J. Appl. Phys. **101**, 023114 (2007); B. Kumar, D. Yadav and R. K. Thareja, J. Appl. Phys. **110**, 074903 (2011).

89. W. T. Nichols, T. Sasaki and N. Koshizaki, J. Appl. Phys. **100**, 114911 (2006); V. Amendola and M. Meneghetti, Phys. Chem. Chem. Phys. **11**, 3805 (2009); T. Tsuji, K. Iryo, Y. Nishimura and M. Tsuji, J. Photochem. Photobiol. A **145**, 201 (2001); Z. Yan, R. Bao, Y. Huang, A. Caruso, S. B. Qadri, C. Z. Dinu and D. B. Chrisey, J. Phys. Chem. C **114**, 3869 (2010); V. Amendola and M. Menghetti, Phys. Chem. Chem. Phys. 15, 3027 (2013); S. Z. Mortazavi, P. Parvin, A. Reyhani, A. N. Golikand and S. Mirershadi, J. Phys. Chem. C **115**, 5049 (2011); A. Schwenke, P. Wagener, S. Nolte and S. Barcikowski, Appl. Phys A **10**, 77 (2011).
90. D. Batani, Laser Part. Beams **28**, 235 (2010); H. M. Smith and A. F. Turner, Appl. Opt **4**, 147 (1965); H.W. Kroto, J. R. Heath, S. C. O'Brien, R. F. Curl and R. E. Smally, Nature **318**, 162 (1985); A. M. Morales and C. M. Lieber, Science **279,** 208 (1998); D. B. Chrisey, A. Pique, R. A. McGill, J. S. Horwitz, B. R. Ringeisen, D. M. Bubb and P. K. Wu, Chem. Rev.**103,** 553 (2003).
91. H. B. Bebb and A. Gold, Phys. Rev. **143**, 1 (1966); M. D. Perry, O. L. Landen, A. Szoke and E. M. Campbell, Phys. Rev. A **37**, 747 (1988); J. K. Chen and J. E. Beraun, Numer. Heat Trans. A: Appl. **40**, 1 (2001).
92. C. Liu, A study of particle generation during laser ablation with applications, Doctoral thesis, University of California, Berkeley (2005); T. Ctvrtnickova, L. Cabalin, J. Laserna, V. Kanicky and G. Nicola, Appl. Surf. Sci. **255**, 5329 (2009); D. Bauerle, Chapter 13, Ultrashort-pulse laser ablation in laser processing and chemistry, 3 rd Edition (Springer-Verlag, New York (2000); J. H. Yoo, S. H. Jeong, X. L. Mao, R. Grief and R. E. Russo, Appl. Phys. Lett. **76**, 783 (2000); K. Y. Niu, J. Yang, S. A. Kulinich, J. Sun, H. Li, and X. W. Du, J. Am. Chem. Soc. **132**, 9814 (2010); T. Sasaki, Y. Shimizu and N. Koshizaki, J. Photochem. Photobiol. Chem. A **186**, 335 (2006); P. Liu, H. Cui, C. X. Wang and G. W. Yang, Phys. Chem. Chem. Phys. **12**, 3942 (2010); S. Venugopal Rao, G. K Podagatlapalli and S. Hamad, J. Nanosci. Nanotechnol.**14**, 1364 (2014).
93. E. Stratakis, Sci. Adv. Mater. **4**, 407 (2012); H. Zeng, X. Du, S. C. Singh, S.A. Kulinich, S. Yang, J. He and W. Cai, Adv. Funct. Mater. **22,** 1333 (2012); V. Kostrykin, M. Niessen, J. Jandeleit, W. Schulz, E. W. Kreutz and R. Poprawe, Proc. SPIE **3343**, 971 (1998); D. Von der Linde, K. Sokolowski-Tinten and J. Barcikowski, Appl. Surf. Sci. **109**, 1 (1997); B.N. Chichkov, C. Momma, S. Nolte, A. Alvensleben and A. Tunnermann, Appl. Phys. A. **63**, 109 (1996); A. Moitello and R. Kelly, Appl. Phys. A **69**, 67 (1999); Q. Lu, S. S. Mao and R. E. Russoa, Appl. Phys. Lett. **80**, 3072 (2002); P. T. Mannion, J. Magee, E. Coyne, G. M. O'Connor and T. J. Glynn, Appl. Surf. Sci. **233**, 275 (2004); E. V. Barmina, M. Barberoglu, V. Zorba, A. V. Simakin, E. Stratakis, C. Fotakis and G. A. Shafeev, Quantum Electron. **39**, 89 (2009); K. Leitz, B. Redlingshofer, Y. Reg, A. Otto, M. Schmidt and S. I. Dolgaev. **12**, 23 (2011); S. Barcikowski, A. Menendez-Manjon

and B. Chichkov, Appl. Phys. Lett. **91**, 083113 (2007); D. Riabininan, M. Chaker and J. Margot, Nanotech. **23**, 135603 (2012).
94. E. B. Barmina, E. Stratakis, C. Fotakis and G.A. Shafeev, Quant. Electron. **40**, 1012 (2010).
95. J. P. Sylvestre, S. Poulin, A.V. Kabashin, E. Sacher, M. Meunier and J. H. T. Luong, J. Phys. Chem. B **108**, 16864 (2004).
96. É. Boulais, R. Lachaine and M. Meunier, *J. Phys. Chem. C* **117**, 9386 (2013).
97. A. Barchanski, C. L. Sajti, C. Sehring, S. Petersen and S. Barcikowski, J. Laser Micro Nano Eng. **6**, 124 (2009).
98. J. P. Sylvestre, A. V. Kabashin, E. Sacher, M. Meunier and J. H. T. Luong, J. Am. Chem. Soc. **126**, 7176 (2004).
99. M. A. Sobhan, M. J. Withford and E. M. Goldys, Langmuir **26**, 3156 (2010); S. Petersen, A. Barchanski, U. Taylor, S. Klein, D. Rath and S. Barcikowski, J. Phys. Chem. C **115**, 5152 (2011)
100. S. Besner, A.V. Kabashin, and M. Meunier, Appl. Phys. A **8**, 269 (2007); S. Besner, A.V. Kabashin, F.M. Winnik, and M. Meunier, J. Phys. Chem. C **113**, 9526 (2009).
101. D. Tan, Y. teng, Y. Liu, Y. Zhuang and J. Qiu, J. Nanopart. Res. **13**, 1183 (2011).
102. A. Menendez-Manjon, J. Jakobi, K. Schwabe, J. K. Krauss and S. Barcikowski, J. Laser Micro Nano Eng. **4**, 95 (2009).
103. E. Stratakis, M. Barberoglou, C. Fotakis, G. Viau, C Garcia, and G. A. Shafeev, Opt. Exp. **17**, 12650 (2009).
104. P. G. Krishna, S. Hamad, S. Sreedhar, S. P. Tewari and S. Venugopal Rao, Chem. Phys. Lett. **530**, 97 (2012); S. Hamad, P. G. Krishna, S. P. Tewari, and S. Venugopal Rao, J. Phys. D: Appl. Phys. **46**, 485501 (2013); P. G. Krishna, S. Hamad, S. P. Tewari, S. Sreedhar, M. D. Prasad, and S. Venugopal Rao, J. Appl. Phys. **113**, 073106 (2013); S. Hamad, P. G. Krishna, V. S. Vendamani, S.V.S. Nageshwara Rao, A. P. Pathak, and S. Venugopal Rao, J. Phys. Chem. C. **118** , 7139 (2014); S. Hamad, P. G. Krishna, Md. A. Mohiddon and S. Venugopal Rao; Appl. Phys. Lett. **104**, 263104 (2014); P. G. Krishna, S. Hamad, Md. A. Mohiddon and S. Venugopal Rao, Appl. Surface Sci. **303**, 217 (2014).
105. L. V. Zhigilei, P. B. S. Kodali, B. J. Garrison, Chem. Phys. Lett. **276**, 269 (1997); L. V. Zhigilei, P. B. S. Kodali and B. J. Garrison, J. Phys. Chem. B **101**, 2028(1997); L. V. Zhigilei,B. J. Garrison, Mat. Res. Soc. Proc. **38**, 49 (1999); L. D. Landau, E. M. Lifshitz, L. P. Pitaevskii, Pergamon Press, Oxford, 1984; K. A. Elsayed, H. Imam, M. A. Ahmed and R. Ramadan, Opt. Las. Tech. **45**, 495 (2013); A. V. Kabashin and M. Meunier, J. Appl. Phys. **94**, 7941 (2003); N. Barsch, J. Jacobi, S. Weiler and Barcikowski, Nanotech. **20**, 445603 (2009).
106. D. K. Das, et al., Appl. Phys. A **91**, 421 (2008); G. Compagnini, M. G. Sinatra, P. Russo, G. C. Messina, O. Puglisi and S. Scalese, Carbon **50**, 2362 (2012); M. Lenzner, J. Kruger, W. Kautek and F. Krausz, Appl Phys A **69**, 465 (1999); J. Byskov-Nielsen, J.-M Savolainen, M.S. Christensen and P. Balling, Applied Physics A **101**, 97(2010); A. Y. Vorobyev, V. S. Makin, and C. Guo, Phys. Rev. Lett. **102**, 234301 (2009).
107. Y. Jee, M. F. Becker, and R. M. Walser, J. Opt. Soc. Am. B **5**, 648 (1988).
108. F. Liang, R. Vallee, D. Gingras, and S, L. Chin, Opt. Mat. Exp. **1**, 1224 (2011); D. K. Sardar, M. F. Becker, and R. M. Walser, J. Appl. Phys .**62**, 3688 (1987); Y. Jee, M. F. Becker, and R. M. Walser, J. Opt. Soc. Am. B **5**, 648 (1988).

2

Experimental and Characterization Techniques

Abstract

This chapter describes the generation methodology of ultrashort laser pulses (USP) from the laser systems utilized in the thesis work. Pulse characterization techniques involved as well the features of USPs and the dispersion effects evoked by the dispersive media it are discussed. Later, methodologies of ultrafast laser ablation in liquids (ULAL), complete details of nonlinear optical experiments (Z-scan, degenerate four wave mixing), and pump-probe experiments are discussed. Finally, experimental procedure of surface enhanced Raman scattering (SERS) which utilizes adsorption of analyte molecules on laser ablated metal targets and cleaning of utilized metal targets are discussed in detail.

2.1. Introduction

The studies of physical properties and characteristics (structural, optical, electronic, Raman and surface morphology) of laser fabricated nanomaterials under various conditions are helpful in predicting their possible applications. The knowledge of working principle, sensing elements and possible errors in measuring the above parameters is useful while understanding their properties. In this chapter, brief descriptions of laser instruments and pulse characterization technique have been provided. Moreover, experimental procedures of ultrafast laser ablation, characterization and working of the various techniques used in the present work are summarized.

2.2. Ultrafast picosecond and femtosecond laser system

The femtosecond (fs)/picosecond (ps) Ti: sapphire laser system is the team of five lasers and brief description of devices involved in this system are presented in this chapter.

2.2.1. Verdi laser head (Pump laser to femtosecond Oscillator)[1]

The Verdi laser head was launched with typical and innovative performance which contains a green continuous laser with little noise, fine line width and the higher quality of diffraction limited mode. This continuous beam is the ideal source for pumping to the Ti: sapphire laser systems. The Verdi head is sealed from the factory which ensures of best performance over the life time of the laser which is shown in figure 2.1. The coherent Verdi head contains gain medium of Neodymium Yttrium ortho vanadate (Nd: YVO_4) which is pumped by diode lasers and produces fundamental wavelength of 1064 nm. Diode lasers directly convert electrical energy to laser energy with high efficiency and tunable output wavelength along with lifetime over a decade. The diode laser output of wavelength 808 nm is communicated to the Verdi head through the fiber optic cables in the umbilical. Second harmonic generation takes place when the fundamental laser beam of 1064 nm passes through the lithium triborate (LBO) nonlinear crystal to generate 532 nm of 10 W and this wavelength excites Ti: Sapphire crystal. The process of SHG occurs when the fundamental wavelength propagates 90^0 to the optic axis. In this regard phase matching takes place by temperature tuning (~150 ^{0}C). Crystal will be damaged by

rapid change in temperature and heating or cooling processes of crystal need to be done in a controlled fashion. The whole process is controlled automatically by the tuning of switch on the rear panel of the power supply.

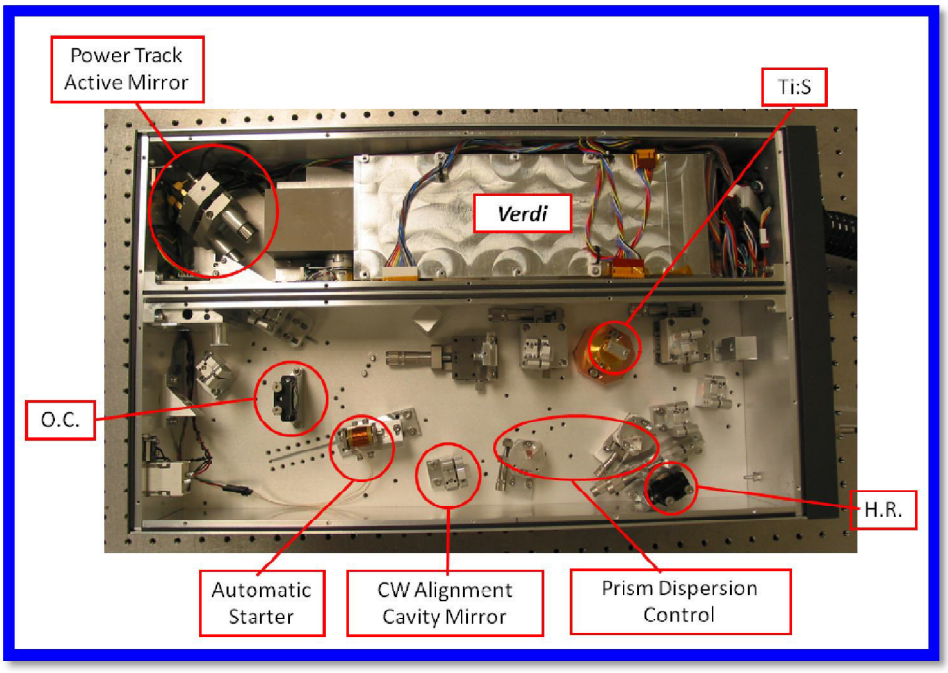

Figure 2.1 Interior parts of Micra which comprise VERDI (upper part), folded short and long cavities (lower part), O.C – output coupler and H.R – high reflector (adopted from Micra manual)[1]

2.2.2. Femtosecond Oscillator -MICRA

The fs oscillator[1] employs passive type modelocking (i.e. Kerr lens modelocking) and in combination with intracavity prism pair produces ultrashort pulses with large bandwidth, low noise and high peak power. The tweaking of prism pair enables the tuning of wavelengths, adjustment of bandwidth with a slit arrangement. The lasing medium of MICRA-Oscillator is of Ti: Sapphire crystal and it is pumped by second harmonic of Nd: YVO_4 laser (532 nm) with the output power of 10 W. The fs Ti: Sapphire laser oscillator is capable of generating Gaussian, transform limited pulses tunable from ~15 fs to ~100 fs in the cavity end mirrors M1 and M2 (both short leg and long leg cavities) with an average out power of 750 mW at repetition rate of which could be set from 76 to 82 MHz . The bandwidth was adjustable from 30 nm to 100 nm at central wavelength of 800 nm and the optimal bandwidth was in the range of 50-60 nm. In the low bandwidth range, the central wavelength was tunable from

750 nm to 860 nm. The schematic of MICRA which comprises the long and short cavities illustrated in figure 2.2.

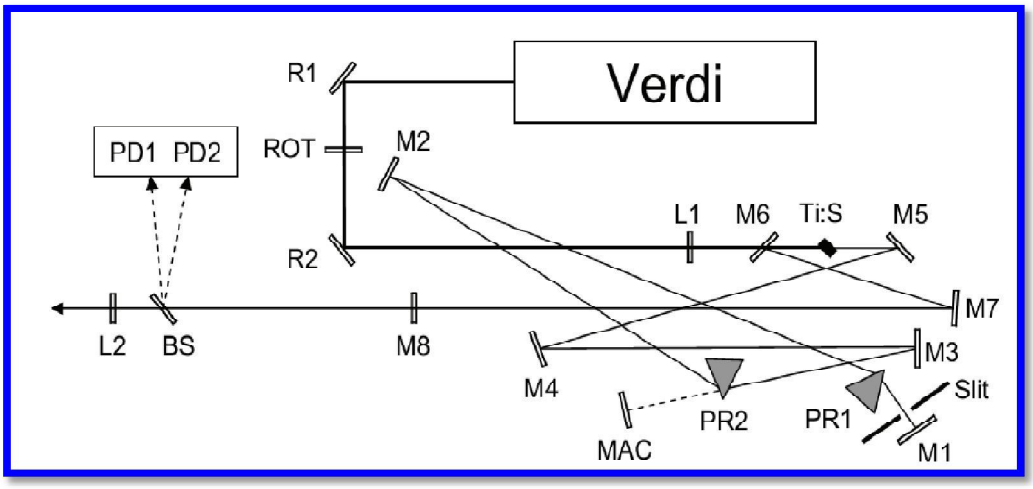

Figure 2.2 Schematic of Micra oscillator head which illustrate the optical components in a clear way [Adapted from Micra manual].[1]

2.2.3. Absorption and emission properties of Ti: Sapphire crystal

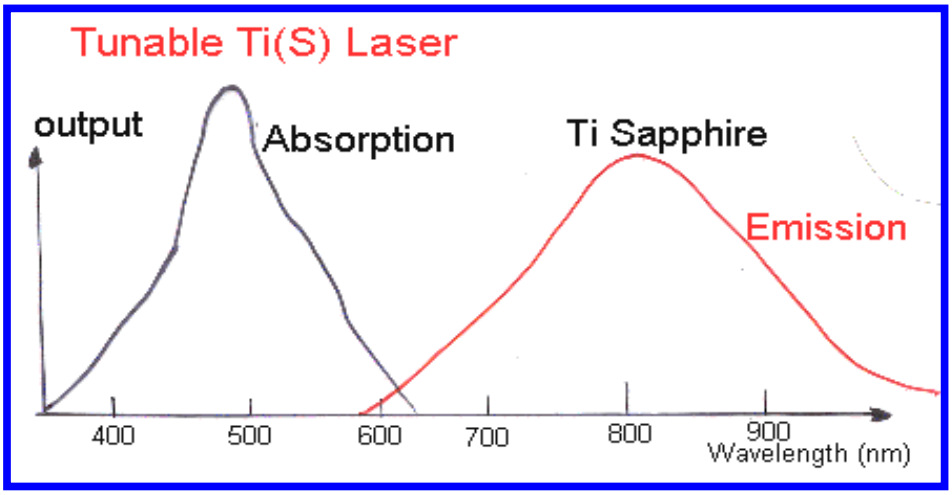

Figure 2.3 Absorption, Fluorescence spectra of Ti^{3+} ion doped sapphire crystal [adopted from ref. 2]

Absorption spectra of Ti^{3+}ion doped sapphire crystal shows a broad continuous peak in 400-600 nm range.[2] The end part of the absorption band (longer wavelengths end) is overlapped with the beginning part (shorter wavelength) of the emission band. Because of this reason, starting point of lasing action is after 650 nm. In addition to this, the tuning range is influenced by losses in cavity, coating on the mirrors, quality of pump mode, input power loses and air absorption. The optics in our MICRA- fs Ti:

Sapphire laser oscillator allows tunability 750 nm – 860 nm range without problematic issues and this wavelength range corresponds to where the emission spectrum has maximum intensity.[1] The absorption and emission spectra of Ti: Sapphire crystal are illustrated in figure 2.3. The emission band transitions occur from the lower vibrational levels of the excited state to the upper vibrational levels of the ground state which is in the range of 600 nm to >1000 nm and this range is well suited for generating fs pulses.

2.2.4. Origin of Modelocking

Many modelocking techniques[3,4] have been developed recently for generating fs laser pulses. Micra employs a passive modelocking technique or Kerr-lens modelocking. In this modelocking, an external modulator or shutter with accurate timing is not necessary. A new phenomenon of self focusing is used automatically to obtain modelocked pulses.

Passive modelocking

Passive modelocking[5] is achieved by introducing a material medium which has saturable absorption (SA) property into the laser cavity, preferably close to one of the cavity mirrors. SA is a property of medium where absorption coefficient decreases as the passing light intensity through the medium increases; thus transmitting intense pulses with relatively little absorption. When a saturable absorber[5,6] is used to modelock a laser, the laser is simultaneously Q-switched. In this case, dye used to show efficient performance as a saturable absorber which can imitate as a fast shutter, provided that the high intensity laser pulse allows saturation of the medium each time when it passes through the cavity. The time of the pulse recovery should be smaller than time taken for single round trip, if not origin of the multiple pulses with different characteristics might occur. Generally, the medium inside the cavity produces spontaneous emission and it causes arbitrary fluctuations in the temporal profile. When these modes pass through the laser medium again, they get amplified providing high intensity. The peak part of fluctuation gets little absorbed and end parts are more absorbed while passing through saturable absorber and therefore, a pulse with high peak power can be generated within the cavity.

Kerr-lens modelocking

Kerr-lens modelocking (KLM) [7,8] is a technique of passive modelocking which is attained by introducing a SA based on self-focusing (Kerr lens)[9,10] effect in the gain medium. The self-focusing phenomena rely on the optical Kerr effect inside the nonlinear medium. The optical Kerr-effect is a third order nonlinear effect which results in change induced in refractive index of the material as the high intensity laser beam is transmitted through the material. At high peak intensities, refractive index of the material depends nonlinearly on propagating field intensity and it can be described as

$$n(I) = n_0 + n_2 I \tag{2.1}$$

Where n_0 is the linear refractive index, n_2 is the coefficient of nonlinear refractive index and I is the instantaneous beam intensity. The shape of laser beam in our case is Gaussian and which can be expressed by the following equation

$$I(r, z, t) = I_{00} (\omega_0/\omega(z))^2 \exp(-2t^2/\tau^2) \exp(-2r^2/\omega^2(z)) \tag{2.2}$$

where I_{00} is the peak intensity at focal position.

The occurrence of the non-uniform intensity distribution in Gaussian profile leads to change in refractive index across the laser beam profile. The intensity experienced by the beam path is greater at the center of path than edges of the beam path. Therefore, the active medium acts as a lens under the Kerr-effect process at higher intensities, leading to self-focusing phenomenon which is known as Kerr-lens effect. The Kerr-lens effect causes a reduction in the beam waist at higher intensities. There are two different mechanisms where the medium can act like a fast saturable absorber (a) hard aperture or additional aperture KLM and (b) soft aperture KLM.[11] In the case of hard aperture KLM, the optical losses are diminished by Kerr-lens effect at an aperture when the laser beam passes to follow each round trip in the resonator. In the case of soft aperture KLM, no additional intracavity elements are needed for the cavity. Local shaping of laser modes is possible with the help of Kerr-lens phenomena. This phenomenon allows to generate modelock pulses by following ways (a) the overlapping of pump beam and generated laser radiation under some conditions results in increasing the gain and (b) the sign of Kerr-lens can be used to remove

artificially induced cavity misalignments. Because of these effects, a clean intense modelocked pulse can be generated with high Q-factor.

2.2.5. Group velocity dispersion (GVD)

The frequency components of an ultrashort pulse propagate with different speeds while passing through a dispersive material. It means that the pulse experiences group velocity dispersion (GVD). GVD[12-15] causes change in temporal profile of the pulse causing broadening (positive chirp)[16,17] or narrowing (negative chirp)[16,17] which depends the conditions of pulse. The term chirp indicates that the temporal profile is not uniform with respect to wavelength. It was demonstrated that when the pulse propagates through dispersive medium with normal dispersion, it turns into positively chirped pulse and anomalous dispersion turns into it negatively chirped pulse. The positively chirped pulse corresponds to the red components leading the blue components and the opposite is in the case of negatively chirped pulse. The various intracavity components establish positive GVD and additionally, self phase modulation (SPM) [18] induces pulse spread in the Ti: Sapphire crystal.

Stable pulses can be produced only when the chirping caused by SPM and medium GVD compensates the negative GVD created by the prism pair.[1] By inserting (or) removing the material inside the cavity the amount of positive GVD can be varied. The pulse also changes its width because of addition of more materials inside the cavity, the balance between the material positive GVD, chirp created by SPM and negative GVD by prism pair get changed.

2.2.6. Ti: Sapphire Chirped Pulse Amplifier (CPA)

Most of the ablation experiments require high peak power lasers since oscillator energies are not enough to perform laser induced plasma based experiments. These types of experiments need amplified laser pulses whose output intensities are much higher than oscillator output. Hence, a regenerative (Legend-F)[19] chirped pulse amplifier was added to this system and Ti:sapphire crystal is a gain medium in the amplifier also. Ti: Sapphire oscillator offers the seed beam for amplification process. The process of ultrashort pulse amplification is not feasible directly to reach high peak powers. Ti: Sapphire also has a large gain band width needed to amplify ultrashort pulses. A limitation comes from the tendency of high intensity beams to

self-focus destructively, which makes it necessary that intensity present in amplifiers be limited to <10 GW/cm^2. But ultrashort pulse can be effectively amplified without any obstacle by employing chirped pulse amplification (CPA) method which was introduced by Strickland et al.[20]

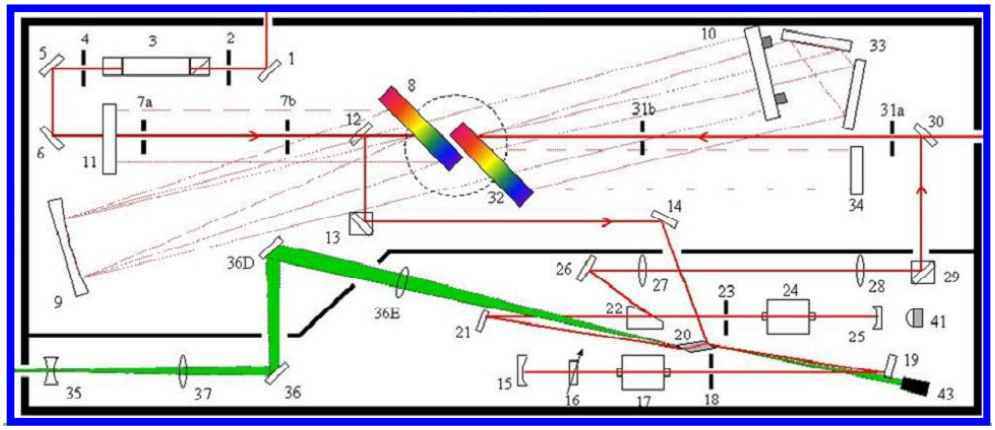

Figure 2.3 Schematic of Legend amplifier (fs) and it subdivisions stretcher, regenerative amplifier, and compressor [adopted from Legend amplifier manual]. [19]

The amplifier laser system (LEGEND) is typically composed of three essential elements to amplify the ultrashort pulse to mJ level[19] and the layout is shown in figure 2.3. Those elements are (a) an optical stretcher (b) a regenerative amplifier (RGA) and (c) an optical pulse compressor. The design of the stretcher and compressor is slightly different due a high amount of bandwidth coming from the oscillator. Different density grooves are used for the stretcher grating (1200 ln/mm) and compressor grating (1500 ln/mm) and it is easier to recompress the optical pulse after amplification.[19]

In the CPA method the oscillator pulse of ~15 fs is stretched upto ~200 ps using single grating pulse stretcher where the peak power of pulse is reduced 10,000 times initial power. The Pockel's cell switches the seed pulse into the resonator. In order to ensure that a single pulse which is chosen from the seed pulse train is admitted to the resonator the Pockel's cell must be switched at the same time with respect to the seed laser every time. To achieve the switching is synchronized to the RF signal generated by the seed laser. The principle of regenerative amplifier is to confine, by polarization, a single pulse picked from a modelocked pulse train, amplify it to an appropriate energy level, and then cavity dump the output. Typically, seed pulse energy with few nJ can be amplified to 2.5 mJ in the fs case (and ~2 mJ in the

ps case). Ti:Sapphire laser rod was optically excited by SHG of Nd: YLF laser pulse (200 ns) of 527 nm wavelength from evolution laser head and the overall amplification possible is ~10^6. Generally, the amplification of Ti: Sapphire laser rod is small upto 3-4 times for single pass. However, the regenerative amplification technique allows the pulse to pass multiple times through the rod (multi-pass) resulting in much higher gain. Consequently, it is easier to recompress the optical pulse after the amplification. The use of negative diffraction order in the stretcher to introduce the right amount of dispersion and groove density compensate for higher phase dispersion coefficients which limits the recompression of ultrashort pulse below 70 fs (~2 ps). Chirped pulse amplified Ti: sapphire laser system (LEGEND, Coherent) delivers 1 kHz nearly bandwidth limited laser pulses of ~40 fs (~ 2 ps) pulse width at 800 nm.

2.3. Ultrashort pulse characterization

The knowledge of pulse duration and phase, of especially ultrashort pulses (<1 ps), is essential for several time-resolved experiments involved in spectroscopy and other applications. Due to the large bandwidth associated with these pulses and combined with the dispersion effects it is essential to characterize these pulses at different parts of the experimental set up. Hence, simple techniques are required to rapidly measure the pulse characteristics at that point. Fast detector and electron streak camera (up to 0.5 ps resolution) can provide the information about ns and ps pulses. There are no optoelectronic devices for measuring the pulse duration which is of the order of tens or hundreds of fs. Autocorrelation[21,22] is only the technique to measure the ultrashort pulse effectively in which width of one pulse is measured by the replica of the same pulse. Here, intensity auto correlation (also known as second order auto correlation) is the generalized technique normally employed to measure the pulse duration using SHG from BBO crystal. The generated SHG signal intensity is the combination of two fundamental intensities and it can be described as

$$I_{SHG} = I(t) * I(t-\tau) \tag{2.3}$$

Detectors are very slow to resolve this beam in time, so they will give the average signal

$$A^{(2)}(\tau) = \int_{-\infty}^{\infty} I(t) I(t-\tau)\, dt \tag{2.4}$$

Where I(t) and I(t-τ) are the intensities of two pump beams and τ is relative delay between the two pulses. From the obtained autocorrelation trace, the input pulse width can be calculated, provided the pulse shape of the input pulse is known. Experimental technique of measurement of the pulse duration is described below.

2.3.1. Autocorrelation experiment

Experiment involves splitting the input pulse into two, delaying one with respect to other and spatially (and temporally) overlapping the two pulses in some instantaneously responding NLO crystal such as SHG crystal in a non collinear geometry. Optical delay was constructed with retro reflector which was made with normal mirrors on the translation stage. The SHG crystal produced signal light at twice of the frequency of input light when path lengths of the both beams were equal (at zero delay). Experimental schematic is similar to the pump-probe experiment which is described in section 2.12 (figure 2.13). Fundamental pulse (at 800 nm, 1 kHz rep. rate, ~40 fs) from amplifier was split into two equal parts [50/50 beam splitter].

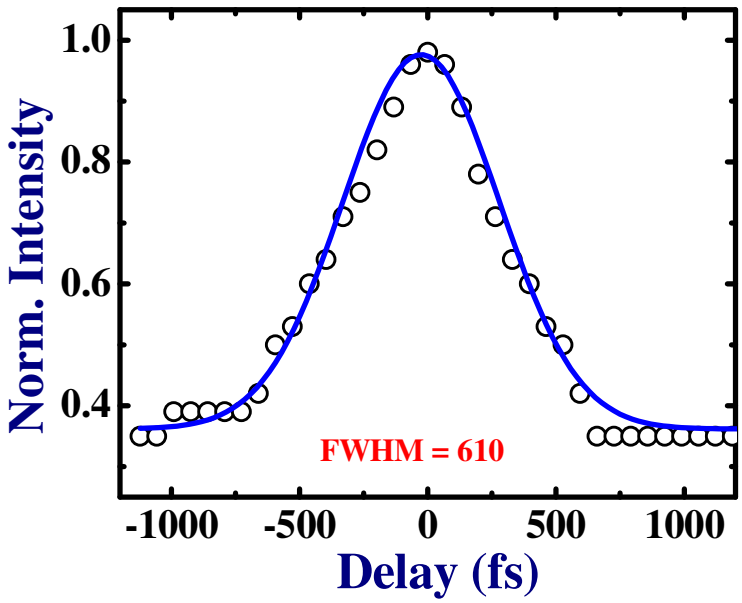

Figure 2.4 Autocorrelation trace from type I BBO crystal with fs laser pulses from amplifier.

Among the two pulses, one pulse was delayed with respect to the former one and these two pulses were focused on to the critically phase matched type II BBO crystal by a convex lens of focal length ~15 cm. The SHG signal light was collected

by photo diode (SM1PD2A) which was connected to a lock in amplifier. Both delay stage and lock in amplifier were controlled by the personal computer. The temporal evolution of SHG signal was recorded at different delays, shown in figure 2.4.

The trace of the autocorrelation signal was fitted with a Gaussian beam profile[22] and estimated the FWHM value was ~610 fs.

For Gaussian pulses $\Delta\tau_p = 0.707\ FWHM = 0.707 \times 610\ fs = 431\ fs$

The discrepancy between the actual pulse width and measured pulse width is because of group velocity mismatch (GVM) and group velocity dispersion (GVD) due to the thickness of the BBO crystal. The GVM and GVD are elevated from the dispersion effects, generated in the media. Generally, phase vector is used to explain the dispersion effect[23-26] and this can be described as

$$\varphi(\omega) = n(\omega)kL = k(\omega)L \tag{2.5}$$

Where k(ω) is phase vector, L is the thickness of the medium and n(ω) is the refractive index of the material at frequency ω. By considering the higher order phase effects involved, the phase term can be expanded using Taylor's series.

$$k(\omega) = k(\omega_0)L + k'(\omega_0)(\omega-\omega_0)L + \frac{1}{2}k''(\omega_0)(\omega-\omega_0)^2 L - - - - - - \tag{2.6}$$

Where first two terms refer to reciprocal of phase velocity and group velocity, and third term related to variation of group velocity with respect to the frequency

$$\left.\begin{aligned} k(\omega_0) &= \frac{\omega_0}{v_\phi(\omega_0)} \\ k'(\omega_0) &= \frac{1}{v_g(\omega_0)} \\ k''(\omega_0) &= \frac{d}{d\omega}\left(\frac{1}{v_g}\right) \end{aligned}\right\} \tag{2.7}$$

GVM is connected to the term $k'(\omega_0)$ which can be calculated from the Sellmeier equation for BBO (SHG) and estimated value of GVM is 180 fs/mm at 800 nm

fundamental wavelength. Moreover, GVD is related to $k''(\omega_0)$ and this can be estimated from the equation[27]

$$\beta = \sqrt{\left\{1 + \left[4ln2\left(D_2 \times \frac{L}{\tau_{in}^2}\right)^2\right]\right\}} \qquad (2.8)$$

Where β is the GVD factor. D_2, L and τ_{in} refer to second order differentiation term, crystal length and pulse width, respectively.

The obtained value of GVD at 800 nm was 74.735 fs^2/mm for BBO. From these calculations, we have estimated the pulse duration once passed through the BBO crystal (~2 mm) to be ~388 fs (GVM × L = 180 fs/mm × 2 mm).[26] But the experimental value measured was ~431 fs. Therefore, the experimental and theoretical pulse width values were ~431 fs and ~360 fs, respectively, and the small discrepancy could be because of GVD.

2.3.2. Measurement of bandwidth for fs/ps pulses

The pulse from MICRA oscillator can be tuned from ~15 fs to ~100 fs with corresponding bandwidth adjustment possible from ~100 nm to ~10 nm by tweaking the prisms.

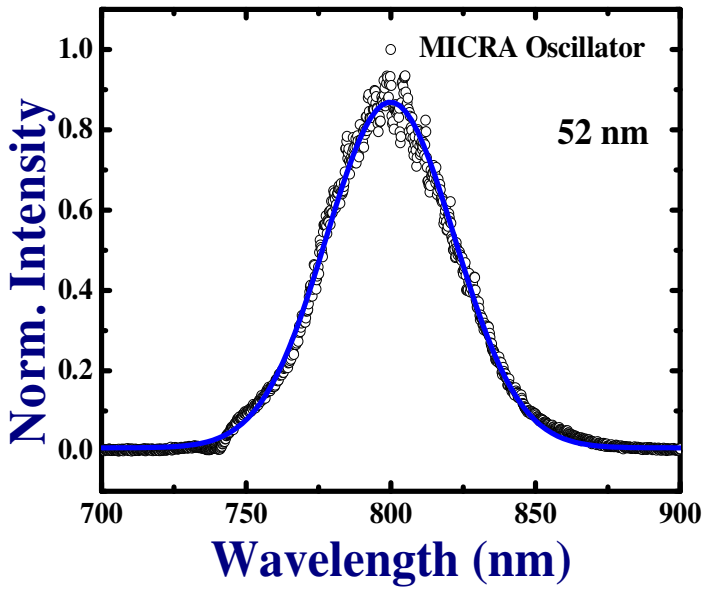

Figure 2.5 Output of MICRA (femtosecond oscillator) as measured by Ocean optics spectrometer (USB 4000). Bandwidth (FWHM) of output was found to be ~52 nm at 800 nm. Open circles are the data and solid line is the fit.

The spectral bandwidth of MICRA pulse plays an important role to get stability in the fs amplifier. In general, the optimal bandwidth of 50-55 nm (FWHM) is sufficient for the operation of fs amplifier and ps amplifier. Figure 2.5 shows a typical spectrum of MICRA oscillator, which was recorded using USB4000 spectrometer with the help of spectra suit software. The spectra bandwidth was estimated by fitting data with Gaussian curve and the obtained value was of ~52 nm. The ps amplifier does not require such bandwidth.

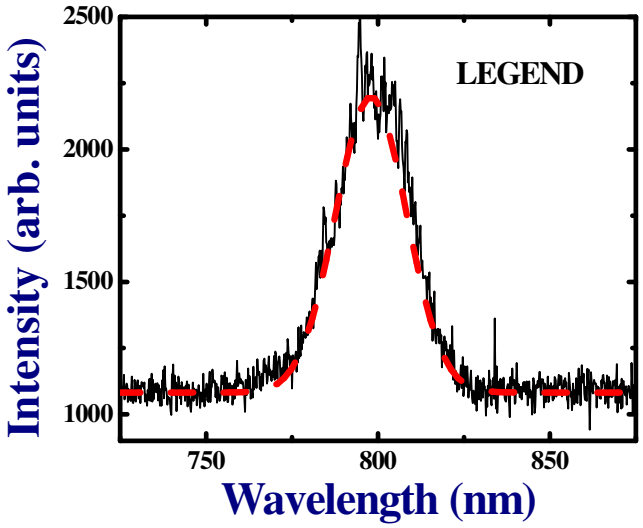

Figure 2.6 Output of fs amplifier measured by a spectrometer (USB 4000). Band width was found to be (FWHM) ~25 nm at 800 nm. Dotted line is the fit while black wriggly line is the data.

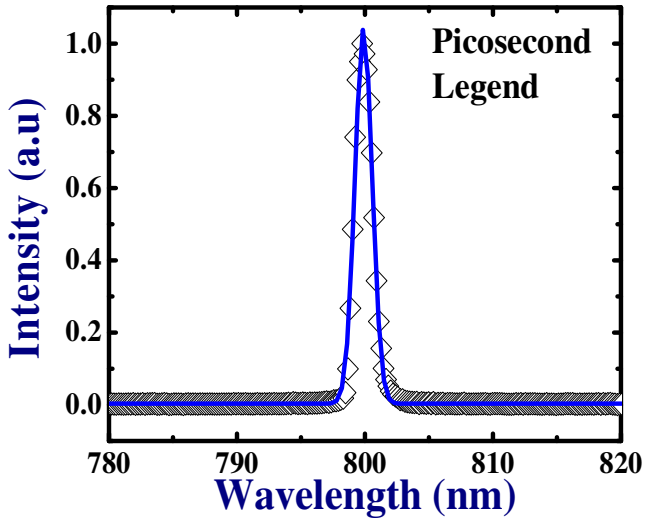

Figure 2.7 Output of fs amplifier measured by a spectrometer (USB 4000). Band width was found to be (FWHM) ~1.1 nm at 800 nm. Solid line is the fit while open diamonds are the data.

The fs and ps amplifiers were designed in such a way that both can be operated at the same time by seeding with MICRA pulse. Figure 2.6 illustrates a wavelength-intensity spectrum of pulse generated from fs amplifier and FWHM value was obtained by fitting with Gaussian. The estimated spectral band width was ~25 nm. Similarly, we recorded ps amplifier spectrum shown in figure 2.7 and FWHM value was ~1.1 nm.

2.3.3. Estimation of pulse width from the spectral bandwidth

The ultrashort pulse width can also be determined from FWHM of spectral width ($\Delta\omega$) curve. According to Heisenberg uncertainty principle, the value of the time-bandwidth product should be less than 1 which is depending on the shape of the pulse and it can be described as $\Delta\nu\ \Delta t$ = constant.

For example in the case of **Gaussian it is 0.441** and **0.315 for sech pulses**, **0.142 for Lorentzian pulses**.[22] In our case, we assume all the lasers offer Gaussian pulses. The ultrashort pulses which follow the time-bandwidth product are said to be **transform limited** pulses and they are clean without any chirp and possesses minimum possible pulse duration. The pulse width were obtained from the time-bandwidth product using inserting bandwidth value, are 18.1 fs, 38 fs and 0.9 ps for MICRA (oscillator), fs amplifier and ps amplifier, respectively.

2.4. Ultrashort laser ablation

All the ablation experiments[28-34]were carried out at a wavelength 800 nm. Copper (Cu)/silicon (Si) nanoparticles (NPs) and nanostructures (NSs) were synthesized by ablating bulk Cu/Si in single (or) more organic liquid media [such as acetone, dichloromethane (DCM), acetonitrile (ACN), chloroform, and methanol] using 1 kHz chirped pulse amplified Ti: sapphire laser system (LEGEND, Coherent) delivering nearly bandwidth limited laser pulses of ~40 fs (~2ps) pulse width at 800 nm. The average power from amplifier was ~2.5 W in fs domain (~2 W in ps domain). The initial laser beam of diameter 8 mm was focused on the surface of Si substrate with the help of a 25 cm focal length of the lens. The solid targets were cleaned in an ultrasonic cleaner with acetone. Cu/Si target was submerged under the organic liquid in a Pyrex cell and effective thickness of liquid layer above the target was ~7 mm. Complete details of the respective experiments are explained in their

chapters and a experimental schematic of ultrashort pulse laser ablation for nanomaterials fabrication is shown in figure 2.8.

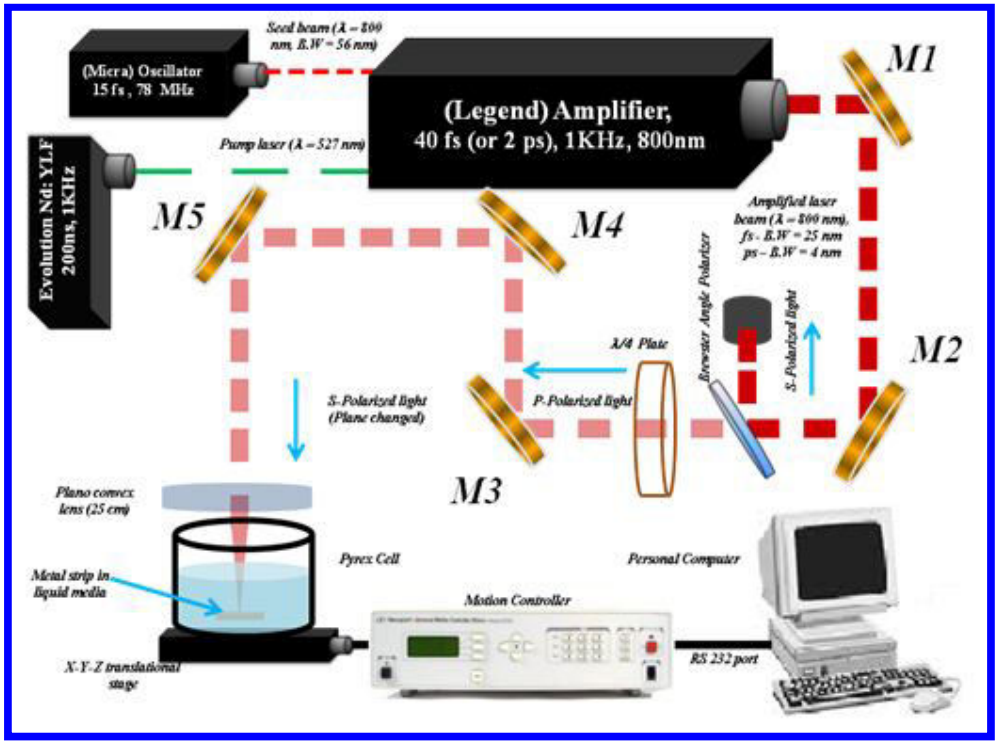

Figure 2.8 Schematic of the ultrashort pulse laser ablation experiments.

The theoretical beam waist ($2\omega_0$) estimated at the focal point in air was ~40 μm for an input beam diameter of ~7 mm. Refractive index and thickness of liquid layer play a crucial role in affecting the laser fluence at focus on the surface of target. Consequently, the position of focal plane shift towards the target which modifies the beam waist on the target surface which is show in figure 2.9. Moreover, the focal plane can shift depending on the liquid media and height of the liquid above the target surface. To avoid this shift, we followed some steps. First, we adjusted the focal plane exactly on target surface in air by listening to the furious sound and observing the light produced by laser induced plasma. The modification of beam waist resulted in deposition of lesser fluence on the target. Second, we evaluated the shift (distance) of the focal plane by following the Menendez-Manjon et al.[35] procedure under the effect of the refractive index (n) of the liquid media and height of the liquid layer from the surface of the target (h) by using the equation described below.[36] Depending on the calculated shift of the focal plane (Δf), focus was adjusted to be exactly on surface of

the target by compensating the shift and moving the lens away from the Pyrex cell which could be -Δf.

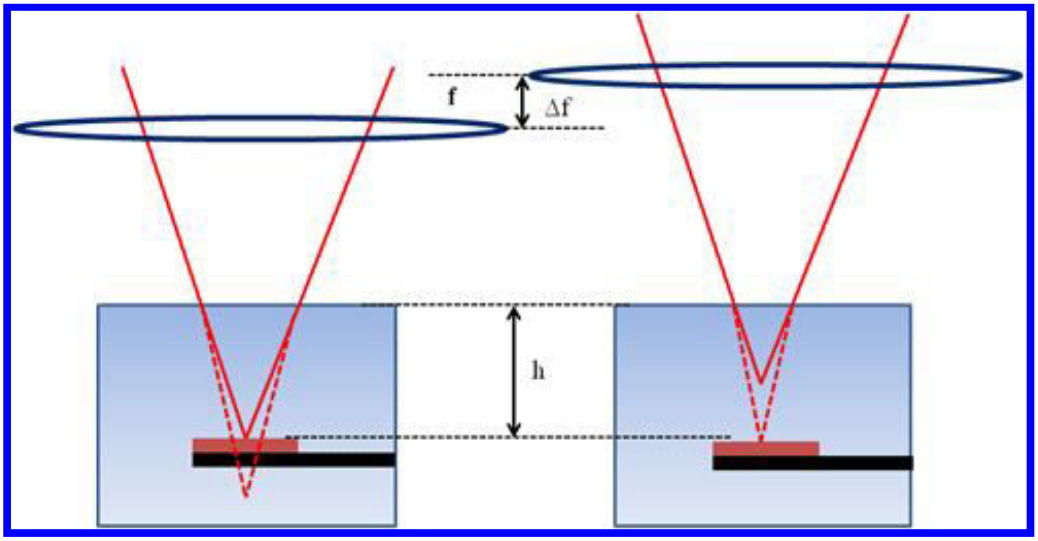

Figure 2.9 Displacement of focal plane when the target is immersed in aqueous media and its correction

$$\Delta f = h\left(1 - \frac{1}{n}\right) \tag{2.9}$$

The beam waist radius can be described on the target surface along the liquid as follows

$$\omega_0 = \sqrt{\left(\frac{\lambda}{n}\frac{(h+n(\Delta f-h))^2+n^2z_R^2}{n^2z_R^2}\right)} \tag{2.10}$$

There is one more complexity behind the beam waist diameter ($2\omega_0$) at focus on the target which plays a significant role in the mechanism of ablation. The produced beam waist diameter on the target in liquid media is considerably more than the beam waist diameter generated in air which is not on the target surface. The increase of beam waist (diameter) on the target in liquid media, could be due to the nano roughness of the metal/semiconductor/dielectric materials (target).[35]

In our experiments, pulse energies of typically 10 μJ – 500 μJ were used and the input energy was controlled by combination of Brewster angle polarizer and half wave plate. The target was placed normal to the laser beam on a three dimensional motorized stage [Nano-direct] with a resolution of 25 nm. The X-Y stages were moved in such a way to draw periodic lines on the substrate with a separation of ~5-

60 µm using scanning speeds of ~0.1-0.3 mm/sec, 0.5 mm/sec in X and Y directions, respectively. Duration of each scan was typically ~40 minutes. After completion of the scan, ablated colloids were collected in air tightened glass bottles. The substrates on which ablation was carried out were cleaned and preserved. The schemes of various experiments are explained in their respective chapters.

2.5. Characterization techniques

2.5.1. Transmission Electron microscopy (TEM)

Transmission Electron Microscopy (TEM) is one of the important techniques in the field of nanotechnology to image the nanoparticles with resolution of ~1 nm. TEM operates on the principle of optical microscopy and it uses electron beam as a source rather than light and much lower wavelength of the electron beam makes it possible to get a resolution thousand times better than with a light microscope. In this technique, the beam of electrons accelerating at 200 kV with velocity of light travel through the vacuum in the column of the microscope and the beam is focused into the ultrathin sample with the help of electro-magnetic lenses. This electron beam interacts with sample when it is transmitted through sample. An image is formed from the interaction of the electrons transmitted through the sample and the image is magnified and focused on to the fluorescent screen which is detected by CCD camera. Moreover, the increasing capability of TEM enables to capture high resolution images in sub nm resolution. This technique is called as high resolution TEM (HRTEM).

The morphology and particle sizes were measured by transmission electron microscopy (TEM) and this technique capability is enhanced by involvement of several techniques such as selected area electron diffraction (SAED) and Energy dispersive X-ray analysis (EDAX) into the TEM instrument. TEM, SAED and EDAX were performed with a FEI technai G2 S-Twin 200 kV instrument. TEM utilized carbon coated copper grids on which a tiny drop of metallic colloid was placed and dried for one day at room temperature.

2.5.2. Selected Area Electron Diffraction (SAED)

Selected area electron diffraction (SAED) is very important technique to determine the crystal phases of nanomaterials and inspect the crystal defects. SAED refers to area which is chosen by user in the image mode where the electron

diffraction pattern needs to be recorded. The image mode is then switched into diffracted mode when SAED aperture is inserted into TEM beam path. SAED can be performed in the region of 100-200 nm which contributes to diffraction pattern on the screen and remaining beam will be blocked. The resultant pattern is recorded using a CCD camera. For polycrystalline samples, more than one crystal contributes to SAED pattern and it is difficult to analyze the data. At a time it is useful to select a single crystal for analysis. It may also select two or more crystals, consecutively, to determine the crystal orientations between them. Moreover, diffraction from a single crystal in a polycrystalline sample if the aperture is small enough/crystal large enough.

2.5.3. Energy dispersive X-ray analysis (EDAX)

When the electron beam displaces electrons in the sample, the atom return to its normal state, by dropping an outer shell electron into the vacant inner shell. This drop results in the loss of a specific amount of energy. This energy is given up in the form of electromagnetic radiation X-rays. Since energy levels in all elements are different, element-specific or characteristic X-rays are generated. The accumulation of these energy counts creates a spectrum representing the chemical analysis of the sample. The microscope is equipped with an Oxford Inca Energy Dispersive X-ray analysis (EDAX) for chemical analysis. Qualitative and quantitative analysis, elemental mapping and line-scans can be performed in this technique

2.5.4. Scanning Electronic Microscopy (SEM)

The field emission scanning electron microscope (FESEM) [Ultra 55 from Carl ZEISS instrument] has become one of the most widely utilized instruments for materials characterization. The SEM has a large depth of field, which allows more of the specimen to be in focus at one time. The SEM also has much higher resolution, so closely spaced specimens can be magnified at much higher levels, because the SEM uses electromagnets rather than lenses and we can have much more control in the degree of magnification. In SEM, the image is formed and presented by a very fine electron beam, which is focused on the surface of the specimen. The beam is scanned over the specimen in a series of lines and frames called a raster. The raster movement is accomplished by means of small coils of wire carrying the controlling current (the scan coils). At any given moment, the specimen is bombarded with electrons over a

very small area. Several things may happen to these electrons. All these effects can be used to produce an image. The secondary electrons are selectively attracted to a grid held at a low positive potential (50 volt) with respect to the specimen. The grid is a disc held at about 10 kilovolts positive with respect to the specimen. The disc consists of a layer of scintillant coated with a thin layer of aluminum. The secondary electrons pass through the grid and strike the disc, causing the emission of light from the scintillant. The light is led down a light pipe to a photomultiplier tube which converts the photons of light into a voltage. The strength of this voltage depends on the number of secondary electrons that are striking the disc. Thus the secondary electrons produced from a small area of the specimen give rise to a voltage signal of a particular strength. The voltage is led out of the microscope column to an electronic console, where it is processed and amplified to generate a point of brightness on a cathode ray tube screen. An image is built up simply by scanning the electron beam across the specimen in exact synchrony with the scan of the electron beam in the cathode ray tube.

2.5.5. UV-Vis absorption spectroscopy

UV-Visible extinction spectra (Jasco V-670) were recorded for all colloidal NPs to find out the surface plasmon peak (or) characteristic absorption peak position. All spectra were measured at room temperature in a quartz cuvette with 1 cm optical path.

2.5.6. Raman spectroscopy and Photoluminescence spectroscopy

Raman spectra and photoluminescence (PL) spectra of all colloidal Si NCs was placed on glass cover slip and allowed to dry for 1 hour and the spectra were recorded using WITec Alpha 300 spectrometer at an excitation wavelength of 532 nm (CW). The sample on the cover slip can be effortlessly recognized through the in-built optical microscope (with an objective lens of 40X) and the spectrum was collected by the in-built spectrometer in the WITec instrument simultaneously. To avoid the heating effect through the accumulation, low power (<5 mW) was used for the both studies.

2.6. Experimental details of SERS/ SEF

Surface enhanced Raman spectroscopy (SERS) is the spectroscopic technique, utilizing typically Cu NSs (or) NPs and Ag coated Si NSs which allows enhancement of the Raman signal from adsorbed organic/explosive analyte species of very lower concentrations. Cu NSs (or) NPs and Si NSs with diverse morphologies were produced by laser ablation. SERS of all analytes such as ANTA, FOX-7, CL-20, R6G, etc. with low concentration were placed on Cu NSs and they were allowed to dry for 1 hour Raman spectra recorded using WITec Alpha 300 spectrometer at an excitation wavelength of 532 nm (CW). The sample on the Cu NSs could be recognized through the in-built optical microscope (with an objective lens of 100X) and the spectrum was collected by the in-built spectrometer in the WITec instrument simultaneously. Acquisition time for recording was 5 s and all spectra and was calibrated with Raman peak of silicon wafer at 520 cm^{-1}. In the Micro Raman spectrometer the laser beam was focused on to the substrate using an objective lens (100X) and the theoretical beam waist estimated was ~600 nm. To estimate enhancement factor, we recorded the normal Raman spectra of analyte with higher concentration which was adsorbed on a cover slip and compared with SERS spectra of analyte at lower concentration in the presence of Cu NSs with different morphology. Similarly, SEF spectra of analytes (10 µL) with low concentration mixed with Cu NPs were placed glass cover slip and spectra were recorded using the above mentioned spectrometer which was compared with florescence spectra of high concentrate analyte. To avoid the heating effect through the accumulation, low power (5 mW) was used for both studies.

2.7. Z-scan Experiments

The efficiency of Kerr nonlinearity of an optical material is generally determined by Z-scan technique. In this technique, the Kerr medium is translated along laser beam propagation direction (Z-axis) (towards and away from focal point) across the focal volume which can be created by external lens and the transmittance at different Z positions is collected. The Kerr nonlinearity is resultant of the combination of nonlinear absorption and nonlinear refraction which can be studied by open aperture and closed aperture Z-scan techniques, respectively.[37-39] Nonlinear absorption is certainly dependent on linear absorption spectra and input peak intensities. Nonlinear absorption can be observed in two ways (i) saturable absorption

(SA) and (ii) reverse saturable absorption (RSA) where the selective excitation wavelength of the laser is in the range of absorption band and far from the absorption band, respectively. In the case of open aperture experiment, the detector collects full transmittance from the sample and the schematic is shown in figure 2.10(a). For third order nonlinearity, we mainly focus on two photon absorption (2PA). On the other hand, closed aperture Z-scan is employed to determine the nonlinear refraction and this schematic is shown in figure 2.10(b). The transmittance from the sample is generally combination of both nonlinear effects. In this measurement, aperture is needed to be close where 25% of transmittance only enters in to the detector (only the center of the Gaussian beam) to avoid the absorption effects.[37] From that we can assure that nonlinear absorption is reduced.

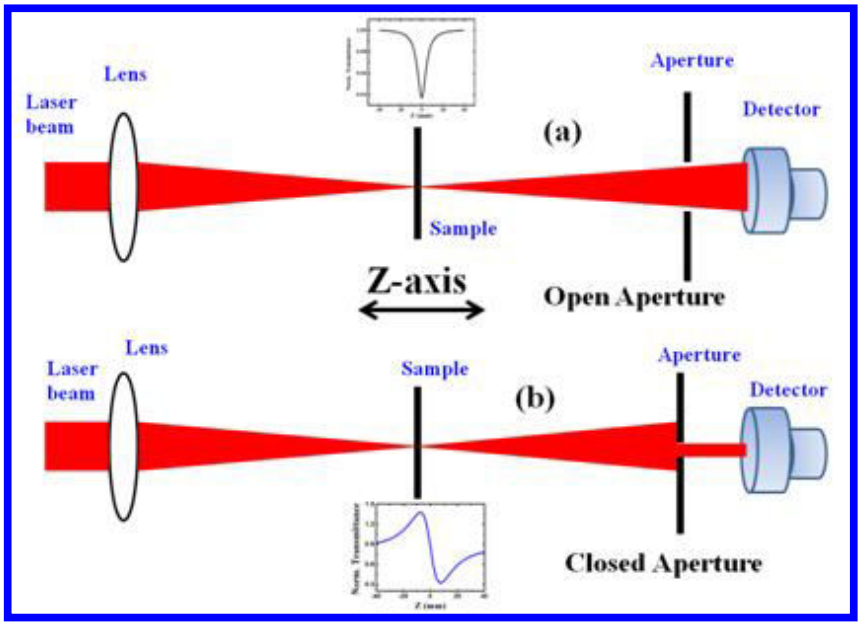

Figure 2.10 Schematic of (a) open aperture and (b) closed aperture Z-scan technique

Additionally, closed aperture scans were performed at low intensities where the contribution from the higher order nonlinear effects is negligible. As a result, the value of change in phase ($\Delta\phi$) will be strictly $<\pi$.[37]The transmittance from the sample demonstrates two types of nonlinear absorption behavior and they are positive and negative nonlinearities. In the case of positive nonlinearities (due to positive lensing) the sample illustrates divergence of the transmitted beam before the focal point. Consequently, the diverged beam will be converged after the focal point and the transmittance reaches to a maximum. Whereas in the case of negative nonlinearity

(negative lensing) the sample demonstrates convergence of the transmitted beam before the focal point and, consequently, the converged beam will be diverged after the focal point and the transmittance reaches a minimum.

2.7.1. Picosecond Z-Scan experiments (1 kHz excitation)

For NLO studies colloidal Cu/Si NPs were placed in 1-mm glass/quartz cuvette and Z-scan studies with ps pulses were performed. Ps pulses were generated by separate Ti: sapphire lasers (Coherent, Legend amplifiers) operating at a repetition rate of 1 kHz with a pulse durations ~2 ps at 800 nm.

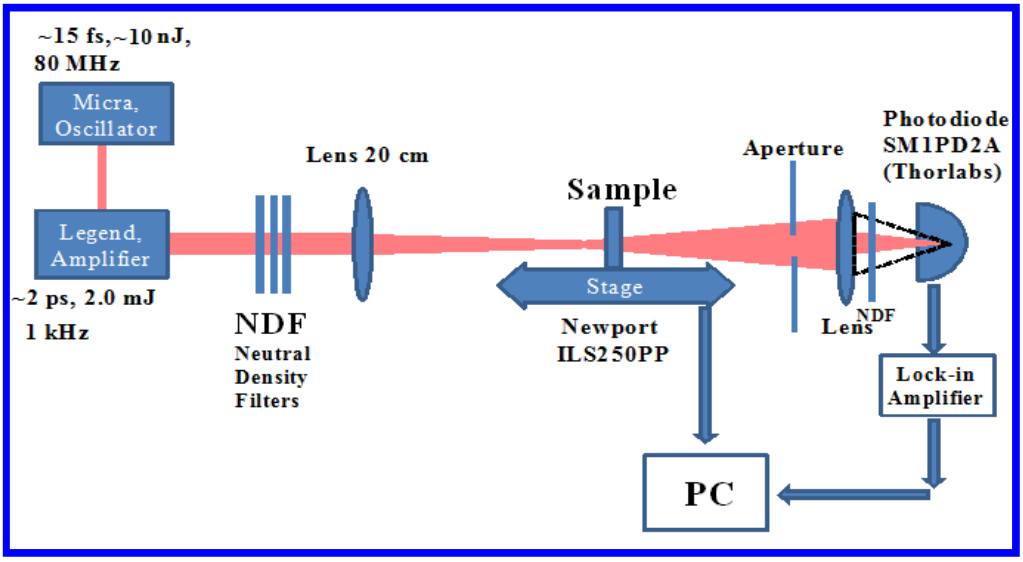

Figure 2.11 Experimental schematic of fs Z-Scan at 800 nm

Z-scan studies[32, 40-42] were performed by focusing the 3-mm diameter input beam using a 200 mm focal length convex lens into the sample and the sample was placed on a high resolution translation stage and the detector (Si photodiode, SM1PD2A, Thorlabs) output was connected to a lock-in amplifier (7265 DSP from Signal Recovery). Both the stage and lock-in amplifier are interfaced which is controlled by a computer program. The picosecond studies were performed with solutions providing ~80-92% (for Cu related NPs) linear transmittances with 800 nm wavelength at different peak intensities for completely understand the intensity dependent nonlinear absorption. The experiments were repeated more than once and the best data were used for obtaining the nonlinear optical coefficients from the best fits. Schematic of the experiment is shown in figure 2.11

2.7.2. Femtosecond Z-Scan experiments (80 MHz excitation)

A Ti: sapphire oscillator (Chameleon, Coherent) was used to investigate NLO properties[43] of Si NPs in solution form at 680 nm wavelength which was pumped with Nd:YVO4 laser of 527 nm wavelength in Verdi, generating pulses of 80 MHz repetition rate and ~140 fs pulse duration. This source was tunable from 680 nm to 1080 nm with 800 nm being the central wavelength. The laser beam passes through the plano convex lens of focal length 10 cm and the sample was moved along the beam propagation path via the focal point and recorded scanned transmittance data manually at every Z position using the detector (Thermal Sensor, Field-Max). The input intensity was cut down by using neutral density filters. The estimated beam waist diameter was to be ~30 µm and corresponding Rayleigh range (Z_r) of ~2 mm which guarantees the thin sample approximation where the sample length << Z_r . Typically, the peak intensities used for the open and closed apertures were 0.38 GW/cm^2 and 0.1 GW/cm^2, respectively. The Z-scan experimental schematic is similar to the figure 2.11.

2.8. Schematic and details of Degenerate Pump-probe experiment

In Pump-Probe spectroscopy, [44-50] the probe pulse provides the information regarding the perturbation induced by the pump pulse. The schematic of a pump-probe setup is shown in figure 2.12. These degenerate pump-probe experiments were carried out by ~70 fs bandwidth limited pulses generated from optical parametric amplifier (OPA- TOPAS-C, Light Conversion, Coherent) and it operates at 1 kHz repetition rate with tunable wavelengths (200–2000 nm). The average power of the pulse was about 150 mW. This OPA was pumped by the Ti: sapphire amplifier with ~50 fs pulses with central wavelength of 800 nm of 2.5 W average power. Typically, studies were performed at 600 nm wavelength. The pulse train from the amplifier was split into two pulse trains. One beam was used as pump which excited the sample. The delay line on the translation stage was inserted in one of the two beams, which is called as probe beam. Both pulses pass through the lenses of focal length of 15 cm and 50 cm with different initial diameters of ~4 mm (pump beam) and ~2 mm (probe beam), respectively and they were allowed to focus on sample. The spatial overlap of the two pulses was aligned into a NLO sample. We strictly followed the ratio of pump to probe intensities to be >20. A chopper was utilized to modulate the

pump beam at 109 Hz and the differential probe transmittance from the sample was recorded by a photodiode (SM05R/M, Thorlabs) which is in the combination of a lock-in amplifier (7265, Signal Recovery). The polarization of pump/probe beams was perpendicular to avoid coherent artifacts.[49] The translation stage was controlled by the ESP motion controller. Both lock-in-amplifier and motion controllers were interfaced with LabView program. Autocorrelation technique was utilized for the optimizing experimental setup for getting the zero delay which provided the spatial and temporal overlap of the beams meeting at the sample.

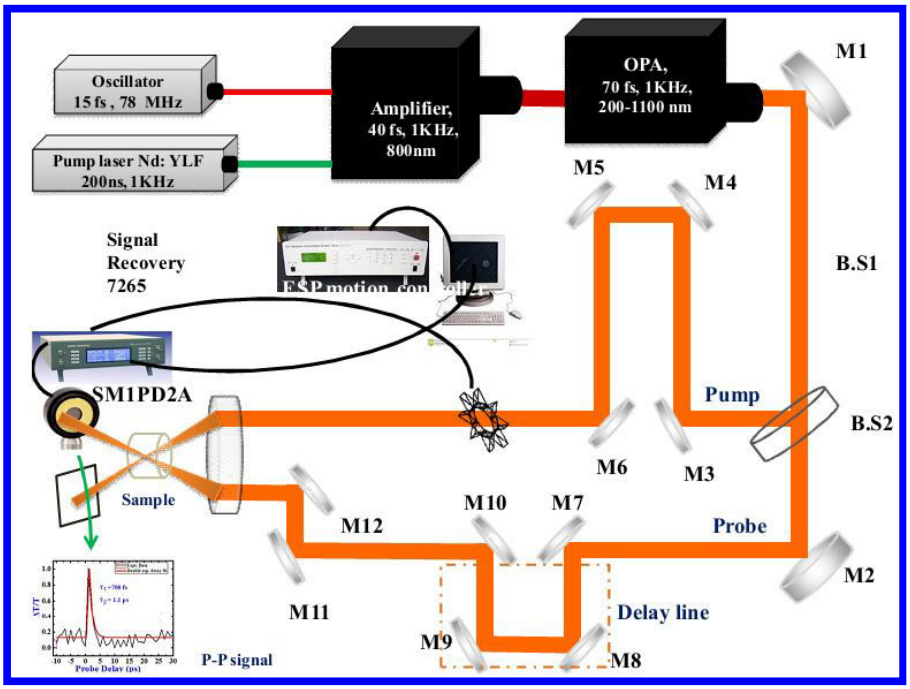

Figure 2.12 Typical schematic arrangement of fs pump-probe experiment at 600 nm.

2.9. Experimental Schematic and Details of Degenerate Four wave mixing

A field interacting with material medium produces an oscillating polarization at an input filed frequency. If two fields interact, oscillating polarization contains the harmonics of individual frequencies, sum frequencies and difference frequencies. Application of the third field at a delay time drive the polarization interacts with the beat frequency of other two and with their sum and difference frequencies. These beatings of the third field with sum or difference frequency of the previous two fields result in the generation of the fourth field. Strength of the fourth field depends on the intensities of input fields and interaction volume.[51] Generation of efficient four wave

mixing signal depend on the phase matching condition.[52-56] Phase matching conditions ensures the addition of microscopic dipole radiation from the molecules at various positions of the sample in the interaction volume to a detectable macroscopic signal. General phase matching condition can be written as

$$\pm\vec{k_1} \pm\vec{k_2} \pm\vec{k_3} \pm\vec{k_S} = 0 \qquad \textbf{(2.11)}$$

$\vec{k_1}, \vec{k_2}, \vec{k_3}$ are the wave vectors of the incident fields and $\vec{k_s}$ is the wave vector of the output field. When the frequencies of input laser fields are equal it is said to be degenerate four wave mixing (DFWM). Interaction volume can be enhanced by utilizing a special beam geometry known as BOXCAR, wherein three input beams are parallel to each other as the three corners of a virtual square and then focused in a sample volume through a lens. Interaction of three beams generates a four wave mixing output. BOXCAR[52-56] geometry in figure 2.13, felicitates the spatial separation of the signal from the input fields as well enhances the interaction volume.

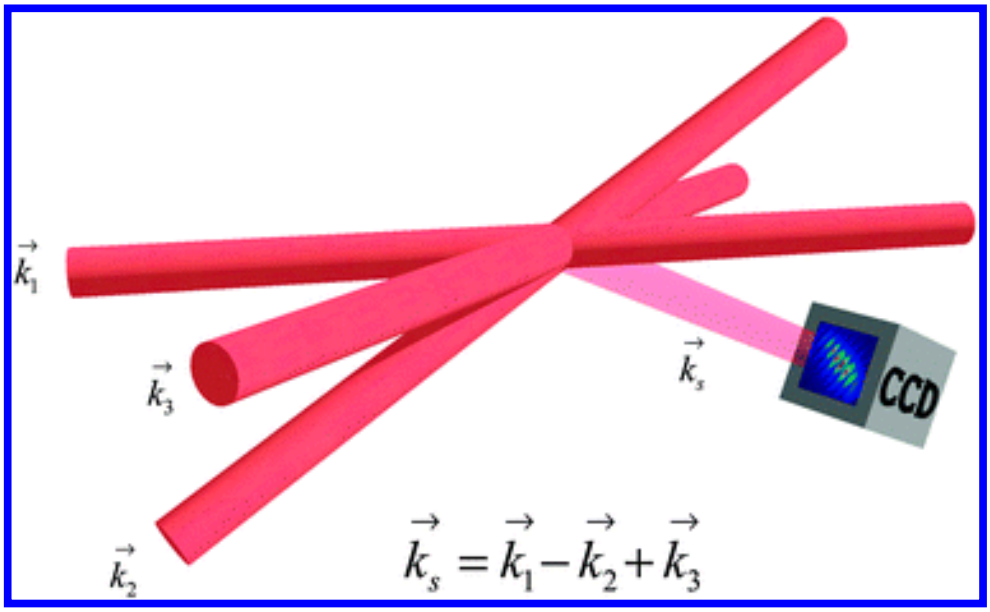

Figure 2.14 Schematic of FWM technique in BOXCARS geometry [image adopted from ref. 57]

NLO properties of NPs colloidal solutions were investigated using fs-DFWM[58-61] in the BOXCAR geometry [with 1 kHz, 800 nm laser pulses (~2 mJ, ~40 fs duration)]. Experimental schematic of fs-DFWM is shown in figure 2.14. The ultrafast NLO properties of Cu suspensions depend on factors such as yield, size and morphologies

of the NPs. Spatial overlap of the three fundamental laser pulses was carried out by a lens of focal length of 15 cm at the sample (Cu suspensions) taken in the cuvette (5 mm path length) made of quartz. Lens with longer focal length was utilized to increase the interaction volume in the sample. Motorized stage (Newport-MILS 100 MTVP) of resolution 0.5 μm, interfaced to ESP motion controller through the Lab VIEW program, was used to overlap the three fundamental pulses of ~40 fs temporally. Before that, autocorrelation of each two beams was carried out to adjust the time zero of the fundamental pulses in the figure 2.14. The four wave mixing transients were recorded as a function of the probe (pulse 1) time delay in steps of 0.066 picoseconds with a fast photodiode (SM1PD2A) which was connected to the lock-in amplifier (Signal Recovery 7265).

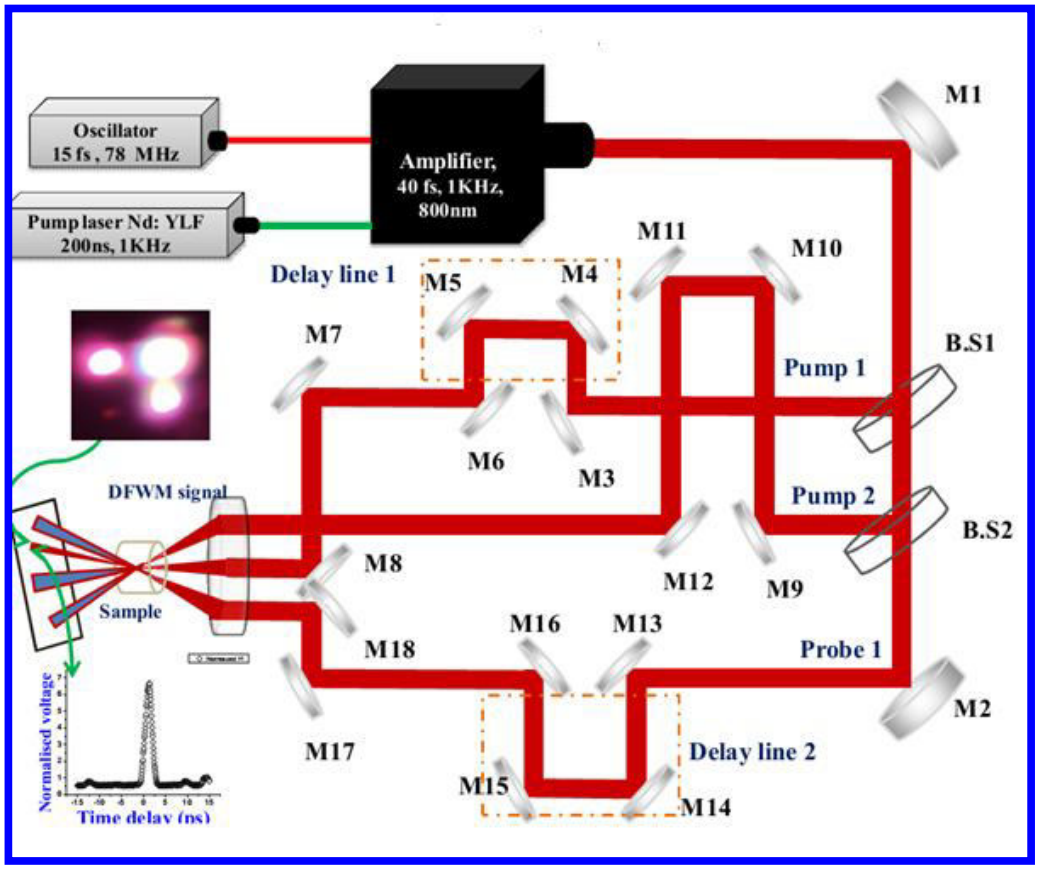

Figure 2.15 Schematic of femtosecond degenerate four wave mixing experiment in BOXCARS geometry.

References

1. Operators manual Micra modelocked Ti: Sapphire laser, Coherent, Santa Clara, CA 95054.
2. http://www.bradallica.com/HET417/Titanium_Sapphire_Lasers.htm
3. W. E. Lamb Jr., Phys. Rev. **134**, A1429 (1964)
4. H. A. Haus, IEEE J. Sel. Top. Quantum Electron. **6**, 1173 (2000)
5. R. Paschotta, Appl. Phys. B **73**, 653 (2001)
6. B. K. Garside and T. K. Lim, J. Appl. Phys. **44**, 2335 (1973)
7. T. Brabec et al., Opt. Lett. **17**, 1292 (1992)
8. U. Morgner et al., Opt. Lett. **24**, 411 (1999)
9. F. Salin et al., Opt. Lett. **16**, 1674 (1991)
10. S. Chen and J. Wang, Opt. Lett. **16**, 1689 (1991)
11. Piché et al., Opt. Lett. **18**, 1041 (1993)
12. J. K. Ranka and A. L. Gaeta, Opt. Lett. **23**, 534 (1998)
13. J. K. Ranka, R. W. Schirmer, and A. L. Gaeta, Phys. Rev. Lett. **77**, 3783 (1996)
14. G. P. Agrawal, Nonlinear Fiber Optics, 4th ed. (Academic, Dan Diego, 2007), Chap. 3
15. S.–Y. Li, F.-M. Guo, Y. Song, A.-M. Chen, Y.-J. Yang and M.-X. Jin, Phys. Rev. A **89**, 023809 (2014)
16. S. Ruhman and R. Kosloff, JOSA B **7**, 1748 (1990)
17. Effects of Dispersion Fiber on CWDM Directly Modulated System Performance, C. R. Campos, and P. R. Horche, Universidad San Pablo CEU, ETSIT, Universidad Politécnica de Madrid, Spain Chapter 3
18. M. D. Perry, T. Ditmire, and B. C. Stuart, Opt. Lett. **19**, 2149 (1994)
19. Operators manual Legend laser system kilohertz, diode pumped, ultrafast Ti:sapphire amplifier, Coherent, Santa Clara, CA 95054.
20. C. D. Strickland and G. Mourou, Opt. Comm. **56**, 219 (1985).
21. Femtosecond Laser Pulses: Principles and Experiments, C. Rullière, Second Edition, Springer, NY (2005)
22. J. –C. Diels and W.R. Rodulph, Ultrashort Laser Pulse Phenomena, (Elsevier, 2006), Chap.9.
23. Recktrebino lecture notes on Ultrashort pulses II
24. M. Ebrahim-Zadeh, Proc. SPIE **6118**, 611809 (2006); M. Ebrahim-Zadeh, Proc. SPIE **6451**, 645106 (2007).
25. K. Moutzouris, Ph.D. Thesis, University of St. Andrews, 2003.
26. V. Petrov, et al., Laser & Photon. Rev. **4**, 53 (2010); Juli, Ph D Thesis, Albert-Ludwigs-Universität Freiburg, page 33 (2007).
27. R. S. S. Kumar, Ph.D. Thesis, University of Hyderabad, 2008.
28. S. Hamad, P. G. Krishna, Md. A. Mohiddon, and S. Venugopal Rao, Appl. Phys. Lett. **104,** 263104 (2014)
29. S. Hamad, P. G. Krishna, V.S. Vendamani, S.V.S. Nageshwara Rao, A.P. Pathak, and **S.** Venugopal Rao , J. Phys. Chem. C. **118** , 7139 (2014)
30. P. G. Krishna, S. Hamad, Md. A. Mohiddon and S. Venugopal Rao, Appl. Surface Sci. **303**, 217 (2014).
31. S. Venugopal Rao, Md. A. Mohiddon and S. Hamad, J. Nanosci. Nanotech. **14**, 1364 (2014)
32. S. Hamad, P. G. Krishna, S. P. Tewari, and S. Venugopal Rao, J. Phys. D: Appl. Phys. **46**, 485501 (2013).

33. P. G. Krishna, S. Hamad, S. P. Tewari, S. Sreedhar, M. D. Prasad, and S. Venugopal Rao, J. Appl. Phys. **113**, 073106 (2013)
34. P. G. Krishna, S. Hamad, S. Sreedhar, S. P. Tewari, S. Venugopal Rao, Chem. Phys. Lett. **530**, 93 (2012).
35. A. M. Manjon, P. Wagener and S. Barcikowski, J. Phys. Chem. C **115**, 5108 (2011).
36. Z. Yan, D. B. Chrisey, J. Photochem. Photobiol. C: Photochem. Rev. **13**, 204 (2012).
37. M. Sheik-Bahae, A.A. Said, T.H. Wei, D.J. Hagan, and E.W. Van Stryland, IEEE J. of Quant. Electron. **QE-26**, 760 (1990); M. Sheik-Bahae, A.A. Said, and E.W. Van Stryland, Opt. Lett. **14**, 955 (1989).
38. T.D. Krauss and F.W. Wise, Appl. Phys. Lett. **65**, 1739 (1994).
39. L.C. Oliveira and S.C. Zilio, Appl. Phys. Lett. **65**, 2121 (1994).
40. S. Venugopal Rao, J. Modern Optics **58**, 1024 (2011)
41. S. Venugopal Rao, T. S. Prashant, T. Sarma, P. K. Panda, D. Swain, and S. P. Tewari, Chem. Phys. Lett. **514**, 98 (2011).
42. S. Hamad, S. P. Tewari, L. Giribabu, and S. Venugopal Rao, J. Porphy. Phth. **16**, 140 (2012)
43. D. Swain, R. Singh, V.K. Singh, N.V. Krishna, L. Giribabu, S. Venugopal Rao, J. Mater. Chem. C **2**, 1711 (2014).
44. A. A. Maznev, T. F. Crimmins, and K. A. Nelson, Opt. Lett. **23**, 1 (1998).
45. G. Cerullo, C. Manzoni, L. Luer, and D. Poli, Photochem. Photobio. Sci. **6**, 135 (2007).
46. J. Mi, L. Guo, Y. Liu, W. Liu, G. You, and S. Qian, Phys. Lett. A **310**, 486 (2003)
47. D. Swain, P.T. Anusha, T. S. Prashant, S. P. Tewari, T. Sarma, P. K. Panda, and S. Venugopal Rao, Appl. Phys. Lett. **100**, 141109 (2012)
48. D. Luo, Q.G. Du, H.T. Dai, H.V. Demir, H.Z. Yang, W. Ji, and X.W. Sun, Scientific Reports **2**, 627 (2012); R.S. Singh, V. Nalla, W. Chen, A.T.S. Wee, and W. Ji, ACS Nano **5**, 5969 (2011); H. Yang, X. Feng, Q. Wang, H. Huang, W. Chen, A.T.S. Wee, and W. Ji, Nano Lett. **11**, 2622 (2011); B. Gu, K. Lou, J. Chen, Y.N. Li, H.T. Wang, and W. Ji, Opt. Express **18**, 26843 (2010); H.I. Elim, Ph.D. Thesis, National University of Singapore, (2005).
49. H. Okamoto, S. Matsumoto, A. Maeda, H. Kishida, Y. Iwasa, and T. Takenobu, Phys. Rev. Lett. **96**, 019706 (2006); N. Kamaraju, S. Kumar, B. Karthikeyan, A. Moravsky, R.O.Lutfy, and A.K. Sood, Appl. Phys. Lett. **93**, 091903 (2008); E.R. Hosler Thesis, University of California, Berkeley (2013).
50. P.T. Anusha, D. Swain, T. S. Prashant, L. Giribabu, S. P. Tewari, and S. Venugopal Rao, J. Phys. Chem. C. **116**, 17828 (2012).
51. C. W. Theil, http://nathan.instras.com/documentDB/paper-52.pdf
52. Y. R. Shen, The Principles of Nonlinear Optics. Wiley-Interscience, New York, (1984).
53. S. Mukamel, Principles of Nonlinear Optical Spectroscopy. Oxford University Press, New York, (1995).
54. W. Demtröder, Laser Spectroscopy: Basic Concepts and Instrumentation. Springer (India), New Delhi, India, (2003).
55. G. L. Eesley, Coherent Raman Spectroscopy. Pergamon Press, New York, (1980).
56. N. Bloembergen, Nonlinear Optics. W. A. Benjamin, Inc., New York, (1965).
57. A. Shalit, and Y. Prior, Phys. Chem. Chem. Phys. **14**, 13989 (2012)

58. T. Hofer, P. Cruck, and W. Kaiser, Chem. Phys. Lett. **224**, 411 (1994).
59. V. Namboodiri, M. Namboodiri, G. Flachenecker and A. Materny, J. Chem. Phys. **133**, 054503 (2010).
60. H. Skendarovic, Phys. Scr. T. **135**, 014037 (2009).
61. G. Boudebs, K. Fedus, C. Cassagne and H. Leblond, Appl. Phys. Lett. **93**, 021118 (2008).

INTENTIONAL BLANK PAGE

3

Fabrication of Copper Nanomaterials: Effects of Liquids, Pulse Energy and Pulse Number

Abstract

This chapter is categorized into three parts wherein first part solely discusses the effect of liquid media (acetone, acetonitrile, DCM, and chloroform) on ablation of Cu targets. Cavitation bubble dynamics involved during the process of ablation are explained using numerical calculations. Second part discuss about the variation of ablation products of Cu as a function of diverse input pulse energies. This study was performed for the Cu targets immersed in acetonitrile. Finally, third part describes the fabrication of Cu nanomaterials (achieved through ps, fs ablation) in methanol, acetone for different pulse numbers. Detailed investigation on modification of threshold fluence as a function of pulse numbers is discussed.

3.1. Introduction

In the present scenario of advances in science and technology, metal nanoparticles (NPs) have received enormous attention due to their potential applications in the fields of biomedicine, photonics, and surface enhanced Raman spectroscopy (SERS).[1-6] The dramatic behavior of metallic nano-entities is attributed to the modification of electronic Eigen states, subject to diverse boundary conditions in the nano-scale, leading to unique electronic, optical, magnetic, and mechanical properties. The spectacular characteristics of nanomaterials, mediated by localized surface plasmon resonances (LSPR), have been successfully exploited in the fields of spectroscopy, and photonics. Ag and Au nanomaterials have been extensively studied as SERS active substrates[7-12] because they demonstrate large signal enhancements compared to other metals since their optical properties are compatible for producing strong surface plasmon resonances in the visible/near-IR spectral range (400 nm-1000 nm). In contrast, copper nanomaterials (NMs) have been studied rarely and applied as SERS active substrates because of thermal instability and partially compatible chemical properties. The main reason behind lower preference of Cu compared to Ag, particularly, is the intrinsic electronic configuration of the former which provides less ratio of real to imaginary parts of dielectric function (3.54 for Cu to 32.4 for Ag). This ratio plays a crucial role in sustenance of plasmon resonances. Furthermore, inherent oxidation effects of Cu metal demands extreme care for avoiding instantaneous oxidation prevailing at the time of fabrication of nanoparticles/nanostructures.

Apart from the elemental semiconductors, other important semiconductors have been obtained by mixing of II-VI (ZnS, ZnSe, ZnTe etc.), III-V (GaN, GaAs, InP etc.), and II-V (Cd_3P_2, Zn_3P_2 etc) group materials. In the last two decades, many research groups have reported that these group mixed semiconductor nanomaterials (NMs) can be utilized as light emitting diodes, quantum dots, second harmonic generation, luminescence, terahertz radiation sources, photovoltaic devices, solar cell etc.[13-14] Relatively, oxide group (ZnO, TiO_2, Bi_2O_3, Cu_2O, CuO etc) NMs were extensively studied for many applications. In the above mentioned oxide group, oxides of copper (Cu_2O/CuO) NPs also have numerous potential properties for applications as solar cells, catalysis, gas sensing, fuel cells, quantum dots, photonics

and virus deactivating applications.[6, 15-19] In earlier research, Cu_2O bulk material was one of the most studied semiconductor material, demonstrated as a first semiconductor, which was used in many applications such as photovoltaic, spintronics and rectifier diodes rather than Si.[20-21]

Many physical and chemical methods have been utilized to fabricate copper / copper oxide NPs and NSs.[22-26] Ultrafast laser ablation in liquid media (ULAL)[27-30] is a preeminent method avoiding multistep chemical synthesis, long reaction times, and can overcome the demerit of Cu material with regard to oxidation. ULAL provides an environment (oxygen free, polar, poor capability of dissolving air) to minimize the effect of oxidation in the process of nanomaterials (NMs) fabrication since ablation occurs underneath the liquid layer. The tremendous advantages of ULAL, in comparison with ablation in air/vacuum medium is that the organic liquids allow the interim interaction of transient metallic plume with the surrounding liquid resulting in formation of metal organosols and provides capability for surface modification as charge distribution, capping of solvent by products.[19, 31-32] Moreover, laser ablation of bulk metal target in suitable liquid media produces periodic (submicron dimensions) surface structures[29, 33-37] for exploiting significant Raman enhancements by supporting the localized surface plasmon resonances (LSPR) and Surface Plasmon Polaritons (SPP). In addition to the specific liquid environments, different overwriting geometries (multiple/double/single line) can be utilized to enhance the possibility of laser induced periodic surface structures (LIPSS) formation. LIPSS align either parallel or perpendicular to input beam polarization and are expected due to the interference of incoming electric filed with surface electromagnetic waves (SEW). These specially patterned surface structures assist in enhancing the Raman signatures even though the surface Plasmons are weaker in Cu compared to Ag or Au. Thus far, several groups have reported fabrication of periodic surface structures using ultrashort pulses for the case when the laser fluences were beyond ablation threshold.[38-39]

In this chapter, three types of representative advances are demonstrated for the fabrication of Cu/CuO NMs. First, the effect of changing the liquid media (acetone, dichloromethane, acetonitrile and chloroform) which plays an important role in controlling of growth, elemental composition and aggregation of NMs were investigated. In the second case, tuning of pulse energy which encourages fabrication

of different size and shaped NMs was implemented. In the last case, varying the pulse numbers allowed generating the aggregated/non-aggregated NPs in liquids and laser induced periodic surface structures (LIPSS) on the substrates. We have extensively investigated and discussed the following in this chapter (a) Cu NPs of different morphologies and laser induced Cu surface structures by ~2 ps ablation of Cu in acetone, dichloromethane (DCM), acetonitrile (ACN) and chloroform (b) copper oxide NPs of different morphologies and laser induced surface structures on Cu target by ~2 ps pulses in ACN under the effect of different laser pulse energies (c) production of laser induced NSs on Cu surfaces using ~2 ps pulses in methanol and ~40 fs pulses in acetone under the influence of different pulse numbers.

3.2. Fabrication of Cu NMs in liquids

3.2.1. Fabrication Process

Cu NPs and NSs have been prepared by ablation of Cu target in liquid media with ~2 ps pulses. The complete details of experiment and experimental schematic have been presented in chapter 2. Pure Cu targets were washed with acetone after sonication to eliminate any residual organic impurities from the surface. The target was placed into a Pyrex cell and covered by a layer of absolute liquids. After ensuring the substrate was perfectly parallel to optical bench, laser pulses were allowed to focus onto the Cu substrate using a plano-convex lens (f = 25 cm). It is crucial to adjust the focus exactly on the surface of substrate immersed in liquid since the refractive index of the liquid medium modifies the focal position resulting in a poor fabrication rate.[40] The beam diameter ($2\omega_0$) estimated at the focus in air was ~40 µm. The typical level of liquid above the metal surface was ~7 mm. Cu targets were placed normal to incident laser beam on a motorized X-Y stage, which was operated through a motion controller (Newport ESP 300). Typical fluence used was ~8 J/cm^2. The scanning speeds of X-Y stages were 0.1 mm/sec in each direction.

The motorized stages were scanned in such way to draw periodic lines on the surface with the given spacing of (a) ~60 µm and (b) ~5 µm. Based on the scanning configuration two types of ablation were carried out (a) single line ablation where in the average number of pulses incident per spot on the target was ~500 (0.1 µm/ms

speed, 1 pulse/ms and assuming a spot diameter of ~50 µm on the target in liquid). Figure 3.1 shows the schematic of scanning and the pulses impact on target while (b) multiple line ablation where in line structures are overlapped. The ablation in this regime is slightly complicated since the spot diameter ($2\omega_0$) was ~50 µm on the substrate and the line separation was ~5 µm. The average number of pulses incident per spot on the target were ~4000. We expect a gradient in the number of pulses incident (perpendicular to the scan direction) and consequently the ablation could be inhomogeneous. Two types of ablations such as multiple line and single line ablation for Cu was demonstrated.

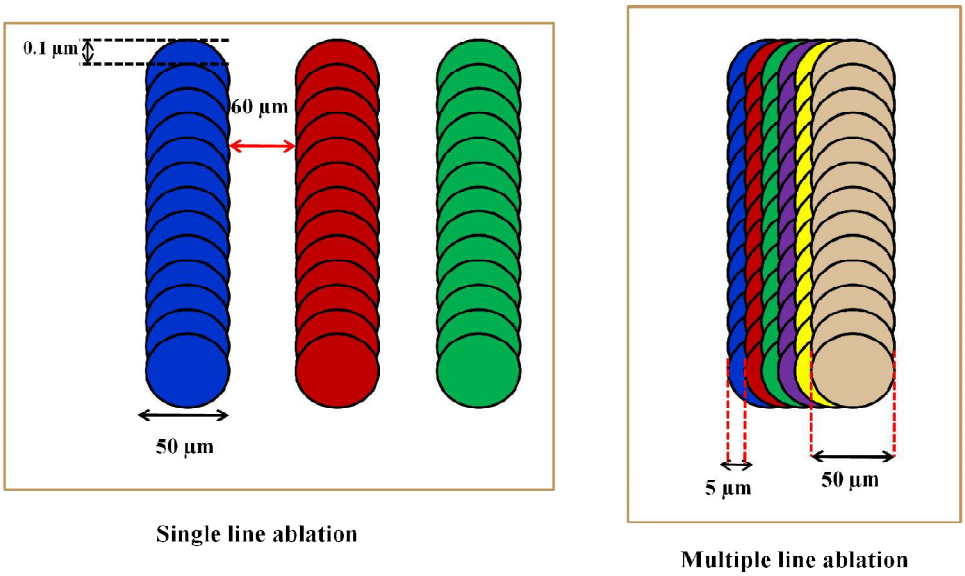

Figure 3.1 schematic of the pulses incident on target.

3.2.2. TEM, SAED and EDAX characterizations of Cu colloids

Cu colloidal NPs have been produced by ps laser ablation in four different liquid media. To avoid the ambiguity, Cu NPs prepared through multiple line (single line) ablation in acetone, DCM, ACN, and chloroform were labeled as MCuNP1 (SCuNP1), MCuNP2 (SCuNP2), MCuNP3 (SCuNP3), and MCuNP4 (SCuNP4), respectively. Morphological studies and particle size measurements were performed by transmission electron microscopy (TEM), selected area electron diffraction pattern (SAED) and energy dispersion X-ray analysis (EDAX) with a FEI tecnai G2 S-Twin 200 kV instrument. TEM utilized carbon coated copper grids on which a tiny drop of metallic colloid was placed and dried for one day at room temperature. TEM images

demonstrated the spherical morphology and well dispersion of NPs with different size distribution in acetone, DCM, ACN, and $CHCl_3$.

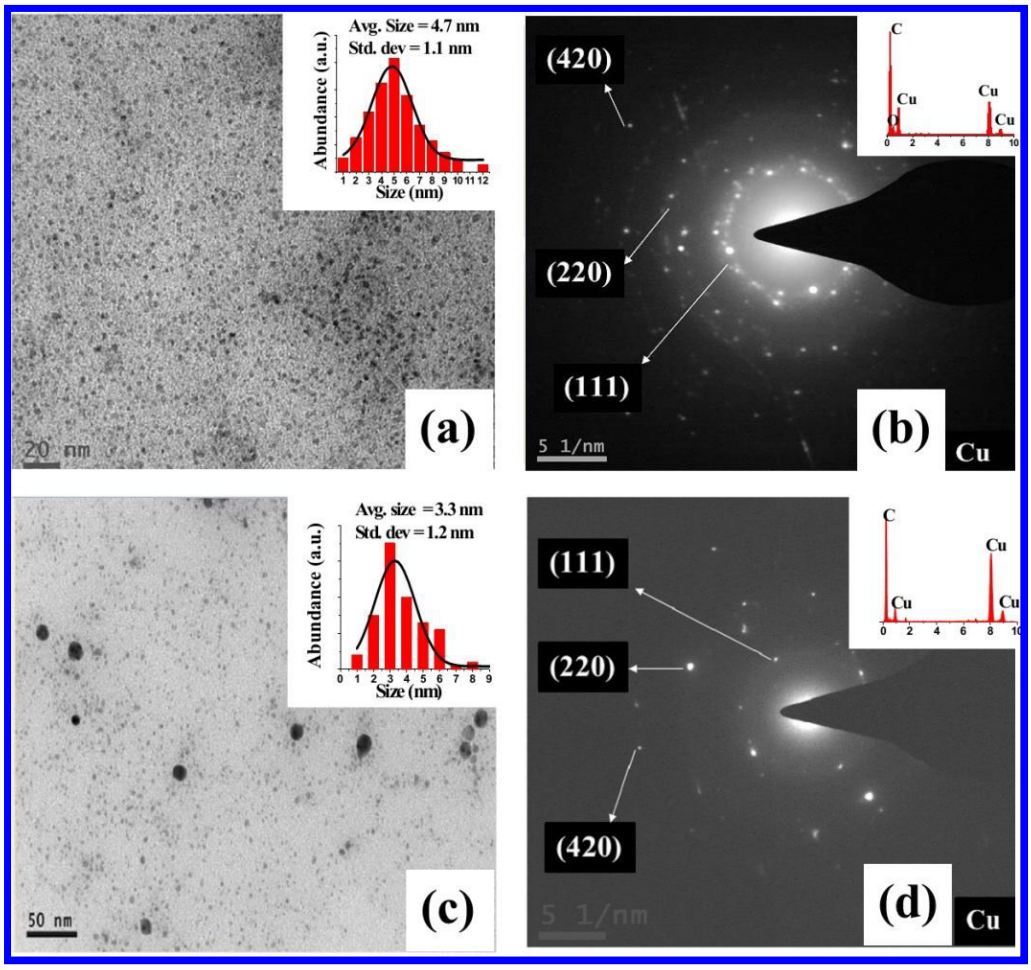

Figure 3.2 TEM images of (a) MCuNP1 (c) SCuNP1. Insets of (a) and (c) depict the NPs distribution (b) SAED spectra of the MCuNP1 and its corresponding EDAX data is shown in the inset (d) SAED spectra of the SCuNP1 and its corresponding EDAX data is shown in the inset.

TEM images of the MCuNP1, SCuNP1 are shown in figures 3.2(a), 3.2(c) and their corresponding SAED patterns are illustrated in figures 3.2(b), 3.2(d) respectively. Insets of the figures 3.2(a), 3.2(c) represents Cu NPs distribution with average sizes 4.7±1.1 nm, 3.3±1.2 nm, respectively, and insets of figures 3.2(b), 3.2(d) depict the EDAX spectra. Polycrystalline nature of the Cu NPs in MCuNP1 and SCuNP1 resulted in concentric ring pattern in SAED data [figure 3.2(b), (d)]. Estimated inter planar spacing (2.07 Å, 1.26 Å, 0.82 Å) was in good agreement with the interplanar spacing of pure copper miller planes (111), (220), and (420), respectively. This was indexed with the standard pattern of the pure cubic phase of copper [PCPDF no. 01-1242]. Figure 3.2(d) illustrates SAED pattern with miller

indices (111), (220) and (420), and their corresponding interplanar spacings 2.09 Å, 1.27 Å and 0.8 Å, respectively. This was also indexed with the standard pattern of the pure cubic phase of copper [PCPDF no. 04-0836]. Likewise, figures 3.3(a), 3.3(c) represents the TEM images of MCuNP2 and SCuNP2 in DCM and insets show the NPs distribution with average sizes of 2.98±0.85 nm, 3.7±1.7 nm, respectively. Figures 3.3(b), 3.3(d) depict the SAED pattern of MCuNP2 and SCuNP2, and inset presents their respective EDAX spectra emphasizing the contribution of the Cu and chloride signatures in the NPs. The SAED pattern of both MCuNP2 and SCuNP2 revealed single crystalline nature. The measured inter planar spacings of 3.38 Å, 1.96 Å and 1.66 Å; 3.42 Å, 3.21 Å, 3.01 Å, 1.96 Å and 1.67 Å matched quite well with the lattice plane separations of CuCl (100), (110), and (112); CuCl (100), (002), (101), (110) and (112) [hexagonal phase, PCPDF no. 09-0017], respectively.

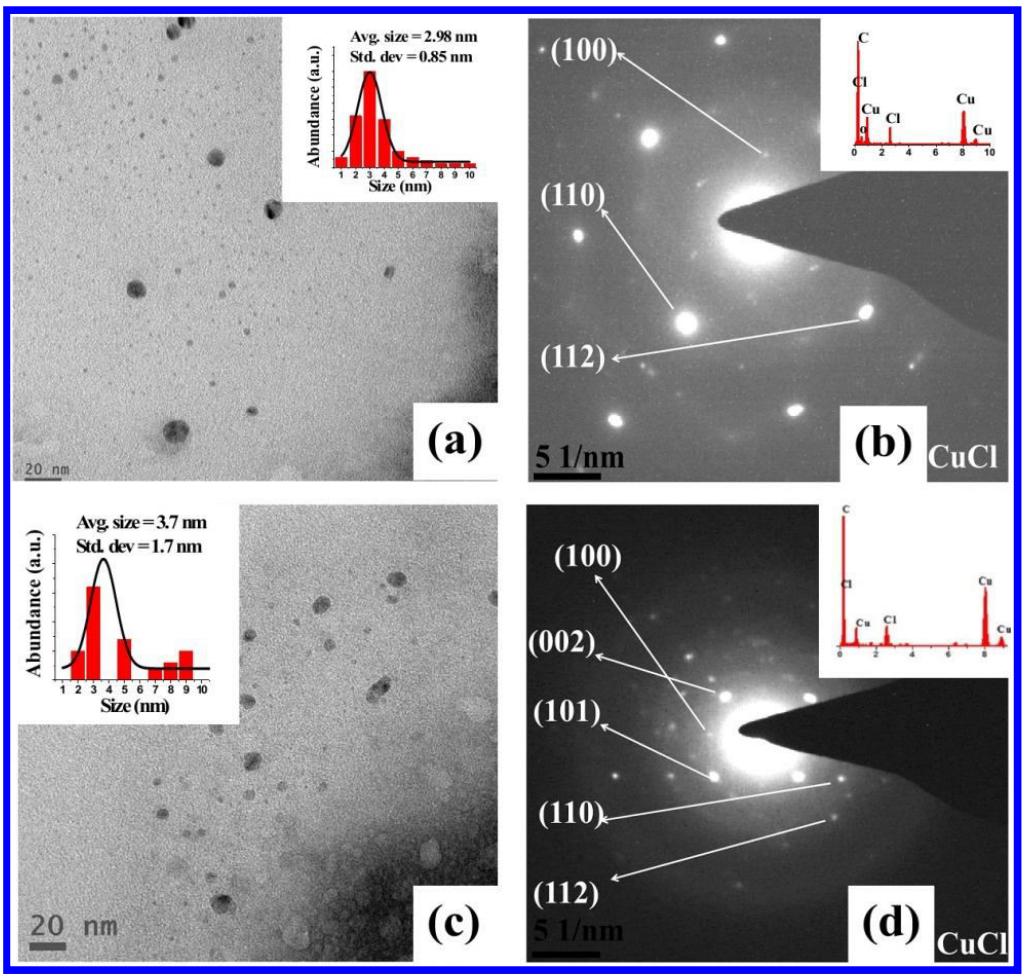

Figure 3.3 TEM images of (a) MCuNP2 (c) SCuNP2. Insets of (a) and (c) depict the NPs distribution (b) SAED spectra of the MCuNP2 and its corresponding EDAX data is shown in the inset (d) SAED spectra of the SCuNP2 and its corresponding EDAX data is shown in the inset

Figures 3.4(a), 3.4(c) represent the TEM images of MCuNP3 and SCuNP3 in ACN with average sizes of 29.2±8.3 nm, 19±6 nm, respectively. Figures 3.4(b), 3.4(d) illustrate the SAED pattern of MCuNP3 and SCuNP3 and Insets demonstrate the EDAX spectra which emphasize the contribution from Cu and oxygen signatures in the NPs. MCuNP3 and SCuNP3 were polycrystalline in nature. Their interplanar spacings (2.50 Å, 2.27 Å, 1.70 Å, 1.29 Å and 1.09 Å; 1.95 Å, 1.71 Å, 1.28 Å and 1.088 Å) extracted from the SAED data were in agreement with the interplanar separations of CuO [Monoclinic phase, PCPDF no. 65-2309] miller planes ($\bar{1}11$), (200), (020), (221) and ($\bar{1}31$); CuO planes ($\bar{1}12$), (020), (221) and ($\bar{1}31$), respectively.

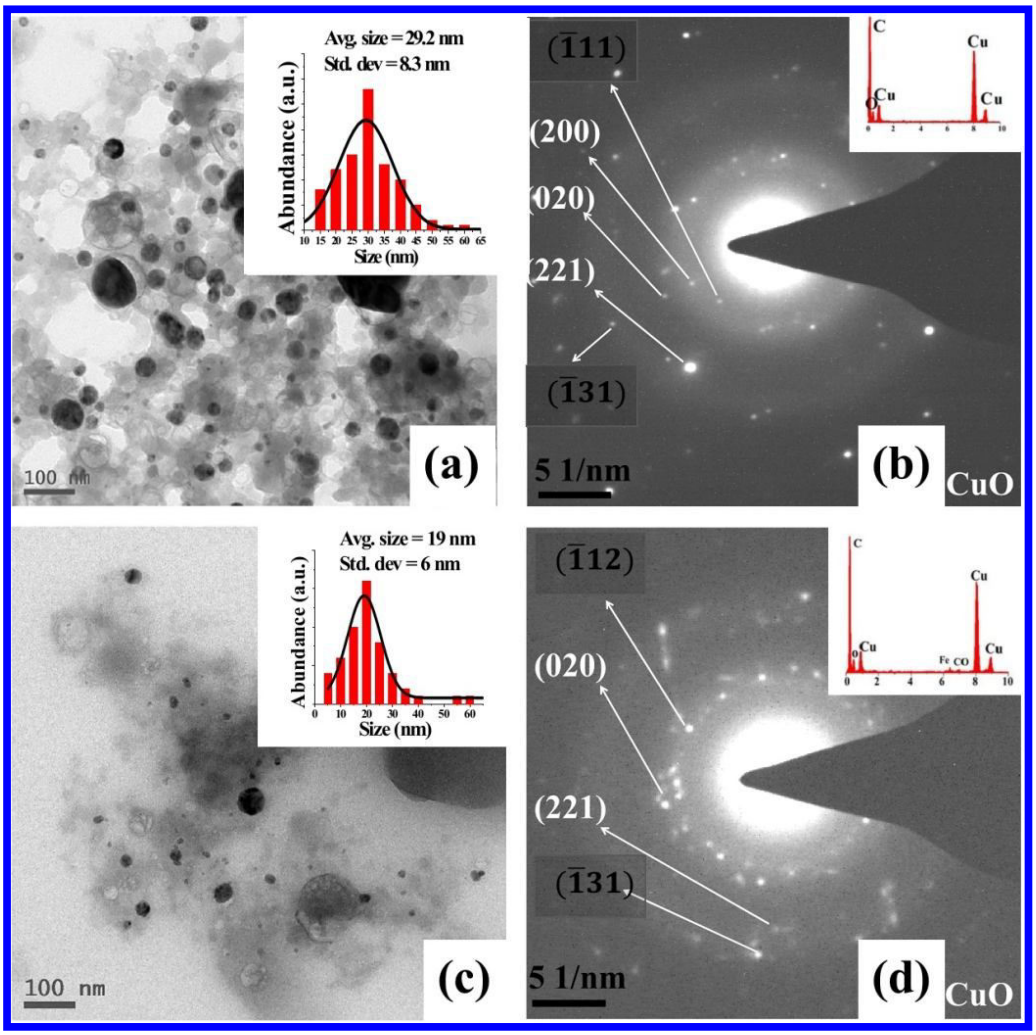

Figure 3.4 TEM images of (a) MCuNP3 (c) SCuNP3. Insets of (a) and (c) depict the NPs distribution (b) SAED spectra of the MCuNP3 and its corresponding EDAX data is shown in the inset (d) SAED spectra of the SCuNP3 and its corresponding EDAX data is shown in the inset.

Figures 3.5(a), 3.5(c) represent the TEM images of MCuNP4, SCuNP4 in chloroform with average sizes of 13±5 nm, 7.2±1.7 nm, respectively. Figures 3.5(b), 3.5(d) depict the SAED pattern of MCuNP4 and SCuNP4. Insets illustrate their respective EDAX spectra which emphasize the contribution from Cu and chloride signature in the NPs. Measured interplanar spacing of MCuNP4 (poly crystalline) and SCuNP4 (single crystalline) were 5.78 Å, 2.92 Å, 1.8 Å, 1.58 Å ; 5.77 Å, 2.91Å, 1.81 Å matched well with the plane separations [Monoclinic phase, PCPDF no. 79-1635] of $CuCl_2$ (001), (200), (112) and (021); $CuCl_2$ (001), (002) and (112), respectively. Further investigations are needed to explain the single crystalline behavior observed in SCuNP4.

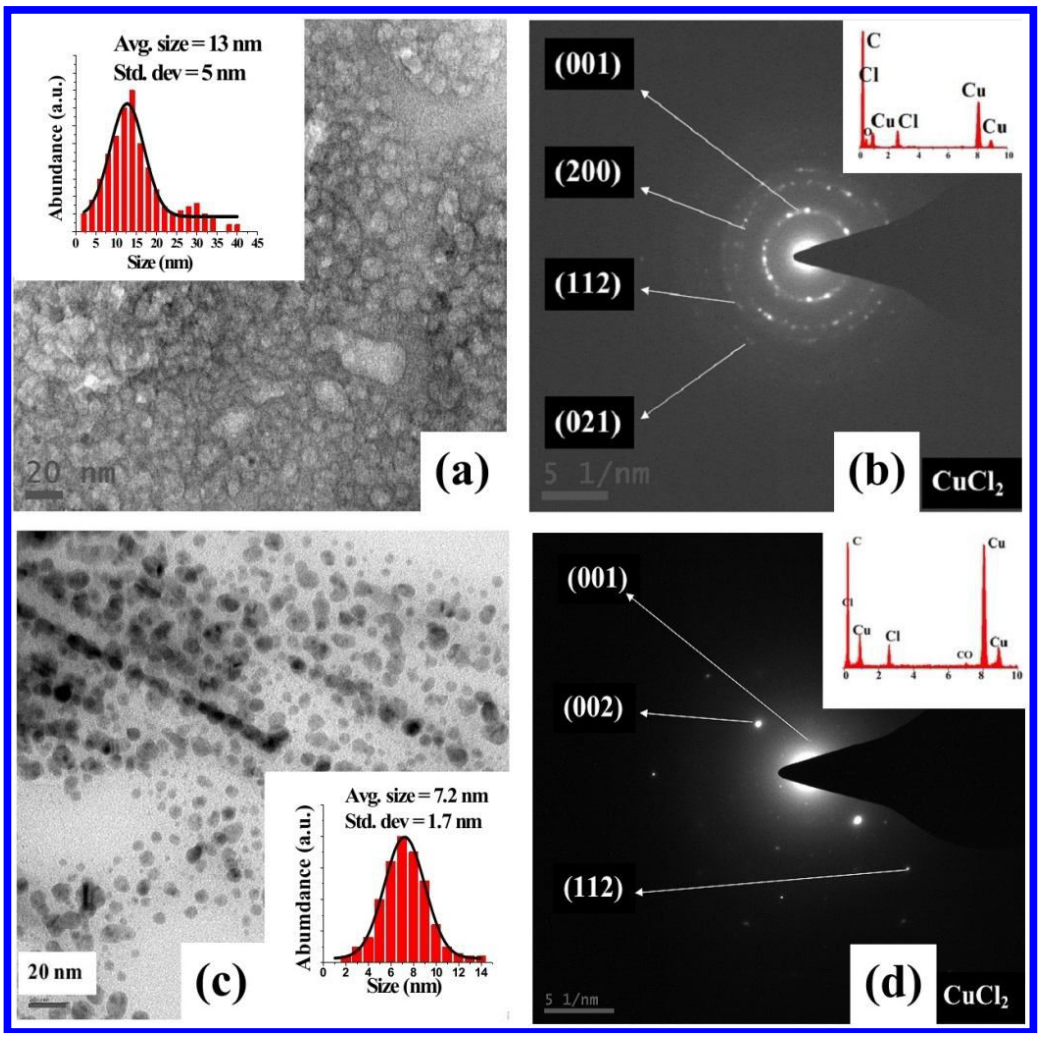

Figure 3.5 TEM images of (a) MCuNP4 (c) SCuNP4. Insets of (a) and (c) depict the NPs distribution (b) SAED spectra of the MCuNP4 and its corresponding EDAX data is shown in the inset (d) SAED spectra of the SCuNP4 and its corresponding EDAX data is shown in the inset

We believe that during the process of ablation, interaction between transient copper species with the chloride ions in the DCM resulted in the fabrication of CuCl NPs in MCuNP2 and SCuNP2. Similarly, highly agglomerated $CuCl_2$ NPs were observed in MCuNP4 and less agglomerated $CuCl_2$ NPs in SCuNP4 when ablation was carried out in chloroform. Since acetonitrile is highly capable of dissolving atmospheric oxygen NPs in MCuNP3 and SCuNP3 were observed to be oxidized (CuO) to a greater extent than in acetone, DCM and chloroform. In the aspect of average sizes, single line ablation displayed better performance where as distribution and yield wise multiple line ablation demonstrated better performance. Monitoring the quantity of matter on the TEM grid is not a reliable method to assert higher yield since the TEM is a local measurement. In fact, absorption spectra may be a more reliable technique to evaluate the yield in each case. The abundance of NPs were extrapolated from the bright field TEM images and were found to be ~1390 (900), ~234 (75), ~158 (71), and ~690 (340) for MCuNP1 (SCuNP1), MCuNP2 (SCuNP2), MCuNP3 (SCuNP3), and MCuNP4 (SCuNP4), respectively. The conclusions obtained from the above characterizations were further strengthened by the analysis of UV-Vis absorption spectra.

3.2.3. UV-Vis absorption spectroscopy of Cu colloids

UV-Vis absorption spectra (Jasco V-670) of colloids were recorded in the spectral range of 200 nm - 800 nm. Figure 3.6 depicts the whole absorption spectra of copper colloids prepared through both multiple and single line ablation while figure 3.7 illustrates only the spectral region within the vicinity of characteristic absorption peaks. Analysis of colloids for both schemes was accentuated with respect to the yield of NPs and their size distribution. MCuNP1 (figure 3.7a-red color, solid curve), SCuNP1 (figure 3.7a-blue color, dotted curve) colloids exhibited golden yellow coloration and SPR peak positions were observed near 580 nm and 566 nm, respectively. The peak position did not alter in both colloids even after several weeks which could be attributed to negligible aggregation effects since the electric dipole moment of acetone is high, resulting in possible formation of an electric double layer (EDL) [41] around the NPs. Surface chemistry may, perhaps, have played a significant role in preventing the aggregation. Characteristic absorption peak for MCuNP2 was observed near 371 nm (figure 3.7b-red color, solid curve) while it was near 375 nm

for SCuNP2 (figure 3.7b-blue color, dotted curve). Probably, interim interaction of Cu ions in the plume with the Cl ions in the surrounding liquid medium resulted in formation of copper chloride NPs. Consequently, charge transfer between metal and the associated ligands[42] could have led to strong absorption of light in the UV spectral region. MCuNP3 (figure 3.7c-red color, solid curve) exhibited light yellow-gray coloration with SPR peak near 601 nm and SCuNP3 (figure 3.7c-blue color, dotted curve) near 588 nm, respectively, indicating that the plasmon peak was red shifted (compared to Cu NPs in Acetone). In all likelihood, this could be due to increased thickness of oxide cladding surrounding the Cu NPs.[43] The interaction of NPs with air oxygen dissolved in ACN could have prevailed during the ablation leading to a red shift of the SPR peak since the solubility of oxygen is high in ACN at room temperature.[44] The absorbance in the case of NPs in ACN was an order of magnitude lower compared to others. This could, possibly, be due to two main reasons explained as follows: (1) If particle sizes are large, higher order polarization resulting from quadrupole, octopole oscillations usually dominate. In general, these multi-pole oscillations have lesser probability of absorption compared to dipole oscillations (2) If the oxide cladding on the metallic nanoparticle is thick then it diminishes the influence of the incident field. Similarly, MCuNP4 (figure 3.7d-red color, solid curve), SCuNP4 (figure 3.7d-blue color, dotted curve), exhibited characteristic absorption peaks near 383 nm, 375 nm, respectively. Among the two cases, multiple line ablation was observed to provide higher absorbance compared to single line ablation. Similarly, MCuNP4 (figure 3.7d-red color, solid curve), SCuNP4 (figure 3.7d-blue color, dotted curve), exhibited characteristic absorption peaks near 383 nm, 375 nm, respectively.

Among the two cases, multiple line ablation was observed to provide higher absorbance compared to single line ablation. This observation revealed that the yield of the NPs was higher in multiple line ablation than in the case of single line ablation. It was apparent from the UV-Vis absorption spectra that characteristic peak position of the colloids obtained through multiple line ablation was red shifted compared to colloids obtained using single line ablation. Only in the case of DCM the sizes of NPs in MCuNP2 were smaller than those obtained in SCuNP2 because of which we observed a small blue shift rather than a red shift. The reason for the discrepancy is not yet clearly understood. We believe that the solvent properties played a major role

and further investigations are pending in this direction to understand the complete mechanism.

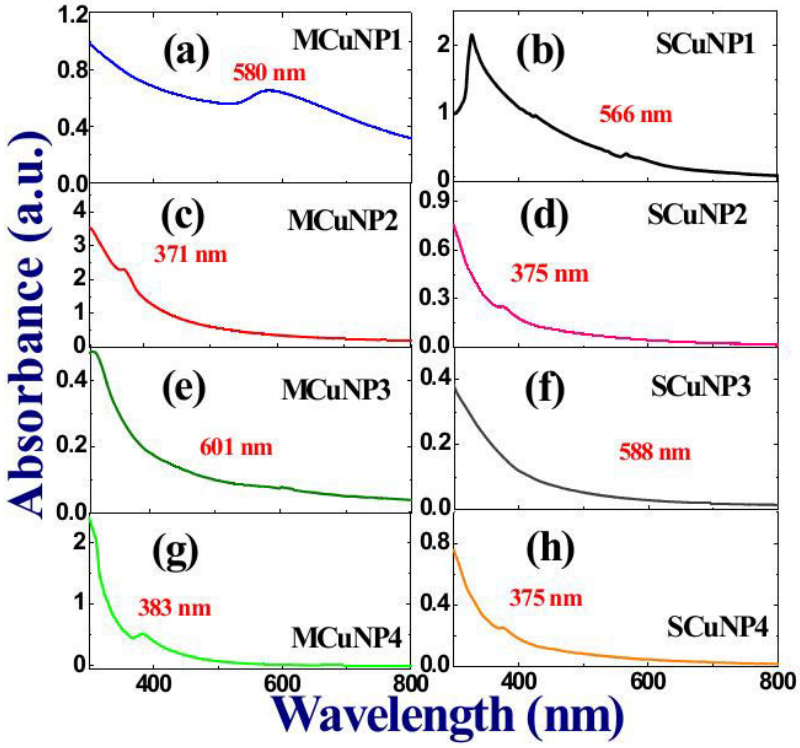

Figure 3.6 UV-Vis absorption spectra of Cu NPs prepared through ULAL (ps) in (a) acetone, multiple line ablation (MCuNP1) (b) acetone, single line ablation (SCuNP1) (c) DCM, multiple line ablation (MCuNP2) (d) DCM, single line ablation (SCuNP2) (e) acetonitrile, multiple line ablation (MCuNP3) (f) acetonitrile, single line ablation SCuNP3 (g) chloroform, multiple line ablation (MCuNP4) (h) chloroform, single line ablation (SCuNP4).

In an earlier study, Miranda et al.[45,46] performed the fabrication of Cu NPs in liquid media with nanosecond laser pulses. The writing conditions[29] in their experiments were different from the present experiments. In our case laser beam was scanned on the surface of the Cu substrate to draw periodic lines with a given separation rather than mere focusing. In general, below ablation threshold polished surface will not melt[47] whereas a roughened surface (ablated multiple times) would offer loosely bound micro-protrusions to the laser beam which decreases the ablation threshold. In the case of multiple line ablation, in-homogeneity could have resulted in an non-uniform melting of tips and micro-protrusions thereby reducing the ablation threshold and consequently increased yield. Higher yield of Cu NPs in multiple line ablation case was confirmed from the observed large plasmon bandwidth of colloids as explained by Garcia et al.[48] Since NPs in MCuNP1, MCuNP2, MCuNP3 and

MCuNP4 had higher density compared to corresponding SCuNP1, SCuNP2, SCuNP3 and SCuNP4 the net electric field at the nanoparticle site is summation of the field due to incident light and the field created by the remaining NPs. Accordingly, resonance condition gets modified resulting in a red shift of the characteristic absorption band.[48]

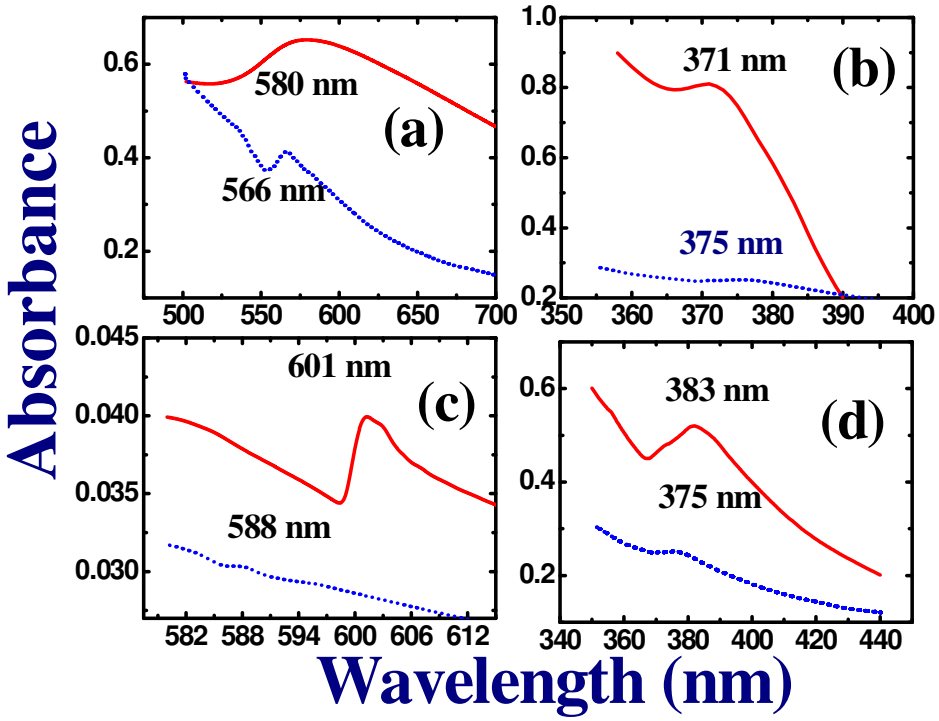

Figure 3.7 Expanded UV-Vis absorption spectra of Cu nanoparticles prepared through picosecond laser ablation in (a) acetone (MCuNP1, SCuNP1), (b) DCM (MCuNP2, SCuNP2), (c) acetonitrile (MCuNP3, SCuNP3) and (d) chloroform (MCuNP4, SCuNP4). Solid lines represent MCuNPs while dotted lines represent SCuNPs.

3.2.4. FESEM characterization of Cu substrates

Ps laser machined Cu substrates were preserved after proper cleaning to remove any surface contaminations. Figure 3.8 illustrates the FESEM images of fabricated NSs on the surface of Cu ablated in (a) acetone (MCuNS1), (b) DCM (MCuNS2), (c) ACN (MCuNS3) and (d) chloroform (MCuNS4) and insets present their respective images with lower resolution (2 μm scale). Surface morphology of multiply ablated Cu substrates MCuNS1 [figure 3.8(a)] and MCuNS3 [figure 3.8(c)] revealed the formation of weakly distinguishable laser induced periodic surface structures (LIPSS) with period of ~400 nm along with cylindrical Cu NPs grains

(length ~300 nm, diameter ~20 nm) and the formation LIPSS with a periodicity 250-300 nm, respectively. In the case of MCuNS2 [figure 3.8(b)], surface topography of Cu substrate consisted of pillar shaped structures of few microns. Moreover, most of the cubic NPs with size of 200 nm were formed on the top of pillar. Similarly in the case of MCuNS4 [figure 3.8(d)], rough ended pillar with few microns size were formed on surface Cu unlike in the case of MCuNS2.

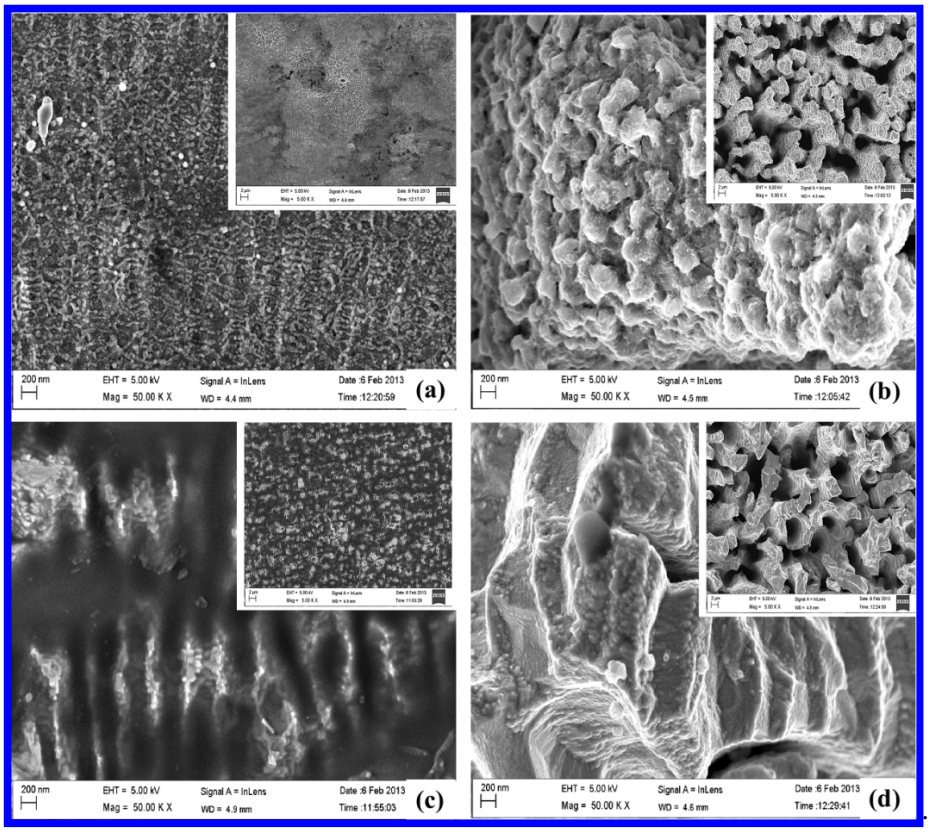

Figure 3.8 FESEM images of substrates (a) MCuNS1 in acetone (b) MCuNS2 in DCM (c) MCuNS3 in ACN and (d) MCuNS4 in $CHCl_3$ fabricated through ultrafast multiple line ablation of Cu. Insets show their corresponding views on a low resolution image (2 µm scale).

Figure 3.9 depicts the FESEM image morphologies of fabricated NSs on the surface of Cu substrates when ablation was carried out in (a) acetone (SCuNS1), (b) DCM (SCuNS2), (c) ACN (SCuNS3) and (d) chloroform (SCuNS4) via single line ablation and insets of figures 3.9 depict their respective images with lower resolution (2 µm scale). We estimated that less number of pulses (~500) per spot were incident on surface compared to multiple ablation case (~4000). LIPSS with a periods of ~300 nm and ~400 nm for SCuNP1 [figure 3.9(a)] and SCuNP3 [figure 3.9(c)], respectively, were observed. In addition to this, spherical NP grains (with NP size of

~50 nm) were formed on the periodic structure surfaces in the case of SCuNP1, which was not observed in SCuNP3 case. Similarly, randomly corrugated structures along with NP grains and less number of triangular NPs (~250 nm size) were observed for the cases SCuNP2 [figure 3.9(b)] and SCuNP4 [figure 3.9(d)], respectively.

The observed ripples could be resultant of the interference of the incident electromagnetic wave and surface scattered electromagnetic wave as proposed by earlier groups working on LIPSS.[49]The periodicity of the ripples is related to the wavelength and angle of incidence of the laser beam as following:

$$\wedge_{\perp} = \frac{\lambda}{\frac{\lambda}{\lambda_S} \pm Sin\theta} \tag{3.1}$$

where $\wedge_{\perp}$ is the period of ripples, λ - incident wavelength of the laser, λ_s - wavelength of the surface wave. For a normal incidence periodicity of the ripples is almost equal to the wavelength of SEW.

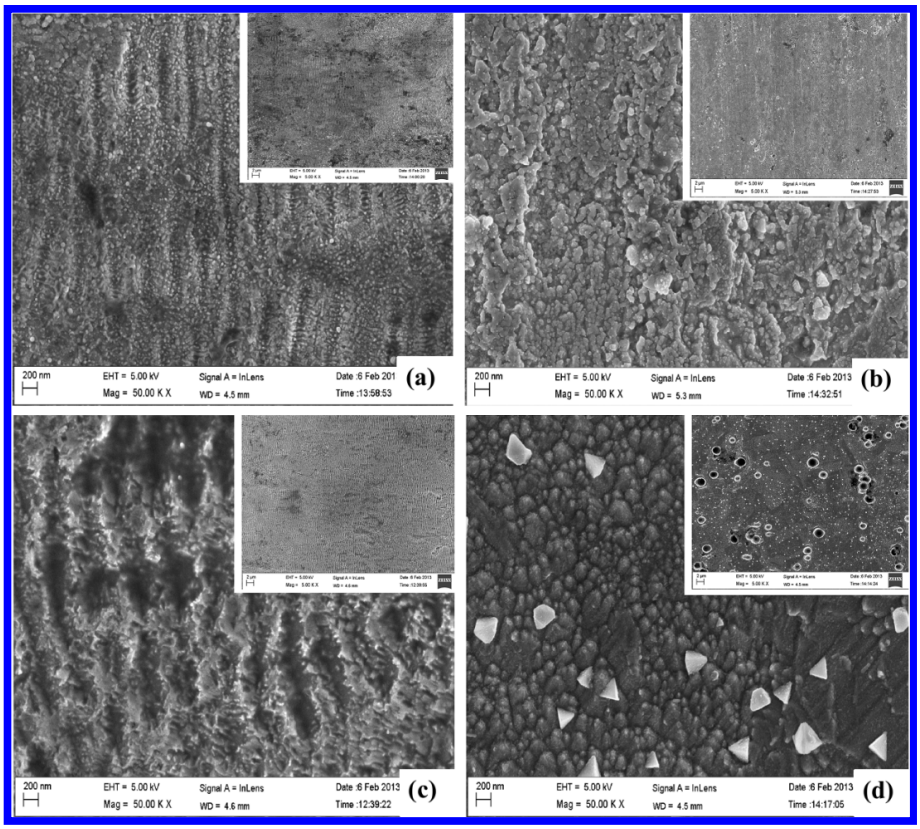

Figure 3.9 FESEM images of substrates (a) SCuNS1 in acetone (b) SCuNS2 in DCM (c) SCuNS3 in DCM and (d) SCuNS4 in chloroform fabricated through ultrafast single line ablation of Cu. Insets show corresponding views on a low resolution image (2 μm scale).

Furthermore, selected liquid media plays a dominant role in the formation of ripple structures which was evident from the FESEM images. Since the properties of liquid medium on metallic plasma plume is different, redistribution of metallic melt under the influence of recoil pressure (depends on the latent heat of vaporization) of liquid molecules was different. Consequently, different nanostructures were obtained. We suppose that there are several generalized mechanisms for the formation of ultrafast laser fabricated NPs and surface structures in liquids, depending on the collapse of cavitation bubble due to simultaneous effects of the recoil pressure of vapor of the liquid and surface tension forces of the melt inside the cavitation bubble, hence the melt splashes which results in the formation of NPs in liquid media and micro/nano structures on the target substrate. The numerical investigation of cavitation bubble in different liquid media is explained in section 3.3.

3.3. Under lying mechanisms of ULAL

A simple picture on the fabrication of Cu NPs and NSs in liquid media can be understood as, when an ultrashort pulse interact with Cu targets valence band electrons respond first to absorb visible/IR wavelengths and transitions occur from valance band to conduction band. In the case of ps pulses (<10 ps) in the near IR region, linear and nonlinear absorption (multi-photon absorption) are the dominant mechanisms. Absorption of laser energy by the valence electrons creates quasi-free carriers.[50] The excited electrons transfer their energy to lattice through electron-lattice coupling and the corresponding characteristic time is ~1 ps. Collisions between the electrons and lattice lead to higher temperatures in the vicinity of laser focused regions and formed plasma will be at high temperatures and pressures. The generated plasma will expand in the surrounding liquid media and produces a shock wave, it enlarges with supersonic velocity within ns to fs. As a result, the vapor layer is formed around the plasma due to the pressure gradient created by shock wave and energy is transferred from the plasma to surrounding liquid media resulting in the production of a cavitation bubble[51, 52] and it may contain gases, vacuum and NPs. The simultaneous effects of recoil pressure of liquid vapor and surface tension forces of the melts inside the cavitation bubble, then it collapse, consequently, material transits to a super critical fluid state and vaporization occurs to interact with surrounding liquid media creating multifaceted structure of nanomaterials.[53,54] The generated NPs

with high kinetic energy in liquid media collide with other solvent molecules which results in the formation of localized plasma and this localized cloud create secondary ablation of the target.[55]

3.3.1. Numerical investigation on the dynamics of the cavitation bubble under the influence of liquid media

The fluence of laser pulse which reaches the target through liquid is lower compared to input fluence. The cavitation bubble forms on the surface of bulk target which can be induced by tensile elastic stress wave of liquid due to temperature difference of plasma and surrounding liquid. The cavitation bubble initially expands upto some extent in aqueous media and subsequently collapse, which is replicated many times as damped harmonic oscillations, can be driven by pulse energy reaches to the target. The change in energy per unit area on the substrate can be estimated by considering nonlinear effects such as self-focusing and super-continuum generation. The temporal dynamics of cavitation bubble allows to calculate the maximum radius and collapse time of the bubble which is described by Raleigh-Plesset equation.[52, 56-57] This model includes the surface tension, viscosity and compressibility of the liquid.

Mathematical Formulation

Consider a system with spherically symmetric of bubble of radius R (t) and the centre of the bubble is located at the origin which follows[58] the continuity equation and it can be written as

$$\frac{1}{r^2}\frac{\partial}{\partial r}\left(r^2 u(r,t)\right) \tag{3.2}$$

$$u(r,t) = \frac{1}{r^2} F(t) \tag{3.3}$$

where F(t) is the function of time and independent of r. The bubble velocity at the boundary can be taken as $u(R,t) = \frac{dR}{dt}$ and thus at the cavity boundary

$$F(t) = R^2 \frac{dR}{dt} \tag{3.4}$$

$$u(r,t) = \left(\frac{R}{r}\right)^2 \dot{R} \quad \left[\because \dot{R} = \frac{dR}{dt}\right] \tag{3.5}$$

The momentum equation or Navier-Stokes equation for ideal fluid at spherical symmetric condition can be written as

$$-\frac{1}{\rho}\frac{\partial p}{\partial r} = \frac{\partial u}{\partial t} + u\frac{\partial u}{\partial r} + \frac{\eta}{\rho}\left[\frac{1}{r^2}\frac{\partial}{\partial r}\left(r^2\frac{\partial u}{\partial r}\right) - \frac{2u}{r^2}\right] \quad (3.6)$$

Substitute equation (3.5) in equation (3.6), then

$$-\frac{1}{\rho}\frac{\partial p}{\partial r} = \frac{2R\dot{R}^2 + R^2\ddot{R}}{r^2} - \frac{2R^4\dot{R}^2}{r^5} \quad (3.7)$$

Where p is the pressure at cavitation bubble wall and the pressure arises far from the bubble cavity can be written as $P_\infty = P(t) + P_a$ …….(3.8), where $P(t)$ is the driving pressure function it consists of sinusoidal envelop with central frequency (ω_0) and the angular frequency (ω) of sinusoid, and P_a is the atmospheric pressure. Consider the various pressure effects act on the cavitation bubble in liquid to move in different directions. They are (a) the liquid applies pressure on the bubble wall to move interior direction owing to viscosity which can be obtained from velocity gradient and it can be found from equation (3.5), with the pressure being,

$$P_\eta = -\frac{4\eta\dot{R}}{R} \quad (3.9)$$

(b) Pressure generated due to the surface tension acts on the wall of the bubble to push inward side and it can be written from Laplace's equation as

$$P_\sigma = -\frac{2\sigma}{R} \quad (3.10)$$

(c) The gas or nanoparticles pressure inside the bubble is acted outward direction

$$P_n(R,t) = P_n(0)\left(\frac{R_0}{R}\right)^{3\gamma} \quad (3.11)$$

Total pressure exerts on the bubble is the sum of all the pressures

$$P_T = P_\eta + P_\sigma + P_n(R,t) = -\frac{4\eta\dot{R}}{R} - \frac{2\sigma}{R} + P_g\left(\frac{R_0}{R}\right)^{3\gamma} \quad (3.12)$$

Where η and σ are viscosity and surface tension of the liquid, P_g is gases or nanoparticles pressure inside the bubble and R_0 is the initial radius of bubble.

Assuming the bubble was stationary at initial condition, at t=0, the driving field $P(0) = 0$ and $\dot{R} = 0$. From equation (3.8), $P_\infty = P_a$, $P_T = P_a\ (at\ R = R_0)$ and

therefore, $P_g = P_a + \frac{2\sigma}{R_0}$..... (3.13). Equation (3.7) is then integrated with respect to r with limits $R\ to\ \infty$ and apply all the boundary conditions, finally resulting in

$$R\ddot{R} + \frac{3}{2}\dot{R}^2 = \frac{1}{\rho}\left(\left(P_a + \frac{2\sigma}{R_0}\right)\left(\frac{R_0}{R}\right)^{3\gamma} - P_a - P(t) - \frac{4\eta\dot{R}}{R} - \frac{2\sigma}{R}\right) \quad (3.14)$$

where $P(t) = P_{pulse}\ \sin\left(\frac{\omega_0 t}{2}\right)\sin(2\pi\omega t)$, P_{pulse} is the pressure calculated from the laser pulse energy. This Raleigh-Plesset second order differential equation was solved numerically with Matlab ODE 45. We have performed these simulations in four liquids by assuming the initial radius of bubble in each liquid which was obtained from the laser spot diameter on the solid substrate. Temporal evaluation of cavitation bubble was collected with a resolution of 1µs.

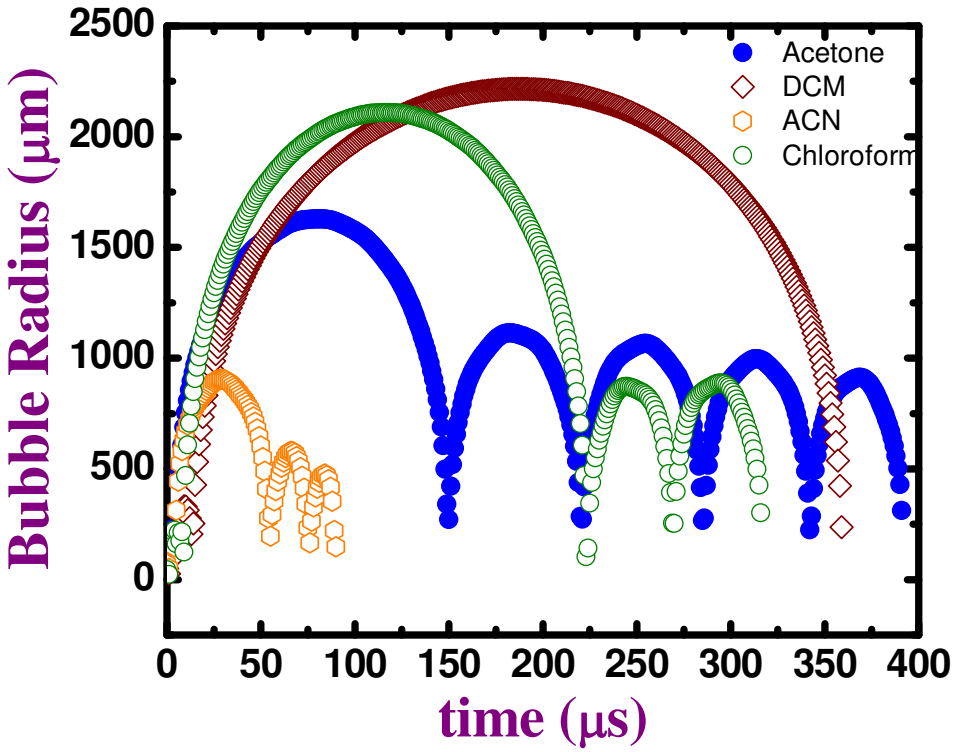

Figure 3.10 The radius of the numerically simulated cavitation bubble generated after the irradiation of ps pulses in (i) acetone, (ii) DCM, (iii) ACN and (iv) chloroform with respect to time.

Figure 3.10 illustrates the numerically simulated result on the temporal evolution of radius of cavitation bubble which was produced through ultrafast laser ablation in different organic liquids such as acetone, DCM, ACN and chloroform. We considered

initial radiuses (R_0) of cavitation bubbles as 60 µm, 50 µm, 70 µm and 45 µm for acetone, DCM and chloroform, respectively, and the driving pressure values were calculated from pulse energy. Based on the initial radius, the cavitation bubble was generated from the ablation of Cu in liquids with ultrashort pulse laser of ~2 ps pulse width numerically. Accordingly, the bubbles reached the maximum radiuses, R_{max} at time, of 1629 µm at 82 µs, 2216 µm at 187 µs, 980 µm at 30 µs and 2109 µm at 118 µs and, also they collapsed after 150 µs, 359 µs, 56 and 223 µs for acetone, DCM, ACN and chloroform, respectively. Subsequently, two/many bubbles successful expanding and collapsing segments were observed in acetone, ACN and chloroform and no evidence of that in the case of DCM upto the time of 360 µs.

The increase in difference between the vapor pressure inside the bubble and hydrostatic or ambient pressure allows the expansion of bubble through the transformation of kinetic energy of the liquid into potential energy of the bubble and gets stopped. This suggests that the energy is transferred to the solid target and it is related to the maximum radius of the bubble [52]

$$E_B = \frac{2\pi}{3} (P_a - P_v) {R_{max}}^3 \tag{3.15}$$

where P_v is the vapor pressure of liquid.

The fabricated NSs on the solid surfaces in our experiments might be accredited to the size of the cavitation bubble. In the cases of DCM [MCuNS2-figure 3.8(b)] and chloroform [MCuNS4-figure 3.8(d)], larger sizes of micro voids were observed on the substrates which might be due to the big cavitation bubble formation, nano size voids were observed in acetone case [MCuNS1-figure 3.8(a)] and these effects were not observed for ACN [MCuNS3-figure 3.8(c)] and, these might be cause of smaller sizes of cavitation bubble formation. We may conclude from our experimental and numerical simulation results that the bubble size is established by the pulse energy and it means that bubble size increases with increasing deposited fluence on the target which can create larger craters on the sample surface.[59-61]

3.4. Ps ablation of Cu NMs in acetonitrile with different pulse energies

3.4.1. Fabrication process

Ps ablation studies were performed on Cu targets in ACN at 800 nm. The initial laser beam diameter was ~8 mm and was focused with 25 cm focal length lens on the surface of Cu substrate. Typical pulse energies used were in the range of 25 – 400 μJ were used. Input energy was controlled by the combination of Brewster angle polarizer and a half wave plate. The target was placed normal to the laser beam on a three dimensional motorized stage [Nano-direct] with resolution of ~25 nm and was controlled by a controller interfaced to PC. Duration of each scan was fixed to ~30 minutes and line to line spacing was ~60 μm. To avoid ambiguity generated colloidal Cu_2O/CuO NPs in ACN were designated as Cu-25, Cu-50, Cu-100, Cu-200, Cu-300 and Cu-400 and, the corresponding substrates as CuS-25, CuS-50, CuS-100, CuS-200, CuS-300 and CuS-400for structures created using pulse energies 25 μJ, 50 μJ, 100 μJ, 200 μJ, 300 μJ and 400 μJ, respectively.

3.4.2. TEM, HRTEM, SAED and UV-Vis spectral characterizations of CuO NPs

Surface morphology and elemental composition of the generated copper oxide NPs by ps laser ablation of Cu in ACN were confirmed from the TEM, HRTEM and SAED. Figure 3.11 demonstrates the TEM image of colloidal copper oxide NPs with different size and shapes obtained by ps ablation as a function of pulse energies (a) Cu-25 (25 μJ), (b) Cu-50 (50 μJ) , (c) Cu-100 (100 μJ), (d) Cu-200 (200 μJ), (e) Cu-300 (300 μJ) and (f) Cu-400 (400 μJ), and inset of figure 3.11(a) – 3.11(g) show the size distribution of NPs. The size distribution was fitted with a Gaussian curve that offered mean size of NPs of ~96 nm for Cu-25, ~34 nm for Cu-50, ~8.6 nm for Cu-100, and ~40 nm for Cu-200. TEM images obtained at 300 μJ (Cu-300) revealed the majority of produced nanomaterials turned into random structures in shape with spherical shaped NPs being present, but smaller in number with ~40 nm mean size. For Cu-400, defined nano rods (NRs) with an average size of ~1 μm length and ~ 50 nm breadth were achieved. Average size of NPs was observed to reduce as the pulse energy increased from ~25 μJ [figure 3.11(a)] to ~100 μJ [figure 3.11(c)]. On the other hand, the average size increased when the pulse energy was further increased upto ~400 μJ [figure 3.11(f)] and the variations of size of NPs versus pulse energy is plotted in figure 3.12.

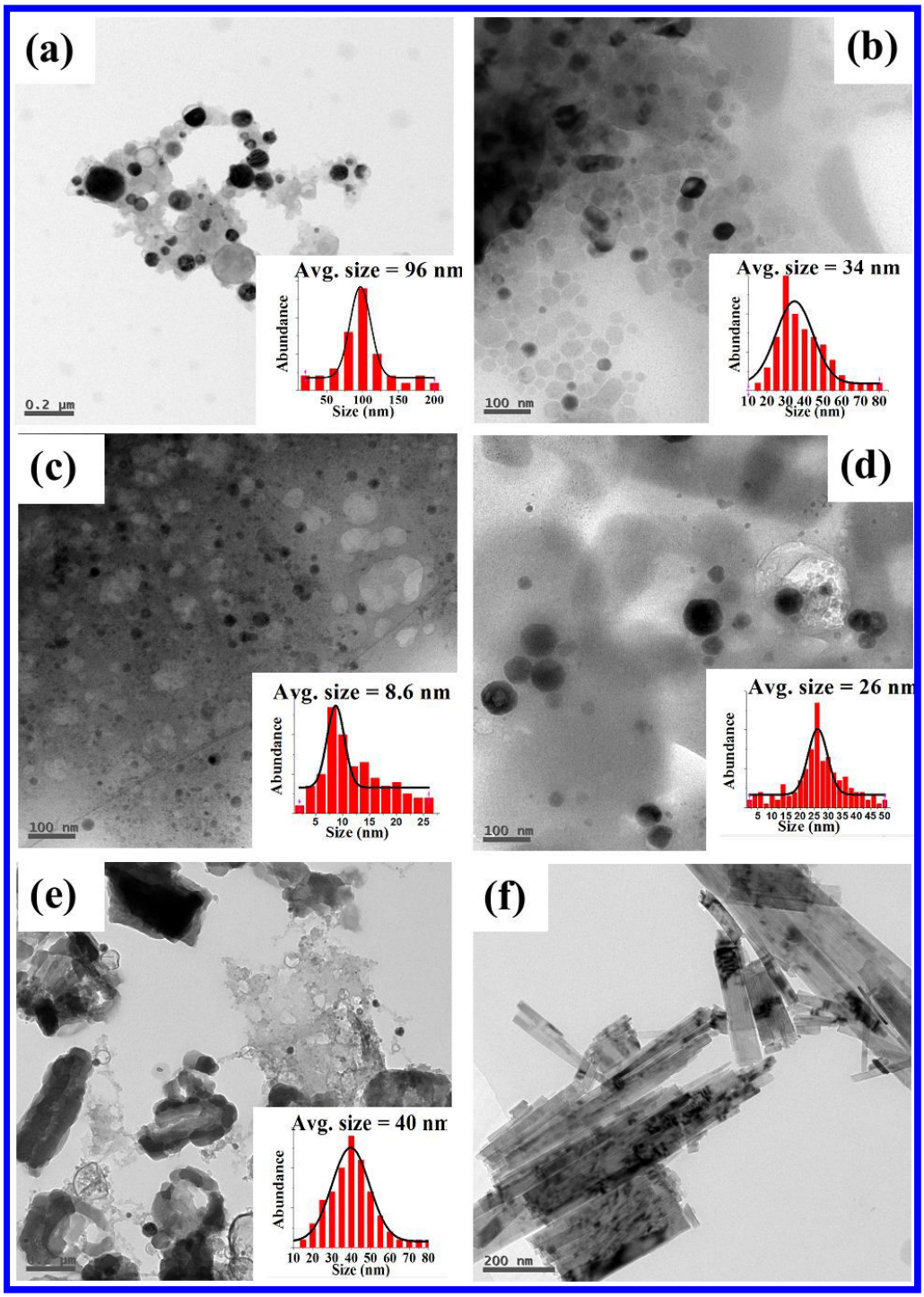

Figure 3.11 TEM images illustrating the copper oxide NPs synthesized by ps ablation of bulk Cu in ACN (a) Cu-25, (b) Cu-50, (c) Cu-100, (d) Cu-200, (e) Cu-300 and (f) Cu-400. Insets show their particle distribution plots.

The mean size of NP depends exclusively on the size of the cavitation bubble at interface between the liquid and target surface. As per previous reports,[59-61] the bubble size increases with increasing the laser pulse energy implying that the pressure

inside the bubble increases. At high/low pulse energies, bubble cannot sustain for long time because of drastically increasing/slightly increasing pressure with respect to time resulting in the formation of agglomerated or big sized NPs. Whereas at intermediate energy, depending on the material, we can obtain a long sustainable cavitation bubble with a gradually increasing pressure with respect to time and therefore, smaller NPs as the outcome.

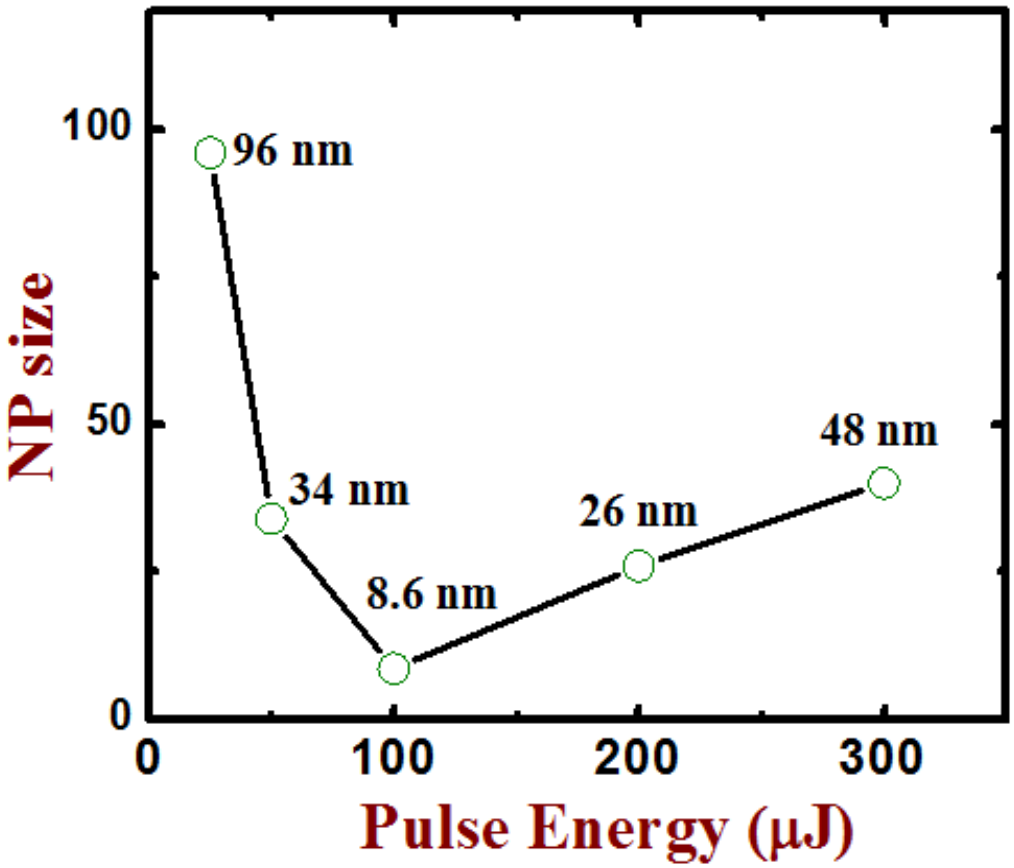

Figure 3.12 Plot illustrates the tuning of Copper Oxide NPs were prepared in ACN with respect to the different pulse energy.

Figure 3.13 depicts the HRTEM images of a single NP (a) Cu-50 exhibiting parallel lattice planes with an inter-planar separation of 3.04 A˚ and 2.42 A˚ corresponding to (110) and (111) lattice planes of Cu_2O, respectively, and (b) Cu-100 demonstrates inter atomic separation of 2.09 A˚ which matched well with Cu_2O (200) crystal plane.

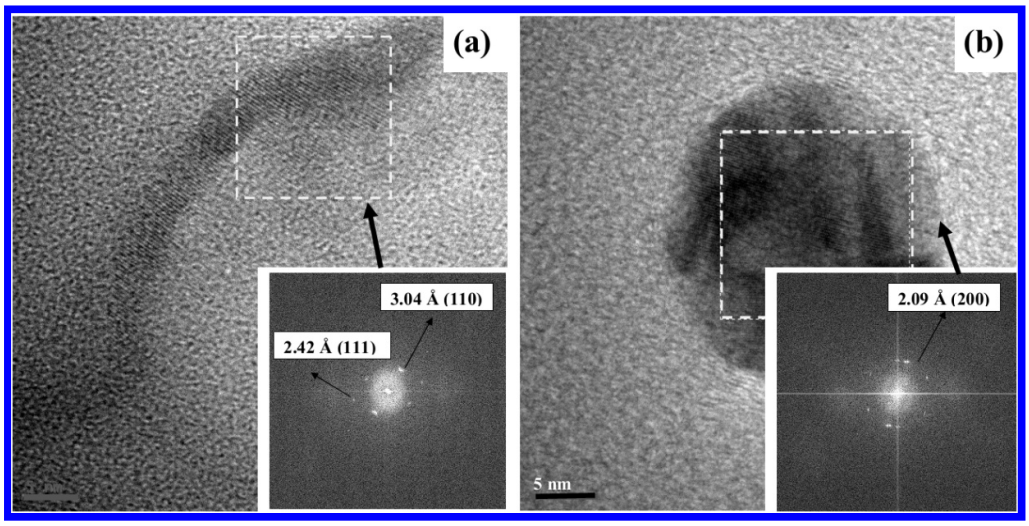

Figure 3.13 HRTEM image of the Cu_2O NPs formed in (a) Cu-50 and (b) Cu-100 show the clear view of lattice planes observed at a different characteristic separations which corresponding to the inter atomic planes of Cu_2O NPs lattice set (200) and inset shows its numerical electron diffraction pattern.

Figure 3.14 shows the SAED patterns of (a) Cu-25 (b) Cu-50 (c) Cu-100 (d) Cu-200 (e) Cu-300 and (f) Cu-400. The SAED pattern demonstrate concentric circle pattern in which each ring represents an individual lattice plane and it was confirmed that the NPs prepared at all energies were polycrystalline in nature, except 400 μJ ablation products where it depicted single crystalline pattern. Only first three planes in each pattern were considered for the evolution of crystallinity and elemental composition. The measured interplanar spacings SAED patterns wonderfully concur with corresponding to Cu_2O crystal planes. Both HRTEM and SAED pattern confirmed that Cu_2O NPs/NRs were produced in all cases. These results are also supported by UV-Vis absorption spectroscopy.

Figure 3.15 illustrates the UV-Vis absorption spectra of colloidal Cu_2O NPs in ACN demonstrating the localized surface plasmon resonance peak (LSPR) near 600 nm (corresponding to grey color of the sample) indicating that the peak shifted to longer wavelengths. According to Mie theory, the appearance of SPR peak for pure Cu NPs is near 580 nm.[62] The observed discrepancy is most likely due to the signature of formation of oxide layer around the particles. Similar SPR peaks of copper oxide nanoparticles have been reported earlier.[63,64] The SPR peak near 600 nm was observed in the cases of Cu-50 and Cu-100.

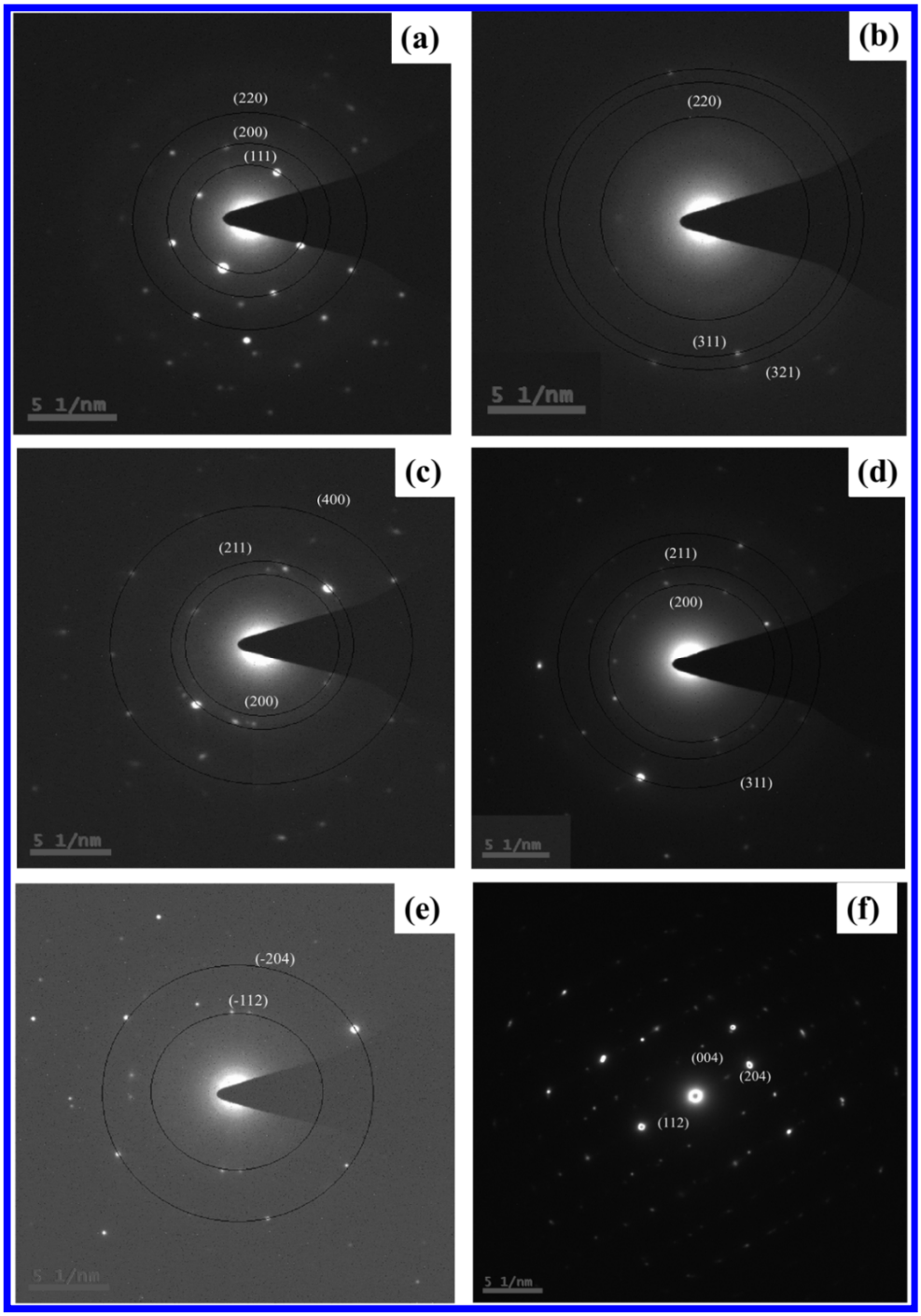

Figure 3.14 SAED pattern images illustrate the Cu_2O NPs synthesized by ps laser ablation of bulk Cu in ACN (a) Cu-25, (b) Cu-50, (c) Cu-100, (d) Cu-200, (e) Cu-300 and (f) Cu-400.

The absorbance of Cu_2O NPs in other cases (Cu-25, Cu-200, Cu-300 and Cu-400) was an order of magnitude lower compared to others. This might, probably, be owing to two major reasons as follows: (1) If particle sizes are big this results in the formation of higher order polarization such as quadrupole, octopole oscillations and

these multi-pole oscillations generally dominate in these cases providing lower probability of absorption compared to dipole oscillations (2) If the oxide layer on the Cu NPs is wide then it reduces the manipulation of the incident light field when recording the UV-Vis absorption spectra. Another absorption peak observed in the UV spectral region (near 289 nm) could be due to metal inter band transitions.[64] This is due to the reactivity of copper metal with oxygen and to form some metal products such as copper oxide and hydroxide. The plasmon peak was observed near 600 nm also proved that copper oxide NPs were formed in liquid.

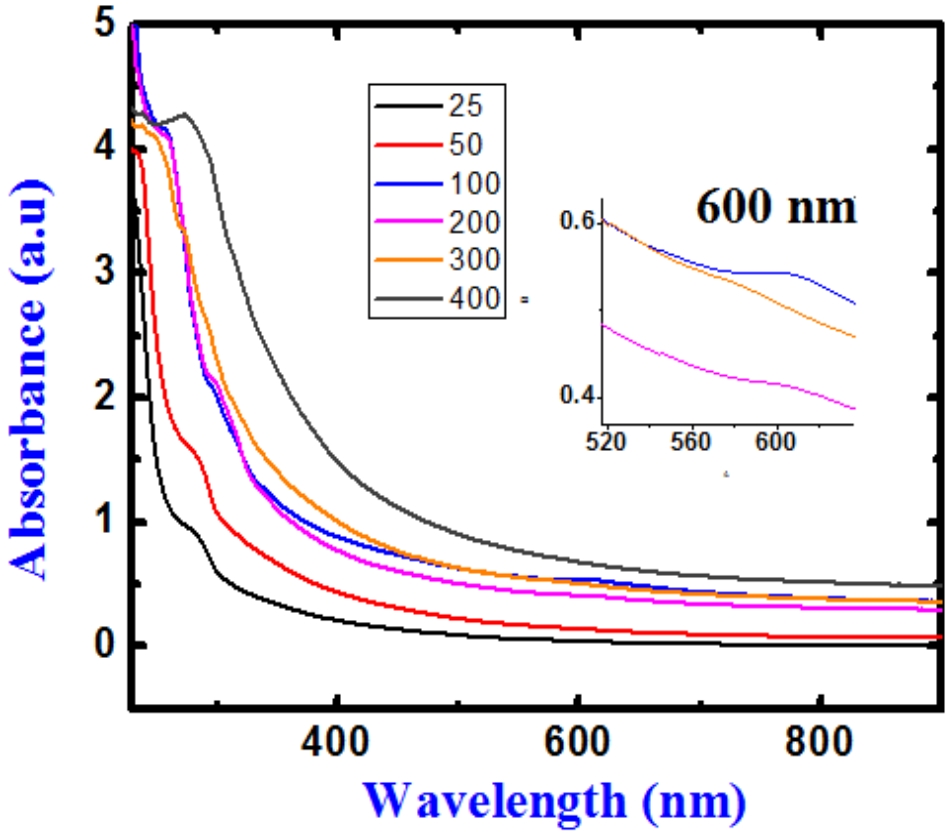

Figure 3.15 UV-Vis absorption spectra of Cu_2O NPs were prepared in ACN with different pulse energies, (i) SPR peak at 600 nm in all the cases, (ii) visualized absorbance in Cu-50 and Cu-100 and (iii) less absorbance in other cases.

3.4.3. FESEM characterizations of Cu substrates

The surface morphology of Cu substrates was characterized by FESEM imaging. Figure 3.16 illustrates the FESEM images of formed surface nanostructures via ps laser ablation on Cu targets with different energies in the range of 25-400 µJ shown in (a) CuS-25 (b) CuS-50 (c) CuS-100 (d) CuS-200 (e) CuS-300 and (f) CuS-400.

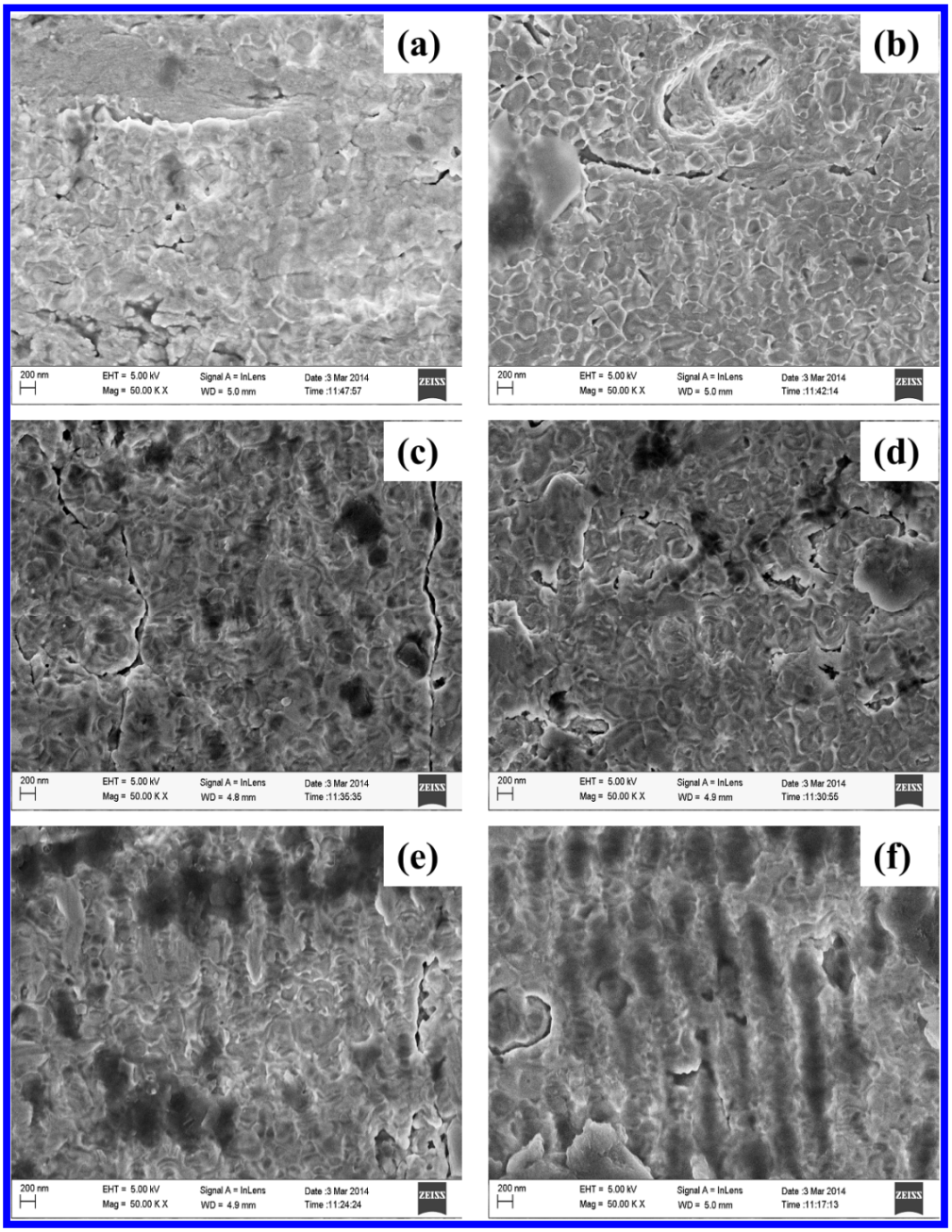

Figure 3.16 FESEM images of surface nanostructures were fabricated on Cu substrate by ps ablation of bulk Cu in ACN (a) CuS-25, (b) CuS-50, (c) CuS-100, (d) CuS-200, (e) CuS-300 and (f) CuS-400

According to the previous reports,[29, 33-37, 65-69] few feasible mechanisms were projected to demonstrate the fabrication of random NSs and LIPSS with period of nearly half the laser wavelength in metals achieved through ps/fs laser ablation. Skolski et al.[70-71] reported the experimental and theoretical investigation on the formation of high/low spatial frequency LIPSS (HSFL/LSFL) on metals using ultrafast lasers. Huang et al.[72] investigated the mechanisms on the formation of sub-

wavelength nanoripples on solid surfaces and demonstrated that target surface ablated by ultrashort laser pulses at damage threshold fluence should act as metal, in spite of metals, semiconductors and dielectrics. Derrien et al.[73] explored the mechanisms of ripple formation on Si using fs pulses and revealed evaluation of the excited free-carrier's density. Recently, our group had observed that complex refractive index and conduction band electron density play crucial role in determining periodicity of HSFL. Several authors[67,74-75] have investigated the intrinsic mechanisms of laser induced periodic surface nanostructure formation in Au, Ag and Cu, demonstrating that the Cu is a suitable metal allowing the formation of LIPSS formation on the surface compared to Ag and Au. In previous reports the phenomena were discussed for ablation attained in air/vacuum whereas we carried out ablation in aqueous media. We observed the random structures at lower energies rising from 25 μJ to 100 μJ where as at high energies LIPSS with different periodicity was observed (from 200 μJ - 400 μJ) and was confirmed from the FESEM images.

To understand the formation of LIPSS on Cu surfaces using six different pulse energies, we considered the dynamics in processes of laser interaction with metals which are related to the electron-lattice system. When the ps pulses interact with Cu metal, free electrons in the metal surface absorb laser pulse energy through inverse Brehmstrahlung and generate surface electromagnetic field. Due to the interaction of incident laser pulse with the generated surface electromagnetic field, energy can be distributed non-uniformly along the metal surface. This non-uniformly distributed energy can be coupled to electrons and allowed to form electron temperature distribution with periodic nature. Consequently, the hot electrons couple to lattice and get relaxed (~1 ps) while transferring the energy to lattice system. The lattice reorganizes itself at the melting state which is followed by re-solidification. Due to the electron – phonon interactions, this ephemeral, two different temperature system will have a tendency to attain equilibrium temperature within few ps. These electron–phonon interactions can be defined by electron-phonon coupling constant. Therefore, two-temperature model is necessarily utilized to demonstrate thermal phenomena in the case of ultrafast laser matter attraction. The growth of LIPSS can be demonstrated on the basis of electron-phonon coupling constant (γ).[74] It was confirmed that the electron-phonon coupling constant is directly related the electron and lattice temperatures, and these temperatures in turn depend on the fluence incident on the

target surface. The input laser fluence should be more than the ablation threshold fluence that could melt the sample surface to generate periodic structures and the earlier reported ablation threshold fluence for Cu 1.7±0.3 J/cm^2. According to previous reports, we understand that the shape of the periodic surface structures change with respect to laser fluence and pulse number. To explore the fluence effect on the development of the LIPSS on Cu target surface, the evaluation of effective spot size on the Cu target surface for various input laser energies was performed.

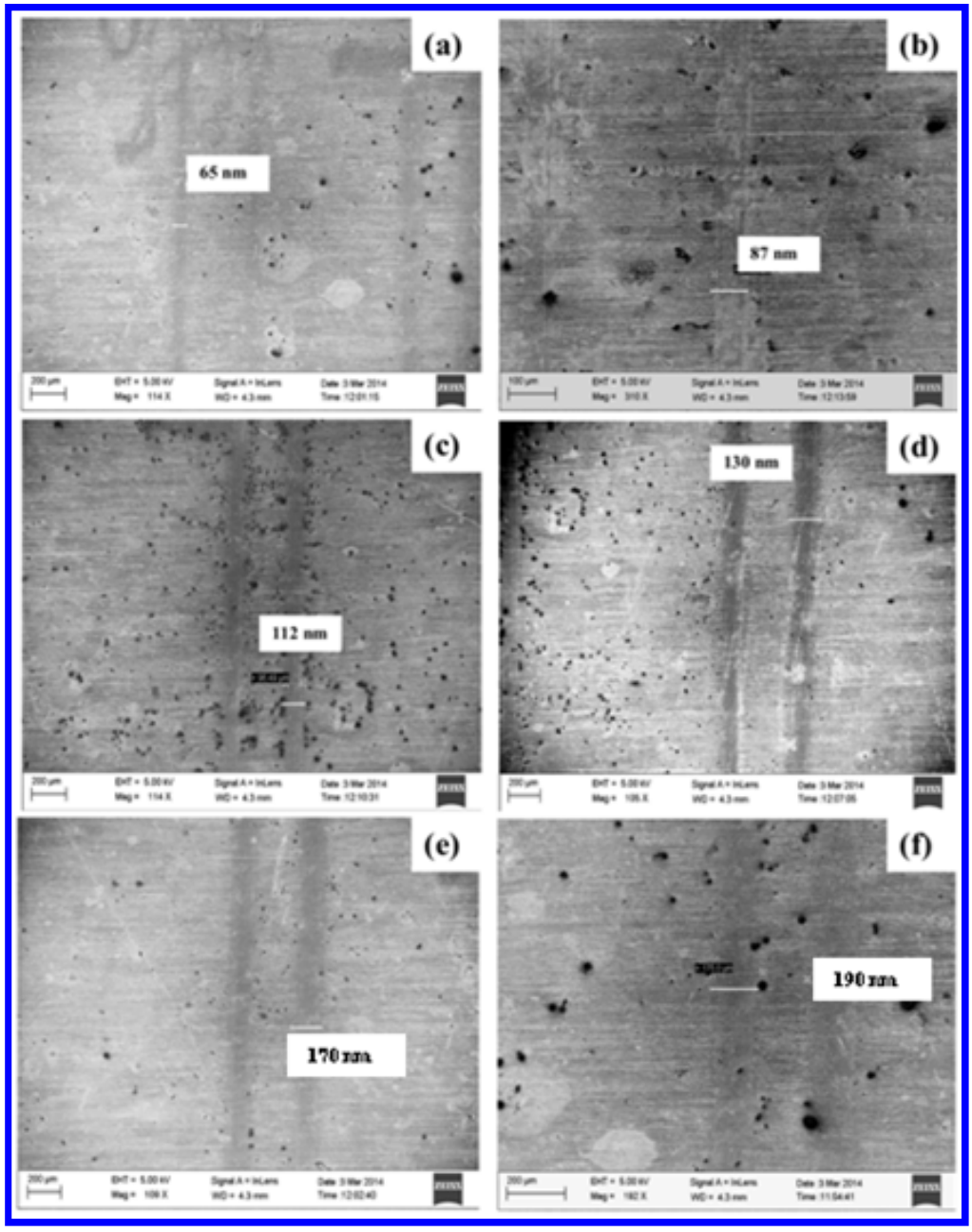

Figure 3.17 FESEM images of the laser drawn single lines on Cu surface with (a) 25 μJ, (b) 50 μJ, (c) 100 μJ, (d) 200 μJ, (e) 300 μJ and (f) 400 μJ

Figure 3.17 illustrates the FESEM images of laser machined single lines on Cu target surface and the width of the lines drawn on Cu target were taken as effective beam diameters of laser beam as suggested by Barcikowski et al.[76] Figures 3.17 (a)-(f) validates the differences observed in the estimated spot sizes of ~65 µm, ~87 µm, ~112 µm, ~130 µm, ~170 µm, ~190 µm for input energies of ~25 µJ, ~50 µJ, ~100 µJ, ~200 µJ, ~300 µJ, ~400 µJ . From the measured spot diameters on the targets and effective number of pulses overlapping within a spot and separation between the lines we could confirm that single line ablation happened in the case of CuS-25, CuS-50 as the lines separation was 60 µm and double line ablation occurred on CuS-100, CuS-200, where the line separation was almost half compared to the spot on target. As a result, half of the ablated line was ablated second time by consequent laser pulses.[29] Whereas in the cases of CuS-300 and CuS-400 the generated spot diameter was much bigger than the line separation and resulted in the formation of multiple line ablation. The effective number of pulses accumulated within the spot area estimated were ~216, ~290, ~746, ~866, ~1700 and 1900 for CuS-25, CuS-50, , CuS-100, CuS-200, CuS-300 and CuS-400, respectively, and the corresponding fluences estimated were ~1.51 J/cm^2, ~1.68 J/cm^2, ~2.03 J/cm^2, ~3 J/cm^2, ~2.67 J/cm^2, ~2.82 J/cm^2, respectively.

We could confirm from our experimental results that periodic patterns were not observed on the surface of Cu in the cases of Cu-25, Cu-50 and Cu-100 [figures 3.16(a)–3.16(c)] since the estimated effective input fluences were less than the ablation threshold fluence (1.7±0.3 J/cm^2) and the surface r.m.s. roughness (measured using surface profilometer) was found to be ~0.8 µm, ~2.7 µm and ~3.6 µm, respectively. Comparatively, the periodic pattern, spread over a small area and less evident, in the case of Cu-200 [figure 3.16(d)] was formed due to a pulse train of ~866 shots at a fluence of ~3 J/cm^2. In the cases of Cu-300 and Cu-400 [figures 3.16(e) and 3.16(f)], LIPSS on Cu surfaces were expanded and more pronounced at fluences of ~2.67 J/cm^2 (~1700 shots), ~2.82 J/cm^2 (~1900 shots), respectively. The measured periodicity of LIPSS for Cu-200, Cu-300 and Cu-400 were ~430 nm, ~420 nm and ~470 nm, and surface r.m.s. roughness was measured to be ~2.6 µm, ~2.4 µm and ~ 1.8 µm, respectively. From the observed data of surface r.m.s. roughness it was concluded that at low input fluence ablation was good and at higher fluences ablation efficiency decreased. From our knowledge and previous reports we believe that

electrons might not transfer the energy to lattice before the expiration of the periodic distribution of electron temperature with a pulse train of fewer shots (input fluences ≤ threshold fluence) due to the active participation of the electron diffusion phenomenon. Therefore, less coupling could have taken place between the electron and lattice and consequently resulting a lower γ value of ~10^{16}.[74,75] However, non-uniform surface heat distribution cannot occur at this position which may not produce periodic surface structures on the surface. In the case of more effective number of pulses (input fluences >threshold fluence), electrons can couple to the neighbor lattice easily to transfer the energy and thermalization will take place between electrons and lattice resulting in a higher γ value might be in the order of ~10^{17}.[74,75] At this position, lattice will also attain temperature profile with periodic behavior. However, non-uniform heat distribution can occur on the metal surface and therefore, LIPSS might be formed on the metal surface.

3.5. Fabrication of Cu NSs with different number of pulses

3.5.1. Ps laser ablation of Cu in methanol using 2 ps laser pulses

In this study, the P-polarized beam (~2 ps) was focused on the Cu target in ethanol at normal incidence. The number of laser pulses N was selected to draw a single on the target surface by varying the scanning speed of X or Y motorized stage. The formation of LIPSS on Cu surfaces was studied with respect to different scanning speeds of 450 400, 350, 300, 250, 200, 150, 100, 50 and 25 µm/sec with the corresponding effective laser shots being N= 211, 240, 285, 346, 400, 550, 933, 1480, 3240 and 6800, respectively at 2.5 J/cm^2 which was more than threshold fluence of Cu (1.7±0.3 J/cm^2). Surface morphology of Cu NSs was investigated by FESEM. FESEM images demonstrate the growth of LIPSS on Cu surface above the ablation threshold fluence. Following ablation performed with N = 211 shots data presented in figure 3.18(a) demonstrated that holes and cracks with micro size were formed on the Cu surface. Along with these, NPs with ~80 nm mean size were also observed on the cracked surfaces. These cracked surfaces turned into nanocavities or random nanoroughness while shots increased from 240 to 346 which are shown in FESEM images of figures 3.18(b) – 3.18(d), respectively. Insets of figure 3.18 represent the FESEM images with higher scale or lower resolution (1 µm scale). As observed from

large scale FESEM images of figure 3.18(b) – 3.18(d), periodic surface structures (with a periodicity of ~500 nm) initiate to appear over the nanocavities or random nanoroughness in few places on the Cu surfaces.

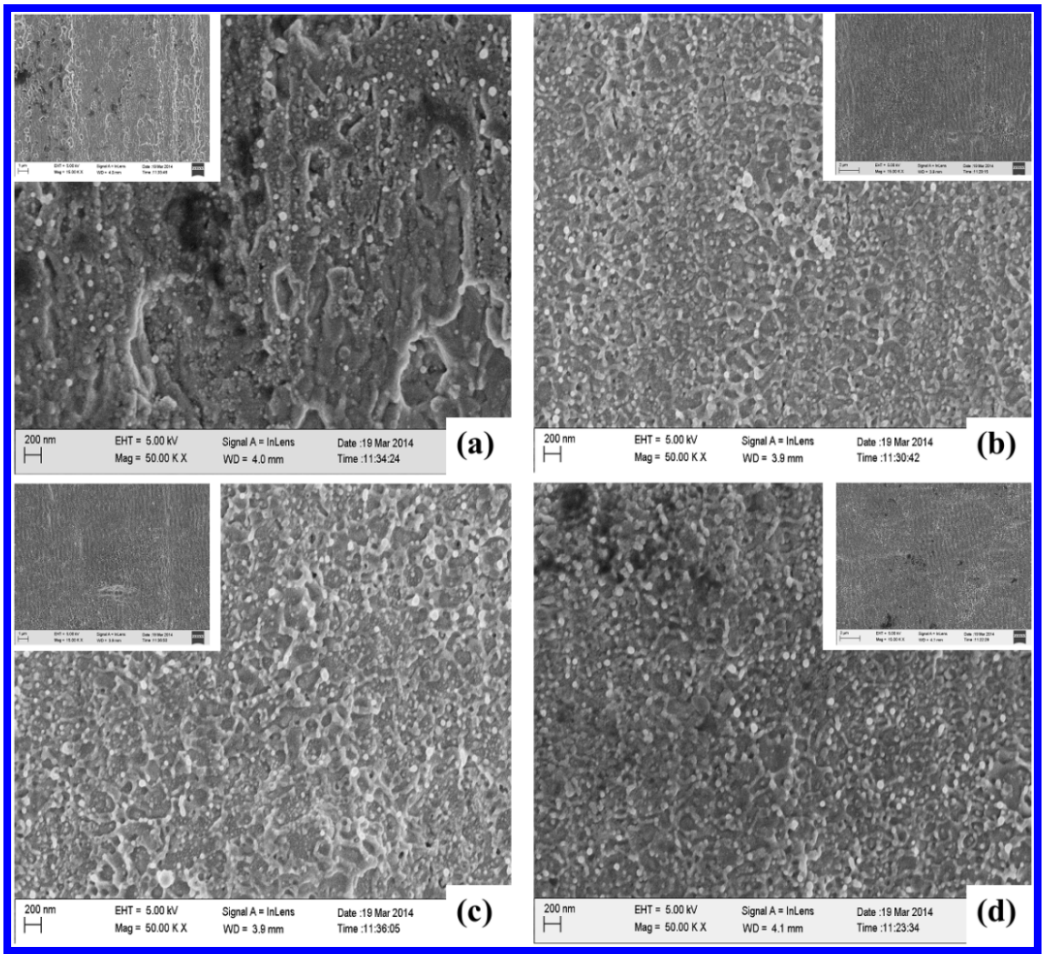

Figure 3.18 FESEM images of laser induced surface structures produced on Cu surfaces using ps pulses after (a) N=211 pulses, (b) N=240 pulses, (c) N=285 pulses and (d) N=346 pulses irradiate the target and insets show their low resolution images.

Figure 3.19 depicts the visuals of LIPSS (~484 nm and ~470 nm) along with large scale image [inset of figure 3.19] for the case of irradiation with (a) 400 and (b) 550 pulses, respectively. However, clear LIPSS were extended to the complete substrate for a pulse train of 933 and 1480 shots [figure 3.19(c) and 3.19(d)] with the periodicity of ~450 nm and ~ 400 nm, respectively. Figure 3.20 illustrates FESEM image of LIPSS complete growth on Cu surface with period of ~365 nm and ~300 nm obtained for (a) 3240 and (b) 6800 pulses, respectively. As observed from FESEM images, starting ablation with fewer shots to more shots the random nanoroughness was converted into nano-clusters with different sizes formed on the top of LIPSS. The

estimated mean sizes of nano-clusters were ~85 nm and ~65 nm [figure 3.19(c) and 3.19(d)]; ~42 nm, and ~50 nm [figure 3.20(a) and 3.20(b)]. On the other hand, the periodicity of LIPSS periodicity decreased from ~500 nm to ~300 nm with increasing laser shots (increase the incubation effects) due to the gradual decrement in the ablation threshold.

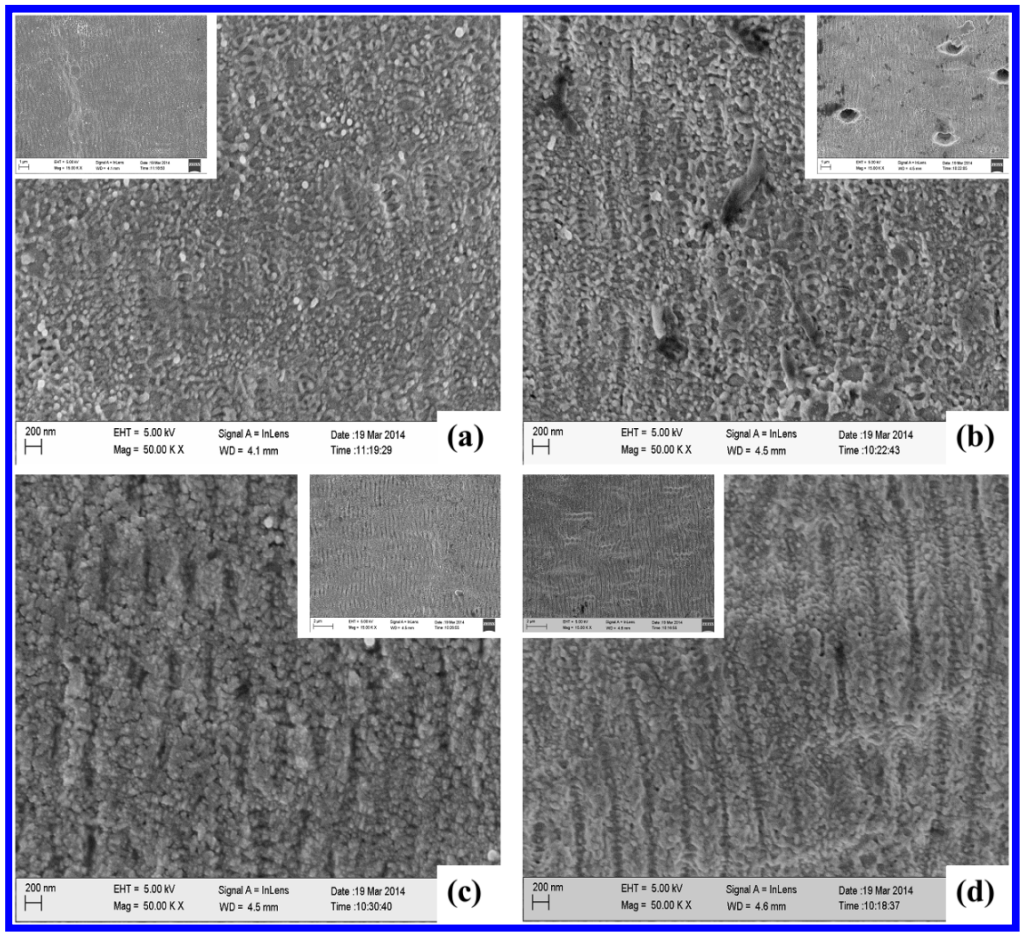

Figure 3.19 FESEM images of LIPSS generated on Cu surfaces using ps pulses after (a) N=400 pulses, (b) N=550 pulses, (c) N=933 pulses and (d) N=1480 pulses incident on the target and insets show their low resolution images.

Over the last decade, production of LIPSS near the ablation threshold fluence has been studied extensively from ns regime to fs regime. However, the observed periodicity of LIPSS was of the order of laser wavelength (λ)[77] in the ns domain where as it was ~λ/4 - λ/2 in the fs domain.[70-71] Our study demonstrated that LIPSS formation with ~2 ps pulses is similar to fs pulses and totally different from ns pulses. In our case, we noticed that LIPSS (~2λ/3) were formed which was roofed by random nanoroughness at few shots whereas at higher of shots clear LIPSS (~λ/3) were

visualized along with nanoclusters formed on their top. The proposed mechanisms behind the formation of LIPSS with fs pulses might be more consistent for our study. Electron-phonon coupling coefficient (γ) is direct reliable parameter for the appearance of clear LIPSS on the metal surface. [74-75]

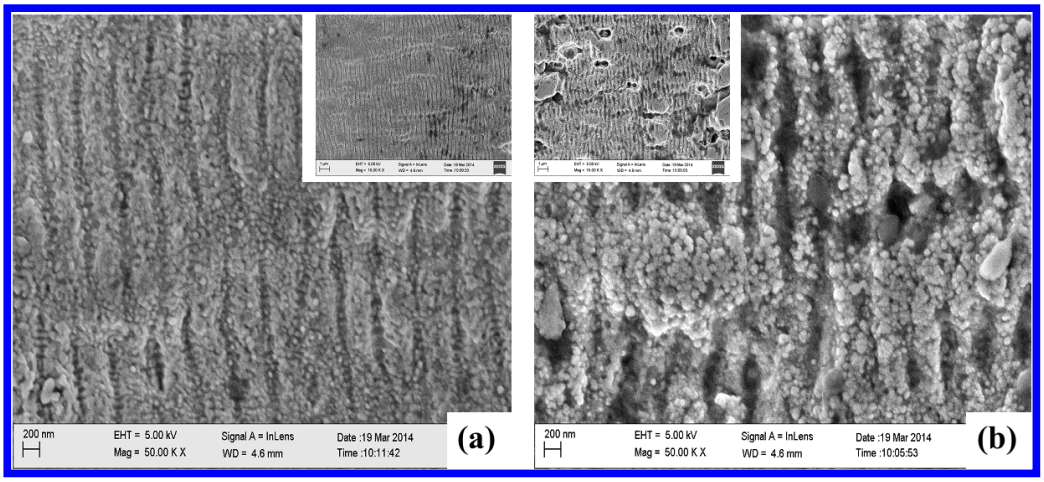

Figure 3.20 FESEM images of LIPSS generated on Cu surfaces using ps pulses after (a) N=3240 pulses, and (b) N=6800 pulses and insets show their low resolution images.

In our study, random NSs appeared on Cu surface for few initial shots. This random nanoroughness can support the interaction of generated surface electromagnetic field with incident field for further increasing number of shots which allows the increase in the value of γ. Consequently, non-uniform distribution of heat energy could have taken place on the metal surface for high γ values which leads to formation of LIPSS clearly. A similar explanation was included in the section 3.4.2.

3.5.2. Fs laser ablation of Cu in methanol using 2 ps laser pulses

In these experiments, Ti: Sapphire amplifier generating ~40 fs laser pulses at 1 kHz repetition rate with 800 nm have been utilized as a source. The beam diameter ($2\omega_0$) estimated on the target in acetone was ~90 µm. The typical level of liquid above the target surface was ~5 mm. The laser beam was focused perpendicularly on Cu plate which was immersed in acetone and Cu plate was positioned on a motorized Nano direct X-Y stage, which was operated through a controller (NTS-25). Typical fluence used was ~2.5 J/cm^2. The number of pulses incident on the target was chosen by varying the speeds of X-Y stages and line-line spacing is of 25 µm. We investigated the development of laser induced surface nanostructures on the metal

target by varying speeds of 400 µm/s, 300 µm/s, 200 µm/s, 100 µm/s and 50 µm/s. The estimated pulse numbers in the focal region [w(z)/d] w.r.t. scanning speeds were ~253, ~300, ~500, ~1000 and ~2000 and corresponding threshold fluences[69] after the ablation were ~0.98 J/cm^2, ~0.95 J/cm^2, ~0.89 J/cm^2, ~0.81 J/cm^2 and 0.74 J/cm^2 for the scanning speeds of 400 µm/s, 300 µm/s, 200 µm/s, 100 µm/s and 50 µm/s, respectively. The surface morphology of ablated targets was characterized by FESEM. The surface roughness was measured by a surface profilometer.

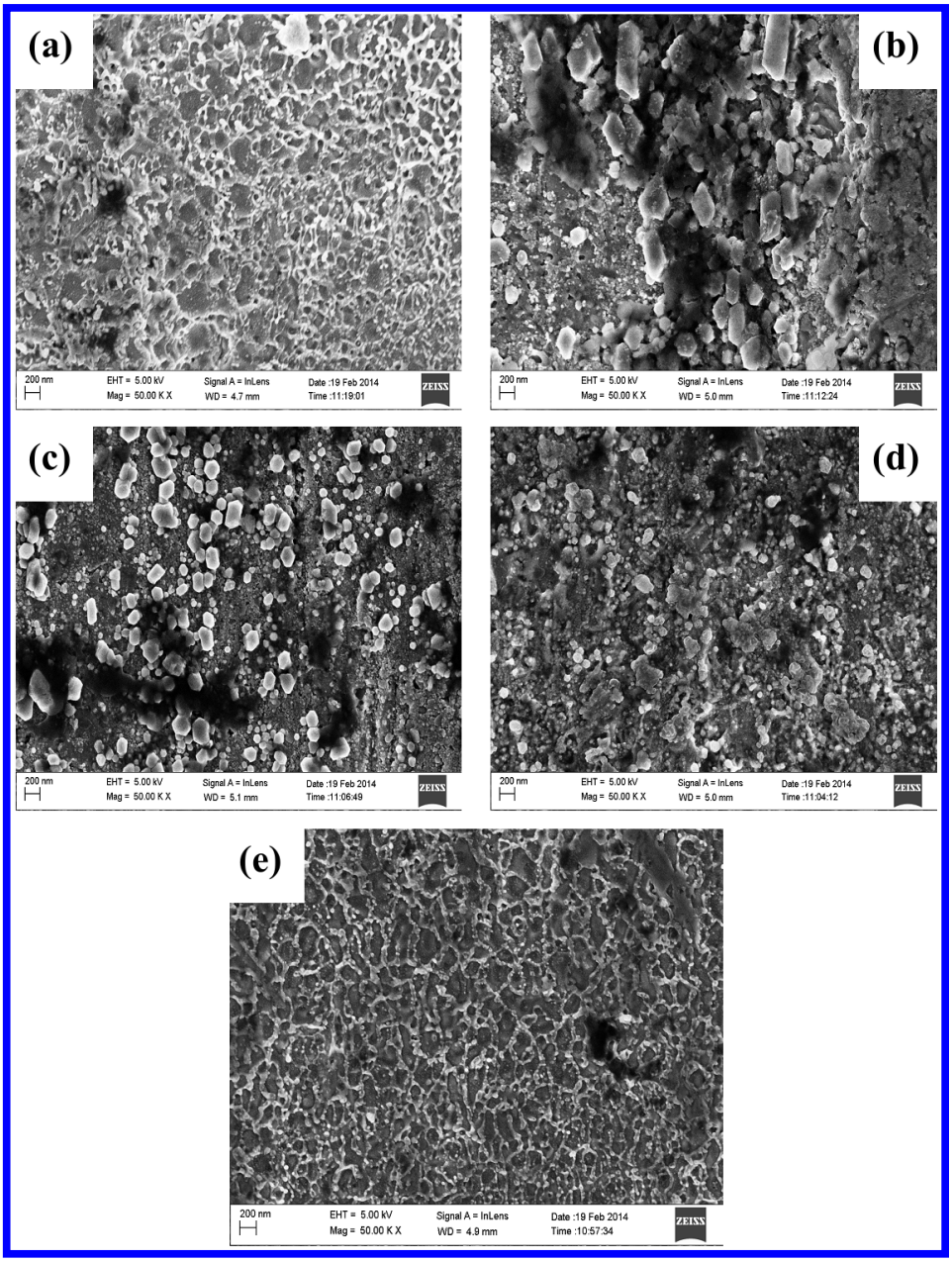

Figure 3.21 FESEM images of NSs on Cu surfaces using ps pulses following with (a) N=253 pulses, (b) N=300 pulses, (c) N=500 pulses, (d) N=1000 and (d) N=2000 pulses irradiate Cu the target.

Figure 3.21 demonstrates the FESEM images of NSs on the Cu metal target obtained by subsequent ablation with (a) N=253, (b) N=300, (c) N=500, (d) N=1000 and (e) N=2000 pulses at slightly above the threshold fluence. Figure 3.21(a) illustrates the random nanostructures covered the metal surface with estimated surface r.m.s. roughness found to be ~700 nm after N=253 pulses. As per the previous literature and our knowledge, the formation of random nanostructures and nanocavities are ascribed due the origin of hydro dynamical process in the aqueous media. With increasing shots, the random nano roughness turns sharper and heavier. The reason behind the production of heavy and rough NSs could be due to large absorption by the nanoparticle grains which might have been formed for earlier pulses on irradiated surface and geometrical effects also contribute because of scattering from sharp edges of NSs. After the ablation with N=253 pulses, the threshold fluence of the Cu metal was reduced to ~0.98 J/cm^2 (before ablation, F_{th} = 2 J/cm^2).[69] Later on N=300 pulses, cuboids (l ~ 400 nm, b ~ 200 nm, h ~ 60 nm) were produced on the Cu surface, as depicted in figure 3.21(b). In this case, the input fluence of the laser pulses (~2.5 J/cm^2) was more than double the ablation threshold (~0.98 J/cm^2), and this played a significant role in growth mechanism. The evolution of nanostructures in the present case takes place due to the existence of pioneer locations which considerably modify the energy distribution of subsequent interaction of laser shots with target and generating multiple cavitation bubbles. Depending on the collapse of the bubbles, some of the NPs can form clusters with larger size[59-61] and these clusters might have been truncated into cuboids or cubes and the ablation threshold reaches to 0.95 J/cm^2 after N=300 pulses.

The threshold fluence of Cu target was observed to reduced from 0.95 J/cm^2 to 0.89 J/cm^2, 0.81 J/cm^2 and 0.74 J/cm^2 as the pulse number increased from N=300 to 500, 1000 and 2000 pulses, respectively.[69] Following the ablation with N = 500 pulses [figure 3.21(c)], N=1000 pulses [figure 3.21(d)] and N=2000 pulses [figure 3.21(e)], hexagonal NPs with ~125 nm size, spherical NPs with ~70 nm and random nanoroughness or nanocavities with mean size of ~2.5 µm were observed. As observed from the results, the cuboids were modified into hexagonal structures with reduced size and then changed in to spherical particles. The main reason could be due to the fragmentation effects.[78]Additionally to that the production of random nanocavities is owing to the cavitation bubble.[59-61]

3.6. Summary

- A detailed investigation on the fabrication of Cu NPs and NSs by ps laser multiple/single line ablation was carried out in organic liquids and their characterizations were carried out. The effects of writing conditions, specifically multiple and single ablation, led to variations in the average size and yield of the NPs and, surface NSs. Additionally, the interaction of short-lived metallic plume with the elements in the surrounding liquid plasma led to the formation of pure Cu (MCuNP1/ SCuNP1), CuCl (MCuNP2/ SCuNP2), CuO (MCuNP3/ SCuNP3) and $CuCl_2$ (MCuNP4/ SCuNP4) NPs.
- The creation and annihilation of cavitation bubble on the surface Cu target in different liquid media led to formation of different type of NSs on the Cu surface. Additionally, we have performed the cavitation bubble study numerically and measured the bubble radius which confirmed that large bubbles could result in big craters and small bubbles could result in small craters.
- Size and yield of CuO NPs generated in ACN by ps laser ablation under effect of pulse energy was studied in detail. The data demonstrated that lower energy (25 μJ) and higher energy (400 μJ) showed the larger sized NPs and intermediate energy (100 μJ) illustrated smaller sized NPs which could be due to the collapse of cavitation bubble. Additionally, periodic surface structures were generated effectively through the overlapping of two/more lines in the effective spot size.
- Effect of pulse numbers on the fabrication of surface structures on the Cu target in ACN with ps pulses was investigated systematically. The FESEM technique was used to characterize the Cu substrates and estimated the periods. The periods of surface structures varied from LSFL to HSFL and the detailed mechanism was discussed. In the same way, investigation on the generation of Cu NSs on the Cu surface by fs laser pulses in acetone has been performed. The data revealed that various size and shapes of NSs were obtained on the surface and which could be confirmed by the collapse of cavitation bubble and the mechanism involved was described.

References

1. N. T. Binh, T. T. V. Khanh, D. N. Quang, N. T. Dinh, A. T. Nguyen and T. T. Hue Adv. Nat. Sci.: Nanosci. Nanotechnol. **3**, 025016 (2012).
2. L. Ziyuan, T. H. Haroldo, P. Patrick, T. Jie, F. Lan, H. H Tan and C. A. Jagadish, J. Phys. D: Appl. Phys.**45**, 305102 (2012).
3. T. Sakano, Y. Tanaka, R. Nishimura, N. N. Nedyalkov, P. A. Atanasov, T. Saiki and M. Obara J. Phys. D: Appl. Phys.**41**, 235304 (2008)
4. H. Sekhar and D. Narayana Rao, J. Nanopart. Res. **14**, 976 (2012).
5. N. Faraji, M. M. W. Younus, A. Kharazmi, E. Saion, M. Shahmiri and N. Tamchek, J. Europ. Opt. Soc. Rap. Public. **7**, 12040 (2012).
6. X. Dou, P.Y. Chung, P. Jiang and J. Dai, Appl. Phys. Lett. **100**, 063702 (2012)**.**
7. D. M. Kuncicky, S. D. Christesen, and O. D. Velev, Appl. Spec. **59,** 401 (2005)
8. M. Ahmad Mohiddon, S.L.D. Varma, M. Ghanashyam Krishna, Chem. Phys. Lett. **588,** 160 (2013)
9. K. Fukami, M. L. Chourou, R. Miyagawa, Á. M. Noval, T. Sakka, M. Manso-Silván, R. J. Martín-Palma, Y. H. Ogata, Materials **4,** 791 (2011)
10. Z. Dai, X. Xiao, L. Liao, J. Zheng, F. Mei, W. Wu, J. Ying, F. Ren, and C. Jiang, Appl. Phys. Lett. **103,** 041903 (2013).
11. S. J. Henley, J. D. Carey, and S. R. P. Silva, Appl. Phys. Lett. **88,** 081904 (2006)
12. S.Y. Han , Q. H. Guo , M. M. Xu , Y. X. Yuan , L. M. Shen , J. L. Yao , W. Liu , and R. A. Gu , J. Coll. Inter. Sci. **378,** 15 (2012)
13. P. V. Kamat, and D. Meisel, Semiconductor Nanoclusters, Studies in Surface Science and Catalysis, Eds. (Elsevier: Amsterdam 1996, p 103).
14. H. Weller, Angew Chem Int Ed Engl, **32**, 41- 53 (1993).
15. P. E. de Jongh, D. Vanmaekelbergh, and J. J. Kelly, Chem. Commun. 1069–1070 (1999) **DOI:** 10.1039/A901232J
16. K. Akimoto, S. Ishizuka, M.Yanagita, Y. Nawa, G. K.Paul, and T. Sakurai, Sol. Energy, **80**, 715 (2006).
17. H. Zhang, Q. Zhu, Y. Zhang, Y. Wang, L. Zhao, and B. Yu, Adv. Funct. Mater. **17**, 2766 (2007)
18. S. Hamad, G. Krishna Podagatlapalli, S. P. Tewari, and S. Venugopal Rao, J. Phys. D: Appl. Phys. **46** , 485501 (2013)
19. S. Hamad, G. Krishna Podagatlapalli, S. P. Tewari, and S. Venugopal Rao, Pramana J. Phys. **82**, 331 (2014)
20. E. H. Kennard and E. O. Dieterich, Phys. Rev.**9**, 58 (1917)
21. L. O. Grondahl and P. H. Geiger, J. Am. Inst. Electr. Eng. **46**, 215 (1927)
22. Q. Liu, X. Ling, H. Liu, J. Hang and Z. Hu, Mat. Chem. Phys. **98**, 519 (2006)
23. H. Wang, J. Zhang, J. J. Zhu and H. Y. Chen, J. Cryst. Growth, **244**, 88 (2002)
24. Z. Meng, X. Xiaodang and Z. Millin, Mate. Lett. **62**, 385 (2008)
25. F. Xu, W. Ji, Z. Shen, S. H. Tang, X. R. Ye and Z. A. Jia, J. Solid State Chem. **147**, 516 (1999)
26. M. A. Al-Mamun, Y. Kusumoto and M. Muruganandham, Mat. Lett. **63**, 2007 (2004)
27. T. Y. Hwang, A. Y. Vorobyev, and C. Guo, Appl. Phys. Lett. **95,** 123111 (2009).
28. C. Wang, Y.C. Chang, J. Yao, C. Luo, S. Yin, P. Ruffin, C. Brantley, and E. Edwards, Appl. Phys. Lett. **100,** 023107 (2012)
29. G.K. Podagatlapalli, S. Hamad, S. P. Tewari, S. Sreedhar, M.D. Prasad, and S. Venugopal Rao, J. Appl. Phys. **113,** 073106 (2013)

30. A. Chou, E. Jaatinen, R. Buividas, G. Seniutinas, S. Juodkazis, E.L. Izake, and P. M. Fredericks, Nanoscale **4,** 7419 (2012)
31. T. Mortier, T. Verbiest, A. Persoons, Chem. Phys. Lett. **382**, 650 (2003)
32. S. Karolı´na, J. Pfleger, and P. Marek, Appl. Surf. Sci. **256**, 2979 (2010)
33. G.K. Podagatlapalli, S. Hamad, S. Sreedhar, S. P. Tewari, and S. Venugopal Rao, Chem. Phys. Lett. **530,** 93 (2013)
34. Y. Yang, J. Yang, C. Liang, H. Wang, X. Zhu, and N. Zhang, Opt. Exp. **17**, 21124 (2009)
35. G. Miyaji and K. Miyazaki, Opt. Exp. **16,** 16265 (2008)
36. G.K. Podagatlapalli, S. Hamad, and S. Venugopal Rao, Appl. Surf. Sci. **303**, 217 (2014).
37. S. Venugopal Rao, G.K. Podagatlapalli, S. Hamad, J. Nanosci. Nanotech. **14**, 1364 (2014).
38. J. Wang, and C. Guo, Appl. Phys. Lett. **87,** 251914 (2005)
39. J. W. Yao, C. Y. Zhang, H. Y. Liu, Q. F. Dai, L. J. Wu, S. Lan, A. Venu Gopal, V. A. Trofimov, and M. L. Tatiana, Opt. Exp. **20,** 905 (2012)
40. A. Menendez-Manjon, P. Wagener and S. Barcikowski, J. Phys. Chem. C **115**, 5108 (2011)
41. R. M. Tilaki, A. Iraji-Zad, and S. M. Mahdavi, Appl. Phys. A. **84**, 215 (2006)
42. Y. Zijie, C. Giuseppe, and B. C. Douglas, J. Phys. Chem. C. **115**, 5058 (2010)
43. A. Nath and A. Khare, J. Appl. Phys. **110**, 043111 (2011).
44. J. M. Achord and C. L. Hussey, Anal. Chem. **52** 601 (1980).
45. M. M. Miranda, C. Gellini, A. Simonelli, M. Tiberi, F. Giammanco and E. Giorgetti, Appl. Phys. A **110,** 829 (2013).
46. M. M. Miranda, G. Cristina, and G. Emilia, J. Phys. Chem. C **115**, 5021 (2011).
47. J. B. Nielsen, J. M. Savolainen, M. S. Christensen and P. Balling, Appl. Phys. A. **101**, 97 (2010)
48. M. A. Garcia, J. Phys. D: Appl. Phys. **44,** 283001 (2011).
49. U. Chakravarty, R. A. Ganeev, P. A. Naik, J. A. Chakera, M. Babu and P. D. Gupta, J. Appl. Phys. **109**, 084347 (2011)
50. D. Von der Linde, K. Sokolowski-Tinten, J. Bialkowski, Appl. Surf. Sci., **109/110**, 1 (1997)
51. Z. Yan and D. B. Chrisey, J. Photochem. Photobiol.C **13**, 204 (2012)
52. A. De Bonis, M. Sansone, L. D'Alessio, A. Galasso, A. Santagata, and R. Teghil, J. Phys. D: Appl. Phys.**46**, 445301 (2013)
53. J. P. Sylvestre, A. V. Kabashin, E. Sacher, and M. Meunier, Appl. Phys., A Mater. Sci. Process. **80**, 753 (2005)
54. R. M. Tilaki, A. Irajizad, and S. M. Mahdava, J. Nanopart. Res. **9**, 853 (2007).
55. J. P. Sylvestre, A. V. Kabashin, E. Sacher and M. Meunier, Appl. Phys. A **80**, 753 (2005)
56. K. S. Suslick and D. J. Flannigan, Annu. Rev. Phys. Chem. **59**, 659 (2008)
57. B. Emil-Alexandru, Microfluid Nanofluid **11**, 511(2011)
58. "Models of Ultrasound Contrast Agents" Duncan Alexander Sutherland**,** An essay of B.Sc. (Honours), Applied Mathematics, University of Sidney.
59. A. Vogel, N. Linz, S. Freidank, and G. Paltauf, Phys. Rev. Lett. **100**, 038102 (2008)
60. A. Vogel, J. Noack, G. Huttman, and G. Paltauf, Appl. Phys. B **81**, 1015 (2005)
61. Y. Yang, J. Yang, C. Liang, H. Wang, X. Zhu, and N. Zhang, Opt. Exp. **17**, 21124 (2009)
62. U. Kreibig and M. Vollmer, Optical Properties of Metal Clusters (Springer

Verlag, Berlin, 1995).
63. A. Nath, A. Das, L. Rangan, and A. Khare, Sci. Adv. Mat. **4**, 106 (2012)
64. R. K. Swarnkar, S. C. Singh and R. Gopal, Bull. Mater. Sci. **34**, 1363 (2011)
65. B. Hopp, T. Smausz, T. Csizmadia, C. Vass, C. Tápai, B. Kiss, M. Ehrhardt, P. Lorenz, and K. Zimmer, Appl. Phys. A **113**, 291 (2013)
66. S. Bashir, M. S. Rafique, C. S. Nathala, and W. Husinsky, Appl. Surf. Sci. **290**, 53 (2014)
67. A. Y. Vorobyev, V. S. Makin, and C. Guo, J. Appl. Phys. **101**, 034903 (2007)
68. Y. Jee, M. F. Becker, and R. M. Walser, J. Opt. Soc. Am. B **5**, 648 (1988)
69. F. Liang, R. Vall´ee, D. Gingras and S. Leang Chin, Opt. Mat. Exp. **1**, 1244 (2011).
70. J. Z. P. Skolski, G. R. B. E. R¨omer, A. J. Huis in't Veld, V. S. Mitko, J. Vincenc Obona, V. Ocelik, and J. Th. M. de Hosson. J. Las. Micro/Nano Eng. **5**, 263 (2010)
71. J. Z. P. Skolski, G. R. B. E. R¨omer, J. Vincenc Obona, and A. J. Huisin't Veld. J. Appl. Phys. **115**, 103102 (2014)
72. M. Huang, F. Zhao, Y. Cheng, N. Xu, and Z. Xu, Phys. Rev, B. **79**, 125436 (2009)
73. T.J.-Y. Derrien, T. E. Itina, R.Torres, T. Sarnet, and M.Sentis, J. Appl. Phys. **114**, 083104 (2013).
74. J. Wang and C. Guo, Appl. Phys. Lett. **87**, 251914 (2005)
75. J. Wang and C. Guo, J. Appl. Phys. **100**, 023511 (2006)
76. S. Barcikowski, A. Menéndez-Manjón, B. Chichkov, M. Brikas, R. Gediminas, Appl. Phys. Lett. **91**, 083113 (2007).
77. J. F. Young, J. E. Sipe and H. M. van Driel, Phys. Rev. B **30**, 2001 (1984)
78. P. Lorazo, P. J. Lewis, and M. Meunier, Phys. Rev. Lett. **91**, 225502 (2003)

4

Fabrication of Silicon Nanomaterials: Effect of Liquids, Pulse Energy and Pulse Number

Abstract

This chapter demonstrates the fabrication of Si NPs in different organic solvents such as acetone, water, DCM, and chloroform. Photoluminescence studies of thus prepared Si NPs and theoretical study on laser induced periodic surface structures (LIPSS) on Si NSs are discussed. Grating periods of LIPSS are described on the basis of electron density, complex refractive index (of Si during the ablation). Correlation between the modeling and experiment on laser induced surface structures is studied and results are presented in detail. Later generation of Si NPs/NSs in acetone and involved dynamics of ablation for different pulse energies are described. Differences in the products (NPs and NSs) obtained using ULAL are described through photoluminescence and Raman studies. Finally the effect of modified Gaussian beam on the productivity of Si NPs and texturing of NSs is elucidated.

4.1. Introduction

Semiconductor nanoparticles (NPs) have been attractive candidates for their essential role play in the fabrication of new materials such as optical gain media,[1,2] nano-crystalline based solar cells,[3] light emitting diodes,[4,5] in bio-imaging processes,[6,7] and photonics[8] due to their unique properties compared to the bulk. The optical, electronic, and structural properties of semiconductor NPs and nanostructures (NSs) are purely size and shape dependent. When the dimensions of material are confined to nano-scale, energy spectrum turns discrete resulting in enlargement of the material's band gap. The properties of nanomaterials deviate significantly from those of bulk and isolated molecules. Silicon (Si) NPs are promising because of their outstanding properties resulting in applications in a variety of fields such as optoelectronics, photovoltaics[9] and biomedical fields.[10,11] Si is an indirect band gap semiconductor material with an intrinsic band gap which ranges in the near infrared region (800 nm - 900 nm). Phonons play an important role in the process of optical transitions in bulk silicon. When bulk Si is reduced to nano scale, the zero-phonon optical transitions are moderately permitted. These zero-phonon optical transitions increase the rate of radiative recombination through band-to-band recombination process.[12] Consequently quantum confinement effects[15,16] render efficient photoluminescence (PL) in the visible region.[17,18] Especially, Si NPs being microelectronic compatible photonic materials have attracted more attention due to their size dependent PL.[19] Additionally, luminescent Si NPs are capable materials of demonstrating large third order nonlinear response[20,21] and possess potential for specific applications such as second harmonic generation.[22]

Silicon NPs have been fabricated through variety of techniques such as sol-gel synthesis,[23] vapor deposition,[24,25] rfsputtering,[26] heavy ion-irradiation,[27] micro-emulsion route,[28] and several other chemical and physical methods. Among all these techniques for fabrication of bulk materials to nano-scale, laser ablation in liquid media (LAL)[29-38] is one of the fast, simple, and versatile methods. Furthermore, LAL guarantees extremely stable NPs without using any capping agents with a highest degree of occupation. Particularly, ultrashort pulsed laser ablation in liquids (ULAL)[39-43] is a unique material processing technique that provides distinct advantages in applications over the ns and continuous wave (cw) laser ablation. In

addition, ultrashort laser pulses allow less thermal damage and a nearly melt free ablation, if carried out close to ablation threshold. Owing to the large peak intensities associated with picosecond (ps) and femtosecond (fs) laser pulses, absorption involves multi-photon processes. Furthermore, within ps and fs timescales the energy cannot be transferred from electron to the lattice instantly. Thermal descriptions maintain individuality between electron and lattice temperature. Therefore, two-temperature model becomes necessary in order to describe thermal phenomena.[44] In the process of Si NPs fabrication, when an ultrafast pulse is incident on silicon target, valence band electrons respond first to absorb visible/IR wavelengths and transitions occur from valance band to conduction band. In the case of fs pulses in the near IR region, linear and nonlinear absorption (multi-photon absorption) are the dominant mechanisms. Absorption of laser energy by the valence electrons creates quasi-free carriers.[45] The excited electrons transfer their energy to lattice through electron-lattice coupling and the corresponding characteristic time is ~1 ps. Collisions between the electrons and lattice leads to the generation of higher heat content in the vicinity of laser focused regions and, consequently, material transits to a super critical fluid state and vaporization occurs to interact with surrounding liquid media creating multifaceted structure of nanomaterials.

Thus far people have reported the influence of pulse duration and pulse energies in size distribution of the fabricated Si NPs.[40,46] Among recent significant reports Intartaglia et al.[46,47] had fabricated Si NPs in liquid media using ~100 fs laser pulses at various pulse energies. The writing conditions in their experiments were different (laser beam was focused at a single point on the target) compared to our experiments. In our experiment the focused laser beam (~40 fs and ~2 ps, FWHM) was scanned on the surface of Si substrate to draw periodic lines with a given separation rather than mere focusing. Furthermore, the scan separation between the line structures was chosen in such a way as to ablate the pre-ablated line structure on the target surface for two or multiple of times and was labeled as double/multiple line ablation (separation of 30 μm). Recently, our group has reported the fabrication of Ag NPs and NSs by ultrafast double line ablation in double distilled water.[48] In addition to NPs, laser induced periodic surface structures (LIPSS) in semiconductors have also been investigated using ps and fs lasers.[49-52,53] In this regime, LIPSS (spikes or ripples) can be produced when the laser fluence is approximately equal to the

threshold fluence of the material. Recently, our group has also reported the fabrication of Aluminum NSs achieved through fs laser ablation of Al in water demonstrating the formation of sub-wavelength nano ripples.[54] In this chapter we present our results from (a) the ps ablation studies of Si in different liquid media (b) pulse energy dependence of generated Si NPs and LIPSS using fs ablation of Si in acetone and (c) fabrication of sub-wavelength LIPSS on the surface of Si under the influence of different pulse numbers using ps pulses in methanol. We have specifically investigated (a) PL studies of the fabricated NPs (b) mechanisms of LIPSS formation and (c) correlating our experimental data with a theoretical model to estimate the periodicity of LIPSS.

4.2. Fabrication of Si NMs in different liquids

4.2.1. Fabrication process

The ablation studies were carried out by a 1 kHz chirped pulse amplified Ti: sapphire laser system (LEGEND, Coherent) delivering nearly bandwidth limited laser pulses (~2 ps) at 800 nm. The amplifier was seeded with ~15 fs pulses from an oscillator. The initial laser beam diameter was ~8 mm and was focused with a convex lens of focal length 25 cm on the surface of Si substrate placed in different solvents such as acetone, water, DCM and chloroform. Typical pulse energy utilized was ~150 μJ. Input pulse energy was controlled by the combination of Brewster angle polarizer and a half wave plate. The target was placed normal to the laser beam on a three dimensional motorized stage with ESP-300 motion controller (resolution of ~250 nm) which was interfaced to a PC. Duration of each scan was ~30 minutes and line to line spacing was ~60 μm. To avoid ambiguity in addressing the generated colloidal Si NCs were labeled as SiNC1, SiNC2, SiNC3 and SiNC4 for samples prepared in liquids of Acetone, Water, DCM, and Chloroform, respectively.

4.2.2. TEM, HRTEM and SAED characterizations of Si colloids

The methodical studies of colloidal Si NCs were produced by ultrafast single line laser ablation of highly doped Silicon [with boron (~10^{18})] target i.e. immersed in four liquids (acetone, water, DCM and chloroform). To avoid the ambiguity, Si NCs

fabricated through single line ablation in acetone, water, DCM, and chloroform were labeled as SiNC1, SiNC2, SiNC3, and SiNC4, respectively. The quantity of NPs and their crystalline nature were observed from TEM and SAED measurements. Figure 4.1 demonstrates the TEM imaging of Si NCs produced in SiNC1 (figure 4.1a) and SiNC2 (figure 4.1c) and insets of figure 4.1(a) and 4.1(c) show the corresponding size histogram distribution of NCs which were fitted with Gaussian curve. The mean diameter was found to be ~9.5 nm for SiNC1 in acetone and ~20 nm for SiNC2 in water. Figure 4.1(b) and 4.1(d) illustrate SAED patterns of SiNC1 and SiNC2 which confirmed the fabricated Si NCs were poly-crystals and the corresponding four- five planes have been considered for estimating the interplanar spacings 3.35 Å, 2.69 Å, 2.35 Å, 1.77 Å and 1.57 Å which agreed well with pure Si (200), (211), (220), (321) and (411) crystal planes of cubic phase for SiNC1.

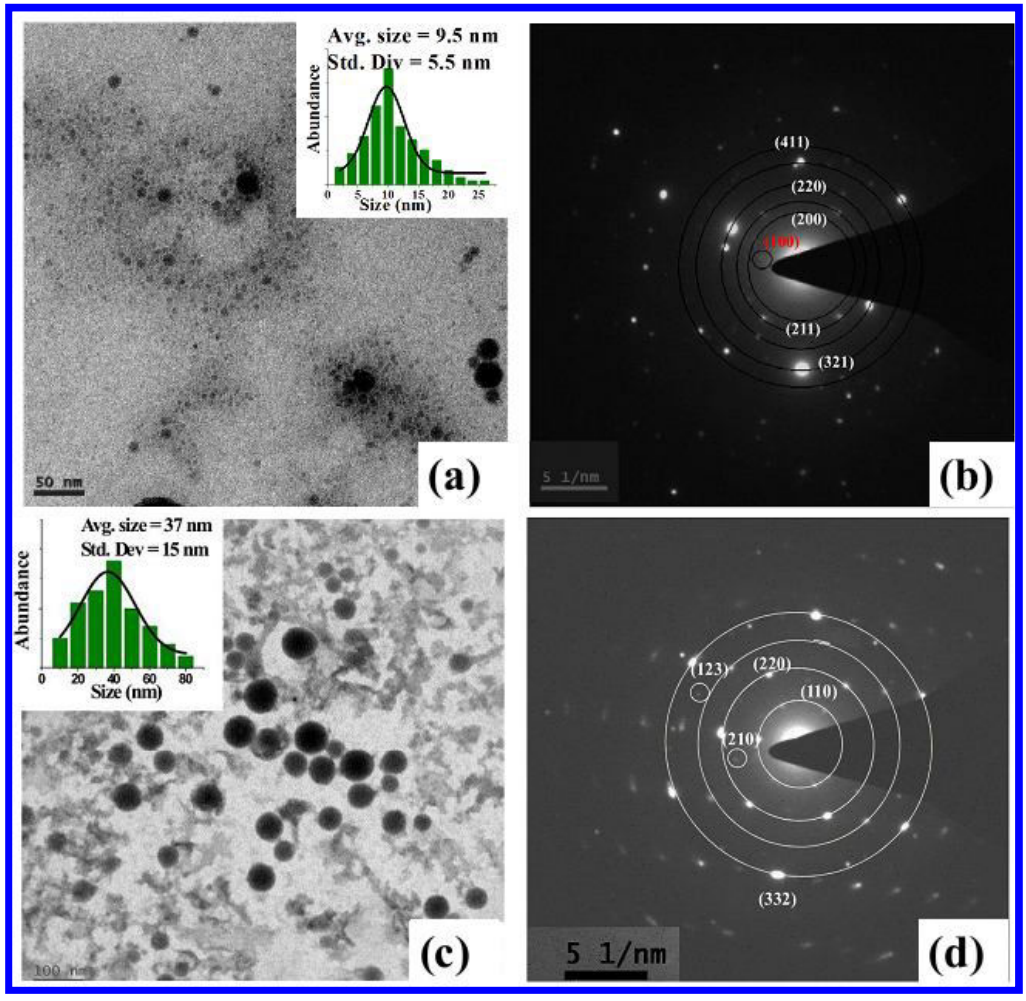

Figure 4.1 TEM imaging of (a) SiNC1 and (c) SiNC2 and, insets of (a) and (c) depict the NPs distribution. SAED spectra of (b) SiNC1 and (d) SiNC2.

Moreover, one of the crystal planes with interplanar spacing of 5.72 Å concurred with Si (100) crystal planes with hexagonal phase. For the case of SiNC2, the interplanar spacings acquired from crystal planes were 2.6 Å and 1.64 Å, well matched with SiO_2 cubic crystal planes of (110) and (210) and, along with two more planes [(220) and (332)] were observed corresponding to the 'd' values being 2.35 Å and 1.42 Å [similar to pure Si with cubic phase]. From the SAED pattern, we confirmed that pure Si NCs and Si/SiO_2 NCs were generated in cases of SiNC1 and SiNC2, respectively.

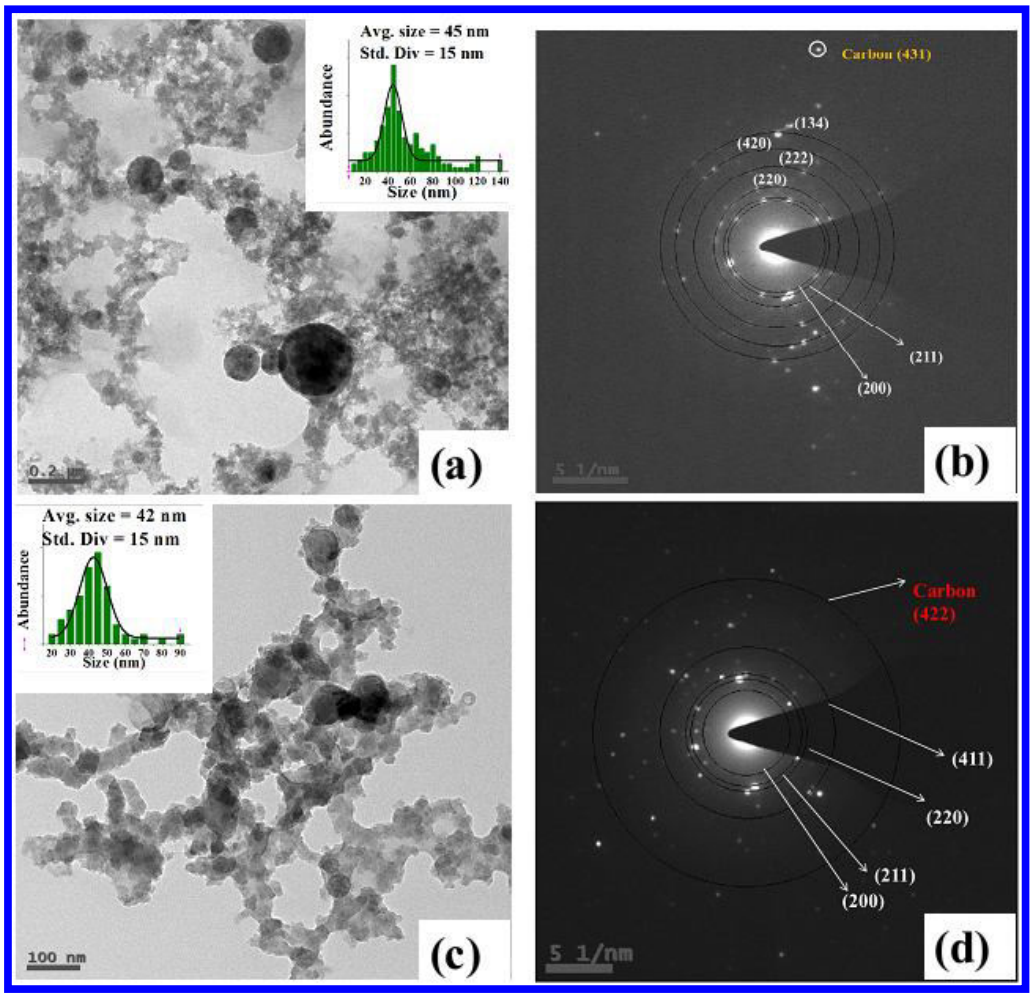

Figure 4.2 TEM imaging of (a) SiNC3 and (c) SiNC4 and, insets of (a) and (c) depict the NPs distribution. SAED patterns of (b) SiNC3 and (d) SiNC4.

TEM data of fabricated Si NCs in DCM (SiNC3) and chloroform (SiNC4) are demonstrated in figures 4.2(a) and 4.2(c), respectively, and insets depict the size distribution histograms. As observed from the TEM images of 4.2(a) and 4.2(c), the

NPs were aggregated spheres covered with thick layers of carbon. The average size was ~45 nm and ~42 nm for SiNC3 and SiNC4, respectively. Figures 4.2(b) and 4.2(d) represent SAED pattern of SiNC3 and SiNC4, respectively. The NCs in SiNS3 depicted polycrystalline phase (cubic phase) with interplanar spacings of 3.34 Å, 2.72 Å, 2.33 Å, 1.92 Å, 1.49 Å, and 1.31 Å corresponding to crystalline Miller planes of Si (200), (211), (220), (222), (420) and (134), respectively.

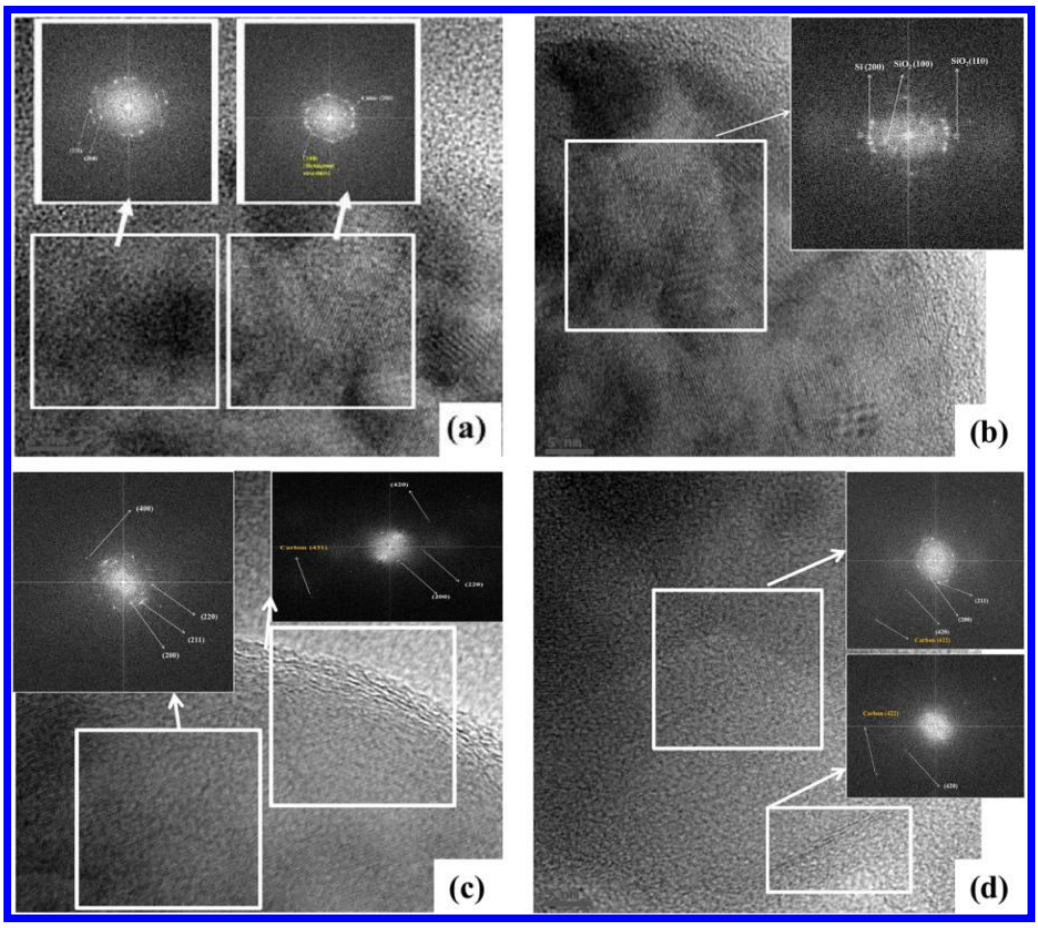

Figure 4.3 HRTEM images of (a) SiNC1, (b) SiNC2, (c) SiNC3 and (d) SiNC4 formed show the view of lattice planes observed at different characteristic separations. Insets show its numerical electronic diffraction pattern of HRTEM images which confirmed the planes of Si, Si/SiO_2, Si-C and Si-C lattice sets, respectively.

Similarly, SAED ring pattern for SiNC4 resembled Si (200), (211), (220), and (411) and their corresponding 'd' values were 3.34 Å, 2.72 Å, 2.33 Å, and 1.57 Å. Moreover, another diffraction ring with lattice spacings for both the cases (SiNC3 and SiNC4) were 0.73 Å and 0.68 Å are ascribed to the 'd' values of Carbon (C) (422) and (431) planes, respectively. From TEM and SAED studies we could conclude that pure Si NCs in acetone (SiNC1), Si/SiO_2 NCs in water (SiNC2), Si NCs covered by

carbon matrix in both DCM (SiNC3) and chloroform (SiNC4) were obtained. These conclusions, acquired from the above characterizations were additionally supported by high resolution TEM (HRTEM) and Raman data of the colloidal Si NCs.

Figures 4.3(a)-(d) illustrate the HRTEM images of SiNC1-SiNC4 and inset shows the FFT of HRTEM images. The FFT patterns of lattice planes from HRTEM correlate the SAED patterns. For SiNC1 [figure 4.3(a)], the interplanar spacings of lattice planes, 5.71 Å and 3.34 Å were attributed to the approximate lattice spacings of hexagonal phase pure Si (100) plane and cubic phase of pure Si (200), respectively. In the case of water (SiNC2), the measured inter atomic separations 4.7 Å and 2.64 Å were in good agreement with SiO_2 (100) and (110) planes, and 3.3 Å belonging to pure Si (200) which is shown in figure 4.3 (b). For chlorine based solvents SiNC3 and SiNC4 [(figure 4.3(c) and figure 4.3(d)], the 'd' values obtained from the FFT of HRTEM images were 0.73 Å (SiNC3) and 0.68 Å (SiNC4) belonging to C (422) and (431) planes in both cases along with Si planes. This characterization validated the formation of Si NCs in carbon matrix.

4.2.3. Raman, UV-Vis absorption and PL studies of Si colloids

Figure 4.4 depicts the Raman spectra of Si NCs produced in SiNC1-SiNC4 with 532 nm excitation. The position and broadening of the crystalline peak determines the nature of Si NCs. The peak position decides the crystalline nature and broadening reflects the size effects. However, we observed both crystalline and amorphous phases in all cases. As seen from the Raman spectra, a prominent peak was observed near 483 cm^{-1} which confirmed the amorphization of nano-entities. The ~514 cm^{-1} peak was detected for all the samples which confirmed the crystalline nature of Si NCs and the peak position of bulk Si (520.8 cm^{-1}) was also recorded as a reference for observing the shift. Other than that, two peaks were identified near 1350 cm^{-1} (D-band) and 1605 cm^{-1} (G-band) in both SiNC3 and SiNC4, which confirmed the presence of carbon along with Si NCs. These studies certify the formation of Si-C nanocomposites in SiNC3 and SiNC4.

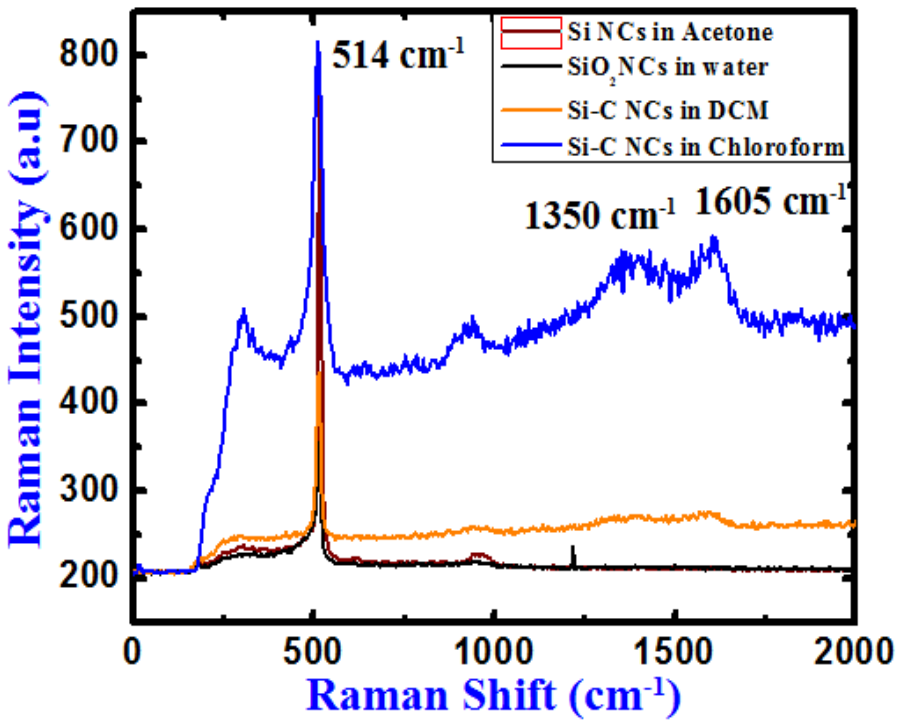

Figure 4.4 Raman spectra of Si NCs in (i) SiNC1, (ii) SiNC2, (iii) SiNC3 and (iv) SiNC4 with crystalline peak around 514 cm^{-1} and amorphous peak around 484 cm^{-1}. Two carbon bands were observed at 1350 cm^{-1} and 1605 cm^{-1} in both SiNC3 and SiNC4.

The Si NCs obtained through ULAL possessed broad absorption band in UV – near infrared (NIR) region of electromagnetic spectrum. The absorption band was observed in the 300 - 800 nm range for all samples with a little intensity difference. The significance of the huge band demonstrated that broad distribution in size of NCs present in liquids. Figures 4.5(a) and 4.5(b) illustrate UV –Vis absorption and photoluminescence (PL) spectra of colloidal Si NCs in different liquids, respectively. Careful observation of the absorption spectra [figure 4.5(a)], revealed the presence an additional band with tiny wavelength shift (328 nm, 282 nm and 274 nm) in the cases of SiNC1, SiNC3 and SiNC4 and no such band was observed in the case SiNC2 (water). The liquid properties could play significant role for this wavelength shift and which might not be due to the differences in sizes of NCs. Figure 4.5(b) represents the PL spectra of colloidal Si NCs deposited on glass slides. All the samples illustrated a significant amount of PL and peaks observed near 455 nm, 480 nm, 482 and 473 nm for SiNC1, SiNC2, SiNC3 and SiNC4, respectively. Moreover, we have verified that the PL spectra is attributed to Si NCs since the PL peak position at 570 nm of glass slide was taken as reference for quantifying the PL peak endorsed to Si NCs.

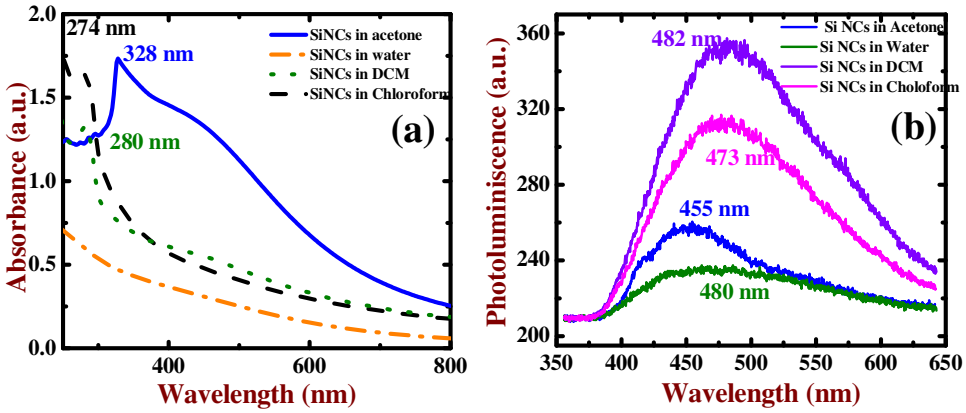

Figure 4.5 (a) UV-Vis absorption spectra and (b) photoluminescence spectra of Si NCs prepared through ps laser ablation in acetone (SiNC1), water (SiNC2), DCM (SiNC3) and chloroform (SiNC4)

As observed from results of PL, the position of PL peak was not dependent on size of NCs. But different peak positions were obtained for different samples which could be due to choosing of different liquid media. Particularly, we observed a shift (blue or red) of peak position in PL spectra of Si NCs in the single liquid medium due to the size effect of Si NCs (see section 4.3) which could be attributed to quantum confinement effect. The PL of generated Si NCs in different liquid media have demonstrated different peak positions due to the interaction of ultrafast laser beam with liquid media producing carbon byproducts. These carbon byproducts could occupy position on the surface of the NC form Si – C material allowing changes in the electronic energy level system. Recently, Intartaglia et al.[55] reported that the interaction takes place between laser and solvent molecule and this influence the PL of Si NCs produced by laser ablation.

4.2.4. SEM and Raman characterization of Si NSs

In our experiments, we produced nanostructures (NSs) on the Si substrates simultaneously along with colloidal Si NCs. In this context, the generated NSs in different liquid media such as acetone, water, DCM and chloroform were labeled as SiNS1, SiNS2, SiNS3 and SiNS4, respectively. The Si surface area exposed to laser ablation in liquids acquires LIPSS, which depend on the preferred liquid media and number of pulses. Here, we attempted to change liquid media to get the NSs on Si substrate using constant number of laser pulses. The FESEM images of Si substrates after the ablation using ultrashort pulses in various liquids are illustrated in figure 4.6.

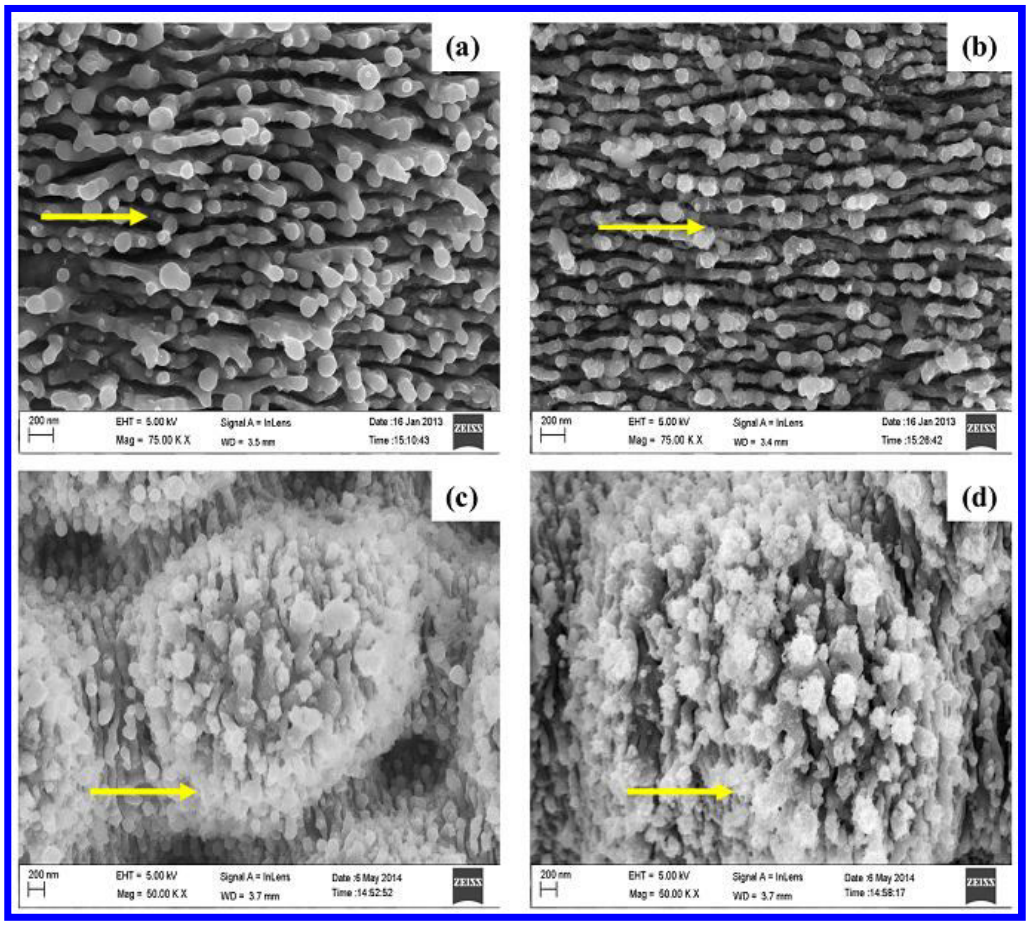

Figure 4.6 FESEM images of laser induced surface structures were fabricated on Si substrate by ps laser ablation of bulk Si in liquid media (a) SiNS1 (b) SiNS2 (c) SiNS3 and (f) SiNS4. The yellow arrow showing the laser polarization direction

The morphological characterization of ablated Si in acetone [SiNS1- figure 4.6(a)] and water [SiNS2- figure 4.6(b)] demonstrated the formation of HSFL with period of ~140 nm and ~105 nm evident from FESEM images, respectively. As per the image shown in figure 4.6, average particle sizes of ~40 nm (SiNS1) and ~55 nm (SiNS2) NCs were observed on the top of each NS. Figures 4.6(c) and 4.6(d) demonstrate FESEM images of the Si surface which was ablated in DCM (SiNC3) and chloroform (SiNC4), respectively. In these liquids, the structures were formed randomly and dissimilar to the LIPSS. These structures might have formed due differences in the liquid properties such as viscosity and surface tension. Moreover, there were aggregating NCs with cloud shape layer formed on the top of the randomly oriented structures which were upper part of the Si surface and no cloud type structures were observed underneath the Si surface. This could be a carbon layer

which was confirmed by Raman spectroscopy. There could be two reasons for the formation of aggregating NCs with cloud shape layer (a) possibly, short-term interaction of generated Si ions in the plasma plume with the C ions in the liquid medium resulted in formation of SiC NCs [56] (b) the reactivity of laser beam with carbon in surrounding liquid to form some carbon products like a layer around the Si NC. Orientation of these surface structures was parallel to the polarization of input laser beam in SiNS1 and SiNS2, and perpendicular to the polarization of input laser beam in SiNS3 and SiNS4. However, further detailed investigation is necessary to understand this behavior. Figure 4.7 represents the Raman spectra of NSs Si Substrates generated by ULA of Si in different liquids of acetone (SiNS1), water (SiNS2), DCM (SiNS3) and chloroform (SiNS4). The peaks were detected at 515, 516, 519 and 515 cm^{-1} which confirmed the formation of nano crystalline Si and one more peak was observed near 483 cm^{-1}, demonstrating the amorphization of substrates. As seen in the Raman spectra, two peaks were observed at 1350 cm^{-1} (D-band) and 1592 cm^{-1} (G-band) in both SiNS3 and SiNC4 and they confirmed that carbon was presented along with Si NCs.

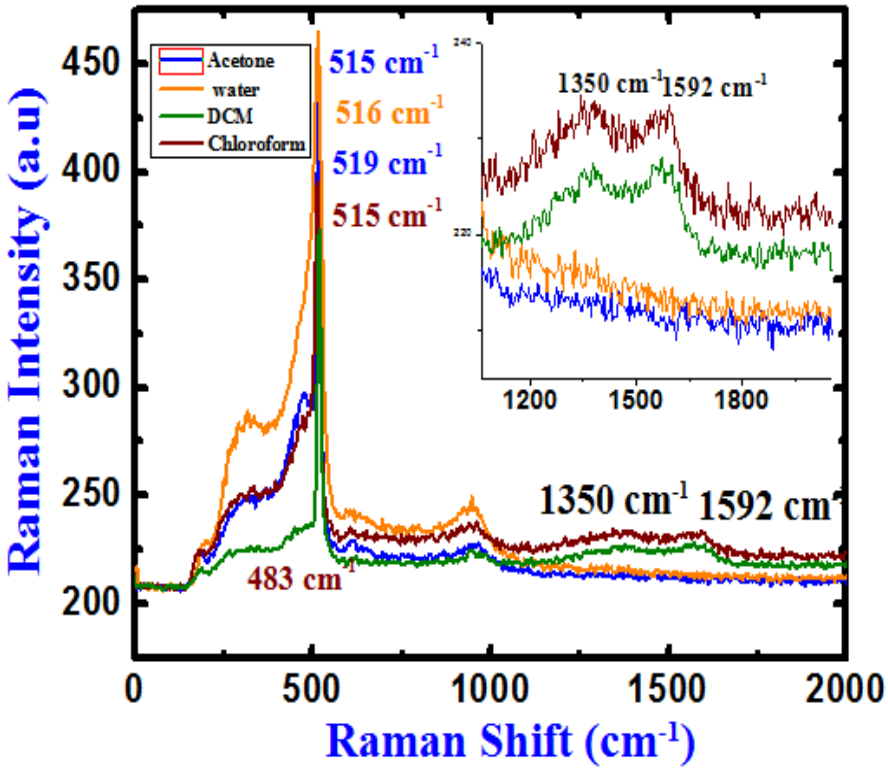

Figure 4.7 Raman spectra of nanostructure on the Si substrates illustrate amorphous peak around 483 cm^{-1} and asymmetric crystalline peak at (i) 515 cm^{-1} in SiNS1, (ii) 516 cm^{-1} in SiNS2, (iii) 519 cm^{-1} in SiNS3 and (iv) 515 cm^{-1} in SiNS4.Two carbon peaks at 1350 cm^{-1} and 1592 cm^{-1} in SiNS3 and SiNS4.

In summary, this study offered a comprehensive look at the elemental composition and size progress of Si NCs and Si NSs in four different liquid media. In the interaction of ultrafast laser with Si in acetone and water, we found HSFL structures with a spacing of ~140 nm in SiNS1 and ~105 nm in SiNS2, and NCs with characteristic size of ~9.5 nm (pure Si NCs) and ~20 nm (SiO_2 NCs) were observed in liquids SiNC1 and SiNC2, respectively. Additionally, a random cloud like submicron structures (SiNS3 and SiNS4) were found in chloride based liquid experiment and aggregated Si NCs in carbon matrix with mean size 45 nm and 42 nm in DCM (SiNC3) and chloroform (SiNC4). The elemental composition of NCs and NSs was confirmed by SAED, HRTEM and Raman spectroscopy. Formation of LIPSS and NCs in liquids could be ascribed to various mechanisms such as nonlinear effects, generating mechanical pressures, interference effects etc.

4.3. Fabrication of Si NMs using different pulse energies

4.3.1. Fabrication Process

Boron doped-type Si (100) target with very low resistivity (<0.005 Ω-cm) was cleaned in an ultrasonic cleaner with acetone. The target was submerged under acetone in a Pyrex cell and effective thickness of liquid layer above the target was ~7 mm. Complete details of the experiments are mentioned in chapter 2. The theoretical beam waist ($2\omega_0$) estimated at the focal point in air was ~40 μm. Typical range of pulse energies used was 10 μJ – 500 μJ and the input energy was controlled by combination of Brewster angle polarizer and half wave plate. The target was placed normal to the laser beam on a three dimensional motorized stage [Nano-direct] with a resolution of 25 nm. The X-Y stages were moved in such a way to draw periodic lines on the substrate with a separation of ~30 μm using scanning speeds of 0.3 mm/sec, 0.5 mm/sec in X and Y directions, respectively. Duration of each scan was ~40 minutes. Refractive index and thickness of liquid (acetone) layer play a crucial role in affecting the laser fluence at focus on the surface of target. Consequently, the position of focal plane shift beyond the target which modifies the beam waist on the target surface. Modification of beam waist results in deposition of less amount of fluence on the target. In the present case, focus was adjusted exactly on the surface of the target through compensating the shift caused by the presence of liquid layer following the procedure reported by Menendez-Manjon et al.[57] After completion of the scan,

prepared colloids were stored in air tightened glass bottles. The substrates were cleaned and preserved. To avoid the ambiguity, prepared colloidal Si NPs in acetone were designated as Si-500, Si-200, Si-100, Si-50, Si-25 and Si-10, and the corresponding substrates as SiS-500, SiS-200, SiS-100, SiS-50, SiS-25 and SiS-10 for pulse energies ~500 μJ, ~200 μJ, ~100 μJ, ~50 μJ, ~25 μJ and ~10 μJ, respectively.

4.3.2. TEM, HRTEM, SAED and EDAX characterizations of Si colloids

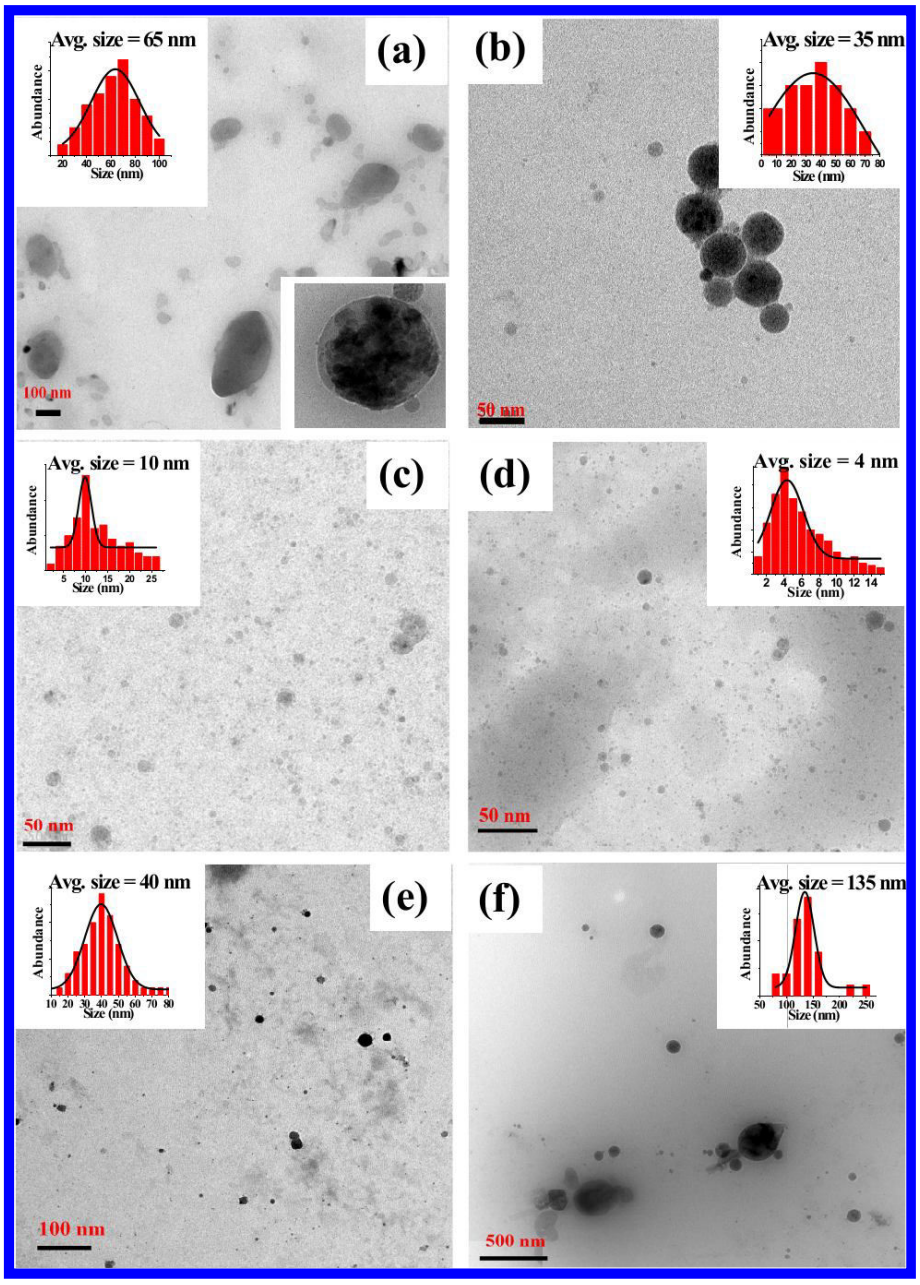

Figure 4.8 TEM images illustrating the Si NPs synthesized by fs laser ablation of bulk Si in acetone (a) Si-500 (inset bottom shows core-shell type Si NP) (b) Si-200 (c) Si-100 (d) Si-50 (e) Si-25 and (f) Si-10. Insets show their particle distribution plots.

Morphology and size distribution of the fabricated Si NPs were carried out by TEM measurements. From the TEM images presented in figure 4.8, the shape of the NPs was mostly spherical in nature and different size distributions were observed for different pulse energies. These images confirmed the formation of well dispersed spherical NPs in each case. Figure 4.8 represents the TEM images of colloidal Si NPs synthesized in acetone as a function of input fluence. The insets of this figure illustrate the histogram of size distribution with an average size ranging 20 - 100 nm in Si-500 [figure 4.8(a)], 5 – 70 nm in Si-200 [figure 4.8(b)], 2 – 25 nm in Si-100 [figure 4.8(c)], 2 - 15 nm in Si-50 [figure 4.8(d)], 15 – 80 nm in Si-25 [figure 4.8(e)] and 80 - 250 nm in Si-10 [figure 4.8(f)]. Gaussian fits of the histogram provided the average particle size of ~65 nm for Si-500, ~35 nm for Si-200, ~10 nm for Si-100, ~4 nm for Si-50, ~40 nm for Si-25 and ~135 nm for Si-10. Average size was observed to decrease as the pulse energy decreased from ~500 μJ to ~50 μJ [figure 4.8(d)]. However, the average size increased when the pulse energy was further decreased to ~10 μJ [figure 4.8(f)]. Size distributions and yield of NPs depend mainly on cavitation bubble dynamics arising from the target surface. The origin and complete dynamics of cavitation bubble followed by NPs fabrication are not clearly understood, especially in the ps/fs ablation case. From our knowledge and data from previous reports we could understand that low input energies generates a sustainable cavitation bubble of smaller size whereas at high input energies the cavitation bubble cannot sustain for long times. Consequently, in the latter case pressure developed across the bubble could have been less since it collapses instantaneously produceing agglomerates of large dimensions. However, in the former case, sustainability of bubble develops higher pressures and hence the collapse result in the formation of lower sized NPs.[58]

Figure 4.9 depicts the HRTEM image of a single Si nanoparticle (Si-50) exhibiting parallel Si lattice planes with an inter-planar separation of 3.29 A˚ (indicated with a white mark) corresponding to (200) lattice planes of Si.

Figure 4.10 illustrates the SAED pattern of colloidal Si NPs in (a) Si-500, (b) Si-200, (c) Si-100, (d) Si-50, (e) Si-25 and (f) Si-10. The SAED pattern demonstrated concentric rings corresponding to individual lattice planes. First three planes were considered for assignment in each pattern. The diffraction pattern for Si-500, Si-200,

Si-100 and Si-50 confirmed that most of the Si NPs possessed poly-crystalline nature and the pattern for Si-25 and Si-10 revealed single crystalline nature of the Si NPs. Figures 4.10 (a)-(f) illustrate SAED patterns and measured interplanar spacings agree very well with respective Si crystal planes in the literature. In addition to this, we observed one more lattice plane with a spacing of 1.59 Å, which agreed with SiO_2 (220) plane in Si-500 [figure 4.10 (a)] and 2.97 Å, which agreed with SiO_2 (110) plane in Si-200 [figure 4.10 (b)]. Insets of figure 4.10 (a) – 4.10 (f) demonstrate the EDAX spectra of colloidal Si NPs. The peaks associated with Si and Oxygen were observed in all cases (pulse energies) except for Si-50 and Si-100 samples. This confirmed that Si NPs were successfully generated without any impurities.

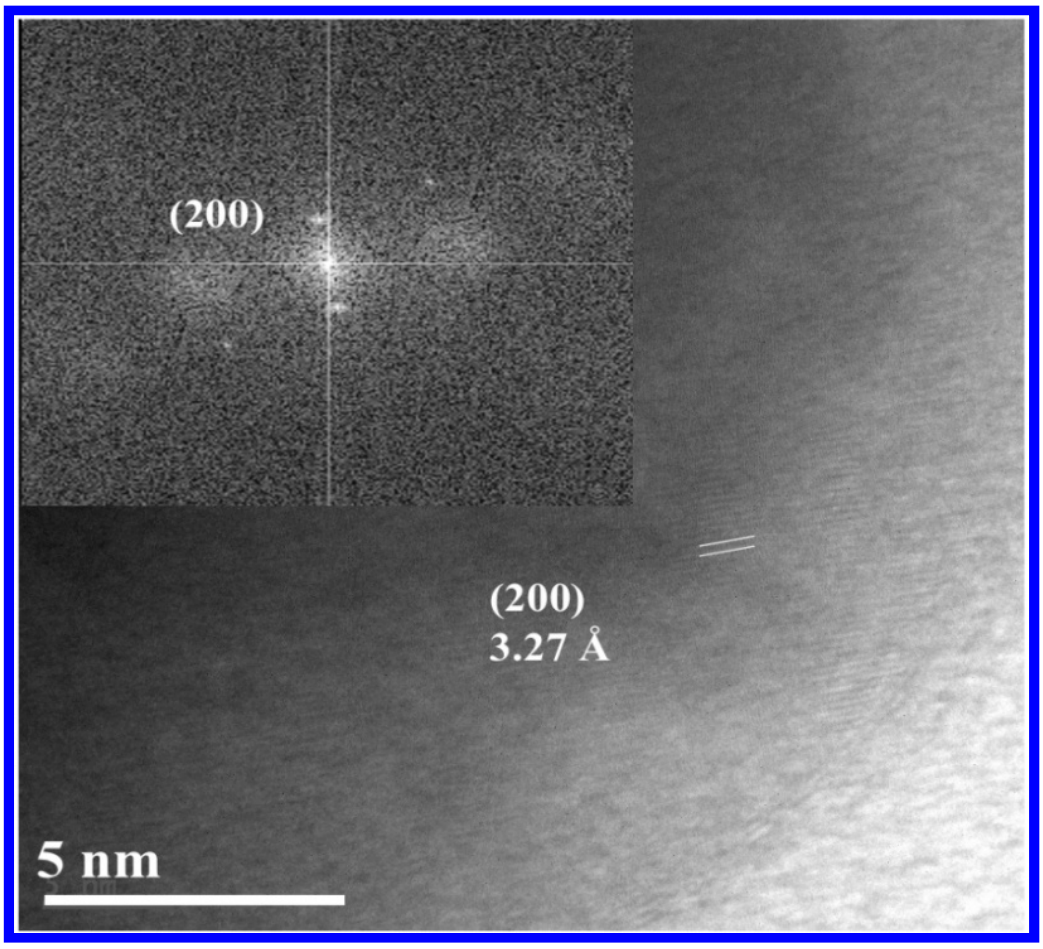

Figure 4.9 HRTEM image of the Si NP formed shows the clear view of lattice planes observed at a characteristic separation 3.27 A˚ which corresponding to the plane of Si lattice set (200) and inset shows its numerical electronic diffraction.

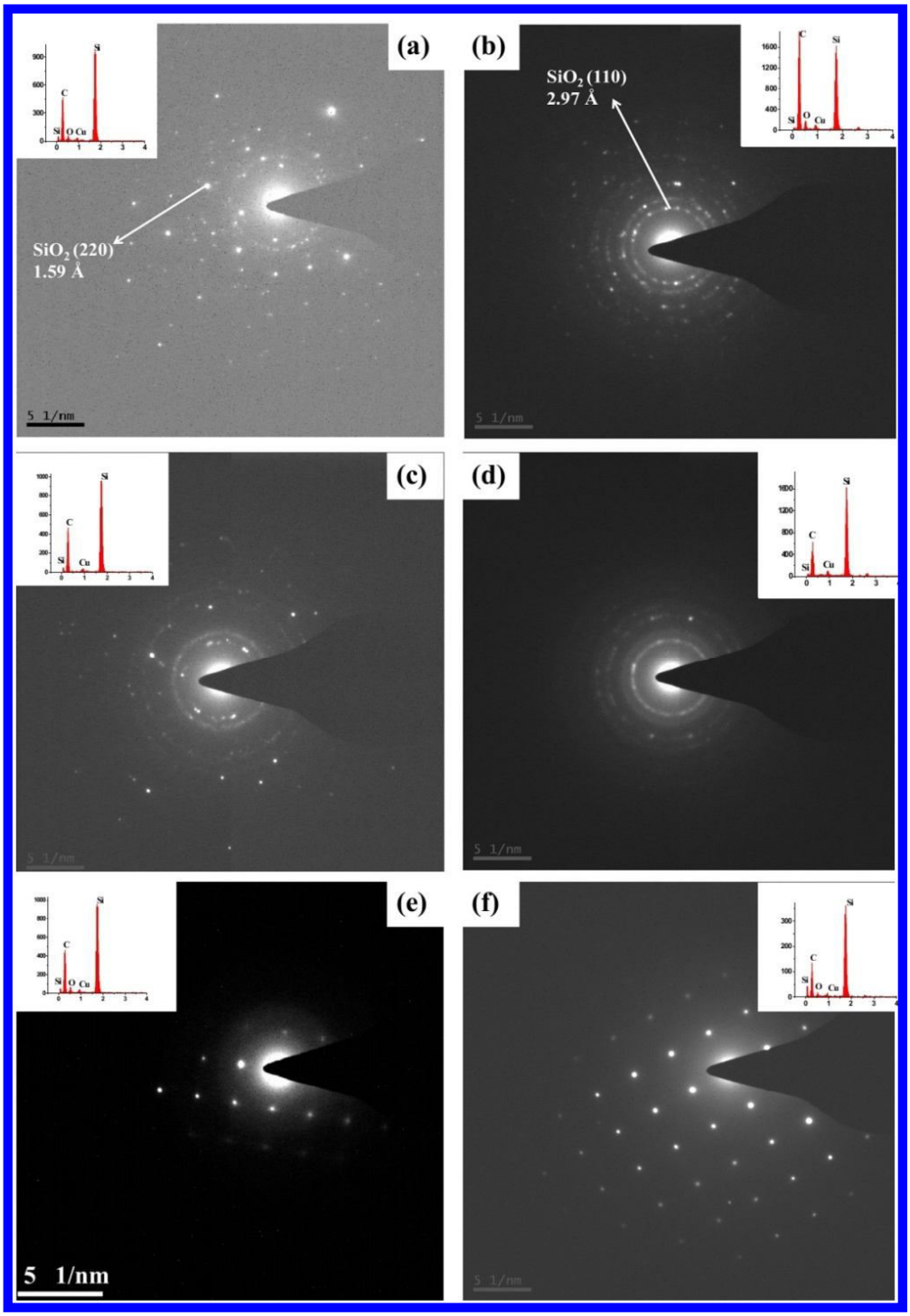

Fig. 4.10 SAED pattern illustrate Si NPs synthesized by fs laser ablation of bulk Si in acetone (a) Si-500 (b) Si-200 (c) Si-100 (d) Si-50 (e) Si-25 and (f) Si-10. Insets show their respective EDAX images.

4.3.3. Raman, UV-Vis and PL characterizations of Si colloids

Raman spectroscopy provides the crystalline/amorphous information of Si NPs. Figure 4.11 depicts the Raman spectra of Si-10, Si-25, Si-50, Si-100, Si-200 and

Si-500. Si-50, Si-100 and Si-200. These samples were observed to posses both amorphous and crystalline nature through the exhibition of 484 cm^{-1} as well as 512.3 cm^{-1} Raman signatures in the spectra. Similarly, Si-10, Si-25 and Si-500 exhibited crystalline phase through elevation of the 516.9 cm^{-1} mode, typical of nanocrystalline Si. To avoid confusion in peak positions, each peak in figure 4.11 is shifted vertically for clear comparison.

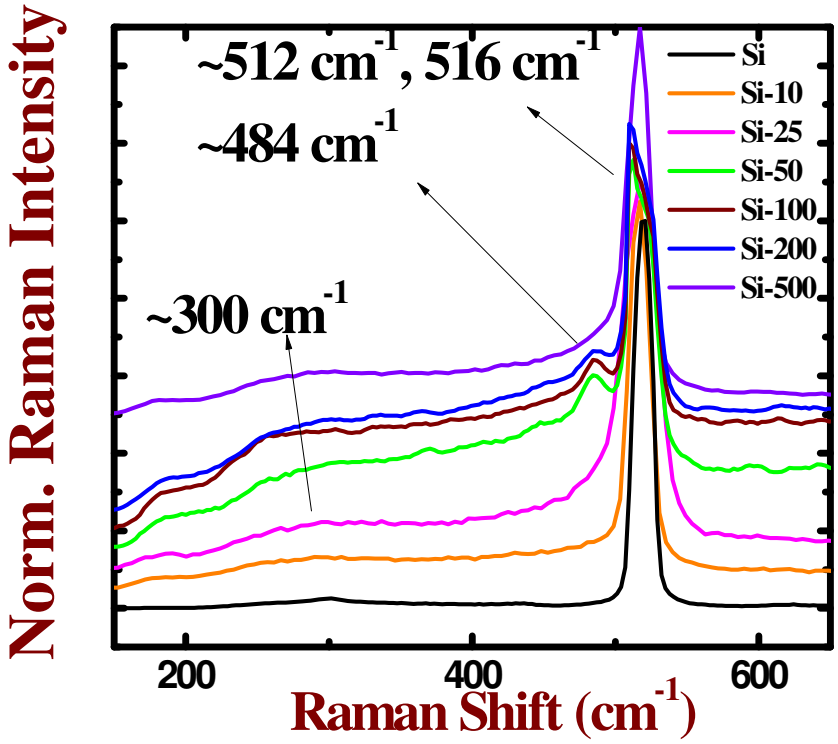

Figure 4.11 Raman spectra of Si NPs (were prepared in acetone) in (i) Si-500, Si-25 and Si-10 with crystalline peak around 516 cm^{-1}, (ii) Si-200, Si-100 and Si-50 with crystalline peak around 516 cm^{-1} and amorphous peak around 484 cm^{-1}, and (iii) bulk Si with crystalline peak 520 cm^{-1}.

From these plots the peak position, representing the crystallinity of Si NPs, was observed to shift towards lower wave-number region along with the broadening of Si crystalline peak, as the particle size decreased.[59-61] As evident from the Raman spectra (figure 4.11), signatures in the 470 cm^{-1} – 492 cm^{-1} region, a prominent amorphous peak was observed at 484 cm^{-1} for Si-200, Si-100, and Si-50. A sign of such phase was not observed for other Si NPs (Si-500, Si-25, and Si-10) and pure Si wafer. The peak position at 520.8 cm^{-1} (crystalline) of pure silicon wafer was taken as a reference for quantifying the peak shift observed in this study. The shift to lower wave-number region and strong asymmetry observed when the input energy

decreased from 500 μJ (Si-500) to 50 μJ (Si-50) could be from phonon confinement[62] in the nano-crystals and amorphous contribution (484 cm^{-1}). With further decrease in pulse energy from 50 μJ (Si-50) to 10 μJ (Si-10), lesser asymmetry was observed which could be due to low amorphous phase of Si NPs[63] and this, possibly, could be the reason for increased sizes of Si NPs. In the course of ablation beneath the liquid molten layer, Si is generally subjected to an abrupt cooling (of ~10^{13}-10^{15} K/s), which provokes re-solidification of the molten droplet. This kind of rapid cooling, and hence the solidification, leads to the observed amorphization. In general, two kinds of amorphization of Si NPs were observed by earlier groups: (a) core-shell type in which amorphous silicon (SiO_x) acts as shell on the core crystalline Si (b) complete amorphization of Si which is particular for the particle dimensions <10 nm.[64, 65]

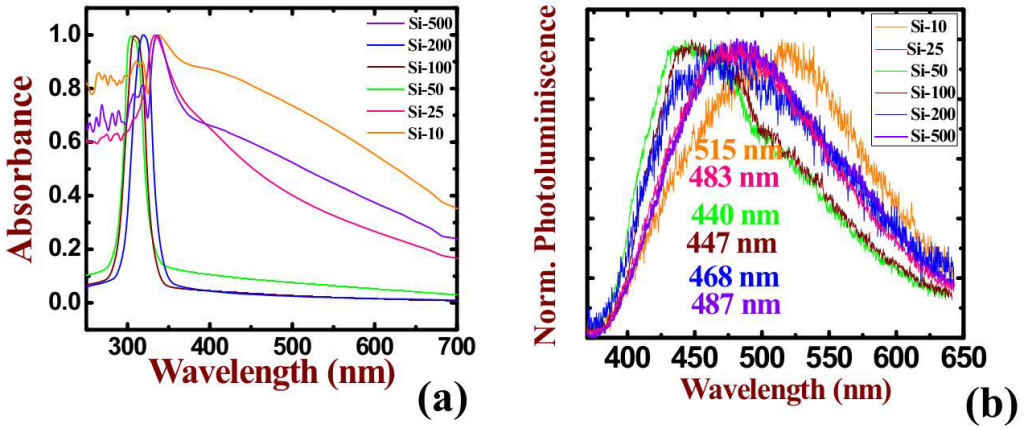

Figure 4.12 (a) UV-Vis absorption spectra of Si NPs (were prepared in acetone) in (i) Si-500 with shoulder peak at 336 nm (broad peak around 400 nm), (ii) Si-200 with shoulder peak at 316 nm, (iii) Si-100 with shoulder peak at 308 nm, (iv) Si-50 with shoulder peak at 304 nm, (v) Si-25 with shoulder peak at 338 nm and (vi) Si-10 shoulder peak 340 and strong broad peak ~420 nm and, (b) Photoluminescence spectra of Si NPs (were prepared in acetone) in (i) Si-500 with emission peak at 487 nm, (ii) Si-200 with emission peak at 468 nm, (iii) Si-100 with emission peak at 447 nm, (iv) Si-50 with emission peak at 440 nm, (v) Si-25 with emission peak at 483 nm and (vi) Si-10 emission peak at 515 nm.

The fabricated colloidal Si NPs possessed strong absorption band in the UV spectral region. Figure 4.12(a) illustrates the UV-Vis absorption spectra of Si NPs in acetone. A methodical blue shift was observed in peak position of absorption spectra corresponding to the decrement in average size of NPs which demonstrates that the band gap of NPs increased. Si NPs in Si-500 showed a strong absorption peak positioned at ~336 nm and a broad peak near 400 nm. When the pulse energy was decreased the peak position was blue shifted along with an increase in the peak intensity. Beyond certain increase in energy the position of absorption peak was red-

shifted (for larger particles). The shifted absorption peak positions were 316 nm (Si-200), 308 nm (Si-100), 304 nm (Si-50) and 338 nm (Si-25). In the case of Si-10, a broad continuous band between 340 - 800 nm (mean size of NPs was ~135 nm) with a broadened peak near ~420 nm was observed. The broad continuous band is attributed to the broad distribution in the sizes of fabricated NPs. The occurrence of UV band absorption for Si NPs with smaller size was reported earlier.[66] Intartaglia et al.[55] have studied the absorption band near 300 nm and attributed it to the carbon byproducts. PL measurements were carried out for the fabricated colloidal Si NPs by depositing them on glass slide (cover slip) and the results are presented in figure 4.12 (b). For the purpose of comparison, PL intensity was normalized at the peak position. Shifting of the PL peak position with respect to the average size of the Si NPs was observed and the data is plotted in figure 4.13. PL peak position was observed to have blue-shift for decreasing energies in the 500–50 μJ. However, it was red-shifted for decreasing energies in the 25–10 μJ range.

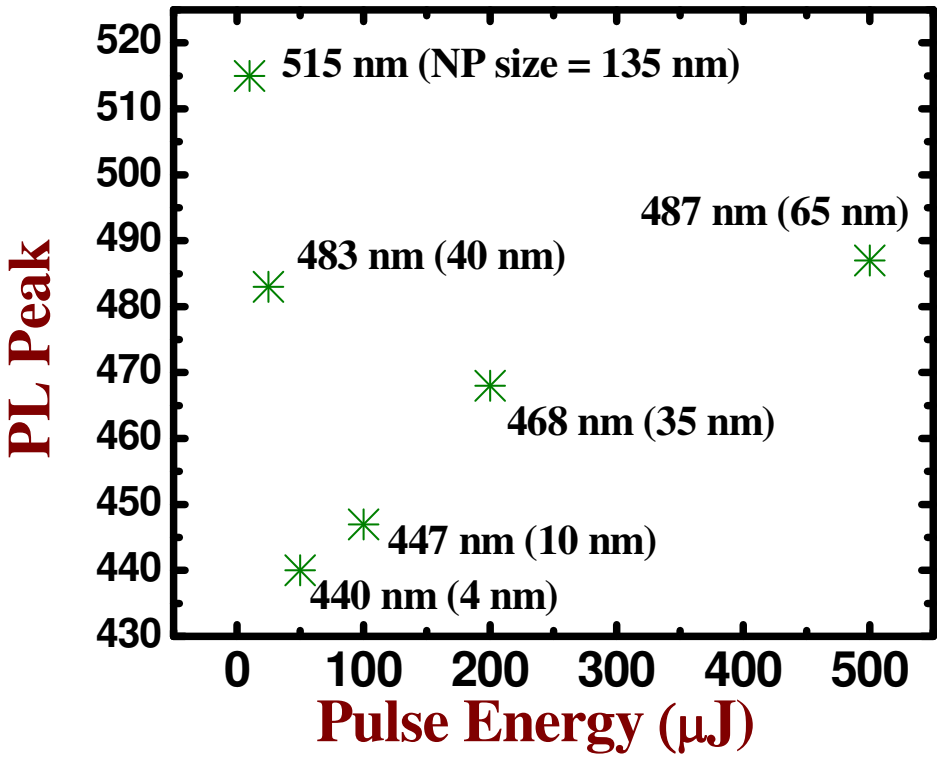

Figure 4.13 Plot depicts the tuning of emission peak of Si NPs were prepared in acetone with respect to the pulse energy.

It was observed that the position of the PL peak purely depended on the size of NPs. First, the position of the PL peak was tuned from 483 nm to 440 nm and later from 440 nm to 515 nm. The tuning range of PL spectrum from 483 nm to 440 nm is attributed to decrease in the size of NPs, which could be from quantum confinement effects.[67] PL observed in the spectral range of 440 nm - 515 nm can possibly, be attributed to increase in the size of particles, which is a result of diminishing quantum confinement effect. Many earlier reports discuss the PL of Si NPs in the visible spectral region of 400 nm–590 nm.[55,68-71]

4.3.4. FESEM and Raman characterization of Si Substrates

Inherent nature of the silicon NSs was evaluated by recording the Raman spectra. The crystalline (amorphous) nature of the NSs induced by fs pulses on Si substrate was characterized by a Raman spectrometer (WI-Tec instrument) using 532 nm excitation. Inspection of the Raman plots of the NSs on SiS-500, SiS-200, SiS-100, SiS-50, SiS-25 and SiS-10, and bulk Si illustrate a similar pattern to that of NPs and comparison of the plots in regions determined as crystalline and amorphous phases, as shown in figure 4.14. Raman spectra showed a shift towards lower wave number and broadening of 520 cm^{-1} peak for all NSs suggesting the presence of nano-crystalline Si. Furthermore, a prominent peak was also observed near 470 cm^{-1} which could be from amorphous nature of NSs formed on Si substrate for all the cases.

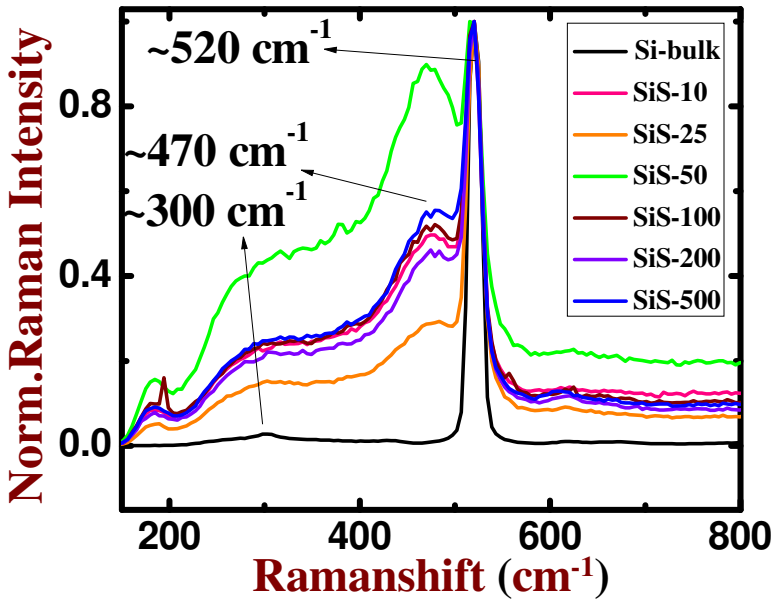

Figure 4.14 Raman spectra of HSFL (nanostructure) on the Si substrates depict asymmetric crystalline peak around 520 cm^{-1}, amorphous peak around 470 $cm^{-1}$and bulk Si with crystalline peak at 520 cm^{-1}.

The surface morphology of the ablated area is Si substrates were characterized by FESEM imaging. Figure 4.15 depicts the FESEM images of formed LIPSS with high spatial frequency (HSF) obtained by fs laser double/multiple line ablation on Si substrates (a) SiS-500 (b) SiS-200 (c) SiS-100 (d) SiS-50 (e) SiS-25 and (f) SiS-10. In some of the earlier studies,[72-82] few probable mechanisms were proposed to explain the production of low spatial frequency (LSF) LIPSS with period of nearly half of the laser wavelength and high spatial frequency (HSF) LIPSS with period much less than the incident wavelength of laser achieved via fs laser ablation.

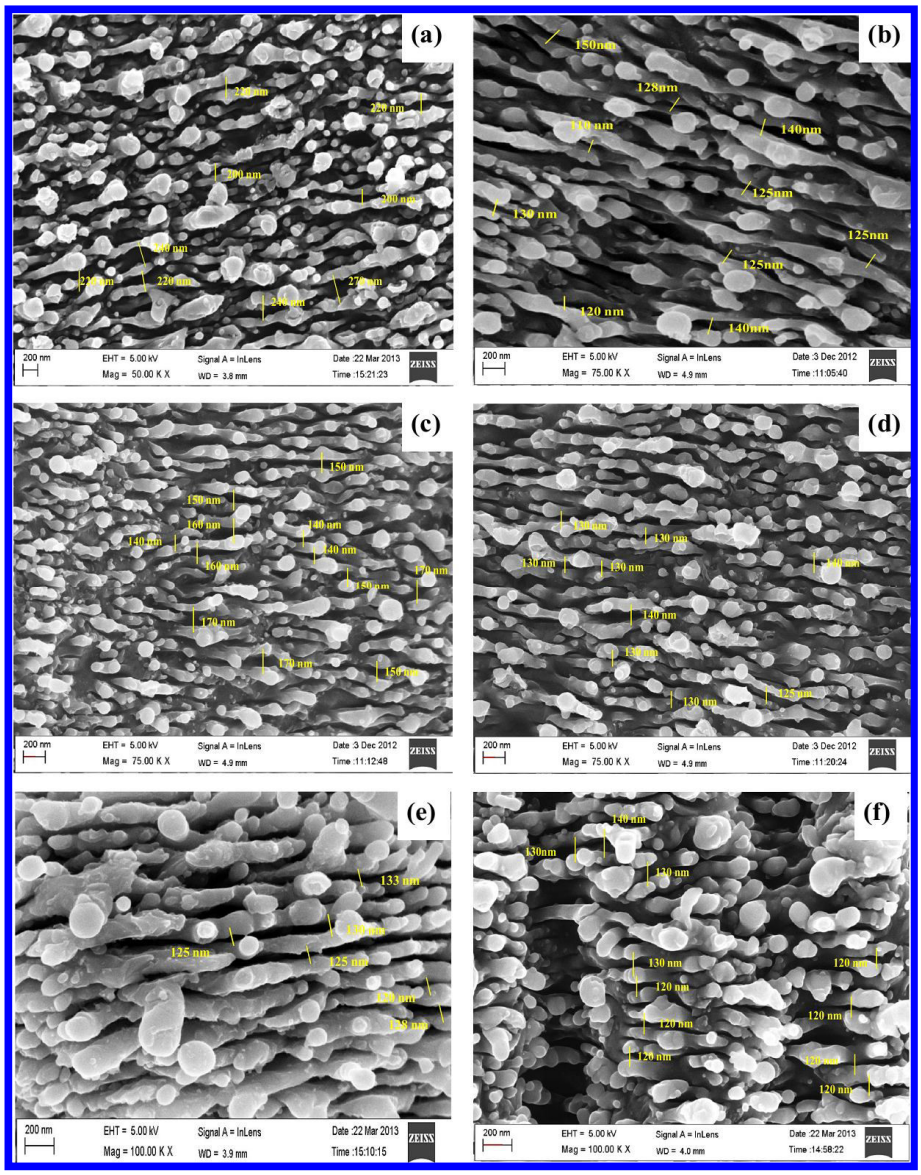

Figure 4.15 FESEM images of HSFL structures were fabricated on Si substrate by fs laser ablation of bulk Si in acetone (a) SiS-500 (b) SiS-200 (c) SiS-100 (d) SiS-50 (e) SiS-25 and (f) SiS-10 and, inset shows their respective high resolution images of 100 nm scale (except b). Laser polarization is parallel to the periodic structure.

Gemini et al.[77] reported self-organized structures with spatial periodicity of ~600 nm on Si using laser fluences just above the ablation threshold. They, however, irradiated the target with large number of pulses. The dependence of spatial periodicity on laser fluence was accounted by the parametric decay of laser light into surface plasma waves. Miyazaki et al.[78] investigated the fundamental mechanisms of fs laser induced periodic surface nanostructure formation in diamond like carbon and GaN and demonstrated that the nanostructures formation can indeed be controlled. Derrien et al.[79] investigated the mechanisms of ripple formation on Si using fs pulses and demonstrated the transient evolution of density of the excited free-carriers. Liu et al.[80] presented an interesting anisotropy phenomenon observed in fs laser processing of crystalline Si. Their results indicated that the surface patterning was dependent on the input laser polarization. In most of the earlier studies the mechanisms were discussed for ablation performed in air/vacuum whereas in our case we performed ablation in liquid.

In the present case HSF LIPSS (HSFL) with an increased periodicity was observed as the pulse energy decreased from 500 μJ -10 μJ and was confirmed from the FESEM images. A closer look at the images ascertained that grains of Si NP were observed on top of the HSFL. The mechanism of the formation of HSFL could be explained from the changes in physical properties of material, i.e. the complex refractive index. When Si absorbs fs pulses it results in the formation of quasi free electrons in the conduction band of solid Si in a time scale <1 ps (electron-phonon recreation time). Absorption of incident light by the valence band electrons and formation of quasi-free electronic states modify the complex refractive index (**n***) of the excited state and conduction band electron density (N_e). According to Drude model[81, 82] complex refractive index and conduction band electron density are related by the following equation

$$\mathbf{n}^* = \sqrt{n^2 - \frac{N_e\, e^2 \tau_d^2}{\varepsilon_0 m_{eff} m_e \left(\frac{4\pi^2 c^2}{\lambda^2}\tau_d^2 + 1\right)}} \qquad (4.1)$$

Where $e = 1.6\times10^{-19}$ c (charge of electron), $m_e = 9.11\times10^{-31}$ kg (electron mass), λ = wavelength of the laser (800 nm), $\varepsilon_0 = 8.85\times10^{-12}$ Fm^{-1}, c = velocity of light = 3×10^8 m/sec, n (= 3.675 at 800 nm) is the refractive index depends on wavelength (λ), m_{eff} = (1.18) effective mass of carriers occurred after the excitation and τ_d = (1 fs)

Drude damping time constant for excitation of silicon in fs regime and 1 ps in ps regime. These values have been taken from.[82,83] N_e is the electron density in the conduction band.

The estimation of electron density (N_e) in the conduction band under fs laser excitation of silicon, which depends on the laser fluence (intensity) along with the changes of linear and nonlinear absorption phenomena occurring after fs excitation were explained earlier by Harzic et al.[82] using the following relation

$$N_e \approx F\frac{\lambda(1-R)}{hc}\left[\alpha_0 + \beta F\frac{(1-R)}{2\sqrt{2\pi}\,t_p}\right] \tag{4.2}$$

where R = 0.329 (surface reflectivity of silicon parallel to the normal),[84] α_0, β are the linear and nonlinear absorption coefficients of silicon, respectively. Values of α_0 (0.85×10^3), β (1.8×10^{-9} cm/W) in the fs regime were considered from earlier reports.[85] Effective pulse duration estimated was (t_p) ~70 fs at the site of sample (effect of dispersion in pulse length when pulse passes through the media), **h** is the Planck's constant. **F** is the fluence of laser pulses is used to ablate the solid.

The observation of HSFL structures are explained on the basis of complex refractive index (n_e^*) and conduction band electron density (N_e). It was observed that N_e was directly related to the fluence of the laser on the target surface and n* directly depend on the N_e. From the theoretical base both n* and N_e were observed to have a direct dependence on the laser fluence. To investigate the effect of fluence on the formation of the HSFL on Silicon surface, effective spot size on the silicon target for different input energies was estimated experimentally. Microscopic images of laser drawn single lines on Silicon surface are shown in figure 4.16. Barcikowski et al.[86] demonstrated that the width of line structure on the ablated surface was considered as effective beam waist of laser beam. Figure 4.16 confirmed the differences in effective spot size (width of the line) even when the experiment was carried out at similar conditions of liquid level above the target and position of focus except the input laser pulse energy. From the figures 4.16 (a)-(f) the estimated spot sizes were ~60 µm, ~80 µm, ~100 µm, ~120 µm, ~270 µm, ~320 µm for the input energies of ~10 µJ, ~25 µJ, ~50 µJ, ~100 µJ, ~200 µJ, ~500 µJ.

Figure 4.17(a) depicts estimated spot sizes and corresponding fluences for each input laser energy. From the estimated spot size and number of pulses per spot and separation between the lines, we confirmed that double line ablation occurred on SiS-10, SiS-25 since the separation (30 µm) between the lines was almost half compared to spot size on target. Consequently, half of the ablated line was again exposed to the laser beam ablating it for the second time.[48] Effective number of pulses calculated [from ω(z)/d where d is pulse spacing] were ~400, ~540 per spot on SiS-10, SiS-25, respectively.

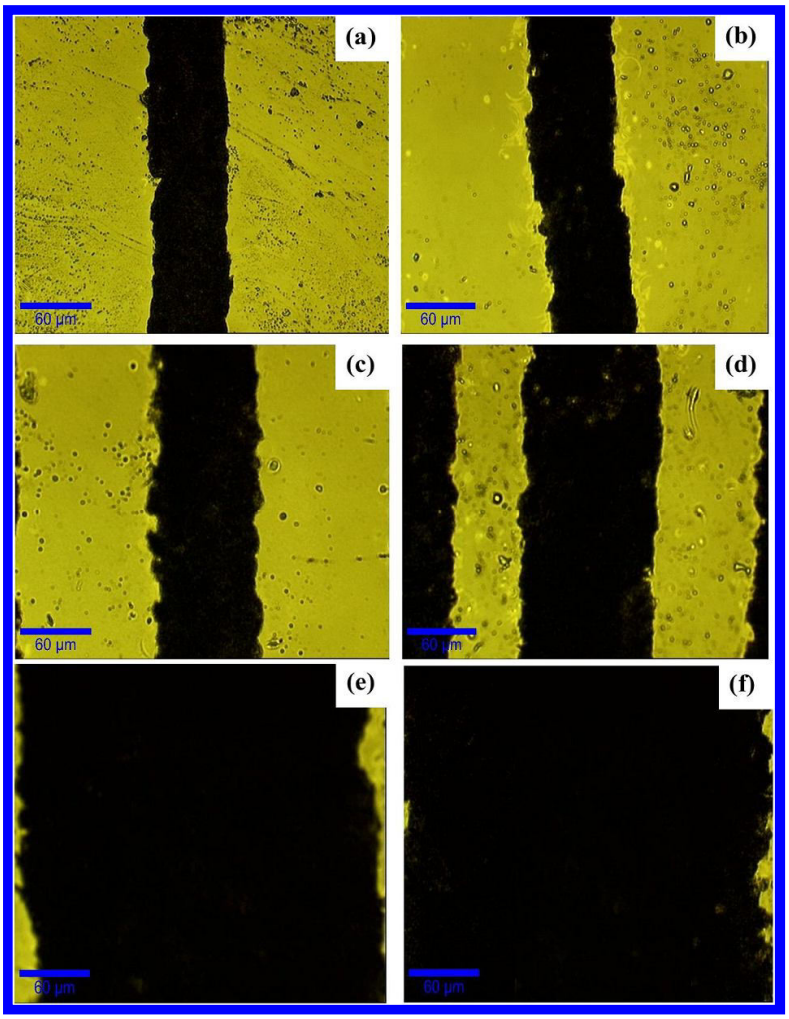

Figure 4.16 Microscopic images of the laser drawn single lines on Silicon surface with (a) 10 µJ, (b) 25 µJ, (c) 50 µJ, (d) 100 µJ, (e) 200 µJ and (f) 500 µJ

In the case of SiS-50, SiS-100, SiS-200 and SiS-500 the estimated spot size was much greater than the separation with corresponding fluences at the point of

ablation on target being ~0.35 J/cm^2, ~0.5 J/cm^2, ~0.63 J/cm^2, ~0.88 J/cm^2, ~0.34 J/cm^2, ~0.6 J/cm^2, respectively. Consequently, overwriting of the surface took place and the effective number of laser pulses per spot estimated was ~990, ~1600, ~4500, and ~5000, respectively. Based on the variations in scheme of ablation, effective fluence (spot size and number of pulses) on the Si surface, better yield of NPs [data presented in figures 4.8] was obtained in the case of Si-50 and Si-100. However, in the case of Si-10, Si-25, and Si-200, the estimated fluence was near to the ablation threshold of Silicon and, therefore, we could see the effect of mere ablation. In the case of Si -500 the dynamics of ablation were unexpected. As the estimated spot size (~320 μm) at this fluence on the Silicon surface was much greater than the given separation between the lines (30 μm), overwriting of the surface could have occurred many times up to the level of saturated ablation, which is designated as multiple ablation. Consequently, we could not get better yield of NPs and correlation between the theoretical and experimental estimations of periodicity failed. Similarly, differences in effective number of laser pulses on the silicon surface led to the production of nano-grating with an average periodicity on SiS-10, SiS-25, SiS-50, SiS-100, SiS-200 and SiS-500 being ~120 nm, ~125 nm, ~130 nm, ~155 nm, ~125 nm and ~230 nm, respectively. These values are in good agreement with the theoretically calculated ($\Lambda=\lambda/2n^*$) period of the gratings of ~121 nm, ~127 nm, ~134 nm, ~150 nm, ~120 nm and ~133 nm for the substrates SiS-10, SiS-25, SiS-50, SiS-100, SiS-200 and SiS-500, respectively. Theoretical estimation of the gratings periodicity was carried out by estimating the electron densities of the conduction band (N_e) and complex refractive index (n*), which are tabulated in table 4.1. Except the case of SiS-500, in other five cases we notice a strong coincidence between theory and experiment and the data is presented in figure 4.17 (b).

Furthermore, our experimental observation of grating periods for the substrates SiS-10, SiS-25, SiS-50, SiS-100, and SiS-200 were in excellent agreement with the prediction of the fluence dependence of grating period reported by Miyaji et al.[87] However, we observed disagreement in the case of SiS-500. The observed discrepancy for SiS-500 could be due to the large increment of beam spot on the target Si surface at that particular input pulse energy. We expect that large number of pulses per spot created a different grating period. From the experimental observations we could conclude that better yield of Si NPs with tunability of PL peak and self

organized HSFLIPSS fabricated through the ablation of Si in acetone occur below the input laser energy 500 µJ. We could observe good agreement between the theory and experiment for periodic Si NSs which were fabricated below the pulse energy 500 µJ.

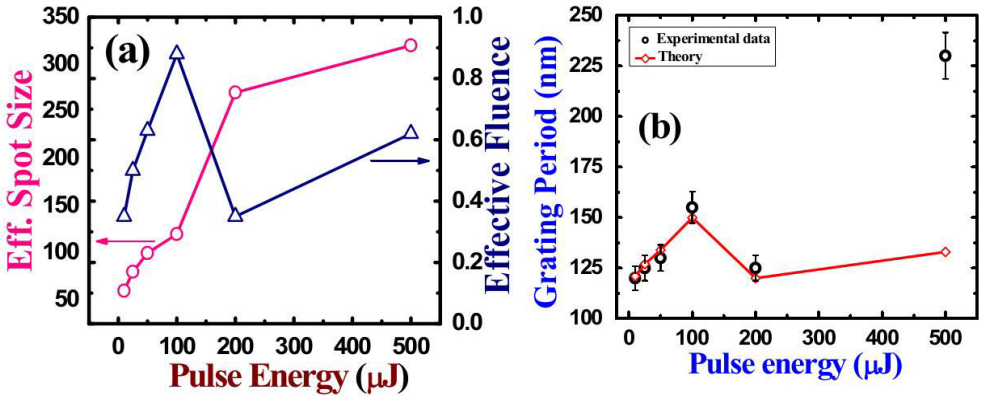

Figure 4.17 (a) Estimated spot sizes (pink-open circles) and corresponding fluences (blue-open triangles) for each input laser energies and, (b) comparison of experimental and theoretical data of HSFL grating period (Λ) as the function of pulse energy.

S. No.	Pulse energy (µJ)	Electron density (N_e) $\times 10^{21}$ cm^{-3}	Complex Refractive index (n*)
1	10	0.94	3.31
2	25	1.34	3.14
3	50	1.72	2.98
4	100	2.38	2.67
5	200	0.92	3.32
6	500	1.69	2.99

Table 4.1 Summary of calculated values of electron density (N_e) and complex refractive indices (n*)

4.4. Fabrication and Characterization of Si NSs with the different pulse numbers

A Ti: sapphire amplified laser (~2 ps) delivering the bandwidth limited pulses at 800 nm with 1 kHz repetition rate has been used for this study. Laser beam with p-polarized was allowed to focus (f = 25 mm) on the surface of polished single crystalline Si (1 mm thickness) which was positioned in quartz cell filled with acetone upto 5 mm length from the front surface of Si. A circular aperture with hard edges was inserted in between the lens and starting point of the laser with diameter of ~3 mm. The experiments were performed by scanning the substrates perpendicular to laser beam with different scanning speeds of 25-600 µm/sec to draw single line with fixed energy 50 µJ and corresponding fluence of 0.6 J/cm^2 near to the ablation threshold fluence. To avoid the confusion in addressing the fabricated Si

nanostructures with different scanning speeds were labeled as NS-1, NS-2, NS-3, NS-4, NS-5, NS-6, NS-7, NS-8, NS-9, NS-10, NS-11, NS-12 and NS-13 for corresponding scanning speeds of 600, 550, 500, 450, 400, 350, 300, 250, 200, 150, 100, 50 and 25 µm/sec, respectively.

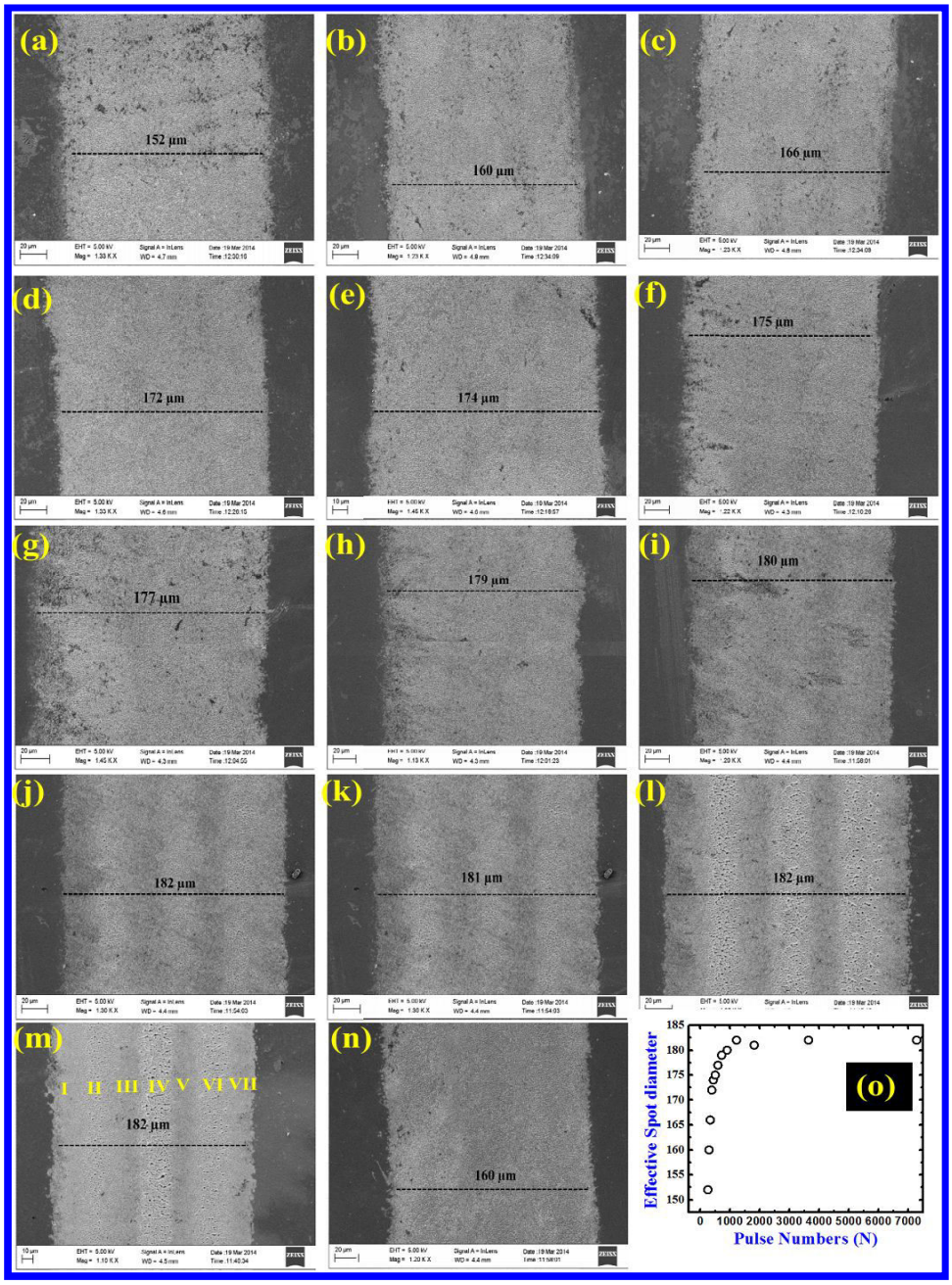

Figure 4.18 FESEM images of the diffracted laser beam drawn single lines on Silicon surface with different scanning speeds (a) NS-600 (600 µm/s), (b) NS-550, (c) NS-500, (d) NS-450, (e) NS-400, (f) NS-350, (g) NS-300, (h) NS-250, (i) NS-200,(j) NS-150, (k) NS-100, (l) NS-50 and (m) NS-25 (25 µm/s) and, (n) line drawn with un diffracted Gaussian beam with 25 µm/s and (o) depicts the estimated spot sizes with respect to the number of pulses incident (or) scanning speed.

Figure 4.18 illustrates the FESEM image of single lines drawn on Si wafer (a)-(m) using modified Gaussian profile due the effect of a hard aperture and structures obtained using unmodified Gaussian beam is illustrated in figure 4.18(n). As per the experimental data shown in figure 4.18(a)-(m), line structure illustrated a non-uniform distribution of the laser ablation and three strongly ablated regions were obtained on Si substrate. Observed differences in the degree of ablation (in the line structure) are tentatively assigned to the ablation due to the modified Gaussian beam profiles from hard edge aperture. These three strongly ablated regions probably represent the three peak intensities those could be due to modified Gaussian field by the hardedge aperture. A clear difference was observed in the strategy of the ablation carried out with normal Gaussian and a modified Gaussian from aperture.

Figures 4.18 (a)-(m) represent large scale FESEM images of the line structure drawn on the Si wafers with different scanning speeds from 600 to 25 μm/sec. A methodical increment in the effective spot diameter in the focal region was observed with respect to decreasing the scanning speed from 600 μm/sec (NS-600) to 150 μm/sec (NS-150) and the estimated sizes were ~152 μm for NS-600, ~160 μm for NS-550, ~166 μm for NS-500, ~172 μm for NS-450, ~174 μm for NS-400, ~175 μm for NS-350, ~177 μm for NS-300, ~179 μm for NS-250, ~180 μm for NS-200, and ~182 μm for NS-150. Saturation was observed from 150 μm/sec (NS-150) to N=25 μm/sec (NS-25) region and the measured spot diameter was ~182 μm. Moreover, the surface profile of the three ablated regions demonstrated a gradual change as a function of the scanning speeds from 600 to 25 μm/sec. To avoid the ambiguity, ablated region of Si target has been categorized into 7 sections. Among them, sections I, III, V and VII exhibited one kind of surface morphology and II, IV and VI illustrated different type of morphology as shown in figures 4.18(a)-(m). The spot diameter was estimated as ~160 μm (for N=7280) for the line structure i.e. drawn by an unmodified Gaussian beam as shown in figure 4.18(n).

Effective number of pulses confronted at the focal region [from $\omega(z)/d$ where d is pulse spacing] estimated were N = 253, 290, 332, 382, 435, 500, 590, 716, 900, 1213, 1810, 3640, and 7280 for the scanning speeds of 600, 550, 500, 450, 400, 350, 300, 250, 200, 150, 100, 50 and 25 μm/sec, respectively. From the estimated pulse

numbers, we believe that spot diameter increases as a function of effective pulse number per spot as shown in figure 4.18 (o).

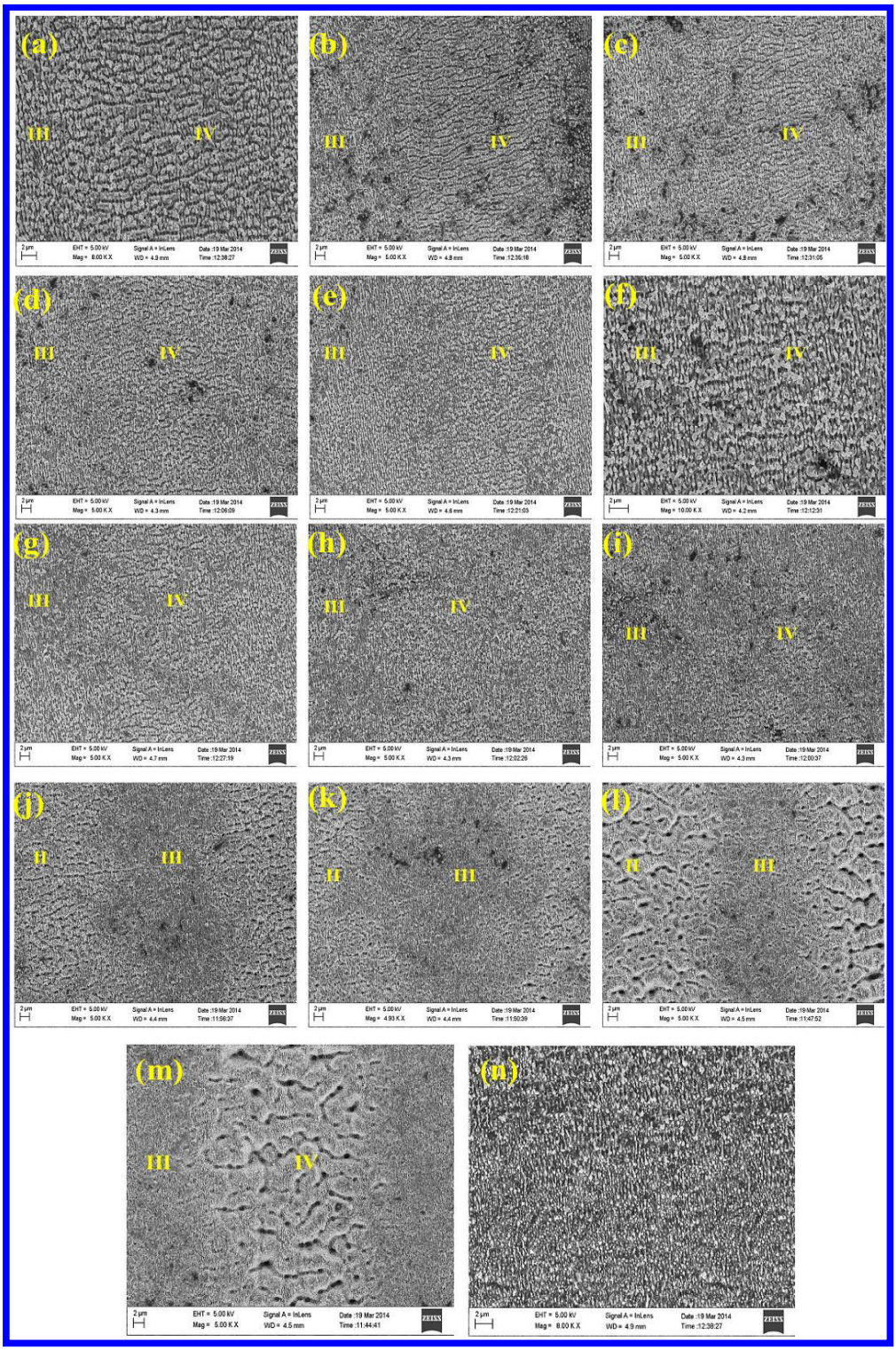

Figure 4.19 (a-m) FESEM images (2 µm scale) of laser induced micron size structures on Si surfaces fabricated using diffracted Gaussian beam (see sections II and IV) with different pulse numbers and (n) using pure Gaussian beam ablated one (no micro structures).

Figures 4.19(a)-(m) depict the FESEM images of Si surfaces ablated by different pulse shots at different scales. Among the various sections, we have considered the regions II and III (or) III and IV sections on ablated Si surface to diagnose the ablation phenomena. With less number of pulses per spot (N=253, NS-600), micron sized periodic structures were observed in II (or) IV section with a periodicity of ~2.2 μm [figure 4.19(a)] and the orientation of the micro-structures was perpendicular to the incident field polarization. Increasing the number of pulses per spot, periodicity of micro structures was decreased to ~1.7 μm at N=382 pulses (NS-450) as shown in figure 4.19(d). For, further increase in the pulses per spot upto N=590 [NS-300, figure 4.19(g)], the micro size structure turned into a structure with random orientation. At 590 pulses per spot (N=716 and 990 pulses), the microstructure evaporated gradually in section II (or) IV as illustrated in figure 4.19(h) and 4.19(i). Finally at very large number of pulses per spot(N=1213, 1810, 3640, and 7280) ablation demonstrated the formation of random microstructures on Si surface with a periodicity ~2 μm, ~2.3 μm, ~3 μm, and ~3.4 μm, respectively [figure 4.19(j) – 4.19(m)]. The polarization of the input field was perpendicular to the observed microstructures.

In this experiment, we studied another type of periodic surface structures [eg HFSL/LFSL] observed in sections I, III, V and VII. These HFSL/LFSL nanoripples are shown in figure 4.20 whose orientation was parallel to the input laser polarization. The formation of HSFL/LFSL structures was investigated using complex refractive index (n_e^*) and conduction band electron density (N_e). It is well known that N_e is directly related to the input fluence as well as reflectivity (R) and absorption coefficient (α) and, n* can be estimated from N_e. To study the influence of reflectivity and absorption coefficient on the formation of the HSFL/LFSL on the target surface, threshold fluence of the silicon ablation at diverse pulses per spot was estimated numerically. Moreover, surface rms roughness (d) of the silicon target was obtained experimentally, for varying number of pulses per spot. The threshold fluence after N pulses (F_{Nth}) [88] was calculated according to the equation $F_{Nth} = F_{1th} N^{S-1}$ where F_{1th} is the threshold fluence at single shot (or for single pulse) and S is the incubation factor (0.9-0.95 in ps regime). Moreover, reflectivity and absorption coefficient was retrieved from Beer lamber'ts law $R = 1-\ln (F_0/F_{Nth})$ and $\alpha = (1-R) / d$, respectively. The estimated F_{Nth}, R, α values after N pulses are summarized in table 4.2.

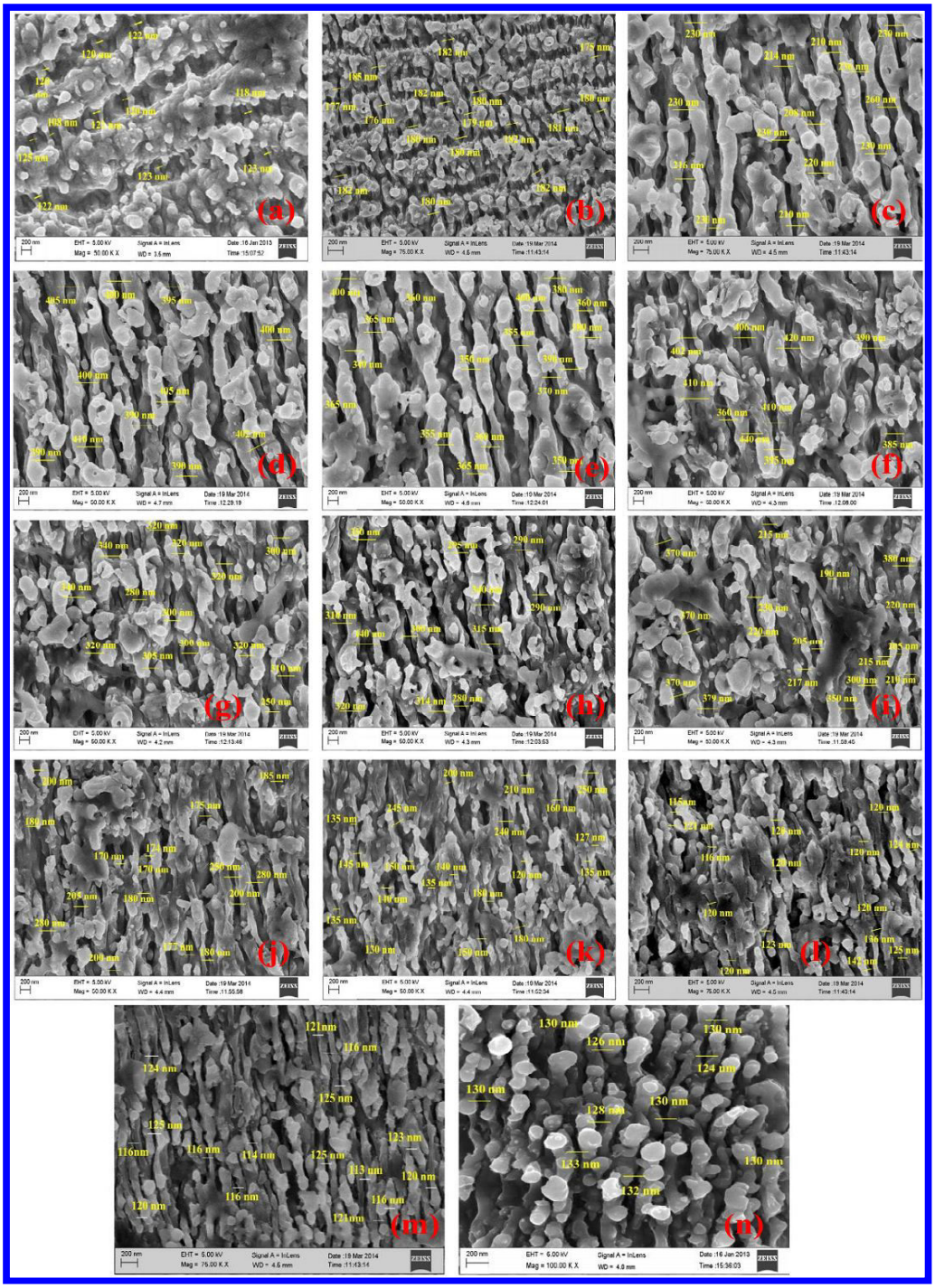

Fig. 4.20 FESEM images of HSFL/LSFL structures were fabricated on Si substrate by diffracted Gaussian beam ablation of bulk Si in methanol with different N = (a) 253, (b) 290, (c) 332, (d) 382, (e) 435, (f) 500, (g) 590, (h) 716, (i) 900, (j) 1213, (k) 1810, (l) 3640, and (m) 7280 and, (n) HSFL formation with un-diffracted Gaussian beam with N=7280

Figure 4.21 illustrates (a) calculated F_{Nth}, (b) reflectivity (R) and (c) absorption coefficient (α) at different number of pulses. According to various ablation

schemes using different effective pulse numbers on the surface of target, superior periodic ripples were [data presented in figures 4.20(a)-4.20(m)] obtained in the case of 253, 290, 332, 382, 435, 500, 590, 716, 900, 1810, 3640, and 7280 pulses at an average periodicity ~122 nm, ~180 nm, ~220 nm, ~395 nm, ~360 nm, ~410 nm, ~320 nm, ~300 nm, ~230 nm, ~180 nm, ~135 nm, ~120 nm and ~116 nm, respectively. Measured periodicities agreed well with the numerically calculated ($\Lambda=\lambda/2n^{*}$) periods of LIPSS of ~111 nm, ~186 nm, ~208 nm, ~400 nm, ~342 nm, ~390 nm ~354 nm, ~295 nm, ~216 nm, ~176 nm, ~132 nm, ~118 nm and ~114 nm for the substrates fabricated using different pulse numbers N=253, 290, 332, 382, 435, 500, 590, 716, 900, 1810, 3640, and 7280, respectively. The numerical estimation of HSFL/LSFL's periodicity was carried out by calculating the electron density (N_e) and complex refractive index (n*) using equations which were mentioned in section 4.2 and estimated values are summarized in table 4.2. We observed a better coincidence among the calculated values with experimentally measured ones and the data is demonstrated in figure 4.21(d).

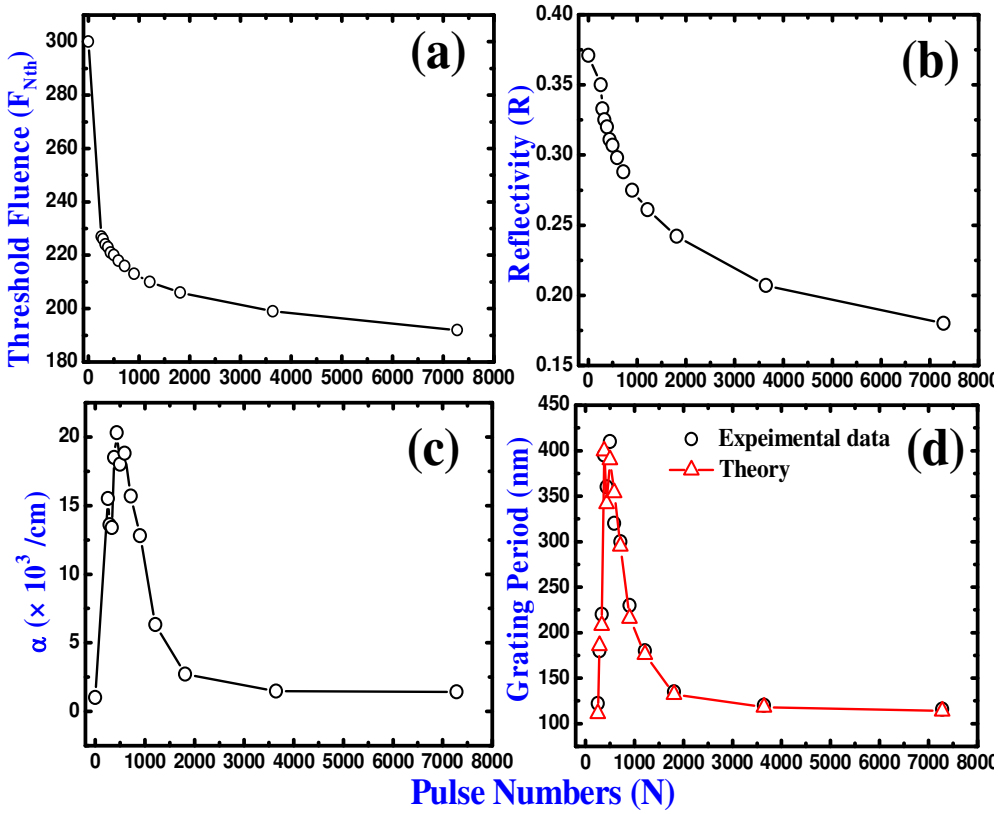

Figure 4.21 The estimated (a) threshold fluences (b) Reflectivity, (c) Absorption coefficient (α) and (d) comparison of experimental and theoretical data of HSFL/LSFL grating period (Λ) as the function of a pulse train of different shots.

Additionally, our experimental investigation on periodicity of the LIPSS was in good agreement with the prediction of dependence of periodicity on number of pulses per spot as reported by Miyaji et al.[87] However, in our experimental investigation, we observed lower number of pulses per spot demonstrated HSFL structure with a periodicity of ~111 nm (N=253) and HSFL structure with periodicity of ~114 nm at higher shots (N= 7280). In contrast, LSFL with periodicity ~ 400 nm - 390 nm was observed at moderate number of pulses per spot (N= 382 and N=500). From the experimental observations we could summarize that the self organized HSFLIPSS were fabricated via the ablation of Silicon in methanol with N=382 pulses and above ~590 pulses per spot on the silicon surface.

Pulse Number (N)	**F_{Nth} (mJ/cm^2)**	**R**	**α (×10^3/cm)**	**Electron density (N_e ×10^{22}/cm^3)**	**Complex Refractive index (n*)**
0	300	0.371	1	---	3.680
253	227	0.35	15.5	0.13	3.596
290	226	0.333	13.6	1.83	2.147
332	224	0.325	13.4	2.02	1.919
382	223	0.32	18.5	2.57	1.000
435	221	0.311	20.3	2.49	1.17
500	220	0.307	18	2.56	1.024
590	218	0.298	18.8	2.52	1.13
716	216	0.288	15.7	2.4	1.352
900	213	0.275	12.8	2.07	1.85
1213	210	0.261	6.32	1.72	2.26
1810	206	0.242	2.7	0.88	3.03
3640	199	0.207	1.47	0.41	3.39
7280	192	0.18	1.41	0.25	3.51

Table 4.2 Summary of numerically calculated values of ablation threshold fluences, reflectivity, absorption coefficient, electron density (N_e) and complex refractive indices (n*) after N pulses.

4.5. Summary

- Influence of the liquid media on the fabrication of Si NPs was investigated. From the experimental data we would conclude that pure Si NPs in acetone, SiO_2 NPs in water, Si-C NPs in DCM and Si-C NPs in chloroform and different sizes were observed. The presence of carbon was confirmed by Raman spectral data. Si colloids in different media illustrated different PL peaks in the UV region which could be due to elemental composition of Si NPs. The laser ablation of Si target in the presence of acetone and water revealed an optimum fabrication of NPs with smaller dimensions and better yield along with well periodic surface substrates than in other two liquids.
- Dependence of yield of the Si NPs, periodicity of the produced HSFLIPSS on the different input laser energy in the process of fs ablation of Si in acetone was investigated systematically through the estimation of effective spot size on the target and corresponding fluences. Size dependent tunability of the PL peak position of the Si NPs was discussed in detail. Complex refractive index and electron density in conduction band were estimated from the effective fluence and theoretically estimated period of gratings agreed well with the experimentally observed periodicity for the substrates SiS-10, SiS-25, SiS-50, SiS-100, and SiS-200 except for SiS-500. Present set of experiments revealed that to obtain a better yield of the Si NPs along with a superior tunability of the PL peak and self organized HSFLIPSS, ablation of Silicon in acetone should be performed below input laser energy of 500 μJ.
- Ablation under the influence of number of pulses with modified Gaussian beam generated by passing it through a hardedge aperture was carried out to fabricate periodic surface structures with periods of ~λ/6-λ/2. Complex refractive index and electron density in conduction band were estimated from estimated threshold fluence of the material at different number of pulses with constant input fluence and theoretically estimated period of gratings were in good agreement with the experimentally observed periodicity.

References

1. L. Pavesi, L. Dal Negro, C. Mazzoleni, G. FranzoÁ, and F.Priolo, Nature, **408**, 440 (2000).
2. J. W. Robert, I. B. George, A. A. Harry, Nat. Mater. **4**, 143 (2005).
3. V. K. Prashant, J. Phys. Chem. C., **112**, 18737 (2008)
4. Q. Dai, C.E. Duty, and M. Z. Hu, Small **6**, 1577 (2010).
5. A.H. Mueller, M.A. Petruska, M. Achermann, D.J. Werder, E.A. Akhadov, D.D. Koleske, M. A. Hoffbauer, V.I. Klimov. Nano Lett. **5**, 1039 (2005).
6. J. H. Park, L. Gu, G. von Maltzahn, E. Ruoslahti, S. N. Bhatia, and M. J. Sailor, Nat. Mater. **8**, 331 (2009).
7. Y. He, Z. H. Kang, Q. S. Li, C. H. A. Tsang, C. H. Fan, S.T. Lee, Angew. Chem., Int. Ed., **48**, 128 (2009).
8. P. Bettotti, M. Cazzanelli, L. Dal Negro, B. Danese, Z. Gaburro, C. J. Oton, G.Vijaya Prakash, and L. Pavesi, J. Phys.: Cond. Matter **14**, 8253 (2002).
9. V. Švrček, H. Fujiwara, and M. Kondo, Acta Materialia **57**, 5986 (2009).
10. D. Kovalev, E. Gross, N. Künzner, F. Koch, V. Yu Timoshenko, and M. Fujii, Phys. Rev. Lett. **89**, 137401 (2002).
11. V. Chirvony, A. Chyrvonaya, J. Ovejero, E. Matveeva, B. Goller, D. Kovalev, A. Huygens, and P. de Witte, Adv. Mater. **19**, 2967 (2007).
12. N. Zurauskiene, S. S. Asmontas, A. Dargys, J. Kundrotas, G. Janssen, E. Goovaerts, S. Marcinkevicius, P. M. Koenraad, J. H. Wolter, R. P. Leon, Solid State Phenom., **99**, 99-108 (2003).
13. V. N. Lutskii, Phys. Status Solidi A. **1**, 199 (1970).
14. Manasreh, O. Semiconductor Hetero junctions and Nanostructures. New York: McGraw Hill, **2005**.
15. B. Delley and E. F. Steigmeier, Phys. Rev. B **47**, 1397 (1993).
16. Serdar Öğüt, James R. Chelikowsky, and Steven G. Louie, Phys. Rev. Lett. **79**, 1770 (1997).
17. G. Ledoux, J. Gong, F. Huisken, O. Guillois, and C. Reynaud, Appl. Phys. Lett. **80**, 4834 (2002).
18. X. Y. Chen, Y. F. Lu, Y. H. Wu, B. J. Cho, M. H. Liu, D. Y. Dai, and W. D. Song, J. Appl. Phys. **93**, 6311 (2003).
19. Clemens Burda, Xiaobo Chen, Radha Narayanan, and Mostafa A. El-Sayed, Chem. Rev. **105**, 1025 (2005).
20. G. Vijaya Prakash, M. Cazzanelli, Z. Gaburro, L. Pavesi, F. Iacona, G. Franzò, and F. Priolo, J. Appl. Phys **91**, 4607 (2002).
21. S. Vijayalakshmi, H. Grebel, Z. Iqbal, and C. W. White, J. Appl. Phys. **84**, 6502 (1998).
22. P. Figliozzi, L. Sun, Y. Jiang, N. Matlis, B. Mattern, M. C. Downer, S. P. Withrow, C. W. White, W. L. Mochán, and B. S. Mendoza, Phys. Rev. Lett. **94**, 047401 (2005).
23. I. Ab Rahman and V. Padavettan, J. Nanomat. **2012**, 15 (2012).
24. A. J. Kenyon, P. F. Trwoga, C. W. Pitt, and G. Rehm, J. Appl. Phys. **79**, 9291 (1996).
25. X. Y. Chen, Y. F. Lu, L. J. Tang, Y. H. Wu, B. J. Cho, X. J. Xu, J. R. Dong, and W. D. Song, J. Appl. Phys. **97**, 014913 (2005).
26. M. Benyoucef, M. Kuball, J. M. Sun, G. Z. Zhong, and X. W. Fan, J. Appl. Phys. **89**, 7903 (2001).

27. Prajakta S. Chaudhari, Tejashree M. Bhave, D. Kanjilal, and S. V. Bhoraskar, J. Appl. Phys. **93**, 3486 (2003).
28. W. L. Liong, S. Sreekantan, S. D. Hutagalung World Academy of Science, Engineering and Technology, **59**, 419 (2009).
29. I Umezu, H Minami, H Senoo, and A Sugimura, J. Phys. Conf. Ser **59**, 392 (2007).
30. Chih-Chia Huang, Kuei-Yi Chuang, Chin-Jie Huang, Tzu-Ming Liu, and Chen-Sheng Yeh, J. Phys. Chem. C **115**, 9952 (2011).
31. V. Švrček, T. Sasaki, Y. Shimizu, and N. Koshizaki, Appl. Phys. Lett. **89** 213113 (2006).
32. Xi-Wen Du, Wen-Jing Qin, Ying-Wei Lu, Xue Han, Ying-Song Fu, and Sheng-Liang Hu, J. Appl. Phys. **102**, 013518 (2007).
33. N. Shirahata, M. R. Linford, S. Furumi, L. Pei, Y. Sakka, R. J. Gates, and M. C. Asplund, Chem. Commun. **31**, 4684 (2009).
34. V. Švrček, T. Sasaki, R. Katoh, Y. Shimizu, and N. Koshizaki, Appl. Phys. B: Laser Opt. **94**, 133 (2009).
35. N. G. Semaltianos, S. Logothetidis, W. Perrie, S. Romani, R. J. Potter, S. P. Edwardson, P. French, M. Sharp, G. Dearden, and K. G. Watkins, J Nanopart Res **12**, 573 (2010).
36. D M Popovic, J S Chai, A A Zekic, M Trtica, M Momcilovic, and S Maletic, Laser Phys. Lett. **10**, 026001 (2013).
37. S. Yang, W. Cai, H. Zhang, X. Xu, and H. Zeng, J. Phys. Chem. C, **113**, 19091 (2009).
38. S. Yang, W. Cai, G. Liu, H. Zeng, and P. Liu, J. Phys. Chem. C **113**, 6480 (2009).
39. F. Chen, D. Zhang, Q. Yang, J. Yong, G. Du, J. Si, F. Yun, and X. Hou, ACS Appl. Mater. Interfaces **5**, 6777 (2013).
40. P. Blandin, K. A. Maximova, M. B. Gongalsky, J. F. Sanchez-Royo, V. S. Chirvony, M. Sentis, V. Y. Timoshenko, and A. V. Kabashin, A*nal. Chem.* B **84**, 3945 (2012).
41. D. Tan, Z. Ma, B. Xu, Y. Dai, G. Ma, M. He, Z. Jin, and J. Qiu, Phys. Chem. Chem. Phys. **13**, 20255 (2011).
42. R. Intartaglia, G. Das, K. Bagga, A. Gopalakrishnan, A. Genovese, M. Povia, E. Di Fabrizio, R. Cingolani, A. Diaspro, and F. Brandi, Phys. Chem. Chem. Phys. **15**, 3075 (2013).
43. B. Sallé, O. Gobert, P. Meynadier, M. Perdrix, G. Petite, and A. Semerok, Appl. Phys. A **69**, S381 (1999).
44. Y.V. Afanasiev, B. N. Chichkov, V. A. Isakov, A. P. Kanavin, and S. A. Uryupin, J Russ Laser Res **20**, 189 (1999).
45. D. von der Linde, K. Sokolowski-Tinten, and J. Bialkowski, Appl. Surf. Sci. **109–110** (0), 1 (1997).
46. R. Intartaglia, K. Bagga, M. Scotto, A. Diaspro, and F. Brandi, Opt. Mater. Exp. **2** (5), 510 (2012).
47. R. Intartaglia, K. Bagga, F. Brandi, G. Das, A. Genovese, E. Di Fabrizio, and A. Diaspro, J. Phys. Chem. C. **115**, 5102 (2011).
48. P.G. Krishna, S. Hamad, S. P. Tewari, S. Sreedhar, and S.V. Rao, J. Appl. Phys. **113**, 073106 (2013).
49. P. M. Fauchet, and A. E. Siegman, Appl. Phys. Lett. **40**, 824 (1982).
50. J. E. Sipe, J. F. Young, J. S. Preston, and H. M. Vandriel, Phys. Rev. B. **27**, 1141 (1983).

51. M. Huang, F. Zhao, Y. Cheng, N. Xu, and Z. Xu, ACS Nano **3**, 4062 (2009).
52. O. Varlamova, F. Costache, J. Reif, and M. Bestehorn, Appl. Surf. Sci. **252,** 4702 (2006).
53. A. Borowiec, and H. K. Haugen, Appl. Phys. Lett. **82**, 4462 (2003).
54. P.G. Krishna, S. Hamad, S. Sreedhar, S. P. Tewari, and S.V. Rao, Chem. Phys. Lett. **530**, 93 (2012).
55. R. Intartaglia, K. Bagga, A.vGenovese, A. Athanassiou, R. Cingolani, A. Diaspro, and F. Brandi, Phys. Chem. Chem. Phys. **14**, 15406 (2012).
56. K. Abderrafi, R. Garcia-Calzada, J. F. Sanchez-Royo, V. S. Chirvony, S. Agouram, R. Abargues, R. Ibanez and J.P. Martinez-Pastor, J. Phys. D. Appl. Phys. 46, 135301 (2013)
57. A. Menendez-Manjon, P. Wagener, and S. Barcikowski, J. Phys. Chem. C. **115**, 5108 (2011).
58. J. H. David, P. G. Costas and Y. C. Tae, J. Appl. Phys. **99**, 083101(2006).
59. G. Faraci, S. Gibilisco, P. Russo, A. R. Pennisi, and S. L. Rosa, Phys. Rev. B. **73**, 033307 (2006).
60. M. N. Islam, A. Pradhan, S. Kumar, J. Appl. Phys. **98**, 024309 (2005).
61. Z. X. Zhaoa, R. Q. Cui, F. Y. Meng, B. C. Zhao, H. C. Yu, and Z. B. Zhou, Mater. Lett. **58**, 3963 (2004).
62. N. Saxena, P. Kumar, A. Avinash, and K. Dinakar, Phys. Status Solidi. A. **209**, 283(2012).
63. W. Zhang, S. Zhang, Y. Liu, T. Chen, J. Cryst. Growth. **311**, 1296 (2009).
64. T. E. Glover, J. Opt. Soc. Amer. B **20**, 125 (2003).
65. Y. Kanemitsu, I. Nakada, and H. Kuroda, Appl. Phys. Lett. **47**, 939 (1985).
66. M. Rosso-Vasic, E. Spruijt, Z. Popovic, K.n Overgaag, B. van Lagen, B. Grandidier, D. Vanmaekelbergh, D. Dominguez-Gutierrez, L. De Cola, and H. Zuilhof, J. Mater. Chem. **19**, 5926 (2009).
67. D. Kovalev, H. Heckler, G. Polisski, and F. Koch, Phys. Status. Solidi. **215**, 871 (1999).
68. V. Svrcek, D. Mariottiand, and M. Kondo, Opt. Exp. **17**, 520 (2009).
69. M. Dasog, Z. Yang, S. Regli, Tonya M. Atkins, A. Faramus, Mani P. Singh, E. Muthuswamy, Susan M. Kauzlarich, Richard D. Tilley, and Jonathan G. C. Veinot, ACS Nano **7**, 2676 (2013).
70. A. Sabri, A. K. Okyay, O. Bulend, J. Phys. Chem. C **116**, 3432 (2012).
71. N. Mansour, A. Momeni, R. Karimzadeh, and M. Amini, Phys. Scr. **87**, 035701 (2013).
72. J. S. Preston, H. M. van Driel, and J. E. Sipe, Phys. Rev. B **40**, 3942 (1989).
73. R.Wagner, J. Gottmann, A. Horn, and E. W. Kreutz, Appl. Surf. Sci. **252**, 8576 (2006).
74. Ronan Le Harzic, H. Schuck, D. Sauer, T. Anhut, I. Riemann, and K. König, Opt. Exp. **13**, 6651 (2005).
75. G. Miyaji, and K. Miyazaki, Appl. Phys. Lett. **103**, 071910 (2013).
76. K. Sokolowski-Tinten, J. Bialkowski, A. Cavalleri, D. von der Linde, A. Oparin, J. Meyer-ter-Vehn, and S. I. Anisimov, Phys. Rev. Lett **81**, 224 (1998).
77. L. Gemini, M. Hashida, M. Shimizu, Y. Miyasaka, S. Inoue, S. Tokita, J. Limpouch, T. Mocek, and S. Sakabe J. Appl. Phys. **114**, 194903 (2013)
78. K. Miyazaki and G. Miyaji, Appl. Phys. A **114**, 177 (2014).
79. T. J.-Y. Derrien, T. E. Itina, R. Torres, T. Sarnet, and M. Sentis, J. Appl. Phys. **114,** 083104 (2013).
80. P. Liu, L. Jiang, J. Hu, W. Han, and Y. Lu, Opt. Lett.**38**, 1969 (2013).

81. K. Sokolowski-Tinten, and D. von der Linde, Phys. Rev. B, **61**, 2643 (2000).
82. R. Le Harzic, D. Dörr, D. Sauer, F. Stracke, and H. Zimmermann, Appl. Phys. Lett. **98**, 211905 (2011).
83. R. A. Ganeev, D. Y. Lei, C. Hutchison, T. Witting, F. Frank, W. A. Okell, T. R. Roschuk, S. A. Maier, J. W. G. Tisch, and J. P. Marangos, Appl. Phys. A **112**, 457 (2013).
84. Handbook of Optical Constants of Solids, edited by E. D. Palik (Academic, Orlando, FL, 1985)
85. A. J. Sabbah, and D. M. Riffe, Phys. Rev. B **66**, 165217 (2002).
86. S. Barcikowski, A. Menéndez-Manjón, B. Chichkov, M. Brikas, and Gediminas Račiukaitis, Appl. Phys. Lett. **91**, 083113 (2007).
87. G. Miyaji, K. Miyazaki, K. Zhang, T. Yoshifuji, and J. Fujita, Optics Express **20** (14), 14848 (2012) J. Opt. Exp. **20**, 14848 (2012).
88. F. Liang, R. Vall´ee, D. Gingras, and S. Leang Chin, Opt. Mat. Exp. **1**, 1244 (2011)

INTENTIONAL BLANK PAGE

5

SERS and SEF Studies using Plasmonic NMs

Abstract

This chapter first describes ultrafast laser induced surface nanostructures fabricated on a Cu target through ablation using different schemes. These NSs were utilized exultantly to investigate the surface plasmon (localized and propagating) mediated enhancements of different analytes using surface enhance Raman scattering (SERS) studies. Multiple utility of these substrates were efficiently demonstrated by collecting the SERS data of organic molecules/explosive molecules such as R6G, ANTA, TNT, FOX-7 and CL-20 at lower concentration on different days which were weeks apart. We achieved significant enhancement factors of ~10^5-10^8 through an easily adoptable cleaning procedure. SERS activity was evaluated through the quantification of adsorption factor and enhancement factors in detailed. Additionally Ag coated Si NSs also demonstrated large enhancements of ~10^6 in SERS measurements. Second, the deployment of complex Cu NPs in corroles/chloroform prepared by ultrafast laser ablation for surface enhanced fluorescence. Florescence enhancement of five orders in magnitude was obtained from corroles conjugated to Cu complex NPs.

5.1. Surface Enhanced Raman Scattering

5.1.1 Introduction

Spontaneous Raman scattering data, though, conveys significant information about fingerprints of the molecules, trace level detection case is not possible due to very small scattering cross-section (~10^{-36} cm^2/molecule). The inherent small Raman scattering cross-section can be extensively enhanced by introducing surface effects from plasmonic NMs. This effect is called as Surface Enhanced Raman scattering (SERS).[1-9] In SERS, any molecule in the vicinity of nanomaterials experiences the combined field due to incident field and local field by the excitation of surface Plasmons which is a direct repercussion of plasmonic metal NPs/NSs with high porosity and, as a result, induced polarizability of the molecule is enhanced. This is termed as electromagnetic enhancement. In the last three decades, Fleischman et al. in 1974[1] was first to experimentally demonstrate that SERS effect over a roughened silver (Ag) surface and achieved of 5-7 orders of magnitude enhancement in Raman signal. They reported that enhancement might depend on the surface area or number of participated molecules in SERS process. Jeanmaire et al.[2] proposed that the obtained Raman modes of pyridine molecules were enhanced in the presence of roughened Ag surface which might be due to the efficiency of Raman intensity enhancement itself. After few years, Seki et al.[4] demonstrated that Raman intensities of different molecules were enhanced in the presence of nano dimensional noble metals (few tens of nm). Till date, reported enhancement factors in SERS experiments are in the range of ~10^4-10^8 and a few groups reporting 10^{14}-10^{15} factors in the case of single molecular detection through the creation of hot spots.[10-12] SERS is one of the most capable techniques for detection of trace level organic, biological and explosive molecules[13, 14] such as Rodhamine 6G, crystal violet, amino acids, RDX (1,3,5-trinitroperhydro-1,3,5-triazine) and TNT (Trinitrotoluene). Efficient SERS necessitates the close contact between analyte and metal NP surface which is at a distance of 20 - 30 Å.[15] The materials such as Ag, Au and Cu in the form of colloids, dried colloids on the plane substrates and nanostructures can be utilized for SERS measurements given that they can produce different types of Surface Plasmons. Plasmons are the quantum of collective oscillations of conduction electrons (free electrons) in the surface of the NMs. SERS intensity is proportional to the fourth

power of electromagnetic field[16] which is related to complex dielectric function with real part with negative value which provides induced polarization in the material under the effect of incident electromagnetic field and imaginary part with positive value providing the absorption of the material.

The detection of organic and explosive molecules were carried out by different groups with the chemically or physically synthesized Plasmonic metal NPs and NSs.[17-19] ULAL is capable of generating definite shaped NPs and surface micro/nano structures[21-26] which can be utilized to achieve significant enhancements in the Raman intensities through well established localized surface plasmon resonances (LSPR) and Surface Plasmon Polaritons (SPP). Lee et al.[27] reported an SERS studies of benezenethiol molecules (10 μM) in the presence of Ag NP and Au NP colloids and NSs fabricated by laser ablation and obtained enhancement factor of order 10^5. Lau et al. [28] investigated that 10 μM concentration of acridine molecules on the laser fabricated Ag, Au, Ta and Ti NSs in water with 350 ps pulses demonstrated superior elevation of Raman signatures at an excitation wavelength of 514 nm and they demonstrated that with a pulse train of shots with higher number. Some of the authors have utilized chemically synthesized Ag and Au SERS active substrates which were reusable for the detection of different molecules after each washing and with superior enhancement.[29-31] Lack of reusability of the Ag/Au NPs and NSs fabricated through LAL is one of the difficulty in this technique. In this context Cu targets possess following advantages (a) they are more economic compared to Ag or Au targets (b) the cleaning procedures of laser ablated Ag/Au substrates[29-31] are cumbersome compared to Cu. It was observed that cleaning was a hard task in the case of plasmonic substrates which possesses long sustainable localized surface Plasmons. For these substrates (especially Ag) a very complicated procedure is needed where as we demonstrate here that for Cu nanostructured surfaces nominal cleaning is sufficient to achieve superior performance.

In this chapter, results from the studies of applications of Cu nanomaterials for SERS and surface enhanced fluorescence (SEF) studies are included. Particularly, in SERS studies we achieved (a) detection of explosives such as ANTA from Cu NSs fabricated using ultrafast multiple/single line ablation of Cu target in acetone, DCM, ACN, and chloroform (b) multiple utility of SERS active Cu nanostructured targets

followed by a simple cleaning procedure for detecting TNT and R6G molecules (c) detection of 1,1-diamino-2,2-dinitroethene (Fox-7), ANTA and CL-20 from the Cu NSs fabricated using different pulse energies in ACN (d) detection of FOX-7 and R6G using the Cu NSs fabricated under the influence of pulse numbers in acetone (e) SERS studies of R6G, ANTA and FOX-7 molecule in the presence of Cu NSs fabricated in chloroform at just above threshold fluence using ~2 ps pulses followed by a simple cleaning procedure and finally (f) Ag plating on Si LIPSS substrates synthesized by fs laser ablation of Si in acetone using as SERS active substrates for the detection of ANTA molecules with 1 μM are presented.

5.1.2 Detection of organic/secondary explosive molecules using SERS active Cu NS targets fabricated in different liquid media

SERS active Cu NS substrates were fabricated by ps laser multiple line and single line ablation of Cu target in acetone, DCM, ACN and chloroform and were labeled as MCuNS1 (SCuNS1), MCuNS2 (SCuNS2), MCuNS3 (SCuNS3), and MCuNS4 (SCuNS4), respectively. The surface topology of the above mentioned substrates were presented (see figure 3.8 and figure 3.9) in chapter 3. Raman spectra of various analytes [ANTA (5-amino-3-nitro-l,2,4-triazole), TNT (trinitrotoluene) and R6G (Rhodamine 6G) of concentrations 10^{-4} M and 10^{-6} M] were recorded using a micro-Raman spectrometer (WITec-Alpha 300) using an excitation source at 532 nm and a 100X objective. Typically, a tiny drop (~10 μl) of ANTA placed on all of the 8 Cu NS substrates to achieve a monolayer of the analyte molecules, they are Cu LIPSS + cylindrical NPs (MCuNS1), pillar shaped structures + cubical NPs (MCuNS2), LIPSS with 250 nm periodicity (MCuNS3), rough ended pillars (MCuNS4), LIPSS + spherical NP grains (SCuNS1), randomly corrugated structures + spherical NP grains (SCuNS2), LIPSS with 400 nm periodicity (SCuNS3) and small number of triangular NPs with ~250 nm size (SCuNS4). Raman spectra were typically recorded for four times at various positions on the target and their average spectra were considered. Later on, utilized Cu substrates were cleaned and sonicated with acetonitrile and again the same substrates were utilized for **the second time** to record Raman spectra of R6G. Subsequently, proper cleaning procedures were again followed and the same substrates were once more utilized, for the **third time,** to record Raman spectra of TNT. The time separation between these three trials was approximately few weeks.

Raman spectra of ANTA from Cu NSs fabricated via ps multiple and single line ablation are shown in figures 5.1(a) and 5.1(b). Significantly observed modes from the data were C-NO_2 symmetric stretching mode (1341 cm^{-1}),[32] N-N symmetric stretching mode (1130 cm^{-1}), NO_2 deformation + ring deformation (840 cm^{-1}), ring torsion + NO_2 deformation (589 cm^{-1}), C–N symmetric stretch mode (1480 cm^{-1}), N4-C5-N1 bending mode (960 cm^{-1}), ring deformation mode (1070 cm^{-1}), and ring def + N–H bend (1303 cm^{-1}).

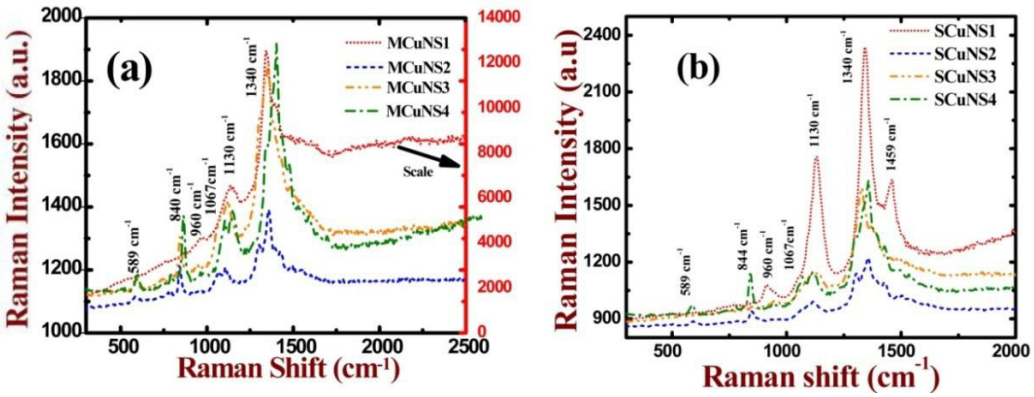

Figure 5.1 SERS spectra recorded from ANTA molecule adsorbed on different (a) multiple line and (b) single line ablated Cu NSs. MCuNS1 (SCuNS1)-red/short dot line, MCuNS2 (SCuNS2)-blue/ short dash line, MCuNS3 (SCuNS3)-orange/short dash line, MCuNS4 (SCuNS4)-olive/dash dot line. The integration time used was 5 s.

The Raman spectra of ANTA from Cu substrates were compared with normal Raman spectra of ANTA [see figure 5.7(b)] obtained using Si target to estimate the enhancement factors (EF) for 1341 cm^{-1} mode using the following formula[33,34]

$$E.F = \frac{I_{SERS}}{I_{Raman}} \frac{N_{Raman}}{N_{SERS}} \tag{5.1}$$

where I_{SERS} is the intensity of surface enhanced signal (at lower concentration), N_{SERS} is number of molecules participating in the enhancement of Raman signal (at lower concentration), I_{Raman} is the intensity of normal Raman signal of analyte (at higher concentration) collected from a plain silicon surface [figure 5.6 (b)] and N_{Raman} is number of molecules contributing to the normal Raman signal of analyte at higher concentration and N_{SERS} and N_{Raman} can be determined by the following equations

$$N_{SERS} = \eta\, N_A\, C_{al}\, V_a \frac{A_{laser}}{A_{NS}} \tag{5.2}$$

$$N_{Raman} = N_A\, C_{ah}\, V_a \frac{A_{laser}}{A_{substrate}} \tag{5.3}$$

Here N_A is the Avogadro's number (6.023×10^{23}), C_{al} is the lower concentration of the analyte (500 μM) on the enhanced surfaces, C_{ah} is the higher concentration of the analyte (0.1M) on the enhanced surfaces, V_a is the volume (10 μl) of analyte placed on substrate, A_{laser} is the effective area of laser spot (1.32×10^{-12} m^2) on the substrate, A_{NS} is the NS area drawn by the laser on Cu substrate is different for MCuNSs and SCuNSs ($5\times5 = 25$ mm^2), $A_{substrate}$ is the area occupied by the liquid on silicon surface ($5^2 = 25$ mm^2) and η is the adsorption coefficient which determines the absorbed percentage of molecules on the Cu substrate, clearly explained in section 5.1.3. For our convenience, the combined form of equations (5.1), (5.2) and (5.3) can be written as following

$$E.F = \frac{I_{SERS}}{I_{Raman}} \frac{N_{Raman}}{N_{SERS}} = \frac{I_{SERS}}{I_{Raman}} \frac{C_{ah} \times A_{NS}}{\eta \times C_{al} \times A_{substrate}} \tag{5.4}$$

The intensity for 1341 cm^{-1} mode for MCuNP1 (LIPSS and cylindrical NPs) was ~5301 (arbitrary units). However, the normal Raman intensity of ANTA from Si target for the same mode recorded with similar experimental conditions was ~10 (arbitrary units). The intensity enhancement (I_{SERS}/I_R), therefore, was estimated to be ~530. We estimated that ~50% of analyte molecules were adsorbed on the Cu substrates [the adsorption coefficient (η) used was 0.5]. E.F.s calculated for the 1340 cm^{-1} mode of ANTA molecule were 1.2×10^6, 3.1×10^4, 7.3×10^4, 7.1×10^4, 1.4×10^5, 3.6×10^4, 7.1×10^4 and 7×10^4 for MCuNS1, MCuNS2, MCuNS3, MCuNS4, SCuNS1, SCuNS2, SCuNS3 and SCuNS4, respectively. In the case of ANTA, large Raman signal enhancements were observed from MCuNS1 and SCuNS1. In particular, in the case of MCuNS1 (SCuNS1) nano cylindrical grains (nanoparticle grains) were observed on the top of LIPSS. Consequently, these substrates could have provided high local fields which resulted in the observed strong enhancements. We also

believe that for these surfaces effects of propagating and localized surface Plasmons were probably appended.

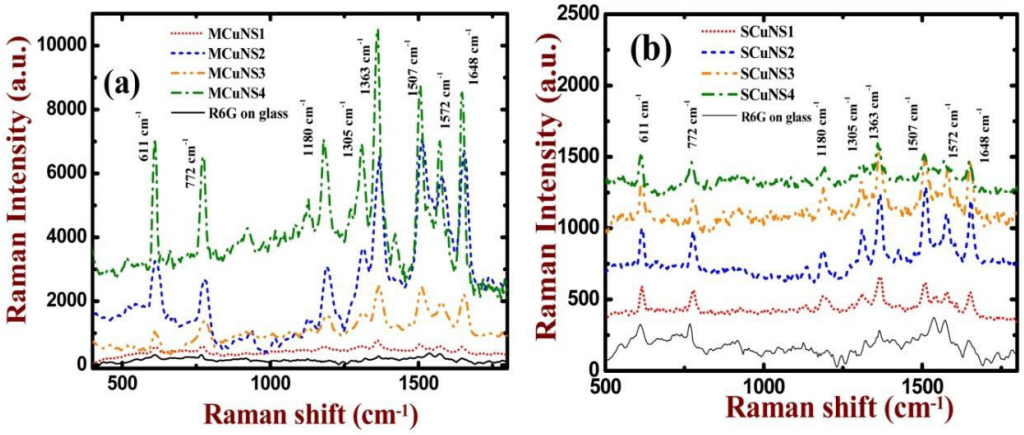

Figure 5.2 SERS spectra recorded from R6G molecule adsorbed on different (a) multiple line and (b) single line ablated Cu NSs. MCuNS1 (SCuNS1)-red/short dot line, MCuNS2 (SCuNS2)-blue/ short dash line, MCuNS3 (SCuNS3)-orange, MCuNS4 (SCuNS4)-olive. The integration time is 5 s for recording the Raman signal.

Similarly, Raman spectra of R6G (data presented in figure 5.2)[21] from the cleaned multiply and singly ablated Cu substrates recorded for the **second time** were analyzed. The prominent enhanced modes of R6G were the aromatic C-C stretch, C-H out plane bend and C-C-C ring in plane bend at 1363 cm^{-1}, 772 cm^{-1} and 610 cm^{-1}, respectively. Evaluation of E.F.s was carried out by comparing reference spectra of R6G (0.25 M concentration) recorded from a cover slip. At low concentrations (~5 μM) of R6G, it is believed that 43 % of molecules (η ~0.43) were adsorbed on Cu NS substrates. Estimated E.F.s of R6G for the 1363 cm^{-1} mode compared with the same mode in normal Raman spectra [see figure 5.7 (c)] were 6.2×10^5, 9.1×10^6, 2.6×10^6, 1.8×10^7, 4.6×10^5, 1.1×10^6, 9.1×10^5 and 3.8×10^5 for MCuNS1, MCuNS2, MCuNS3, MCuNS4, SCuNS1, SCuNS2, SCuNS3 and SCuNS4, respectively. Among the substrates investigated MCuNS2, whose surface topography comprised of micron sized pillars, and MCuNS4, containing roughened pillars along with nanoparticle grains, demonstrated stronger enhancements [21] compared to others.

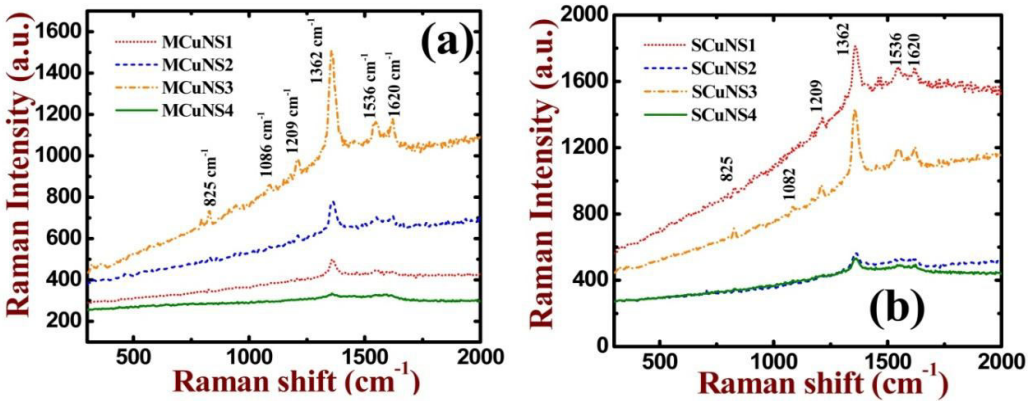

Figure 5.3 SERS spectra recorded from TNT molecule adsorbed on different (a) multiple line and (b) single line ablated Cu NSs. MCuNS1 (SCuNS1)-red, MCuNS2 (SCuNS2)-blue, MCuNS3 (SCuNS3)-orange, MCuNS4 (SCuNS4)-olive. The integration time is 5 s for recording the Raman signal.

Figure 5.3 illustrates the Raman spectra of the **third** testing sample TNT[13], recorded from the 8 Cu targets subsequent to appropriate cleaning. The recorded Raman spectra revealed that NO_2 symmetrical stretch mode corresponding to 1362 cm^{-1} was predominantly elevated. Additionally, two more peaks were observed, one at 1616 cm^{-1} which corresponds to C-C aromatic stretching vibration and another mode at 790 cm^{-1} (C-H out of plane bend). Corresponding E.F.'s calculated for 1362 cm^{-1} mode were ~4.2×10^4, ~7.7×10^4, ~2.2×10^5, ~1.6×10^4, ~2.5×10^5, ~5.8×10^4, ~1.9×10^5 and ~5.2×10^4 for MCuNS1, MCuNS2, MCuNS3, MCuNS4, SCuNS1, SCuNS2, SCuNS3 and SCuNS4, respectively. Raman spectra collected from three analytes using the same Cu targets demonstrated a small reduction in enhancements from analyte 1 to analyte 3. However, the enhancements were reasonably large even in the third trial. Our experimental data demonstrated that nanostructured Cu targets possess potential for elevating the Raman signatures of diverse analytes. We believe that three reasons could possibly contribute to the Raman signal enhancement. First, the coupling of incident photons to localized and propagating surface Plasmons leading to the elevation of evanescent fields.[35] These evanescent fields influence the individual vibrating dipoles to reradiate more number of photons thus enhancing the Raman signal. Second, the mentioned coupling of incident photons to LSPR might have fulfilled the condition that dimensions and shape[35] of the nanomaterials performed perpendicular surface plasmon vibrations with respect to the planar surface of the target. Third, whenever the separation between the nano dimensional materials (nanoparticles or nano-tips) is optimized then combined electron resonances of

individual structures enhances the probability of coupling and hence enormous amount of evanescent fields[36] are possible and sometimes specifically compatible to certain modes of interest. Consequently, some substrates demonstrated better Raman signature enhancement for a specific molecule. Estimated E.F.s in our experiments were significantly stronger compared to E.F.s obtained with Cu targets prepared by other methods.[37,38] Moreover, we strongly believe that Cu is well suited for fabricating SERS active substrates via laser ablation at minimal costs compared to other plasmonic metals.[39]

5.1.3. Adsorption factor calculation

The procedure we followed for adsorption factor calculations was proposed by Langmuir in Langmuir isotherm and adapted from earlier reports.[40-43] Accordingly, we recorded the SERS spectra of ANTA and R6G for different concentrations which were adsorbed on MCuNS3 and MCuNS4, respectively. The data is illustrated in figure 5.4 where a plot in between SERS intensity and concentration was obtained

The data was fitted with the equation $N = N_0 \left(\frac{Kc}{1+Kc}\right)$ (5.5)

Where N = number of molecules adsorbed, N_0 = number of molecules adsorbed at saturation, c = concentration of analyte and K= binding equilibrium constant. According to the referred manual,[44] Raman intensity is proportional to N at different concentrations and to N_0 at saturation level. From the plots, the best fits provided binding equilibrium constant (K) of 8.8×10^4 M^{-1} and 1×10^3 M^{-1} for R6G and ANTA, respectively. The critical characteristic of the Langmuir isotherm[40-43] can be expressed in the form of adsorption factor η, which is defined as $\eta = \frac{1}{1+Kc_0}$ --------- (5.6), where c_0 is the initial concentration at saturation level is of 15 µM for R6G and 1 mM for ANTA.

By substituting K and c_0 values in equation (5.6) we obtained the adsorption factor (η) values of ~0.43 and ~0.5 for R6G and ANTA, respectively.

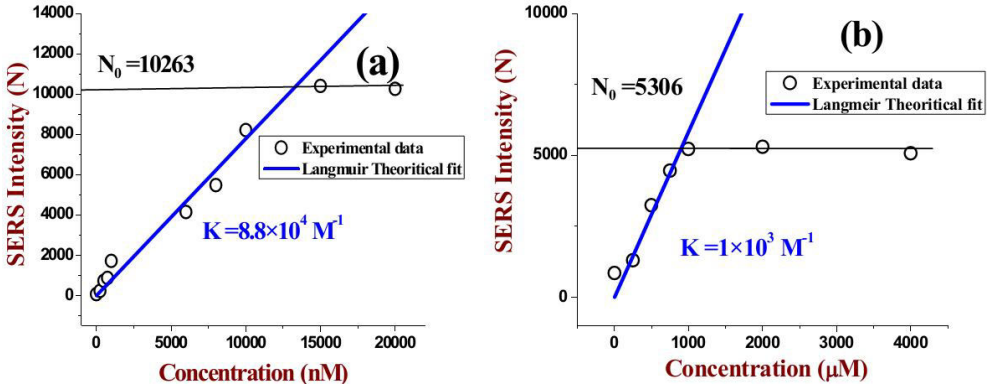

Figure 5.4 Langmuir adsorption isotherm plots of (a) R6G and (b) ANTA molecules which were adsorbed on laser machined copper NSs such as MCuNS4 and MCuNS3, respectively.

.

5.1.4. Fabrication of SERS active Cu substrate in chloroform using ps pulses

In the ps laser ablation Cu metal target was placed at the bottom of Pyrex cell filled with liquid of ~5 mm thickness above the surface of metal target. The spot size on the sample surface was estimated to be ~90 μm. Typical fluence of ~2.5 J/cm^2 and an ablation time of 30 minutes were used. The liquid filled Pyrex cell with Cu target, placed on the X-Y stage (Newport), was translated to draw periodic lines on Cu target at separation of ~60 μm. Morphologies of the fabricated Cu NSs in chloroform was characterized by FESEM and the data is presented in figure 5.5(a). The morphology and applications of Cu/CuCl NPs generated at the same time are presented in section 5.2. The FESEM image demonstrated formation of micron sized structures with sharp edges and magnified image depicted random nanostructures with roughness of ~700 nm. Surface activity of Cu NS was investigated by recording the Raman spectra of three adsorbed molecules [R6G (1×10^{-9} M and 5×10^{-7} M), ANTA (1×10^{-6} M and 2×10^{-4} M), FOX-7 (1×10^{-6} M and 2×10^{-4} M)] on the Cu NS. The Raman spectra were recorded at 532 nm with a 0.9 NA objective. SERS spectra of R6G (1×10^{-9} M and 5×10^{-7} M) were recorded with 10-20 μL deposited on Cu NS to form a monolayer. An average of 10 spectra collected is illustrated in figure 5.5(b). E.F.'s were evaluated[33, 34] by comparing the SERS spectra with normal Raman spectra of R6G [see figure 5.7(a)] which were deposited on plane silicon surface for the most prominent Raman peak of 1363 cm^{-1} corresponding to in plane aromatic C-C stretch. Enhancement factor was estimated using the equation 5.4. In case of R6G, at 1×10^{-9} M and 5×10^{-7} M concentrations the absorbed molecules (~35% and ~43%) on the Cu

NS were estimated by following a process reported in our article.[45] The estimated E.F.'s for the 1363 cm^{-1} mode were ~6×10^{8} and ~1.8×10^{7} for 1×10^{-9} M and 5×10^{-7} M concentrations, respectively. Assignments of other spectral modes are presented in table 5.1. Large enhancement in the case of R6G could be due to the rough edges arising from micron sized structures on Cu surface. SERS spectra of R6G, at 1×10^{-9} M is shown in figure 5.6(a)

Raman shift (cm^{-1})				
S. No.	**Surface enhanced Raman modes**		**Normal Raman modes**	**Mode Assignment**
	1×10^{-9} M	5×10^{-7} M	0.25 M	
1	611	611	610	C-C-C ring in-plane bend
2	772	772	767	C-H out-plane bend
3	1180	1180	-	C-C stretch
4	-	1305	1315	Not assigned
5	1363	1363	1364	Aromatic C-C stretch
6	-	1507	1530	Aromatic C-C stretch
7	1572	1572	1572	Aromatic C-C stretch
8	1648	1648	1644	Aromatic C-C stretch

Table 5.1 Observed Raman active modes of R6G adsorbed on Cu NSs and plane silicon, and their mode assignments.

Later, the substrate was cleaned by sonication in acetone for half an hour and dried at room temperature. After two weeks, the same Cu substrate was utilized again by recording the SERS spectra of an explosive molecule (ANTA) at 1×10^{-6} M and 2×10^{-4} M concentrations. SERS spectra of ANTA [in Fig 5.5(b)] molecule adsorbed on the Cu NSs substrate. The spectral modes of ANTA[32] have been observed with lower intensity at 1×10^{-6} M in the Raman spectrum. The vibrational modes were observed at 533 cm^{-1} and 615 cm^{-1} associated with NH_2 deformation and NO_2 deformation, respectively. The main characteristic mode detected at 1337 cm^{-1} with lower intensity along with 1577 cm^{-1} mode assigned to C-NO_2 symmetrical stretch and C-NH_2 symmetrical stretch+NH_2 bend, respectively. For 2×10^{-4} M concentration the characteristic mode at 1337 cm^{-1} was elevated with good signal to noise ratio and some more modes were detected at 844 cm^{-1}, 955 cm^{-1} and 1126 cm^{-1}, which were not observed in SERS spectra at 1×10^{-6} M concentration. It was also observed that modes at 533 cm^{-1}, 615cm^{-1} and 1577 cm^{-1} were not elevated clearly in the present case. It should be noted that no modes were observed in normal Raman spectra of ANTA [0.2 M, see figure 5.7(b)]. We estimated that ~47% and ~50% ANTA molecules were

adsorbed on the NS substrate[45] for the concentrations of 1×10^{-6} M and 2×10^{-4} M, respectively. The evaluated E.F.'s for the 1337 cm^{-1} mode were ~1.4×10^{7} and ~2.8×10^{5} at 1×10^{-6} M and 2×10^{-4} M concentrations, respectively. Assignments of other spectral modes of both concentrations are summarized in table 5.2. SERS spectra of ANTA recorded at lower concentration (1×10^{-6} M) are shown in figure 5.6(b).

Raman shift (cm^{-1})				
S. No.	**Surface enhanced Raman modes**		**Normal Raman modes 0.2 M**	**Mode Assignment**
	1×10^{-6} M	2×10^{-4} M		
1	533	-	NO	NH_2 deformation
2	615		NO	NO_2 deformation
3	-	844	NO	NO_2 deformation + ring deformation
4	-	955	NO	N4-C5-N1 bending
5	-	1126	NO	N-N symmetrical stretching mode
6	1337	1337	NO	C-NO_2 symmetrical stretching mode
7	1577	-	NO	C-NH_2 symmetrical stretch + NH_2 bend

Table 5.2 Observed Raman active modes of ANTA adsorbed on Cu NSs and plane silicon, and their mode assignments.

One day later, the SERS spectra of another explosive molecule (FOX-7) was recorded for third time after appropriate cleaning of the substrate. SERS spectra of FOX-7 [depicted in figure 5.5 (b)] demonstrated the characteristic Raman bands[46, 47] corresponding to symmetric C-NO_2 stretching and NH wagging at 1340 cm^{-1} with lower intensity at a concentration of 1×10^{-6} M whereas at 2×10^{-4} M concentration the mode intensity was clearly enhanced. Moreover, spectral characteristic mode at 1483 cm^{-1}, corresponding to out of layer symmetric NH wagging (NO and NH rocking), was observed in both the cases. The calculated E.F.'s for the 1340 cm^{-1} mode compared with the same mode in normal Raman spectra [see figure 5.7(d)] were ~2.5×10^{5} and ~4.2×10^{4} for 1×10^{-6} M and 2×10^{-4} M concentrations, respectively. SERS spectra of FOX-7 recorded at lower concentration (1×10^{-6} M) are shown in figure 5.6(c). Assignments of all other modes are summarized in table 5.3.

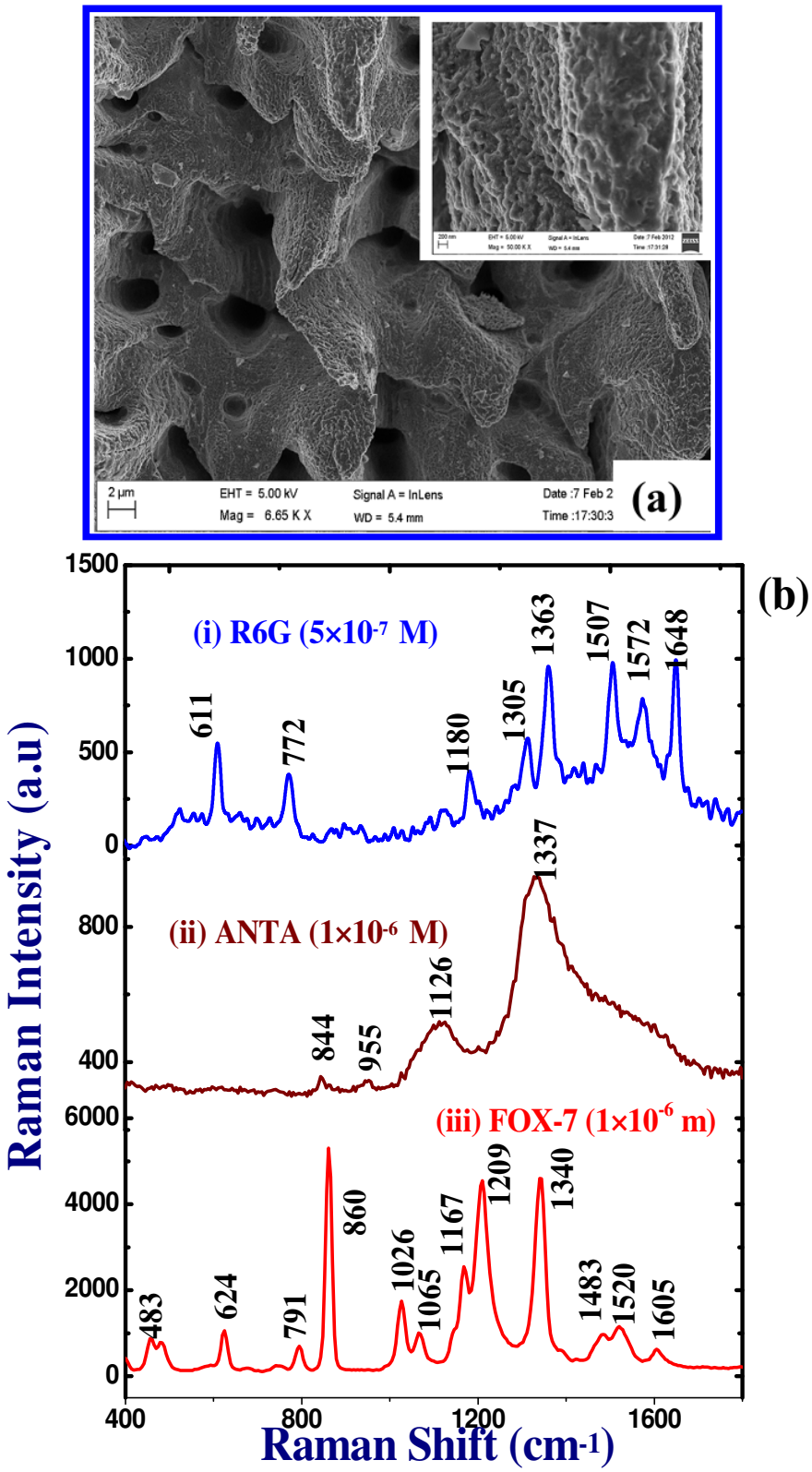

Figure 5.5 FESEM image of NS's on the Cu substrate prepared in chloroform and (b) SERS spectra recorded from **(i)** R6G (blue /top - 5×10^{-7} M) **(ii)** ANTA (wine/middle - 2×10^{-4} M) and **(iii)** FOX-7 (red/bottom - 2×10^{-4} M) adsorbed on Cu NSs.

S. No.	Raman shift (cm^{-1}) Surface enhanced Raman modes 1×10^{-6} M	2×10^{-4} M	Normal Raman modes 0.2 M	Mode Assignment
1		320	320	Out of layer H wagging
2		396	399	In-layer asymmetric NH wagging
3		483	480	Symmetric NO and NH wagging
4		624	624	Out of layer symmetric NH wagging
5		791	790	C-NO_2 rocking mode
6		860	856	NO and NH rocking
7		1026	1025	In-layer asymmetric NH wagging
8		1065	1067	In-layer symmetric NH wagging
9		1167	1167	C-C stretch and NH wagging
10		1209	1205	Asymmetric C-NO_2 stretching and NH wagging
11	1340	1340	1343	Symmetric C-NO_2 stretching and NH wagging
12	1483	1483	1482	Out of layer symmetric NH wagging, NO and NH rocking
13		1520	1528	C-NH_2 bending mode and C-C stretching
14		1605	NO	NH_2 bending

Table 5.3 Observed Raman active modes of FoX-7 adsorbed on Cu NSs and plane silicon, and their mode assignments.

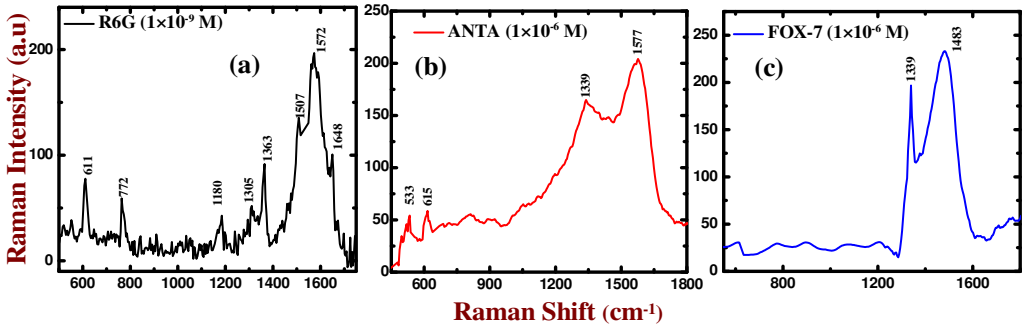

Figure 5.6 SERS spectra of (a) R6G (1×10^{-9} M), (b) ANTA (1×10^{-6} M) and (b) Fox-7 (1×10^{-6} M) recorded with lower concentration on Cu NS substrate at the excitation wavelength 532 nm. The time of integration was 5 s.

The rough edges on Cu substrate demonstrated larger enhancements in R6G compared to ANTA and FOX-7. We believe that the following arguments support our observations (a) the dimensions of explosive molecules are smaller than R6G molecules and these molecules might not have electromagnetically attached to rough edged Cu structures appropriately. This suggests that rough edged Cu structure was not compatible to generate sufficient local fields which invoke electric dipoles vibrations and, therefore, resulted in lower enhancements in the Raman signal of explosive molecules (b) the amount of explosive molecules adsorbed on the Cu structural surface could be less compared with R6G molecules due to the dissimilar sizes of molecules (c) screening of local filed effects on freshly adsorbed explosive molecules by the possible residual R6G molecules present on the nanostructured target. However, further detailed studies are necessary before tangible reasonsare identified. From our previous studies[45] and present results we firmly believe that the Cu structures with rough edges are more compatible with R6G providing larger SERS signal and Cu nanostructured (or) periodic ripple substrates are well matched for explosive molecules for generating the enhanced Raman signal. Further improvements in SERS signal can be achieved by combining the benefits of both nanostructures and nanoparticles on a single substrate.[48]

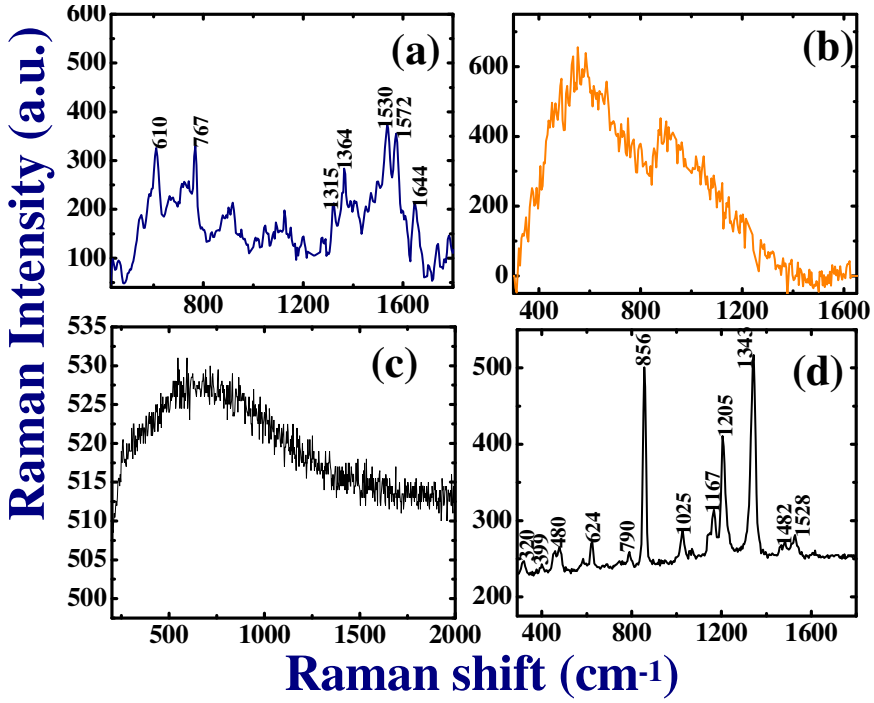

Figure 5.7 Normal Raman spectra of (a) R6G, (b) ANTA (c) TNT and (d) Fox-7 recorded on plain silicon substrate at the excitation wavelength 532 nm. The time of integration was 5 s.

5.1.5. Identification of analyte molecules using SERS active Cu substrates synthesized with different pulse energies

The fabricated structures on Cu substrates under the influence of different pulse energies (25 – 400 μJ) in ACN were also utilized for SERS studies to detect explosives in trace level concentrations. These SERS substrates were designated as Cu-25, Cu-50, Cu-100, Cu-200, Cu-300 and Cu-400 for 25 μJ, 50 μJ, 100 μJ, 200 μJ, 300 μJ and 400 μJ, and the observed surface nano roughness were ~800 nm, ~2400 nm, ~3600 nm, ~2500 nm + LIPSS with ~430 nm periodicity, ~ 2360 nm + LIPSS with ~420 nm and ~ 1600 nm + LIPSS with ~470 nm, respectively. The FESEM images of the fabricated substrates were presented in the section 3.3. Figure 5.8 illustrates the enhanced Raman spectra of FOX-7 which was adsorbed on Cu substrates were recorded at 532 nm and a 100X objective. In general, a little drop (~10 μl) of FOX-7 (concentration of 25 μM) placed on substrates to achieve a monolayer of the molecules. The Raman spectra revealed that C-NO_2 symmetrical stretch mode corresponding to 1342 cm^{-1} was predominantly elevated along with other modes. The other observed modes were attributed to symmetric NO and NH wagging mode, out of layer symmetric NH mode, symmetric rocking C-NO_2 mode, NO and NH rocking mode, asymmetric NH wagging mode, symmetric NH wagging mode, asymmetric C-NO_2, NH_2 bending and C-C + symmetric NH stretching modes corresponding to 483 cm^{-1}, 620 cm^{-1}, 792 cm^{-1}, 861 cm^{-1}, 1024 cm^{-1}, 1067 cm^{-1}, 1205 cm^{-1}, 1510 cm^{-1} and 1595 cm^{-1}, respectively. We considered that 45 % of molecules (η ~0.45) were adsorbed on Cu NS substrates. The procedure of enhancement factor (E.F) calculation was already presented in the earlier section 5.1.2. The estimated E.F for the predominant mode of 1342 cm^{-1} were of 3×10^5, 2.8×10^5, 1.9×10^5, 4.1×10^5, $1.3\times10^5$and 2.3×10^5 for CuS-25, CuS-50, CuS-100, CuS-200, CuS-300 and CuS-400, respectively. The obtained E.F were ~10^5 for all the 6 type Cu NSs since they might have produced identical local fields through even the excitation of different types of surface Plasmons. We have chosen one SERS active substrate (CuS-200) among 6 substrates for second measurement of different analyte molecules since all of them demonstrated similar performance.

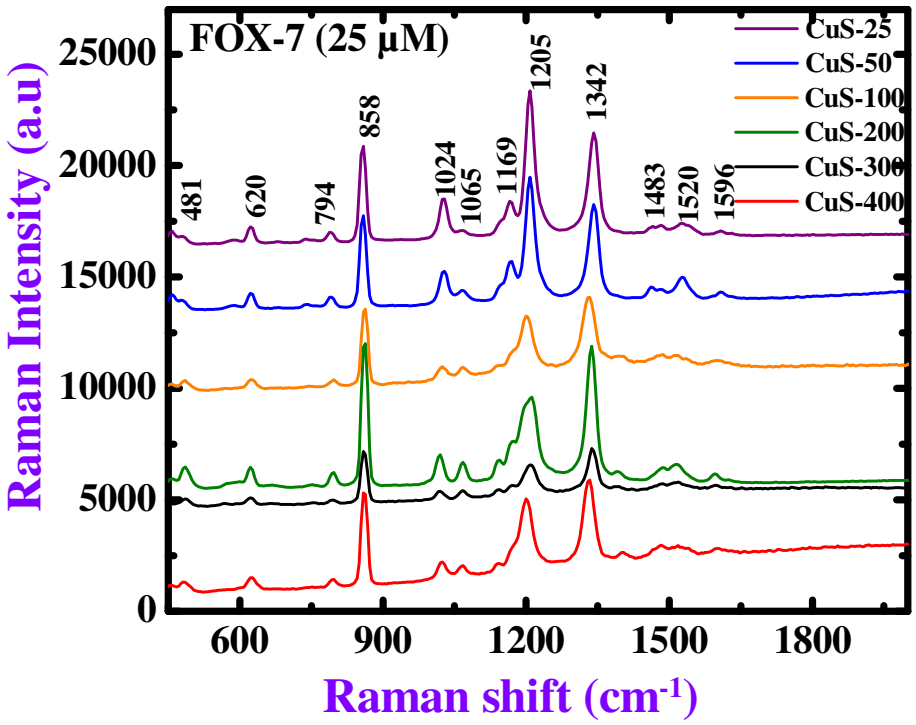

Figure 5.8 SERS spectra of Fox-7 molecules adsorbed on Cu NSs fabricated through ULA of Cu in ACN at different pulses energies

We picked up ANTA molecule as our second testing sample to probe the Cu NSs after proper cleaning within a week. Figure 5.9 shows the SERS spectra of ANTA molecule with a concentration of 1×10^{-6} M adsorbed on Cu surface r.m.s. roughness of~2500 nm + LIPSS with ~430 nm periodicity (CuS-200). The enhancement was notable even at the concentration of 1×10^{-6} M and the Raman peak was typically elevated at 1340 cm^{-1} corresponding to the C-NO_2 symmetric stretch which is the characteristic peak of ANTA molecule. Along with characteristic modes, other modes were also observed near 953 cm^{-1} and 1130 cm^{-1} and those were corresponding to N4-C5-N1 bending mode and N-N symmetric stretching mode, respectively. The other Raman modes were not detected at these concentrations which were elevated at higher concentrations (500 nM) as shown in figure 5.1. It is believed that ~40% (η ~0.4) molecules were adsorbed on Cu NS substrate. The performance of SERS active substrate has been evaluated by calculating E.F. For E.F, normal Raman spectrum intensity of ANTA (0.2 M) was compared with enhanced Raman spectrum. The estimated E.F for the characteristic peak of ANTA molecule at 1340 cm^{-1} was ~1.2×10^{8}. The large enhancement in ANTA molecule could be accredited due to huge

local field via the excitation of strong localized surface Plasmons provided by Cu surface with r.m.s. roughness of ~2500 nm which might have supported additional field through the propagating surface Plasmons due to LIPSS.

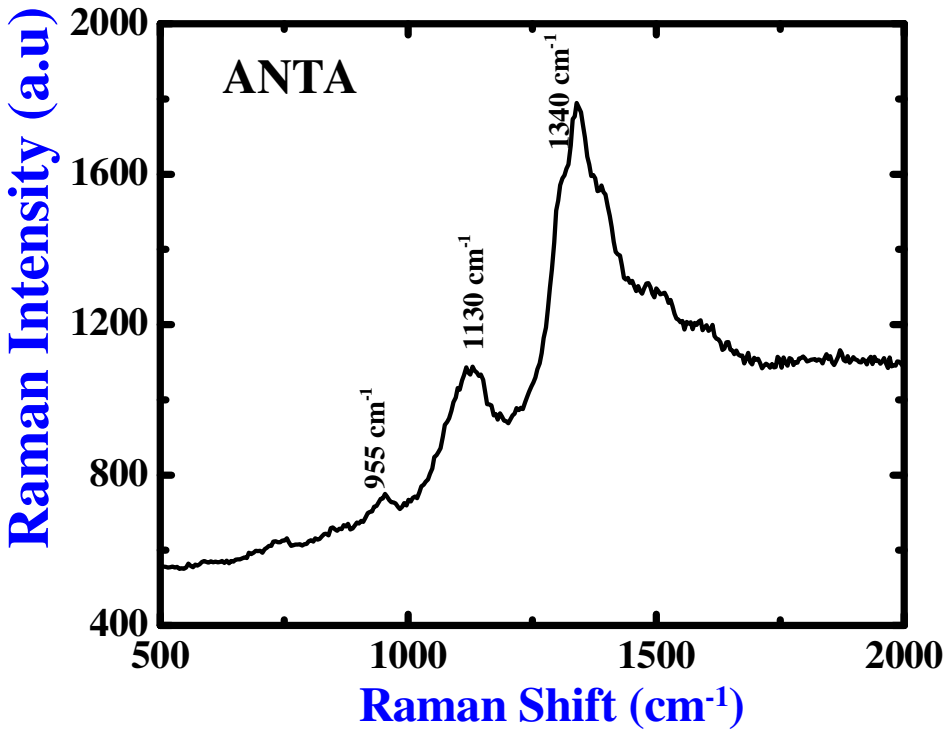

Figure 5.9 SERS spectra of ANTA (1×10^{-6} M) adsorbed on Cu-200 substrate fabricated through ULA of Cu in ACN at 200 µJ

A week later, we chose CL-20 molecule with 1×10^{-6} M concentration as our third analyte for recording SERS on the same substrate (Cu-200) after perfect cleaning. Figure 5.10 depicts the enhanced Raman spectrum of CL-20 which illustrates the most significant Raman modes[49] at 1331 cm^{-1} and 1372 cm^{-1} corresponding to characteristic modes (NO_2 symmetric stretch) of explosive which are related to nitro-aromatic (or) nitramine. The other enhanced Raman modes were elevated significantly at 834 cm^{-1}, 1055 cm^{-1}, 1065 cm^{-1} and 1277 cm^{-1} which were attributed to NC torsion + NO_2 deformation, NC torsion + ring torsion + NCH deformation, NN stretch + NC stretch and NO stretch + CC torsion, respectively. It is supposed that ~40% molecules were sat down properly on Cu NS substrate. The evaluated E.F was ~ 4.5×10^{5} for the characteristic mode of 1331 cm^{-1} compared with normal Raman spectrum of CL-20 (0.1 M).

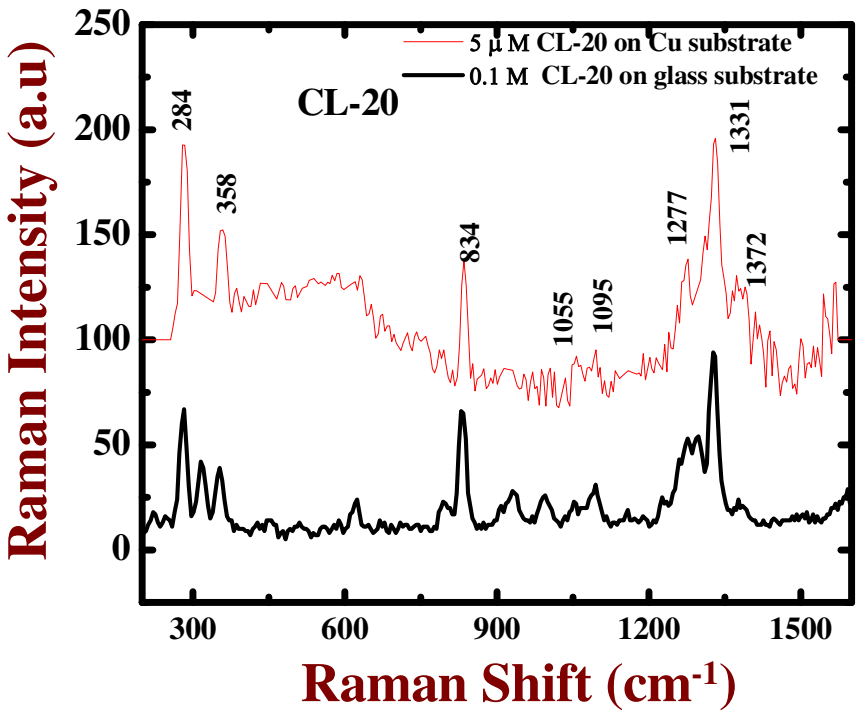

Figure 5.10 SERS spectra of CL-20 (1×10^{-6} M) adsorbed on Cu-200 substrate fabricated through ULA of Cu in ACN at 200 µJ

5.1.6 SERS studies of Cu NSs synthesized with different number of fs pulses

The NSs were produced on Cu targets in acetone with different scanning speeds. The estimated pulse numbers in the focal region [w (z)/d] with respect to scanning speeds were ~250, ~300, ~500, ~1000 and ~2000 for the scanning speeds of 400 µm/s, 300 µm/s, 200 µm/s, 100 µm/s and 50 µm/s, respectively. The morphology on Cu substrates (after the ablation) was random nanoroughness with r.m.s. value of ~1.6 µm, cuboid (l ~ 400 nm, b ~ 200 nm, h ~ 60 nm), hexagonal with ~125 nm size, spherical particles with ~70 nm and random NSs with r.m.s. roughness of ~1.8µm for a pulse train of different shots such as ~250, ~300, ~500, ~1000 and ~2000 and they were labeled as CuNS-250, CuNS-300, CuNS-500, CuNS-1000 and CuNS-2000, respectively. FOX-7 was taken as a probe molecule for recording the Raman spectra. The molecule was diluted to 25 µM concentration and then placed on Cu NSs fabricated by different pulses numbers and 0.1 M was the reference concentration which was coated on plane silicon substrate. Consequently, they were dried out and

then the Raman spectrum from Cu nanostructured and plane Si surfaces were recorded and the data is illustrated in figure 5.11.

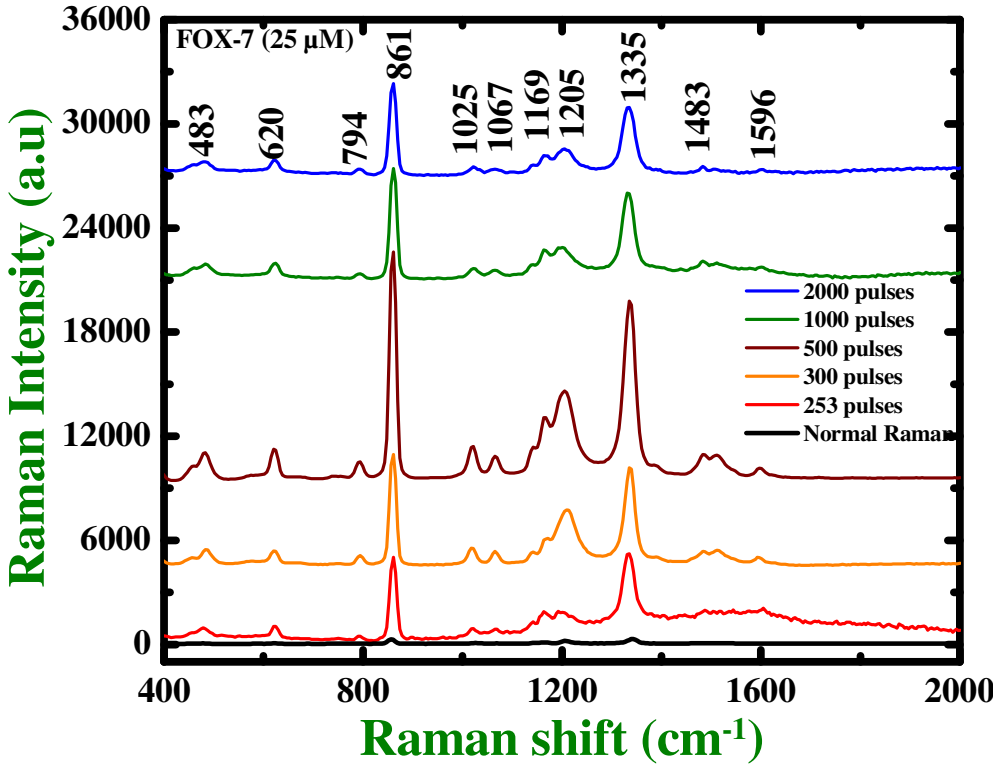

Figure 5.11 SERS spectra of FOX-7 (25×10^{-6} M) adsorbed on Cu NS substrates fabricated through fs ablation in acetone under the influence of pulse number at constant fluence of 2.5 J/cm^2

As observed from the data in figure 5.11, the characteristic Raman mode at 1339 cm^{-1} was observed with less intensity in normal Raman spectrum along with some other modes. On the other hand, in SERS spectra the modes got intensified (30-50 times) which were elevated in normal Raman spectrum with less intensity. The elevated modes were 483 cm^{-1}, 620 cm^{-1}, 794 cm^{-1}, 861 cm^{-1}, 1025 cm^{-1}, 1067 cm^{-1}, 1169 cm^{-1}, 1205 cm^{-1}, 1335 cm^{-1}, 1483 cm^{-1} and 1596 cm^{-1} corresponding to symmetric NO and NH wagging, out of layer symmetric NH wagging, C-NO_2 rocking mode, NO and NH rocking, In-layer asymmetric NH wagging, In-layer symmetric NH wagging, C-C stretch and NH wagging, asymmetric C-NO_2 stretching and NH wagging, Symmetric C-NO_2 stretching and NH wagging, out of layer symmetric NH wagging, NO and NH rocking, C-NH_2 bending mode and C-C stretching, and NH_2 bending, respectively. To evaluate the capability of Cu NS substrates, E.F was estimated by considering the intensity in SERS spectra which was compared with intensity from normal Raman spectra. The E.Fs calculated were 2×10^5, 3.6×10^5,

7×10^5, 2.8×10^5 and 2.3×10^5 for random NSs with roughness of ~1.6 µm (CuNS-250), cuboids with length of ~400 nm (CuNS-300), hexagons with ~90 nm size (CuNS-500), spherical particles with ~100 nm (CuNS-1000) and random NSs with r.m.s. roughness of ~1.8 µm (CuNS-2000), respectively. The estimated E.F was ~ 10^5 for all the type of Cu NSs. However, hexagonal NPs demonstrated 2-3 times higher enhancement than random NSs, cuboid NPs and spherical NPs. We believe that higher enhancement was obtained due to (a) the intensification of local electric field at sharp edges of hexagonal NP which might be have acted as hotspots through the excitation of localized surface Plasmons and (b) combined oscillations of surface Plasmons due to sharp edges of two hexagonal NPs could have also contributed in this amplification of local field.

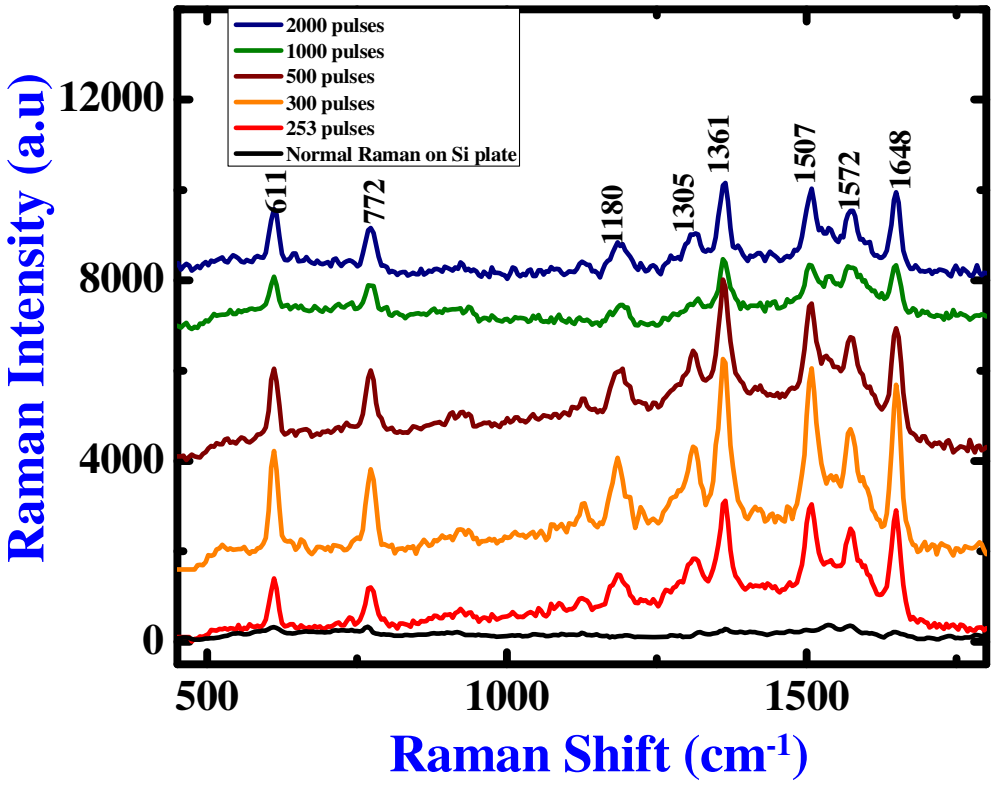

Figure 5.12 SERS spectra of R6G (5×10^{-6} M) adsorbed on Cu NS substrates fabricated through ULA in acetone under the influence of pulse number at constant fluence of 2.5 J/cm^2

Figure 5.12 illustrates the SERS spectra of R6G (5×10^{-6} M) recorded from a pulse train of different shots ablated Cu substrates after cleaning. Following of earlier reports,[25] the observed modes in normal and enhanced Raman spectra were allocated. The Raman mode observed at 1361 cm^{-1} corresponding to aromatic C-C stretch vibration, is called as the characteristic mode of R6G molecule. The modes present at

611 cm^{-1}, 772 cm^{-1} and 1180 cm^{-1} are due to C-C-C ring in-plane bend, C-H out-plane bend and C-C stretch, respectively. The Raman peaks observed at 1507 cm^{-1}, 1572 cm^{-1} and 1648 cm^{-1} were mainly from the contribution of aromatic C-C stretch. The feasible E.Fs for the principal vibrational mode 1361 cm^{-1} were 3.4×10^6, 8.4×10^6, 6×10^6, 2.5×10^6 and 3.2×10^6 for CuNS-250, CuNS-300, CuNS-500, CuNS-1000 and CuNS-2000, respectively. Among all the Cu substrates inspected CuNS-300, whose surface morphology involved of cuboids (l ~ 400 nm, b ~ 200 nm, h ~ 60 nm), and CuNS-500 (covering dimers of hexagonal NPs), demonstrated superior enhancement than other Cu NSs. The fabricated metal NSs such as Ag, Au, Ti and Ta in water with 350 ps pulses depicted superior SERS activity of acridine molecules of 10 μM concentration for more number of pulses incident on the target.[27]

5.1.7 SERS active Ag coated Si substrates fabricated with fs pulses

5.1.7.1. Introduction

Over the last two decades, chemically, physically and laser based synthesized noble metal NPs/NSs have been proved to play a crucial role in realizing the true potential of surface enhanced Raman scattering (SERS).[11, 50-58] In recent years, semiconductor (or) dielectric nano-roughness coated with Plasmonic metals received strong attention in the hot area of SERS.[59-61] For example, surface layers were produced by vacuum evaporation,[62] immersion plating,[63] electrochemical plating[64] and lithographic techniques,[65] etc of Ag/Au on non SERS active NS substrates were fabricated by chemical and physical methods. However, Yang et al.[66] reported the fs laser fabricated micro/nano structures on Si wafer, coated with Ag layer through thermal deposition for SERS detection of bio-molecules. ZhiQing et al.[67] projected a quick and straightforward method to fabricate large area SERS active Si substrates by fs laser pulses which were covered with Au thin film, demonstrated ~ 10^7 enhancements for R6G molecule. Moreover, Ag coated on randomly formed silica NSs generated by fs ablation technique was explored as SERS active substrates.[68] We investigated Ag layer coating on the LIPSS along with NPs with ion beam deposition which were formed on Si surface by fs laser ablation in acetone. The combine advantage of both propagating and localized surface Plasmons results in larger enhancement in SERS.

5.1.7.2. Synthesis and SERS activity of Ag thin film coated SERS active Si NSs

Ag thin films were deposited on ablated Si substrates in a home-built ion beam deposition system evacuated by a turbo molecular pump (TMP). The dc ion source (DC25 Oxford Applied Research, UK) was a Kaufmann-type ion source capable of producing ion beams of 2.5 cm in diameter with maximum beam energy of 1.5 keV. The ions were extracted and accelerated by applying a suitable potential to a dual-grid ion extraction system. Cathode current was maintained at 10 m Amp with an ion beam energy of 80 eV and extraction voltage of -40V. The deposition chamber was evacuated to a base pressure of 2×10^{-6} Torr before introducing argon gas into the system. The pressure during deposition was 3×10^{-3} Torr. A 3 inch diameter and 4 mm thick Ag target was kept at 45 degree to the incident ion beam direction. The substrates were held at room temperature during deposition, and substrates are mounted on a substrate holder, which was 8 cm from the target at 45 degree angle and in source axis. Acceleration voltage, cathode current, deposition pressure and extraction voltages were well calibrated to reach deposition rate of 2 nm/min. The deposition was carried for 10 minutes to reach ~20 nm thick films on all the ablated Si substrates and was confirmed from EDAX data.

Figure 5.13 demonstrates the recorded Raman spectra of ANTA molecule with concentration of 1×10^{-6} M on Ag thin film coated Si NSs and 0.1 M on plain silicon wafer (reference spectrum), using micro Raman spectrometer with an excitation of 532 nm and integration time of 0.5 s. It is evident that Raman modes were largely enhanced on Ag thin film coated Si NSs compared with the modes on plane silicon at higher concentration of 0.1 M. The Peak at 1339 cm^{-1} is assigned to C-NO_2 symmetric stretch vibration which can be called as characteristic mode of the molecule while the other Raman modes at 952 cm^{-1}, 1125 cm^{-1} and 1585 cm^{-1} and, those are corresponding to N4-C5-N1 bending mode, N-N symmetric stretching mode and C-NH_2 symmetrical stretch + NH_2 bend, respectively. The Raman intensity was observed to increase as the periodicity of LIPSS increased from 120 nm to 155 nm. However, Raman intensity decreased when the periodicity was further increased to ~230 nm. The size of formed NPs on LIPSS might also have played a significant role to add their contribution in Raman intensity enhancement. It is considered that a small percentage of molecules (η~0.37) in the hot spots contributed to enhanced Raman

intensity. To explore the enhancement capability of Ag metal plating Si NSs, E.F's were evaluated by comparing the SERS intensity with normal Raman intensity. Based on the intensities of the characteristic peak at 1339 cm^{-1} in all SERS spectra, the E.Fs were ~1.2×10^7, ~1.3×10^7, ~2×10^7, ~5.32×10^7, ~2.5×10^7 and ~1.4×10^7 for different periodicity of LIPSS (size of particle placed on the top of LIPSS) of ~120 nm (80 nm), ~125 nm (90 nm), ~130 nm (60 nm), ~155 nm (65 nm), ~125 nm (110 nm) and ~230 nm (90 nm), respectively. Our Raman data revealed that the Ag metal plating on Si NSs possesses potential for detecting the Raman modes of ANTA analyte with larger enhancement and this might be ascribed to large amplification of local electric field, which is due to the combination of localized surface Plasmons and propagating surface Plasmons produced on the surfaces of spherical NPs and periodic surface structures, respectively.

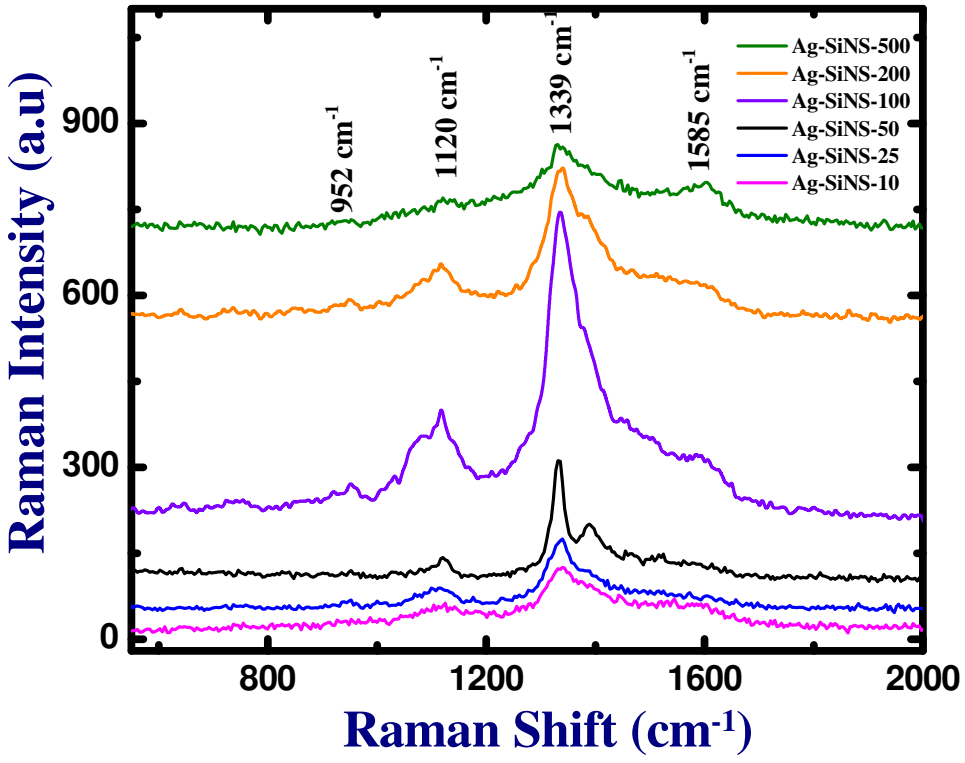

Figure 5.13 Raman spectra of ANTA (1×10^{-6} M) molecules dispersed on Ag coated Si NSs fabricated using different pulse energies.

We are also attempting to combine both metal NSs and NPs for further enhancement in the Raman signal. Our independent studies (performed separately) on copper colloids do indicate strong SERS signal. We intend to place these nanoparticles on nanostructures and repeat the SERS measurements. This kind of

hybrid SERS techniques wherein we can use these substrates along with nanoparticles (both of them can be washed to obtain clean substrates again) will be a potential technique and could meet the detection limits for field deployment. Furthermore, following our recent NS's fabrication on Silicon targets[69] (see chapter 4) we could use them in two ways (i) place nanoparticles and analytes in these groves for SERS studies (ii) since these structures are periodic one can coat Au, Cu layers and use them for SERS studies.

5.2. Cu/CuCl Nanocomposites prepared by ps pulses for SEF studeis

5.2.1 Introduction

Over the last two decades plasmonic metal nanoparticles (NPs) have encountered the potential applications in biotechnology,[70] chemistry,[71] and photonics[21, 72] due to their outstanding optical properties. Plasmonic metal NPs have been proved to play a crucial role in realizing the true potential of surface enhanced Raman scattering (SERS)[11, 50-58] and surface enhanced florescence (SEF) techniques.[73-79] Efficient SERS demanded the contact between analytes and metal NP surface usually, is 20-30 Å.[15] At these distances, fluorescence of analytes is extensively quenched and minor enhancements have been observed than those obtained in SERS. When the analytes are placed in the vicinity of NPs (>50 Å) enhancement in the fluorescence is significantly orders of magnitude higher, which is referred to as surface enhanced fluorescence (SEF).[80] SEF has been extensively utilized as an efficient tool for imaging and detection in the fields of life sciences and chemical sciences by improving the quantum yield, excitation rates of fluorophore.[81] The primary reason behind SEF is enhanced local fields in the proximity of fluorophore which in turn amplifies the radiative decays and their quantum yields.[76] The effect of Plasmons on fluorophore depends on the shape, size, and chemical composition of the metal NPs. Thus far SEF studies were focused on fluorophores attached to noble metal films such as silver and gold NPs which were fabricated by different physical and chemical methods and obtained significant enhancements of fluorescence intensity.[82-85] Cu NPs/NSs have not been studied effectually for SEF since their absorption cross-section depend on the imaginary component of dielectric function [5.8 for Cu, which is higher than for Ag (1.66) and Au (1.86)] exhibiting an absorption maximum nearby

560 nm.[86] Due to this the possibility of fluorescence quenching by Cu NMs prevails because the emission band of most analytes fall in the 560–740 nm spectral region. We achieved a characteristic absorption band of Cu NPs near 400 nm (from 580 nm) through chlorination of Cu NPs performed during the fabrication of Cu NPs in ps laser ablation.[72,87] This is due to direct adsorption of Cl^- ions on metal NPs those originate from solvent disintegration through laser ablation.[72, 87] It was also recently reported that the characteristic absorption band of ns (532 nm) and fs (800 nm) laser generated Au NPs in chloroform appeared in the UV region.[88] Mortier et al.[89] accomplished the SPR band near 565 nm for Au NPs fabricated through ablation of Au wire in chloroform with ns pulses at 1064 nm. Karolı´na et al.[90] demonstrated UV region characteristic absorption bands for Au NPs fabricated at different pulse energies in chloroform and 5, 10, 15, 20-tetrakis-4-pyridylporphine (TPyP). Our earlier studies suggested that spherical chlorinated Cu NPs in chloroform achieved by irradiating ~2 ps, 800 nm pulses depicted characteristic absorption band in the 370–390 nm spectral region and cubical NPs demonstrated absorption bands in UV/visible spectral region.[87]

Corroles have been preferred for our studies because they are tetrapyrrolic organic molecules and generally demonstrate porphyrin type spectra,[90] with strong absorption in the visible region. Moreover, the pyrole–pyrole linkage appears to provide strong fluorescence properties in corroles than the porphyrin counterparts.[90,91] These assets demonstrate potential for using corroles in real time applications such as cancer diagnostics, optical limiting and solar cells and photonics.[91] In this part, we demonstrate (a) fabrication of Cu colloids in diluted triphenyle corrole (TPC) and Tritolyl corrole (TTC) solutions (25 μM) using ps ablation method (b) fabrication of stable chlorinated Cu NP by ablating pure copper targets in chloroform (c) significant orders of magnitude enhancement in SEF studies from TTC and TPC using Cu/CuCl nanocomposites fabricated in chloroform than the chlorinated Cu NPs suspended in diluted corrole solutions and SEF studies which are in the order of 10^5-10^7.

5. 2.2. Fabrication process

In this study Cu targets were ablated in chloroform and in diluted TPC, TTC (2.5×10^{-5} M) solutions to fabricate chlorinated Cu NPs and suspensions of chlorinated Cu NPs in corroles, respectively. Briefly, in the ULAL method Cu metal target is

placed at the bottom of Pyrex cell filled with liquid. Typical height of the liquid above the surface of metal target was ~5 mm. The spot size on the sample surface was estimated to be ~90 μm. Typical fluence of ~2.5 J/cm^2 and an ablation time of 30 minutes were used. The liquid filled Pyrex cell with Cu target was placed on a motorized X-Y stage which was controlled by a ESP 300 motion controller. The stages (Newport) were translated to draw periodic lines on Cu target at separation of ~60 μm. To avoid ambiguity the fabricated Cu colloids in TTC, TPC and pure chloroform are labeled as NP1, NP2 and NP3, respectively. The shape/size of NPs and absorption characteristics were characterized by TEM, UV-visible absorption spectra, respectively. It was observed that the morphologies of fabricated NPs were spherical in nature. Crystallographic phases and composition of fabricated NPs were confirmed by selective area electron diffraction pattern (SAED).

5.2.3. Characterization of Cu colloids in chloroform

Figures 5.14(a), 5.14(c) illustrate the TEM images of NP1, NP2 and insets show the size distribution. It was observed that the morphologies of fabricated NPs were spherical in nature. Following a Gaussian fit of the size distribution histogram; average sizes of the NPs were found to be ~9.5 nm and ~38 nm in NP1 and NP2, respectively. Figures 5.14(b), 5.14(d) illustrate the SAED spectrum of NP1 and NP2, respectively. The shape of SAED pattern revealed that the particles were nanocrystalline in structure and the measured inter planar separations (d) for NP1 were 3.2 Å and 2.6 Å, in agreement with those of copper chloride (CuCl) crystal planes [(200), and(211)] and 2.2 Å, 1.82 Å and 1.28 Å matching with Cu (111), (200) and (220) planes. In the case of NP2,'d' values were 4.6 Å, 2.8 Å, 1.7 Å in good agreement with CuCl planes of (110), (210), (123), and the atomic spacing values of 2.19 Å, 1.81 Å, and 1.36 Å in good agreement with Cu crystal planes of (111), (200), and (220).SAED results revealed that Cu NPs and CuCl NPs were formed in the colloidal solutions. Similarly, from the TEM images of NP3 presented in figure 5.13 (e) it is evident that majority of produced NPs were smaller in size with a few NPs with large dimensions. The mean diameter of small particles, evaluated by Gaussian fit, was ~11 nm [inset of figure 5.14(e)]. Similarly, the estimated average size of NPs with larger dimensions was ~25 nm.

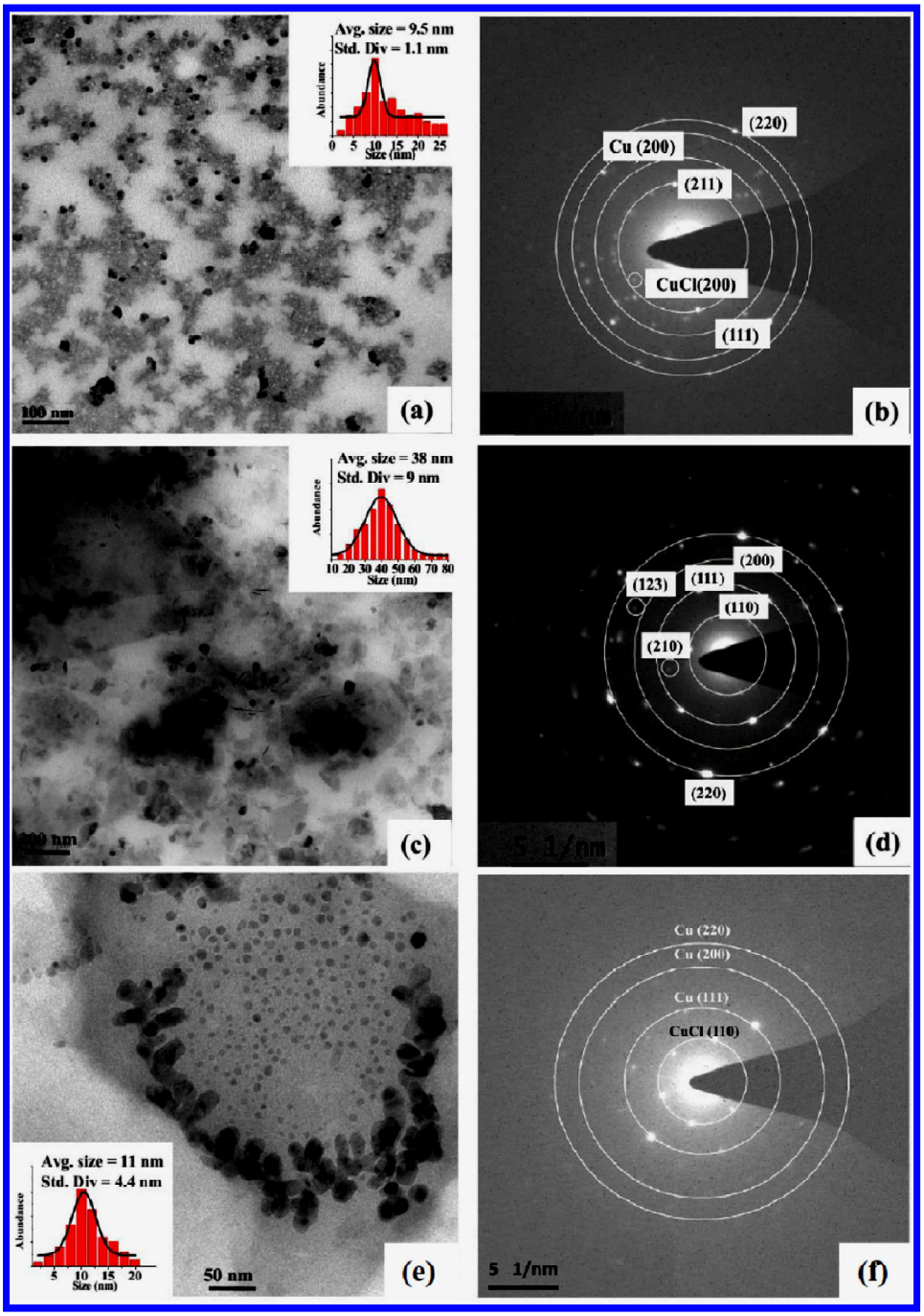

Figure 5.14 TEM micrographs of corrole/Cu colloids prepared in liquid media: (a) NP1 in TTC, (c) NP2 in TPC and (e) NP3 in chloroform. Insets of (a), (c) and (e) illustrate the size distribution. (b), (d) and (e) SAED patterns of NP1 in TTC, NP2 in TPC and NP3 in chloroform.

Figure 5.14(f) illustrates SAED pattern of NP3 and it is evident that NP-3 phase was nanocrystalline. The ring pattern in SAED was indexed with cubic phase of CuCl crystal planes, which were confirmed from the measured inter-planar spacing (estimated from the diameter of rings in SAED image). The prevalence of CuCl (110)

with ‘d’ spacing of 4.5 Å and Cu (111), (200), and (220), with corresponding ‘d’ spacing values of 2.18 Å, 1.81 Å and 1.29 Å, respectively, confirmed the formation of cubic phase for both Cu and CuCl NPs.

Figures 5.15(a) and 5.15(b) illustrate the UV-Visible absorption spectra of both NP1 and NP2 colloidal solutions. The spectra demonstrated a small SPR peak near ~590 nm in both the cases of NP1 and NP2. These small humps in the spectra confirmed the presence of Cu NPs in solution. Moreover, the characteristic absorption peak observed near 350 nm in both the cases (NP1 and NP2) corresponds to the formation of CuCl NPs in colloidal solution. Similar characteristic peaks of copper chloride NPs have been reported recently by our group[72,87] One more absorption peak was observed in the UV-region (near 300 nm) which is assigned to the metal inter-band transitions. This could be due to the reactivity of Cu with atmospheric oxygen forming some metal products such as copper oxide and hydroxide. The other, broad absorption peak at 656 nm in the spectra confirmed that corrole molecules within the colloidal solution have not been damaged due to laser ablation. However, the characteristic peak of corrole molecule near 550 nm was blue shifted to 510 nm which, probably, could be due to the formation of corrole radicals.[90] Figure 5.14(c) illustrates the absorption spectra of NP3 and the absorption band obtained in UV-region was near 376 nm. There was also a small absorption band observed near 594 nm confirming the presence of Cu NPs in NP-3 similar to the case of NP1 and NP2. Insets of figure 5.15(a)-(c) depict the magnified spectra of absorption peak. The presence of a band in the UV/Visible region and yellow coloration of the samples suggest the formation of Cu/CuCl nanocomposites and CuCl NPs. From the obtained characterization data we believe that at some stage of ablation process a sandwich type of material such as $TTC^{-2}/Cu^{+3}/Cl^{-}$ (or) $TPC^{-2}/Cu^{+3}/Cl^{-}$ could have been produced on the surface of Cu NP and finally TTC-Cu-Cl and TPC-Cu-Cl colloidal solutions were formed in NP1 and NP2, respectively.[90] The provisional interaction of short-lived metallic plume with Cl ions in the surrounding chloroform environment at the time of ablation results in CuCl NPs and Cu NPs in small amounts. Whereas in the case of NP3 there could be formation of CuCl layer on the surface of the Cu NPs allowing the formation of Cu/CuCl nanocomposites and the characteristic band of the CuCl layer overcame the absorption band in the SPR region.

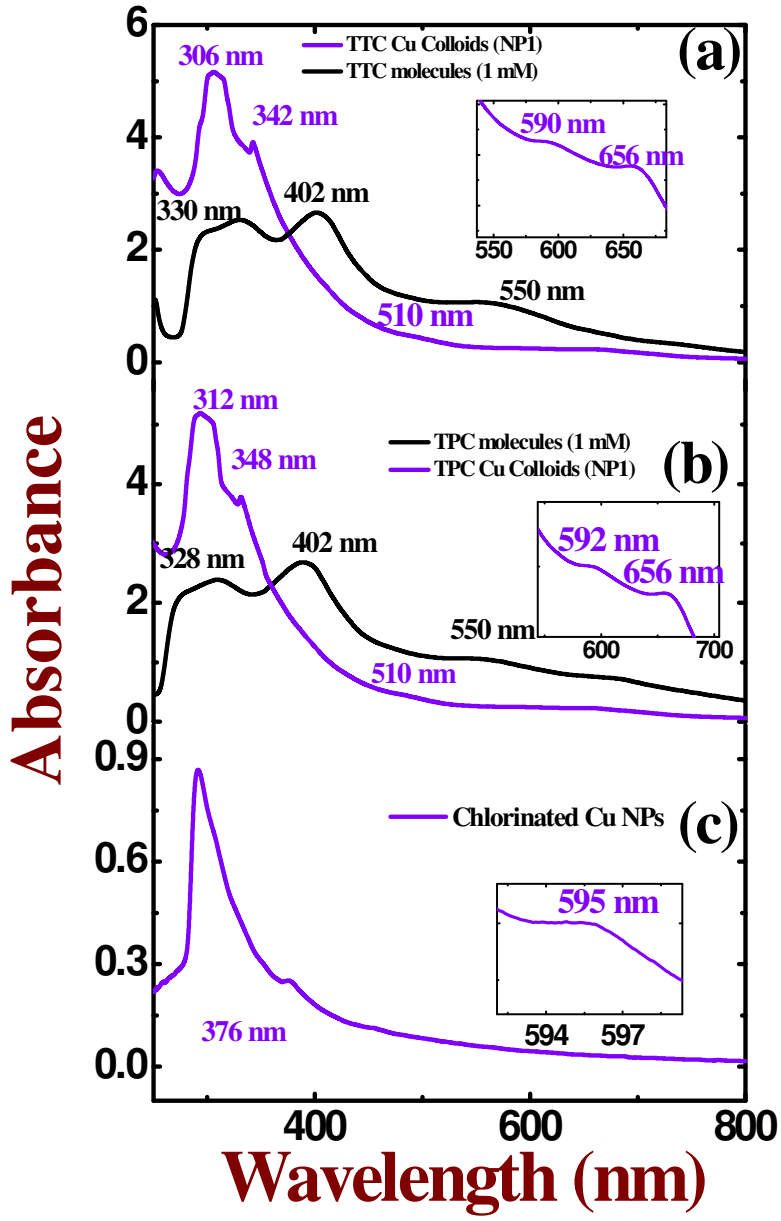

Figure 5.15 UV-Vis absorption spectra of colloidal corrole and chlorinated Cu NPs.**(a)** TTC (NP1) **(b)** TPC (NP2) and **(c)** chloroform (NP3).

5.2.4. SEF studies

SEF spectra have been recorded using micro-Raman spectrometer (WiTec-300 alpha) with 532 nm excitation source and spectra were collected through a CCD camera. The laser beam was focused on analytes placed on Cu substrates using microscopic objective [100 X, NA=0.9] and back scattered signal was collected through the same objective. Two types of SEF measurements have been performed. A tiny drop (~10 µL) of (a) manually mixed corroles solution (1 nM) and chlorinated Cu

NPs and (b) colloidal corrole Cu NPs were deposited on the cover slips. Three SEF spectra were recorded at different positions on the substrate and an average of the 3 spectra obtained was considered for analysis. Typical acquisition time used was 5s.

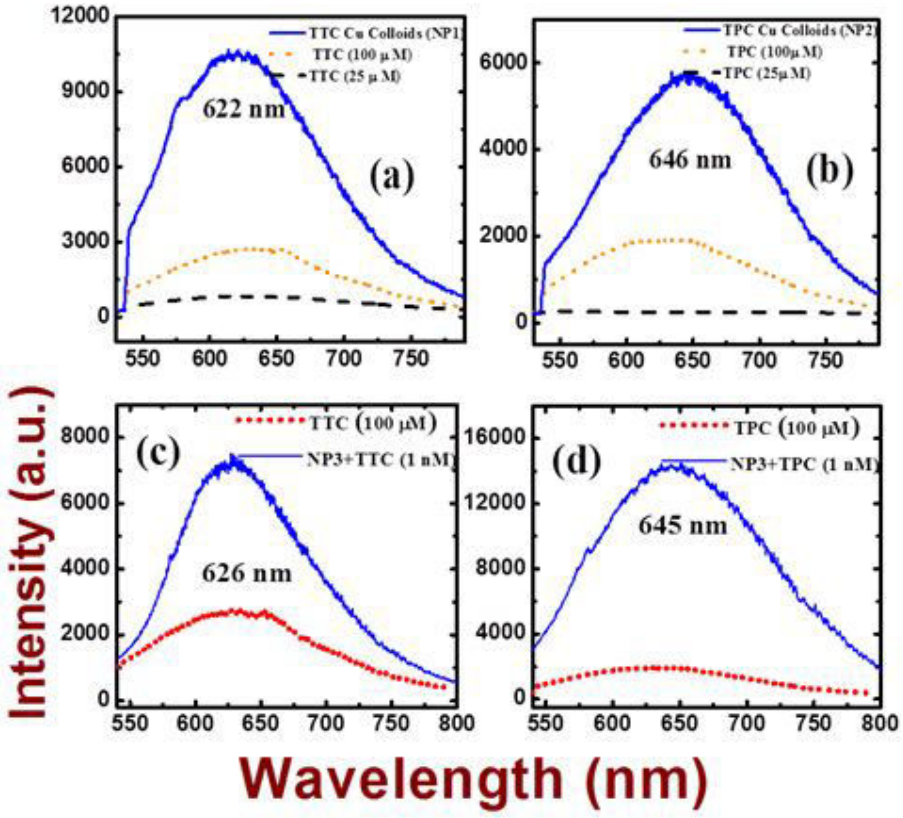

Figure 5.15 SEF spectra recorded from **(a)** TTC Cu Colloids (NP1) and **(b)** TPC Cu colloids (NP2). TTC (100 μM) and TPC (25 μM) spectra are represented by orange/dotted line and black/dashed line, respectively. The spectrum of NP1 (NP2) is represented by blue/solid line. SEF spectra recorded from **(c)** TTC and **(d)** TPC corroles adsorbed on NP3 individually. TTC (TPC) spectra are represented by red/dotted lines and TTC/TPC + NP3 by blue/solid lines. The integration time used was 5 s.

Figure 5.15 demonstrates the SEF spectra from (a) NP1and (b) NP2. The enhancements were estimated by comparing with characteristic bands obtained in normal fluorescence spectra (NFS) of TTC (100 μM) and TPC (100 μM) at higher concentrations. Comparison of SEF and NFS of both TTC and TPC revealed that the intensity of fluorescence band in SEF spectra was enhanced by 13 and 333 times, respectively. Evidently, similar bands appeared in SEF (622 nm for TTC and 646 nm for TPC) spectrum and NFS as well. We did not observe any visible peak shift in SEF spectra compared to the peaks in NFS. A tiny drop (~10 μL) of manually mixed solution of corroles (1×10^{-9}M) and Cu/CuCl NPs in chloroform was placed on the glass slide and dried. Recorded SEF spectra of these dried samples are shown in

figures 5.16(c) and 5.16(d). The spectra illustrated very high intensity at 626 nm and 645 nm for TTC and TPC, respectively. SEF spectra of lower concentration (10^{-9} M) analytes (TTC and TPC) were compared with the higher concentration (1×10^{-4} M) spectra to estimate the E.F.'s and were found to be ~$2.7\times10^{5}$and ~7.1×10^{5} for TTC and TPC, respectively.

Fluorescence enhancements in the present case, possibly, occurs due to (a) electromagnetic mechanism which motivates the amplification of incident field through excitation of surface Plasmons (b) increase of quantum yield and radiative decay rates. In the first case of TTC-Cu-Cl and TPC-Cu-Cl colloidal solutions, fluorophores (TTC and TTC) were strongly adsorbed on metal surfaces inciting quenching of fluorescence.[80,93] Moreover, there could be re-absorption of the fluorescence emission band through the attached Cu NPs whose SPR band falls in the range of fluorescence band of fluorophore.[80] Due to the re-absorption, fluorescence might have quenched significantly. In the second case, fluorophores (TTC and TPC) might not completely sit on the Cu NPs surface since it was a passive mixing of Cu NPs to TTC and TPC. In this case, due to the local field effect[93] of Cu NPs which were in the proximity of fluorophores, significant fluorescence enhancement was observed with very minimal quenching of fluorescence.[80,93]Furthermore, re-absorption of fluorescence emission band by the Cu NPs in the neighbourhood was possibly absent since their surface was passivated by CuCl layer.

5.3. Summary

- SERS spectra of ANTA demonstrated that large Raman signal enhancements were observed from (MCuNS1 and SCuNS1) multiple line ablated and single line ablated Cu NSs in acetone. In particular, MCuNS1 (SCuNS1) nano cylindrical grains (nanoparticle grains) were observed on the top of LIPSS. Additionally, among the substrates investigated MCuNS2 (in DCM), whose surface topography comprised of micron sized pillars, and MCuNS4 (in chloroform), containing roughened pillars along with nanoparticle grains, demonstrated stronger enhancements for R6G. Finally, the substrates ablated in four liquids through multiple and single line ablations were observed to illustrate the similar Raman enhancement for TNT. The reproducibility of the

Cu targets for trace level detection of explosive molecules was dealt with a simple cleaning procedure.

- The trace level detection of an explosive molecule FOX-7 from CuS-25, CuS-50, CuS-100, CuS-200, CuS-300 and CuS-400 were fabricated with different pulse energies, was studied by SERS technique with 532 nm excitation. Estimated EFs for FOX-7 (25 μM) were in the range of ~10^5 for all the substrates. Moreover, SERS of ANTA and CL-20 molecules from Cu-200 revealed that large enhancement and estimated E.Fs were in the range of 10^5 – 10^8 through the simple cleaning process.
- The produced Cu NS with different pulse numbers such as CuNS-250, CuNS-300, CuNS-500, CuNS-1000 and CuNS-2000, were utilized for SERS studies. Among all the Cu substrates studied CuNS-300 and CuNS-500 demonstrated superior enhancement for FOX-7 and R6G than other Cu NSs, respectively.
- Ag plating Si NSs have been synthesized using ion beam deposition system and they were utilized for SERS studies of ANTA molecules of concentration 1 μM. Ag-SiNS-100 demonstrated the superior enhancement ~10^7 than others.
- Complex Cu NPs were fabricated in TTC, TPC and chloroform by means of ps laser ablation such as TTC-Cu-Cl, TPC-Cu-Cl colloidal solutions and Cu/CuCl nanocomposites, respectively. Significant enhancements (~10^5) in the fluorescence were obtained for TTC/TPC placed on Cu/CuCl nanocomposites compared to the case wherein fluorophores were directly adsorbed (E.F. ~333) on the substrates (TTC-Cu-Cl, TPC-Cu-Cl colloids).

Reference

1. M. Fleischman, P. J. Hendra and A. McQuillan, J. Chem. Phys. Lett. **26**, 163 (1974).
2. D. L. Jeanmaire and R. P. V. Duyne, Annu. Rev. Phys. Chem, **84**, 1 (1977)**.**
3. M. G. Albrecht and J. A. Creighton, J. Am. Chem. Soc. **99**, 5215 (1977).
4. H.J. Seki, J. Electron Spectrosc. Relat. Phenom. **39**, 239 (1986).
5. M. Moskovits, Rev. Mod. Phys. **57**, 783 (1985).
6. A. Crookell, M. Fleischmann, M. Hanniet and P. J. Hendra, Chem. Phys. Lett. **149,** 123 (1988).
7. D. B. Chase and B. A. Parkinson, Appl. Spectrosc. **42,** 1186 (1988).
8. S. M. Angel, L. F. Katz, D. D. Archibald and D. E. Hongis, Appl. Spectrosc. **43**, 367(1989).
9. K. Kniepp, Exp. Tech. Phys. **38**, 3 (1990).
10. S. Nie and S. R. Emory, Science **275**, 1102 (1997).
11. K. Kneipp, Y. Wang, H. Kniepp, L. T. Perelman, I. Itzkan, R. R. Dasari and M. Feld, Phys. Rev. Lett. **78**, 1667 (1997).
12. D. L. Stokes, D. Hueber and T. Vo-Dinh, Towards single molecule detection with SERS detection with SERS detection using solid substrates, Pittsburgh Conference, New Orleans, LA, 1-5 March 1998.
13. P. M. Fierro-Mercado, and S. P. Hernandez-Rivera, Int. J. Spec. Article ID 716527 (2012). http://dx.doi.org/10.1155/2012/716527
14. T. Ivan and H. Jörg, J. Raman Spectrosc. **44,** 536 (2013)
15. J. R. Lakowicz, C. D. Geddes, I. Gryczynski, J. Malicka, Z. Gryczynski, K. Aslan, J. Lukomska, E. Matveeva, J. Z hang, R. Badugu, and J. Huang, J. Fluoresc. **14**, 425 (2004)
16. J. Fontana, J. Livenere, F. J. Bezares, J. D. Caldwell, R. Rendell, and B. R. Ratna, Appl. Phys. Lett. **102,** 201606 (2013)
17. Y. Sun and Y. Xia, Science. **298**, 2176 (2002).
18. B. Wiley, Y. Sun, B. Mayers and Y. Xia, Chem. A. Eur. J. **11**, 454 (2005).
19. Y. Xia and N. J. Halas, MRS Bull. **30**, 338 (2005).
20. C. L. Nehl, H. Liao and J. H. Hafner, Nano Lett. **6**, 683 (2006).
21. P. Gopala Krishna, S. Hamad, S. P. Tewari, S. Sreedhar, M.D. Prasad, and S. Venugopal Rao, J. Appl. Phys. **113,** 073106 (2013)
22. P. Gopala Krishna, S. Hamad, S. Sreedhar, S. P. Tewari, and S. Venugopal Rao, Chem. Phys. Lett. **530,** 93 (2013)
23. Y. Yang, J. Yang, C. Liang, H. Wang, X. Zhu, and N. Zhang, Opt. Exp. **17**, 21124 (2009)
24. G. Miyaji and K. Miyazaki, Opt. Exp. **16,** 16265 (2008)
25. G.K. Podagatlapalli, S. Hamad, and S. Venugopal Rao, Appl. Surf. Sci. **303**, 217 (2014).
26. S. Hamad, P. Gopala Krishna, S. Sreedhar, S. P. Tewari, and S. Venugopal Rao, Proc. of SPIE **8245**, 82450L-1 (2012)
27. I. Lee, S. W. Han and K. Kim, J. Raman. Spectrosc. **32**, 947 (2001).
28. T.S. Lau, G. Levi, F. Bozon-Verduraz, A.V. Petrovskaya, A.V. Simakin and G. A. Shafeev, App. Surf. Sci. **254**, 1236 (2007).
29. L. Yang, Z. Bao, Y. Wu and J. Liu, J. Raman Spectrosc. **43**, 848 (2012)
30. Q. Su, X. Ma, J. Dong, C. Jiang, and W. Qian, ACS Appl. Mater. Interfaces **3,** 1873 (2011)

31. Y. Wang, N. Lu, W. Wang, L. Liu, L. Feng, Z. Zeng, H. Li, W. Xu, Z. Wu, W. Hu, Y. Lu, and L Chi, Nano Research. **6,** 159 (2013)
32. L. Yang, Z. Bao, Y. Wu, and J. Liu, J. Raman Spectrosc. **43,** 848 (2012)
33. J. A. Ciezak, and S.F. Trevino, Chem. Phys. Lett. **403,** 329 (2005)
34. E. C. Le Ru, E. Blackie, M. Meyer, and P. G. Etchegoin, J. Phys. Chem. C. **111,** 13794 (2007)
35. Y. Yang, Z. Y. Li, K. Yamaguchi, M. Tanemura, Z. R. Huang, D. L. Jiang, Y. H. Chen, F. Zhou, and M. Nogami, Nanoscale **4,** 2663 (2012)
36. K. M. Kosuda, J. M. Bingham, K. L. Wustholz, and R. P. Van Duyne, Comprehensive Nanosci. Tech. **3**, 263 (2011).
37. L. Gunnarsson, E. J. Bjerneld, H. Xu, S. Petronis, B. Kasemo, and M. Ka¨ll, Appl. Phys. Lett. **78**, 802 (2001)
38. B. Lu-Yang Chen, J. Yu, T. Fujita, and M. Chen, Adv. Funct. Mater. **19**, 1221 (2009)
39. J. Cejkova, V. Prokopec, S. Brazdova, A. Kokaislova, P. Matejka, and F. Stepanek, Appl. Surf. Sci. **255**, 7864 (2009)
40. L. Polavarapu and L.M. Liz-Marza´n, Phys. Chem. Chem. Phys. **15**, 5288 (2013).
41. K. R. Hall, L. C. Eagleton, A. Acrivos, and T. Vermeulen, I & EC Fundamentals, **5**, 212 (1966)
42. N. Ahalya, R.D. Kanamadi, and T.V. Ramachandra, Ind. J. Chem. Tech. **13**, 122 (2006),
43. K.Y. Foo, and B.H. Hameed, Chem. Eng. Journal **156**, 2 (2010); J. He, S. Hong, L. Zhang, F. Gan, and H. Yuh-Shan, Fres. Env. Bul. **19**, 2651 (2010).
44. (http://www.hood.edu/uploadedFiles/Hood_College/Home/Academics/Departments/Chemistry_and_Physics/Thermo.Lab.Manual.Adsorption.pdf) with title "Adsorption of Pyridine Measured with SERS".
45. S. Hamad, G. Krishna Podagatlapalli, M. A. Mohiddon, S. Venugopal Rao, Appl. Phys. Lett. **104**, 263104 (2014)
46. J. A. Ciezak, and S.F. Trevino, Chem. Phys. Lett. **403,** 329 (2005)
47. Z. A. Dreger, Y. Tao, and Y. M. Gupta, J. Phys. Chem. A. **118,** 5002 (2014).
48. Z.-M. Jin, W. Gu, X.-B. Shi, Z.-K. Wang, Z.-Q. Jiang, and L.-S. Liao, Adv. Opt. Mater. **2,** 588 (2014).
49. M. Ghosh, V. Venkatesan, N. Sikder, and A. K. Sikder, Central Euro. J. Energ. Mate., **10**, 419 (2013)
50. L. En-Chiang, J. Fang, P. Se-Chul, S. Thomas, J. Pezoldt, and H. O. Jacobs, Adv. Mater.**25**, 3554 (2013)
51. G. Santoro, S. Yu, M. Schwartzkopf, P. Zhang, S.K.Vayalil, J. F. H. Risch, M. A. Rübhausen, M. Hernández, C. Domingo, S.V. Roth, Appl. Phys. Lett. **104**, 243107 (2014)
52. S. Botti, S. Almaviva, L. Cantarini, A. Palucci, A. Puiu and A. Rufoloni, J. Raman Spectrosc.**44**, 463 (2013)
53. J. Mbah, K. Moorer, L. Pacheco-Londoño, S. Hernandez-Rivera, and G. Cruz, J. Raman Spectrosc. **44**, 723 (2013)
54. Surface-Enhanced Raman Scattering - Physics and Applications, edited by K. Kneipp, M. Moskovits, and H. Kneipp (Springer, 2006)
55. C. Wang, Y. C. Chang, J. Yao, C. Luo, S. Yin, P. Ruffin, C. Brantley, and E. Edwards, Appl. Phys. Lett. **100,** 023107 (2012).
56. F. Mei, X. Xiao, Z. Dai, J. Xu, Y. Zhou, C. Zhong, and L. Wu, J. Appl. Phys. **114**, 083523 (2013)

57. L. Guo, C. Xing Zhang, L. Deng, G. X. Zhang, H. J. Xu, and X. M. Sun, J. Appl. Phys. **115**, 213101 (2014)
58. E. Sheremet, R. D. Rodriguez, D. R. T. Zahn, A. G. Milekhin, E. E. Rodyakina, and A. V. Latyshev, J. Vac. Sci. Technol. B **32**, 04E110 (2014)
59. S. Chan, S. Kwon, T.-W Koo, P. L. Lee, and A. A.Berlin, Adv. Mater.**15**, 1595 (2003)
60. H. Lin, J. Mock, D. Smith, T. Gao, and M.J. Sailor, J. Phys. Chem. B.**108**, 11654 (2004)
61. A.Yu. Panarin, S.N. Terekhov, I.A. Khodasevich, and P.-Y. Turpin, Proc. of SPIE **6728**, 672828 (2007)
62. Z. Pan, A. Zavalin, A. Ueda, M. Guo, M. Groza, A. Burger, R. Mu, and S. H. Morgan, Appl. Spectrosc. **59**, 782 (2005).
63. L. Haohao, J. Mock, D. Smith, T. Gao, and M. J. Sailor, J. Phys. Chem. B, **108**, 11654 (2004)
64. X. Hou, and Y. Fang, J. Colloid. Interface Sci. **316**, 19 (2007)
65. Q. Xu, R. P. -Castillejos, Z. Li, and G. M. Whitesides Nano Lett. 6, 2163 (2006).
66. J. Yang, J. Li, Z. Du, Q. Gong, J. Teng and M. Hong, Scientific Reports **4**, 6657 (2014)
67. Z. ZhiQing, Y. ZhenDong, Z. Peng and W. ZhenLin, Science China. Physics, Mechnics and Astronomy, **56**, 1806 (2013)
68. Y. Han, X. Lan, T. Wei, T. Hai-Lung and H. Xiao, Appl. Phys. A **97**, 721 (2009)
69. S. Hamad, G. Krishna Podagatlapalli, V.S. Vendamani, S.V.S. Nageswara Rao, A.P. Pathak, S.P. Tewari and S. Venugopal Rao, J. Phys. Chem. C. **118**, 7139 (2014)
70. J. Ramos, T. Potta, O. Scheideler, and K. Rege, ACS Appl. Mater. Interfaces **6**, 14861 (2014)
71. L. Kyeong-Seokm, and M. A. El-Sayed, J. Phys. Chem. B **110**, 19220(2006)
72. S. Hamad, P. Gopala Krishna, S. P. Tewari, and S. Venugopal Rao, J. Phys. D: Appl. Phys. **46**, 485501 (2013)
73. S. D. Choudhury, R. Badugu, K. Ray, and J. R. Lakowicz, J. Phys. Chem. C **116**, 5042 (2012)
74. J. R. Lakowicz, Anal. Biochem.**298**,1 (2001)
75. J. R. Lakowicz, K. Ray, M. Chowdhury, H. Szmacinski, Y. Fu, J. Zhang, K. Nowaczyk, Analyst **133**, 1308 (2008)
76. Near-Infrared Surface-enhanced Fluorescence using Silver nanoparticles in solution, Thesis by M. D. Furtaw, University of Nebraska, 2013
77. Z. Zhang, P. Yang, H. Xu, and H. Zheng, J. Appl. Phys.**113**, 033102 (2013)
78. K. Saravanan, B.K.Panigrahi, R. Krishnan, and K.G.M. Nair, J. Appl. Phys. **113**, 033512 (2013)
79. Chris D. Geddes, and Joseph R. Lakowicz, J. Fluores. **12,** 121 (2002)
80. R. J. Amjad, M. R. Sahar, M. R. Dousti, S. K. Ghoshal, and M. N. A. Jamaludin, Opt. Exp. **21**, 14282 (2013)
81. J. R. Lakowicz, Principles of fluorescence spectroscopy 3rd ed.; Springer: New York, 2006.
82. A. Kinkhabwala, Z. Yu, S. Fan, A. Yuri, K. Mu¨llen, and W. E. Moerner, Nat. Phot.**3**, 654 (2009)
83. S. Kuhn, U. Hakanson, L. Rogobete, and V. Sandoghdar, Phys. Rev. Lett. **97**, 017402 (2006)

84. J. Zhang, Y. Fu, M. H. Chowdhury, and J. R. Lakowicz, Nano Lett.**7,** 2101 (2007)
85. Y. Chen, K. Munechika, and D. Ginger, Nano Lett.**7**,690 (2007)
86. Y. Zhang, K. Aslan, and M. J. R. Previte, and C. D. Geddes, Appl. Phys. Lett. **90,** 173116 (2007)
87. S. Hamad, P. Gopala Krishna, S.P. Tewari, S. Venugopal Rao,Pramana-J. Phys. **82**, 331 (2014); P.T. Anusha, D. Swain,T.S. Prashant, S. P. Tewari, L. Giribabu and S. Venugopal Rao, J. Phys. Chem. C **116**, 17828 (2012)
88. A.V. Simakin, V.V. Voronov, N.A. Kirichenko, G.A. Shafeev, Appl. Phys. A **79**, 1127 (2004)
89. T. Mortier, T. Verbiest, A. Persoons, Chem. Phys. Lett. **382**, 650 (2003)
90. S. Karolı´na, J. Pfleger, and P. Marek, Appl. Surf. Sci. **256**, 2979 (2010)
91. V. S. Shetti, U. R. Prabhu and M. Ravikanth, J. Org. Chem. **75**, 4172 (2010).
92. S. Hamad, S. P. Tewari, L. Giribabu and S. Venugopal Rao, J. Porphy. Phth.**16**, 140 (2012)
93. G. Corrado, S. Sanchez-Cortes, O. Francioso, and J.V. Garcia-Ramos, Anal. Chim. Acta **616,** 69 (2008)

INTENTIONAL BLANK PAGE

6

NLO, Time Resolved Spectroscopic Studies of Cu and Si Colloids

Abstract

In this chapter we discuss the fundamentals of nonlinear optical (NLO) properties and basic physics involved in it. The features of Z-scan, four wave mixing and pump-probe techniques along with brief experimental procedures of techniques are also discussed. Ps NLO studies of laser fabricated colloidal Cu NPs, corrole conjugated Cu NPs and fs NLO studies of colloidal Si NPs generated by ultrafast laser ablation in different liquid media have been performed by Z-scan open aperture (OA) and closed aperture (CA) techniques to obtain the NLO coefficients [nonlinear absorption and nonlinear refraction]. Along with Z-scan experiments, fs degenerate four wave mixing (fs-DFWM) experiment in BOXCARS geometry was also utilized to extract third order nonlinear susceptibility for colloidal Cu NPs, corrole conjugated Cu NPs. Finally, the excited state dynamics of Cu/Si colloids by fs pump-probe experiments are discussed.

6.1. Introduction

Development of photonic devices to process information with large speeds (using all-optical techniques) has been the motivation for materials scientists to synthesize and investigate novel nonlinear optical (NLO) materials. There are large numbers of novel materials fabricated for NLO applications with fs or ps time response.[1] The attention on new NLO materials has been confined mainly to the progress of optical limiters for sensor protection[2], mode-locking elements[3], in optical switching[4], etc.

6.2. Nonlinear optical processes

When intense laser pulses interact with material nonlinear optical (NLO) effects are manifested beyond certain input peak intensities. The electrons oscillations follow anharmonicity which produce light with different frequency and amplitude from the fundamental beam. The electrons are responsible for the nonlinearity in the material and their oscillations create induced dipole moments, which are responsible for the applied field dependent polarization. The induced polarization can be described by the following equation

$$\tilde{P}(t) = \epsilon_0[\chi^{(1)}\tilde{E}(t) + \chi^{(2)}\tilde{E}^2(t) + \chi^{(3)}\tilde{E}^3(t) + \cdots] \quad (6.1)$$

The quantity ϵ_0 is the electric permittivity of vacuum, $\chi^{(1)}$ is linear optical susceptibility, $\chi^{(2)}$ and $\chi^{(3)}$ are refered as second and third order NLO susceptibilities, respectively. $\tilde{P}(t)$ and $\tilde{E}(t)$ are known as induced polarization and applied electric field, respectively. The second order susceptibility can be provided by the non centro-symmetric media only since this media do not exhibit property of inversion symmetry (for example SHG crystals such as BBO, KTP, KDP etc). Second harmonic generation, sum frequency generation and difference frequency generation phenomena occur due to second order nonlinear optical susceptibility$[\chi^{(2)}]$. The inversion symmetry property can be demonstrated by other samples such as liquid media, solids with amorphous phase and some of the inorganic crystals etc. and therefore, $\chi^{(2)}$ cancels out identically. But, both media exhibit third order NLO interactions and provide third order nonlinear optical susceptibility$[\chi^{(3)}]$.

6.3. Third order nonlinear interactions

In the case of third order process, the induced polarization can be described as[5]

$$\tilde{P}^{(3)}(t) = \epsilon_0 \chi^{(3)} \tilde{E}^3(t) \tag{6.2}$$

The applied electric field equation for a monochromatic light is illustrated as

$$\tilde{E}(t) = E_0 \, Cos\omega t \tag{6.3}$$

By substituting equation (6.3) into the equation (6.2) and following $Cos3\theta = 4Cos^3\,\theta - 3Cos\theta \; (\theta = \omega t)$

The resultant nonlinear polarization equation can be written as

$$\tilde{P}^{(3)}(t) = \frac{\epsilon_0}{4}(\chi^{(3)} {E_0}^3 \, Cos3\omega t + \chi^{(3)} {E_0}^3 \, Cos\omega t) \tag{6.4}$$

From the above equation, the first term represents the third harmonic generation at frequency 3ω which is generated by incident light frequency ω.

6.3.1. Nonlinear Refractive Index

The second term in equation (6.4) contributes towards the nonlinear refractive index (n_2) experienced by incident optical field which is real part of complex third order susceptibility. The total refractive index with the involvement of intensity dependent nonlinear refractive index can be written as $n = n_0 + n_2 I$, where n_0 refers to the linear refractive index, I represents laser intensity and n_2 is the intensity dependent (or) nonlinear refractive index which can be obtained from material's self focusing (or) self defocusing phenomenon. In this process, when the transverse mode of intensified laser light passes through the material which acts as a positive (or) negative lens,. The relation between n_2 and $\chi^{(3)}$ is described as follows[5]

$$n_2 = \frac{3}{2\epsilon_0 c n_0^2} \chi^{(3)} \tag{6.5}$$

where c is the velocity of light

6.3.2. Nonlinear Absorption

Nonlinear absorption is the phenomena which provide information on the imaginary part of third order nonlinear susceptibility. In this case, the material absorbs more than one photon simultaneously (or) step wise at higher intensities of pulsed laser. There are mainly two types of nonlinear absorption observed from materials (a) reverse saturable absorption (RSA) or two photon absorption (2PA) or multi-photon absorption (MPA) (b) saturable absorption (SA).

Reverse Saturable Absorption (RSA)

The process involving transition between ground state and excited state through an instantaneous absorption of two (or more) photons can be called as two photon absorption (or multi-photon absorption) at higher peak intensities. The nonlinear absorption equation which is the combination of linear absorption, two photon (or multi photon absorption) coefficient can be described as

$$\alpha(I) = \alpha_0 + \beta I + \gamma I^2 + \cdots \tag{6.6}$$

Here, α_0 is the linear absorption coefficient, β and γ refer to two and three photon absorption coefficients, respectively.

Once the laser beam interacts with material at higher peak intensities, the electrons get excited and make a transition from ground state to excited state by the simultaneous absorption of two/more photons. These transitions are feasible in within singlet ground (S_1) and singlet higher excited state (S_n) or through triplet states and the whole process depends on the pulse duration, applied field intensity and excitation wavelength of laser beam. The phenomenon is described as excited state absorption (ESA) if it involves two step two photon absorption (either in singlet or in triplet states). In the case of two photon absorption (2PA) (or) ESA, the absorption cross-section of excited states will be higher than the absorption cross-section in the case of linear absorption. In this case, the nonlinear absorption increases with increasing input intensity leading to lower transmission.

Saturable Absorption

In saturable absorption (SA) case, the absorption cross-section reduces with increasing input intensity which provides greater transmission. SA will be possible when the ground state absorption cross-section will be more than excited state absorption cross-section. This can be written in an equation form as [5]

$$\alpha(I) = \alpha_0 \frac{1}{1+{}^{I}/_{I_S}}, \; I = \frac{I_{00}}{1+({}^{z}/_{z_0})^2} \tag{6.7}$$

Here, I_{00} and I_S are laser peak intensity and saturation intensity, respectively, z_0 is the Raleigh range and z refers to laser beam propagation direction. If the excitation intensity I is lesser than I_s, we can consider SA as a third order process and in such cases $-(\alpha_0/I_s)$ is the equivalent of nonlinear absorption coefficient β (negative nonlinear absorption),[6] to a good approximation.

Some of the samples show complicated nonlinear absorption process (SA and RSA), e.g., RSA in SA and SA in RSA. The possibility of these two phenomena occurs only at higher peak intensities where materials could show SA behavior at the lower intensities (or) the excitation wavelength will be resonant with the absorption of the material. To interpret the switching from SA to RSA, we combine saturable absorption coefficient and two photon absorption (TPA, β) coefficients yielding the total absorption coefficient [7, 8] as

$$\alpha(I) = \alpha_0 \frac{1}{1+{}^{I}/_{I_S}} + \beta I \tag{6.8}$$

where the first term describes the negative nonlinear absorption and the second term describes positive nonlinear absorption such as RSA and/or TPA

NLO materials are also interesting in development of technologies in the fabrication of waveguides[9, 10] with intensity dependent refractive indices. Variety of large NLO properties has been established by metal NPs in different matrices fabricated by different methods.[11-24] Metal NPs are promising compared to other NPs from the viewpoint of surface Plasmon resonance (SPR).[25-26] The unique NLO properties of metal NPs can be attributed to their SPR bands. Metal NPs and Si NPs[27] in different matrices have been proved to be attractive for their large NLO coefficients

and ultrafast response times, [28] resulting from the enhancement of local electric field in the vicinity of the SPR band.

6.4. Z-scan measurements

The NLO mechanisms mainly observed in the case of metal NPs[29-32] are SA, switching [SA in RSA or RSA in SA] and simultaneous two/three photon absorption (2PA or 3PA). Experimentally observed SA, switching and simultaneous 2PA cases of metal NPs can be attributed to the intra-band (or) inter-band transitions. The occurrence of SA[31] is possible in two cases with excitation at 800 nm (1.55 eV) (a) intra-band electronic excitations within the conduction band occurring at lower peak intensities in the vicinity of SPR[32] and (b) inter-band electronic excitations taking place from d-band to s- (or) p-band. Further pumping leads to excitation into higher excited states in conduction band since the free-carrier absorption cross-section will be significant at higher peak intensities and this is reflected in the switching from SA to RSA. Further pumping (highest peak intensities) can result the observation of 2PA/3PA since the electrons, through intra-band transitions, can be excited from the ground state of conduction band to higher lying excited states of conduction band (or) d-band to higher lying excited states of conduction band (inter-band transitions) via simultaneous absorption of two/three photons depending on the photon energy and the band gaps.

To determine β, γ and I_s, from the open aperture Z-scan data we used equations (6.6), (6.7) and (6.8) for fitting the experimental details.

$$\frac{dI}{dz'} = -\alpha(I)I \tag{6.9}$$

where z' corresponds to sample length.

Assuming a spatial and temporal Gaussian profile for laser pulses the normalized energy transmittance for the process of nonlinear absorption given by Sheik-Bahae et al.[33] the equation for 2PA/3PA open aperture (OA) normalized transmittance given by [33-35]

$$T_{OA} = \frac{\int_{-\infty}^{+\infty} P(t)\,dt}{\int_{-\infty}^{+\infty} P_i(t)\,dt} \tag{6.10}$$

Where *P(t)* is transmitted power through the sample and $P_i(t)$ is the initial power on the sample and the equation for 2PA open aperture nonlinear transmittance is given by [33, 35]

$$T_{OA}(2PA) = \frac{1}{\frac{1}{\pi^2} q_0(z,0)} \int_{-\infty}^{\infty} [1 + q_0(z,0)\exp(\tau^2)]\, d\tau \tag{6.11}$$

Three-photon absorption (3PA) equation is

$$T_{OA}(3PA) = \frac{1}{\pi^{1/2} P_0} \int_{-\infty}^{\infty} ln\{[1 + p_0^2 exp(-2x^2)]^{1/2} + p_0 \exp(-x^2)\}\, dx \tag{6.12}$$

where, $q_0(z,0) = \frac{\beta I_{00} L_{eff}}{1 + \left(z/z_0\right)^2}$, $p_0(z,0) = \frac{2\gamma I_{00}^2 L'_{eff}}{1 + \left(z/z_0\right)^2}$.

I_{00} is the peak intensity, z is the sample position, $z_0 = \pi\omega_0^2/\lambda$ is the Rayleigh range: ω_0 is the beam waist at the focal point (z=0), λ is the laser wavelength; effective path length in the sample of length L for 2PA, 3PA is given as $L_{eff} = \frac{1 - e^{-\alpha_0 L}}{\alpha_0}, L'_{eff} = \frac{1 - e^{-2\alpha_0 L}}{2\alpha_0}$

If $q_0<1$ or $p_0<1$ eq.(6.11) or (6.12) can be expanded in a Taylor series as

$$T_{OA}(2PA) = \sum_{m=0}^{\infty} (-1)^m \frac{q_0^m}{(m+1)^{3/2}} \tag{6.13}$$

$$T_{OA}(3PA) = \sum_{m=1}^{\infty} (-1)^{m-1} \frac{p_0^{2m-2}}{(2m-1)!(2m-1)^{1/2}} \tag{6.14}$$

Furthermore, if the higher order terms are ignored, we obtain:

$$T_{OA}(2PA) = 1 - \beta I_{00} L_{eff} \Big/ \left(1 + \left(z/z_0\right)^2\right) 2^{3/2} \tag{6.15}$$

$$T_{OA}(3PA) = 1 - 2\gamma I_{00}^2 L^1{}_{eff} \Big/ \left(1 + \left(z/z_0\right)^2\right) 3^{3/2} \tag{6.16}$$

Similarly the normalized closed aperture transmittance is given by[33-35]

$$T\left(\frac{z}{z_0}\right) = 1 - \frac{4\left(\frac{z}{z_0}\right)\Delta\phi_0}{\left[\left(\frac{z}{z_0}\right)^2 + 1\right]\left[\left(\frac{z}{z_0}\right)^2 + 9\right]} \tag{6.17}$$

Where Z is the sample position, $z_0 = \pi\omega_0^2/\lambda$ is the Rayleigh range: ω_0 is the beam waist at the focal point (Z=0), λ is the wavelength; $\Delta\phi_0$ is the nonlinear phase shift. Nonlinear refractive index can be determined from $\Delta\phi_0$.

The difference between the peak and valley transmission ($\Delta T_{p\text{-}v}$) written in terms of the on axis phase shift at the focus as,

$$\Delta\phi_0 = \frac{\Delta T_{p-v}}{0.406(1-S)^{0.25}} \quad (6.18)$$

Where S (25%) is the aperture linear transmittance and is calculated using $S=1-\exp(-2r_a^2/\omega_a^2)$; where r_a is the aperture radius and ω_a is the beam radius at the aperture.

The real and imaginary parts of the third-order nonlinear optical susceptibility ($\chi^{(3)}$) can be determined from β and n_2 and the equations are described as

$$\left.\begin{aligned} &\text{Re } |\chi^{(3)}| \ (m^2/V^2) = 2n_0^2 c\varepsilon_0 n_2 \ (m^2/W) \\ &\text{Im } |\chi^{(3)}| \ (m^2/V^2) = (1/2\pi) n_0^2 c\varepsilon_0 \lambda\beta \ (m/W) \\ &|\chi^{(3)}| \ (SI) = [(\text{Re } |\chi^{(3)}|)^2 + (\text{Im } |\chi^{(3)}|)^2]^{1/2} \end{aligned}\right\} \quad (6.19)$$

where 'ε_0' is the vacuum permittivity, 'n_0' is the linear refractive index of the sample and c is the velocity of light in vacuum.

In this chapter, the nonlinear absorption and n_2 of Cu/Si NPs were determined by Z-scan (open aperture and closed aperture) technique using ~2 ps and ~140 fs pulses. Fs degenerate pump-probe technique was utilized to determine the relaxation dynamics of Cu/Si NPs. Moreover, fs degenerate four wave mixing (DFWM) was exploited for resolving $\chi^{(3)}$ of Cu NPs and corrole conjugated Cu NPs.

6.4.1 Z-scan Experiments

Ps pulses were generated by Ti: sapphire amplifier (Coherent, Legend) operating at a repetition rate of 1 kHz. The input beam was spatially filtered to obtain a pure Gaussian profile in the far field. Z-scan studies[6, 36-38] were performed by focusing the 3-mm diameter input beam using a 200 mm focal length convex lens into the sample in ps domain. The experiment was performed with the samples placed in 1-mm glass/quartz cuvette which was positioned on a high resolution translation stage and the detector (Si photodiode, SM1PD2A, Thorlabs) output was connected to a lock-in amplifier. Both the stage and lock-in amplifier were controlled by a computer program. The nonlinear absorption studies were performed by open aperture (OA) Z-scan method with different peak intensities to completely understand the intensity dependent nonlinear absorption. To determine the nonlinear refraction of metal NPs we used closed aperture (CA) Z-scan technique. These CA studies were performed at

lower peak intensities where the contribution from the higher order nonlinear effects is negligible (the value of $\Delta\phi$ estimated in all the cases was $<\pi$).

6.4.2. NLO studies of colloidal Cu NPs

The third order NLO properties of the Cu colloids such as pure Cu NPs in acetone, CuCl NPs in DCM, CuO NPs in ACN and $CuCl_2$ NPs in chloroform, were investigated at a wavelength of 800 nm with ~2 ps pulses using the standard Z-scan technique. These Cu colloids were generated by multiple line (single line) ablation of Cu in acetone, DCM, ACN and chloroform which were designated as MCuNP1 (SCuNP1), MCuNP2 (SCuNP2), MCuNP3 (SCuNP3) and MCuNP4 (SCuNP4), respectively. Open aperture Z-scan data provides information about the nonlinear absorption [related to imaginary part of third order NLO susceptibility, $\chi^{(3)}$] properties while the closed aperture Z-scan data provides information on sign and magnitude of the nonlinear refractive index n_2 [related to the real part of $\chi^{(3)}$]. The linear transmittance was typically >95% for all the NPs except MCuNP1, MCuNP3 (>80%).

Figure 6.1 depicts the complete open aperture data obtained for all investigated 8 nanoparticles at both lower (open squares - 80 GW/cm^2) and higher (open stars - 125 GW/cm^2) peak intensities. Three distinct behaviors were observed: (a) reverse saturable absorption (RSA) type of behavior which could be attributed to two-photon absorption (2PA; β) (b) an effective three-photon absorption (3PA; γ_{eff}) type of behavior and (c) a switching mechanism from saturable absorption (SA) to RSA. The open aperture data of MCuNP1 [figure 6.1(a)] and MCuNP3 [figure 6.1(e)] illustrates the behavior of switching from SA to RSA at lower peak (open squares - 80 GW/cm^2) intensity and pure RSA at higher peak intensity (open stars - 125 GW/cm^2). The data obtained at higher peak intensities was fitted efficiently using only β. At lower peak intensity, SCuNP1 [figure 6.1(b)] data was fitted to β while SCuNP3 [figure 6.1(f)] did not show any NLO behavior. At higher peak intensity, both the samples SCuNP1 and SCuNP3 exhibited RSA type of behavior and the data was fitted successfully using γ_{eff} [2PA + ESA] and β, respectively. The resonances of SCuNP1 (565 nm and 310 nm) and SCuNP3 (588 nm) might have led to this observation. The open aperture data of MCuNP2 [figure 6.1(c)], SCuNP2 [figure 6.1(d)], MCuNP4 [figure 6.1(g)] and SCuNP4 [figure 6.1(h)] revealed that

2PA was dominant at both peak intensities with 800 nm excitation which can be accredited to the SPR band of nano colloids formed nearly 400 nm.

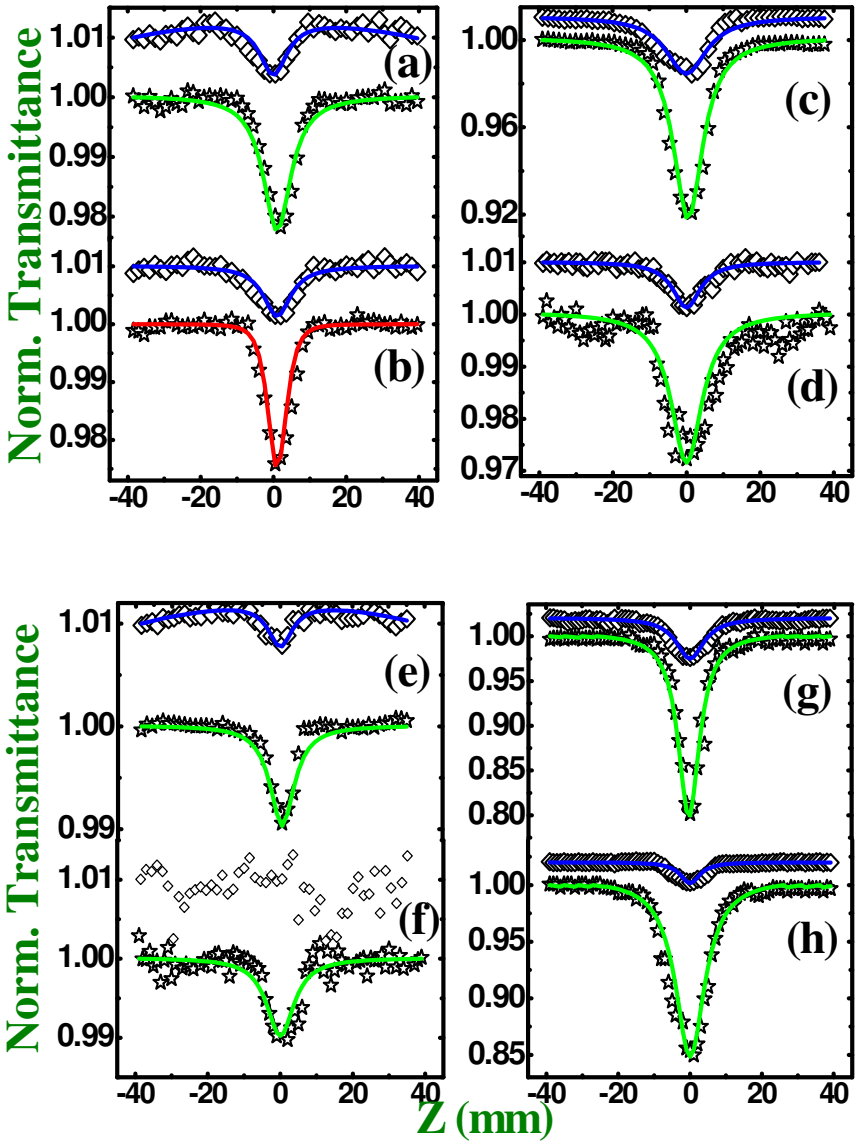

Figure 6.1 Open aperture Z-scan curves obtained for **(a)** MCuNP1 (b) SCuNP1 with varying input intensities I_{00} = 80 GW/cm^2 (open squares), I_{00} = 125 GW/cm^2 (open stars). Open aperture Z-scan curves obtained for **(c)** MCuNP2 (d) SCuNP2 with varying input intensities I_{00} = 80 GW/cm^2 (open squares), I_{00} = 125 GW/cm^2 (open stars). Open aperture Z-scan curves obtained for **(e)** MCuNP3 (f) SCuNP3 with varying input intensities I_{00} = 80 GW/cm^2 (open squares), I_{00} = 125 GW/cm^2 (open stars) and **(g)** MCuNP4 (h) SCuNP4 with varying input intensities I_{00} = 80 GW/cm^2 (open squares), I_{00} = 125 GW/cm^2 (open stars). Solid lines are the theoretical fits.

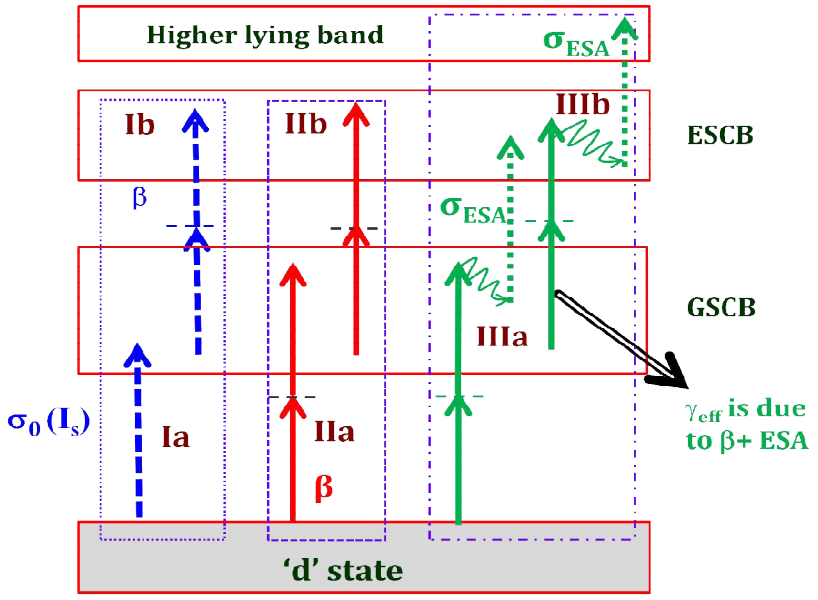

Figure 6.2 A generalized energy band diagram of the observed CuNPs (pure Cu NPs, CuO NPs, CuCl NPs, $CuCl_2$ NPs) explaining various nonlinear absorption phenomena. ESCB refers to excited state conduction band, GSCB refers to ground state conduction band.

It is extremely difficult to model the nonlinear absorption independently for NPs of different sizes and composition.[37] In such materials[30,32,38] the contributions to nonlinear absorption can result from electrons participating in following transitions: (a) completely occupied 'd' band to unoccupied conduction band and/or (b) within the conduction band (ground states to excited states) due to plasmon resonances[30] and (c) free carrier absorption from excited conduction band to high lying states. Figure 6.2 depicts a generic energy band diagram portraying various mechanisms of (a) saturable absorption: In the case of MCuNP1 and McuNP3 we observed residual absorption at 800 nm and, therefore, expect saturation at lower peak intensities with probable transition from'd' band to the 'p' (conduction) band and is depicted by **Ia** in the figure 6.2. However, at higher peak intensities one expects 2PA as depicted by **Ib** with transitions from ground state conduction band (GSCB) to excited state conduction band (ESCB). Due to two-photon resonance (800 nm + 800 nm) between GSCB and ESCB 2PA dominates with negligible contribution from SA at higher peak intensities (b) Instantaneous 2PA with possible mechanisms are depicted in second box marked as **IIa** (between 'd' band and GSCB) and **IIb** (between GSCB and ESCB) (c) 2-step 3PA (2PA + ESA) at very high peak intensities as depicted by processes in box **IIIa** and **IIIb** (excited state absorption induced from ESCB in this case). The figure is generic in the sense that we have assumed a fixed gap between the states and different

photon energies whereas in reality the band gaps could be different (including SPR positions) for these eight different NPs with single energy photon excitation (1.55 eV for 800 nm ps photon). We had earlier modeled such complicated nonlinear absorption phenomena in different organic moieties and the relevant equations are documented in our earlier publications.[6, 39-41] Similar approach was used and the experimental data was fitted with appropriate equations to estimate nonlinear absorption coefficients. Amongst all MCuNP4 exhibited largest β, n_2, and $\chi^{(3)}$ values. The values of nonlinear refractive index (n_2) were obtained for all colloidal solutions at an intensity of 33 GW/cm^2 using closed aperture (CA) Z-scan method and the data is shown in figure 6.3. Figure 6.3 (a) illustrate the CA data of MCuNP1 (triangles) and SCuNP1 (circles) which exhibit positive nonlinearity (like solvent) with n_2 = 6×10^{-16} cm^2/W, smaller than the solvent magnitude (n_2 = 19×10^{-16} cm^2/W) and the observed sign of n_2 for MCuNP1 and SCuNP1 was negative.

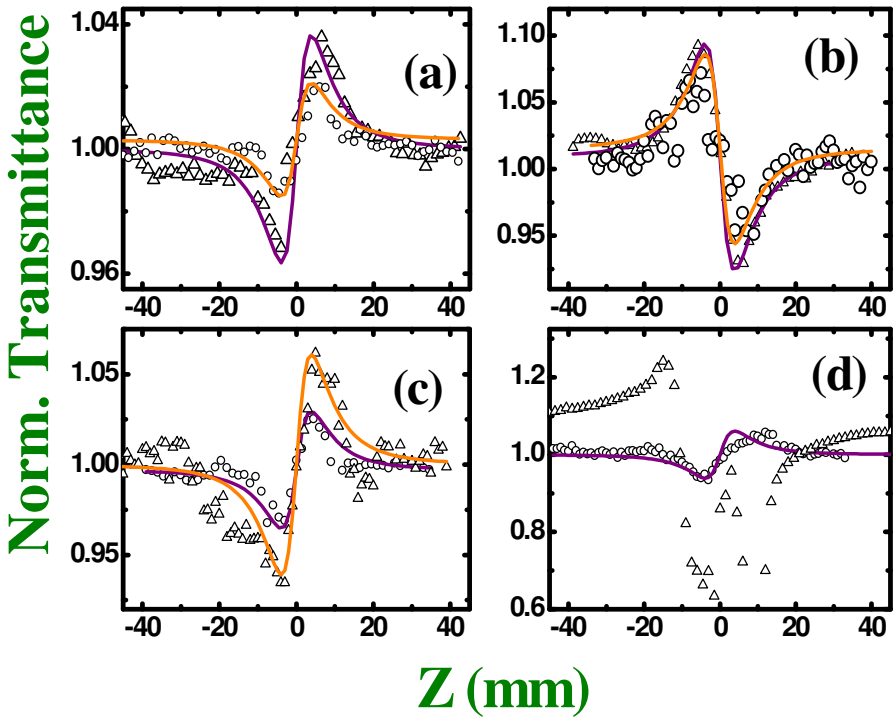

Figure 6.3 Closed aperture Z-scan curves obtained for (a) MCuNP1 (Open triangles), SCuNP1 (Open circles) (b) MCuNP2 (Open triangles), SCuNP2 (Open circles) (c) MCuNP3 (Open triangles), SCuNP3 (Open circles) (d) MCuNP4 (Open triangles), SCuNP4 (Open circles). Closed aperture studies were performed at a peak intensity of 33 GW/cm^2. Solid lines are the theoretical fits.

Figures 6.3(b)–6.3(d) represent CA data of MCuNP2 (SCuNP2), MCuNP3 (SCuNP3) and MCuNP4 (SCuNP4). Observed sign of the nonlinearity was negative (negative) for MCuNP2 (SCuNP2), positive (positive) for MCuNP3 (MCuNP3). The

data was fitted using standard equation (6.17)[42] to estimate the magnitudes of n_2. The contribution from solvents (DCM, ACN and chloroform) (positive nonlinearity) was also identified. The estimated nonlinear coefficients corresponding to the all NPs are listed in table 6.1. There are few reports [43] of NPs fragmentation using short laser pulses. In an earlier report[44] simultaneous occurrence of fragmentation and optical nonlinearity were observed with metal nanoparticles. In the process of scanning sample across the focus there could have been fragmentation occurring in the NPs studied in our case. The experiments were repeated 2-3 times and the values of coefficients observed were within the experimental error range **(±15%)**. The values cited are an average value of these measurements. We had also recorded the UV-visible absorption spectra of the colloidal solutions before and after the Z-scans and we could not observe any major differences in the plasmon peak position/width, again within the experimental errors of our measurements. The fluences corresponding to our Z-scan measurements and were found to be ~0.52 J/cm^2 (for minimum input energy of 2 μJ and assuming a spot size radius of 35 μm; $F = E_{in}/\pi\times\omega^2$) and ~1.04 J/cm^2 (for maximum input energy of 4 μJ and assuming a spot size of 35 μm). The amount of time NPs were exposed to such fluences was **~10 seconds**. The fragmentation, if at all occurred, would be within the focal volume of the beam which was few μl whereas the cuvette (1-mm path length) can hold 0.35 ml, which probably could be the reason for absorption spectra not revealing any spectral changes. Further detailed studies will be necessary to completely evaluate the fragmentation effects on the NLO coefficients.

The magnitudes obtained in our case were compared with NLO coefficients of some of the recently synthesized and reported NPs [45-56] and the data is summarized in Table 6.2. Some of the reported coefficients were stronger in magnitude than those of ours since (a) they used longer pulses (ns) for measurements compared to short pulses (2 ps) in our case (b) in their case excitation was close to SPR and, therefore, is expected to enhance the nonlinearities. In our case the coefficients obtained (except for MCuNP1 and MCuNP3) are in the non-resonant domain. Comparison of the obtained NLO coefficients revealed the magnitudes of nonlinearities were generally higher for multiply ablated NP's compared to singly ablated NP's.

Peak Intensity (GW/cm^2)	Sample	β (cm/W) × 10^{-11} and [I_S (W/cm^2) × 10^7]	n_2^* (cm^2/W) × 10^{-15}	$\lvert\chi^{(3)}\rvert_{(e.s.u)}$ × 10^{-13}	Size (nm)
82	MCuNP1	0.10 [2.90]	0.90	0.80	4.7±1.1
	SCuNP1	0.40	0.40	0.35	3.3±1.2
125	MCuNP1	0.52	-	-	-
	SCuNP1	$\gamma_{eff} = 1.70\times10^{-22}$ cm^3/W^2	-	-	-
82	MCuNP2	0.90	-	-	-
	SCuNP2	0.30	-	-	-
125	MCuNP2	1.40	-2.00	1.78	2.98±0.85
	SCuNP2	0.70	-1.30	1.15	3.7±1.7
82	MCuNP3	0.05 [2.00]	-	-	-
	SCuNP3	-	-	-	-
125	MCuNP3	0.23	1.20	1.07	29.2±8.3
	SCuNP3	0.33	0.80	0.71	19±6
82	MCuNP4	1.50	-	-	-
	SCuNP4	0.67	-	-	-
125	MCuNP4	6.00	-2.10	1.90	13±5
	SCuNP4	1.20	1.40	1.21	7.2±1.7

Table 6.1 Measured NLO coefficients of Cu colloids prepared through multiple, single line ablation in acetone, DCM, ACN, Chloroform at different peak intensities. * n_2 was calculated using 33 GW/cm^2

Sample	Preparation Method	Laser wavelength & Pulse width	β or α_2 (cm/W)	n_2 (cm^2/W)	$[\chi^{(3)}]$ (e.s.u.)	Ref.
Cu Nanocomposite.	Ion implantation	532 nm & 7ns 26 ps (10 Hz)			8.8×10^{-10} 8.4×10^{-11}	[45]
PGO film with Cu/Cu_2O NPs	Melting Process	800 nm & 150 fs (76 MHz)			6.8×10^{-10}	[46]
Cu:SiO2 nanoparticle composite	Ion implantation	540–610 nm & 200 fs			$1.6\text{-}3.1\times10^{-9}$	[47]
Cu/SiO_2 composition	Ion implantation	532 nm 1064 nm & 38 ps			-2.1×10^{-7} -1.2×10^{-7}	[48]

Cu/SiO_2 films	Multi target sputtering method	590 nm & 150 fs			-1.8×10^{-10}	[49]
CuNPs in ZnO matrix	Ion implantation (high dose)	532 nm, 7.5ns 55 ps	5.46×10^{-3} 2.07×10^{-3}			[50]
SG:Cu and SLSG:Cu	Ion implantation	1064 nm & 35 ps			-37.8 and 9.56×10^{-10}	[51]
Cu:Bi_2O_3 nanocomposites film	Multi target magnetron sputtering	800 nm & 120 fs (10 Hz)	0.11×10^{-6}	-0.78×10^{-11}	1.45×10^{-9}	[52]
Cu:Al_2O_3	Pulsed laser deposition	596 nm & 6 ps (3.8 MHz)	(0.75- 0.5) $\times10^{-4}$	-(0.25-0.38) $\times10^{-9}$		[53]
Cu:Al_2O_3	Pulsed laser deposition	596 nm & 6 ps (3.8 MHz)	-2.34×10^{-5}	2.93×10^{-10}		[54]
Cu:Al_2O_3	Pulsed laser deposition	600 nm & 7 ps	$0.8 - 4\times10^{-5}$	$0.9 - 10\times10^{-10}$		[55]
Cu colloidal solutions	Chemical synthesis	532 nm 1064 nm, 35 ps			-(19± 9.5) $\times10^{-15}$ (5.8± 2.9) $\times10^{-15}$	[56]

Table 6.2 Summary of nonlinear optical coefficients of Cu NPs in different matrix synthesized using different techniques.

6.4.3. NLO studies of Corrole conjugated Cu NPs

NLO studies were performed on TTC-Cu-Cl and TPC-Cu-Cl colloidal NP solutions of sizes ~9.5 nm and ~38 nm, respectively, fabricated through the ps laser ablation of Cu in Tritolyl corrole (TTC) and Triphenyl corrole (TPC) at a concentration of 25 µM and an input fluence of 2.5 J/cm^2. The entire details of the fabrication TTC-Cu-Cl and TPC-Cu-Cl colloidal solutions are mentioned in chapter 5. The NLO study was performed of these NPs by Z-scan technique at 800 nm. The linear transmittance obtained from the samples was 0.76, 0.9, 0.8 and 0.92 for TTC-Cu-Cl colloids, TTC, TPC-Cu-Cl colloids and TPC, respectively. Figure 6.4 illustrates the open aperture Z-scan data of (a) TTC-Cu-Cl colloids, (b) TTC, (c) TPC-Cu-Cl colloids and (d) TPC recorded at a peak intensity of 138 GW/cm^2. The data exhibited RSA and was fitted with transmittance equation. The 2PA coefficient (β) values extracted from the fits were 12×10^{-12} cm/W, 5.6×10^{-12} cm/W, 15×10^{-12} cm/W and 9.5×10^{-12} cm/W for TTC-Cu-Cl colloids, TTC, TPC-Cu-Cl colloids and TPC, respectively. The acquired 2PA coefficients of TTC-Cu-Cl colloids and TPC-Cu-Cl colloids were nearly twice compared with the coefficients of reference sample TTC and TPC, which could be due the effect of local field produced by surface Plasmons

of Cu NPs in solution. The nonlinear coefficients of few samples in the presence of Cu NPs were reported earlier.[45-55] However, further studies are initiated to understand the nonlinear absorption dynamics in such complex NPs.

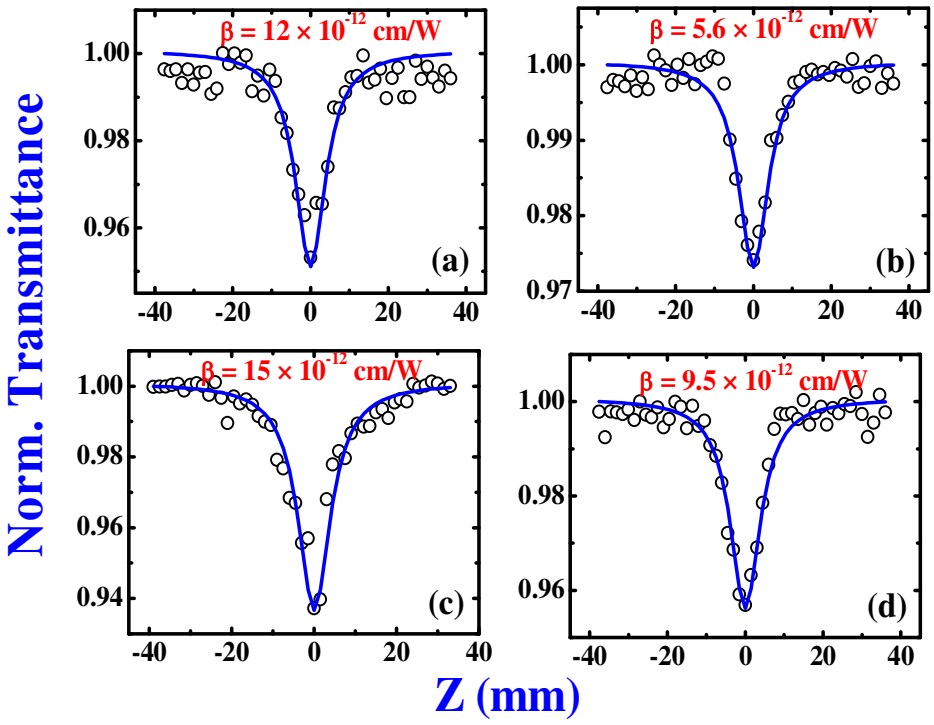

Figure 6.4 Open aperture Z-scan data of (a) TTC-Cu-Cl colloids, (b) TTC, (c) TPC-Cu-Cl colloids and (d) TPC were recorded at 138 GW/cm^2 with 800 nm wavelength by ~2 ps pulses.

Figure 6.5 illustrates the closed aperture Z-scan data of corrole conjugated Cu colloids (TTC-Cu-Cl and TPC-Cu-Cl colloids) which demonstrated positive nonlinearity [figure 6.5(a)] and negative nonlinearity [figure 6.5(c)] at a peak intensity of 33 GW/cm^2 and the data was fitted[42] using standard equation (6.17) to extract the value of nonlinear refractive index (n_2) as 2.2 ×10^{-15} cm^2/W and 1.1 ×10^{-15} cm^2/W, respectively. Moreover, the organic moieties (TTC and TPC) also exhibited positive nonlinearity with small values of n_2 of 1.3×10^{-16} cm^2/W and 9.5×10^{-16} cm^2/W [Fit not shown in (b)]. Both open and closed aperture Z-scan data confirmed that the corrole molecules (TTC and TTC) were influenced under the effect of local field generated by Cu NPs. The estimated values of β, n_2, $Im[\chi^{(3)}]$, $Re[\chi^{(3)}]$ and $|\chi^{(3)}|$ at 800 nm excitation are provided in table 6.3.

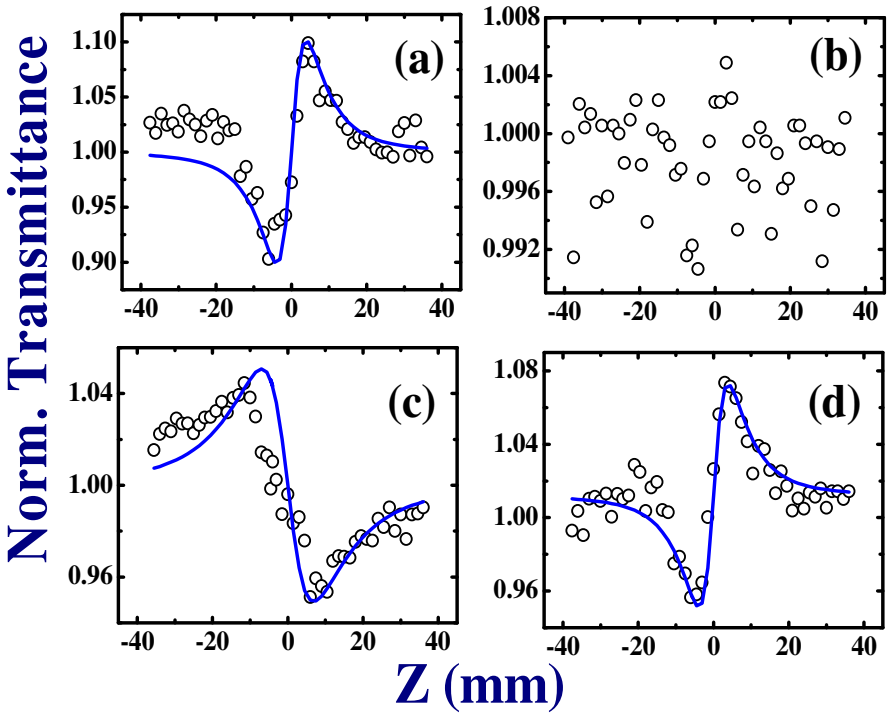

Figure 6.5 CA Z-scan data of (a) TTC-Cu-Cl colloids, (b) TTC, (c) TPC-Cu-Cl colloids and (d) TPC were recorded at 33 GW/cm^2 at 800 nm using ~2 ps pulses

Furthermore, the nonlinear absorption data of TTC and TPC was recorded with the higher concentration (0.5 mM).[6] Figures 6.6(a) and 6.6(b) illustrate the closed aperture Z-scan data recorded at 800 nm for TPC at an intensity of 33 GW/cm^2 and TTC at an intensity of 40 GW/cm^2, well below the peak intensities where the contribution from solvent starts to be significant. Both the samples exhibited negative nonlinearity as discovered by the peak-valley signature. The magnitudes of n_2 evaluated, using the standard procedure (6.17),[42] were 1×10^{-14} cm^2/W for TPC and 0.6×10^{-14} cm^2/W for TTC, respectively. To determine the irradiance dependence of nonlinear absorption, we performed our measurements at different input laser energies. Figures 6.7(a) and 6.7(b) present the obtained intensity dependent Z-scan curves for TPC and TTC. In particular, we noted that the increase of laser intensity induced a switching from SA to RSA to purely RSA behavior in the case of TPC. For the case of TTC we observed switching from SA to RSA. In figure 6.7 (a) open circles represent the results obtained at high peak intensity of 122 GW/cm^2 which clearly demonstrates pure RSA (2PA). Intriguingly, lower intensity data (open squares at 55 GW/cm^2 and open stars at 93 GW/cm^2, respectively) demonstrates that

the nonlinear absorption transformed from SA to RSA. Figure 6.7(b) shows the Z-scan curves with open squares denoting the data obtained at 98 GW/cm^2.

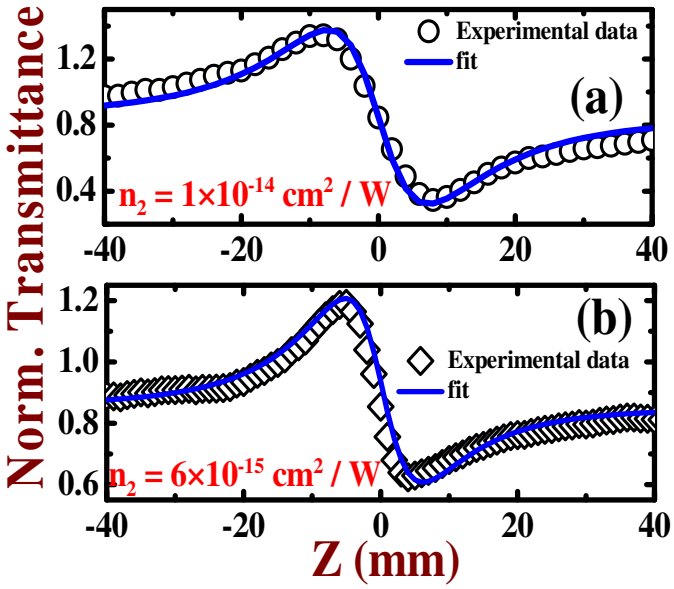

Figure 6.6 Closed aperture Z-Scan curves (open circles) for (a) TPC with I_{00} = 33 GW/cm^2 (b) TTC with I_{00} = 40 GW/cm^2 obtained at 800 nm for a concentration of 5 × 10^{-4} M. Solid lines are fits.

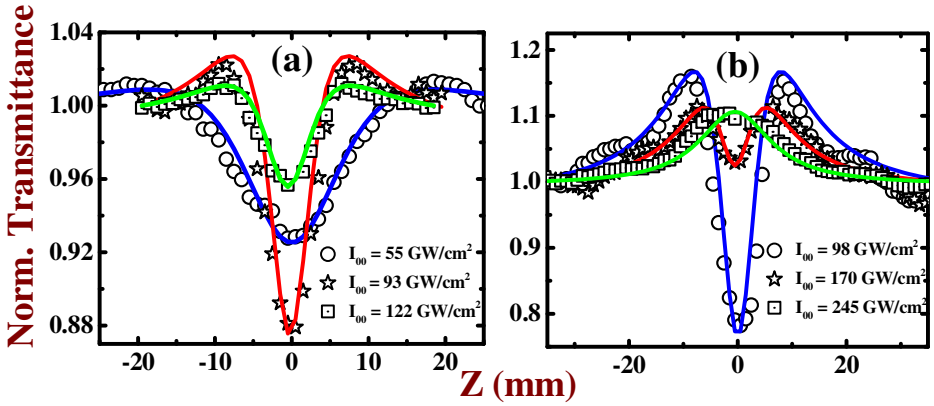

Figure 6.7 Open aperture Z-Scan curves obtained for (a) TPC with varying input intensities like (open squares, β=4.3×10^{-11} cm/W and I_S=38.5 GW/cm^2) I_{00} = 55 GW/cm^2, (open stars, β=5×10^{-11} cm/W and I_S=30GW/cm^2) I_{00} = 93 GW/cm^2 and (open circles, β=2.8 ×10^{-11} cm/W) I_{00} = 122 GW/cm^2 (b) TTC with (open squares, β=1.6×10^{-11} cm/W and I_S=310 GW/cm^2) I_{00} = 98 GW/cm^2, (open stars, β=2.8×10^{-11} cm/W and I_S=67 GW/cm^2) I_{00} = 170 GW/cm^2 and (open circles, β=5.4×10^{-11} cm/W and I_S=31GW/cm^2) I_{00} = 245 GW/cm^2. The concentration used was 5 × 10^{-4} M. Solid line is theoretical fit.

When the linear absorption is significant and with low peak intensity the transmission increases monotonically (SA) and the same was observed at lower peak intensities. However, for increasing intensities (open circles representing the data at 245 GW/cm^2 and open stars at 170 GW/cm^2, respectively) the nonlinear absorption of sample changed from SA to RSA. The observed behavior can be qualitatively

explained using the energy level diagram of Corroles depicted in figure 6.8. For lower peak intensities the population in the ground state is bleached initially (S_0 states to S_1 states). Further pumping leads to excitation into higher excited singlet states (S_2 state) since the excited state absorption cross-section is significant at higher peak intensities and this is reflected in the switching of SA to RSA. This can be considered as two-step 2PA (β) and the data has been fitted according to the equations (6.8), (6.9), (6.13). Measured values I_S, β, n_2, $Im[\chi^{(3)}]$, $Re[\chi^{(3)}]$ and $|\chi^{(3)}|$ at 800 nm excitation are provided in table 6.3.

Sample	**β (cm/W)**	**n_2 (cm^2/W)**	**Im[$\chi^{(3)}$] (S.I)**	**Re [$\chi^{(3)}$]**	**$\lvert\chi^{(3)}\rvert$ e.s.u**
Cu-TTC-Cl	12×10^{-12}	2.2×10^{-15}	8.5×10^{-23}	2.4×10^{-21}	1.8×10^{-13}
Cu-TPC-Cl	15×10^{-12}	1.1×10^{-15}	1.1×10^{-22}	1.2×10^{-21}	8.8×10^{-14}
TTC (25μM)	5.6×10^{-12}	1.3×10^{-16}	3.9×10^{-23}	1.4×10^{-22}	1.1×10^{-14}
TPC (25μM)	9.5×10^{-12}	9.5×10^{-16}	6.7×10^{-23}	1×10^{-21}	7.6×10^{-14}
TTC (0.5mM)	54×10^{-12}	6×10^{-15}	3.8×10^{-22}	6.6×10^{-21}	4.7×10^{-13}
TPC (0.5mM)	28×10^{-12}	10×10^{-15}	1.9×10^{-22}	11×10^{-21}	7.8×10^{-13}

Table 6.3 Summary of nonlinear coefficients obtained in the present study

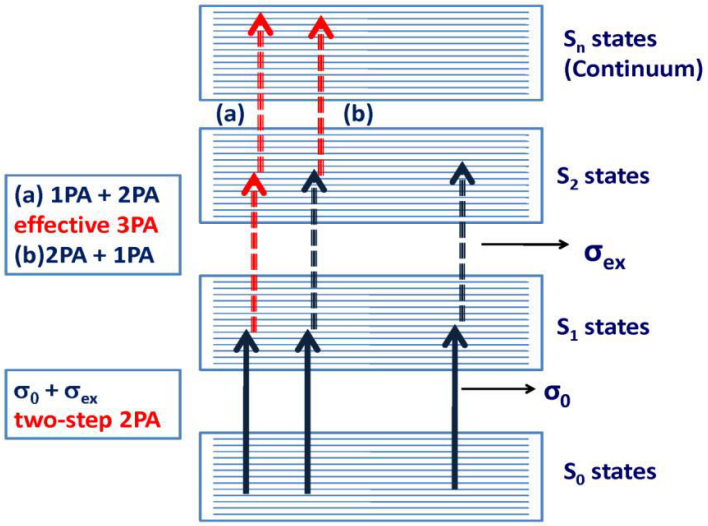

Figure 6.8 Energy level diagram of Corroles explaining the various nonlinear absorption processes.

6.4.4. NLO studies of Si colloids

We investigated the third order nonlinearity of laser fabricated Si NPs in different liquid media (acetone, water, DCM and chloroform) by Z-scan technique with fs oscillator pulses at 680 nm wavelength. Figure 6.9 illustrates open aperture (OA) Z-scan measurements of (a) Si NPs in acetone (b) Si/SiO_2 NPs in water (c) Si-C NPs in DCM and (d) Si-C NPs in chloroform, recorded at a peak intensity of 0.38 GW/cm^2. As observed from the obtained OA data, all the NPs (except Si/SiO_2 NPs) demonstrated a dip in the transmittance when the sample was reached the focal point and the dip designates pure RSA.

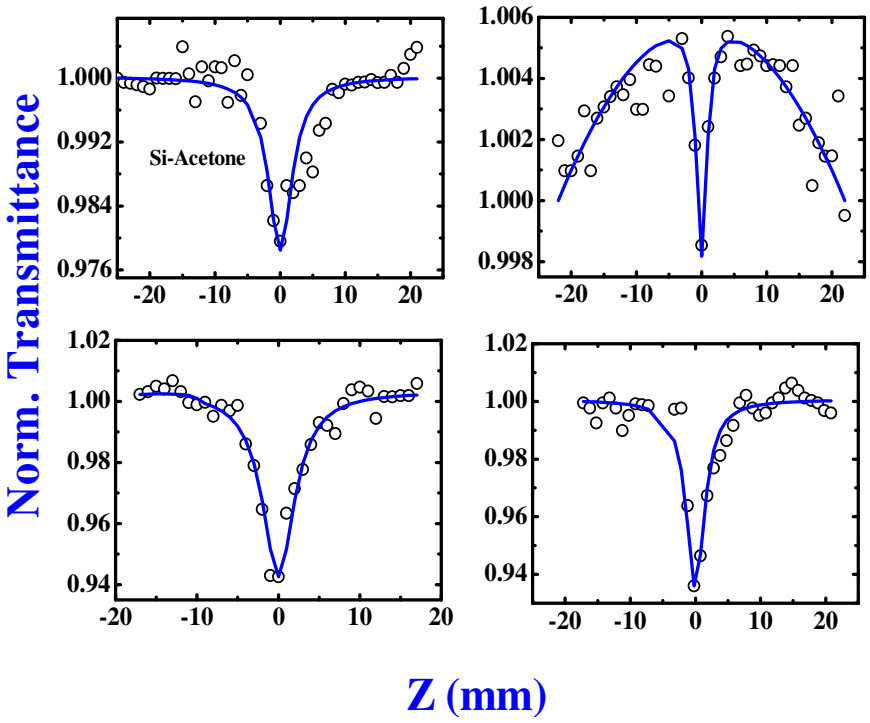

Figure 6.9 Open aperture Z-scan data of (a) Si NPs in acetone, (b) Si/SiO_2 NPs in DCM, (c) Si-C in DCM and (d) Si-C NPs in chloroform were recorded at 0.38 GW/cm^2 with 680 nm wavelength by ~150 fs pulses.

To analysis OA data, we fitted the RSA signature with standard transmittance equation (6.15) which contains 2PA coefficient and the estimated values of 'β' were 1.9×10^{-11}cm/W, 6×10^{-11}cm/W and 6.2×10^{-11}cm/W for Si NPs in acetone, Si-C NPs in DCM and Si-C NPs in chloroform, respectively. The presence of nonlinear absorption at the excitation of 680 nm could be based on the inter band transitions which is related to the strong linear absorption near 300 nm. On the other hand, Si/SiO_2 NPs in

water illustrated a switching behavior which specifies RSA in SA and the data was fitted with the combination of saturation intensity and nonlinear absorption coefficient (or 2PA) to follow the standard procedure. The switching behavior could be due to broad absorption band in the linear absorption spectra which covers the excitation wavelength of 680 nm. The estimated I_S and β values are 1.2×10^{4} W/cm^2 and 2×10^{-10} cm/W, respectively.

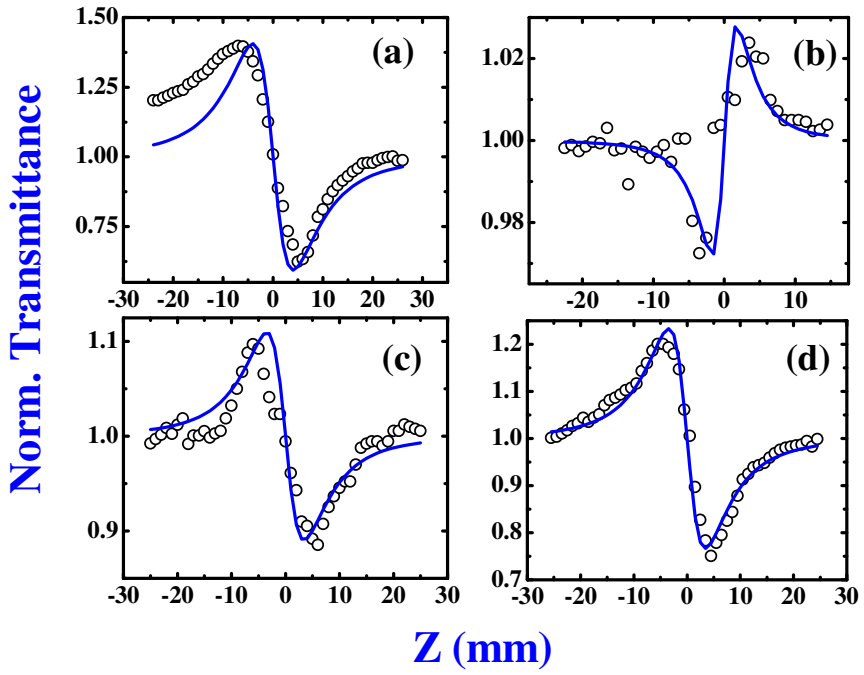

Figure 6.10 Closed aperture Z-scan data of (a) Si NPs in acetone, (b) Si/SiO_2 NPs in DCM, (c) Si-C in DCM and (d) Si-C NPs in chloroform were recorded at 0.1 GW/cm^2 with 680 nm wavelength using ~150 fs pulses.

Figure 6.10 shows the closed aperture data of (a) Si NPs in acetone (b) Si/SiO_2 NPs in water (c) Si-C NPs in DCM and (d) Si-C NPs in chloroform, recorded at a peak intensity of 0.1 GW/cm^2. Some of the authors reported that Si NPs in different media showed higher nonlinearities.[27] Our recorded data demonstrated a peak-valley signature which confirmed that all the NPs (except Si/SiO_2 NPs) illustrated self defocusing behavior while Si/SiO_2 NPs demonstrated self focusing behavior (indicating negative and positive nonlinearities). The n_2 values obtained from the fitted data using equation (6.17)[42] were 8.2×10^{-13} cm^2/W, 4.9×10^{-14} cm^2/W, 1.9×10^{-13} cm^2/W and 4×10^{-13} cm^2/W and, estimated $|\chi^{(3)}|$ values are of 1.9×10^{-14} e.s.u, 2×10^{-13} e.s.u, 6.7×10^{-14} e.s.u and 7.1×10^{-14} e.s.u for Si NPs, Si/SiO_2 NPs, Si-C in

DCM and Si-C in chloroform, respectively. Moreover, the observed strong nonlinearity in these NPs could be due to combination of electronic nonlinearity and thermal nonlinearity since large number of pulses was incident on the sample (80 MHz). The solvent nonlinearity was negligible compared to the nonlinearities of NPs.

6.5. Excited state dynamics colloidal NPs

Along with NLO properties, relaxation dynamics of electrons have gained more attention in coinage metals due their real time applications in the fields of optical data storage systems and ultrafast communication systems.[57-59]These dynamics can be tuned principally by optimizing the size, shape, solvent[60-62] and synthesis technique of NPs. The transient signature of metal NPs can be obtained by the excitation of surface Plasmons and the coherent spike in the transient signature disappears when the collective oscillations of excitons drop their phase. After that segment, the distribution of energy will take place in the electron system and later to the lattice system of NP owing to the thermalization process. These thermalization processes can be monitored by time resolved pump-probe technique.[63-67] In this technique, ultrafast pulses excites the excitation of SPR band which can provide both radiative transitions (electron-electron relaxation) and thermal relaxations such as electron-phonon relaxation and phonon-phonon relaxation. The thermal process depends on the fluence of the pump pulse. Ultrafast time resolved spectroscopy was exploited to investigate electron dynamics such as electron–electron relaxation and electron–phonon relaxations of metallic films with thickness of 10-100 nm.[68-74] Link et al.[75] reported the ultrafast transient data of colloidal Au NPs demonstrating two decay times (3.1 ps and 90 ps) at 400 nm excitation, corresponding to the electron - phonon relaxations and phonon-phonon relaxation, respectively, and also they concluded that the life times increased with increasing excitation laser fluence. Ahmadi et al.[76,77] demonstrated both electron - phonon relaxations and phonon-phonon relaxation for Au NPs (30 nm) at excitation wavelengths of 380 nm and 600 nm. Ag NPs (10 nm) also exhibited two life times of 2 ps and 40 ps where NPs were probed within the range of 660 nm - 790 nm by fs pump-probe spectroscopy.[78] Similar lifetime was observed in the case of Ag NPs with size in the range of 10 - 50 nm by other groups.[79] Tokizaki et al.[80] reported that Cu NPs in glass template also showed comparable life time of 0.4 ps which assigned to the electron-electron relaxation. In

contrast, semiconductor NPs demonstrated only two kind of relaxation dynamics which are electron-phonon decay (> 2 ps) and phonon-phonon decay (> 10 ps).[81, 82] Especially, colloidal Si NPs with different sizes depicted two life times of 1-2 ps and 10-15 ps and the results confirmed that size dependent life times were also possible.[83] Our group[84-86] reported the fs excited state dynamics of organic moieties in solution form by degenerate pump-probe spectroscopy at 600 nm.

6.5.1. Pump-probe experiments

The excited state dynamics of Cu/Si colloidal NPs have been investigated by degenerate fs Pump-probe technique at 600 nm.[84-86] The colloidal NPs were excited with ~70 fs pulses from OPA (TOPAZ) operating at 1 kHz and pumped by fs Ti: sapphire regenerative amplifier at 800 nm. The pump and probe peak intensities used were ~200 GW/cm^2 and ~5 GW/ cm^2, respectively and we ensured that the sample was not affected by the probe intensity. A chopper was inserted in to pump beam path. The frequency of pump beam was modulated at 109 Hz. The two beams were focused in a non-collinear geometry, while travelling the same path length. The transient dynamics was collected by recording the transmitted probe signal using photodiode (SM05R/M, Thorlabs). The chopper and photodiode were connected to lock in amplifier. To avoid the diffraction pattern which arises from coherent artifact phenomena, we kept the polarization of two beams perpendicular to each other. The detailed experimental setup has been described in chapter 2.

6.5.2. Pump-probe Spectroscopy of Cu colloids

In general, ESA and MPA [e.g. 2PA, 3PA] are demonstrated in metal NPs depending on the excitation wavelength and input peak intensities. To understand complete dynamics of the nonlinear absorption, it is needed to study the excited state dynamics of electronic states. Figure 6.11 demonstrates temporal evolution dynamics recorded for (a) pure Cu NPs in acetone (SCuNP1) (b) CuCl NPs in DCM (SCuNP2) (c) CuO NPs in ACN (SCuNP3) and (d) $CuCl_2$ NPs in chloroform (SCuNP4) at 600 nm. Based on the absorption spectra of samples, these can show different types of absorption phenomena and those can demonstrate the single/multi exponential decays. The differential pump transmission can be expressed by the following equation 6.20

$$\frac{\Delta T}{T} = y + \exp\left(-\frac{t}{\tau_1}\right) + \exp\left(-\frac{t}{\tau_2}\right) \quad (6.20)$$

Where y refers to amplitude, ΔT represents the difference arising in the probe transmission which is provoked by pump intensity, T represents probe transmission when pump is off, t is the excitation time and, τ_1 and τ_2 are single and double decay times of excited states.

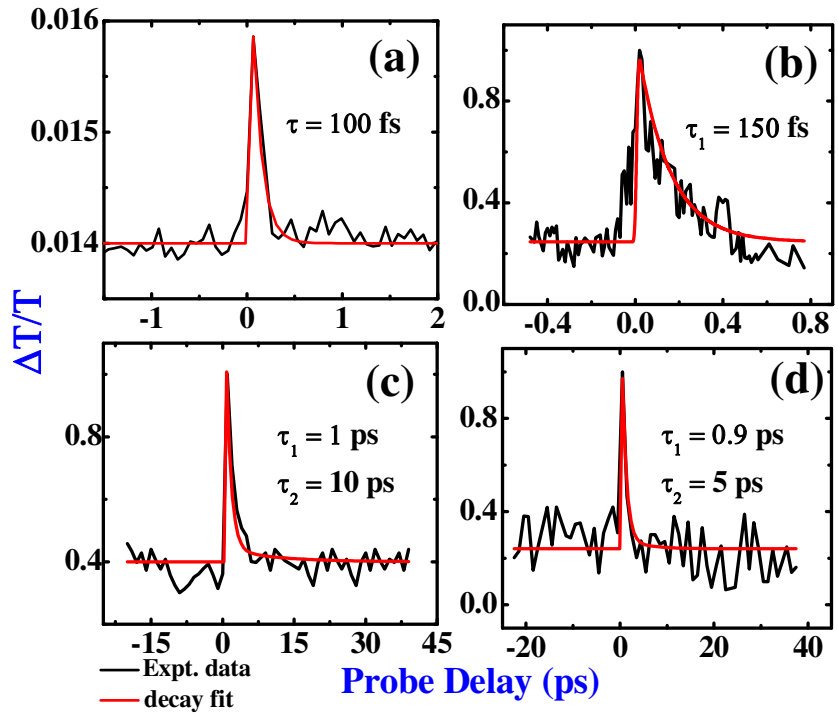

Figure 6.11 Transient photo bleach spectra of (a) Cu NPs in acetone, (b) CuO NPs in ACN, (c) CuCl NPs in DCM and (d) $CuCl_2$ NPs in chloroform were reordered at excitation of 600 nm wavelength with 70 fs pulses using Degenerate Pump-Probe spectroscopy technique.

All these colloidal Cu NPs exhibited photo-bleaching phenomena. The data of transient dynamics were perfectly fitted with single and double exponential decays (τ_1 and τ_2). The quicker components (τ_1 = 100 fs and τ_1 = 150 fs) for Cu NPs [figure 6.11(a)] and CuO NPs [figure 6.11(c)], could be due to the intra band transitions between S band to P band (SPR band) nearer to the excitation wavelength and is attributed purely to electron-electron relaxation phenomena. In the case of noble metal NPs, the coupling of electrons and phonons are weakly influenced by the size effects of NPs (3–13 nm).[87] In the case of CuCl NPs [figure 6.11(b)], a faster decay (τ_1 = 1

ps) was obtained which could be attributed to characteristic absorption band of NPs that covers 300 to 600 nm (maximum near 370 nm) with a possibility of electron – electron interaction. Whereas the longer decay (τ_2 = 10 ps) could be due to electron-phonon relaxations owing to presence of Cl^- ions or DCM molecules.[88] As observed from figure 6.11(d) [$CuCl_2$ NPs] the data was fitted with two exponential decays with life times of τ_1 = 0.9 ps and τ_2 = 5 ps. The obtained life times could be assigned to electron – electron relaxation (τ_1 = 0.9 ps) and electron–phonon relaxations (τ_2 = 5 ps), and could be due to the presence of Cl^- ions or chloroform molecules.[88] These relaxation dynamics can be explained clearly by using a two temperature model.[89]

6.5.3. Pump-probe spectroscopy of Si colloids

Figure 6.12 illustrates transient dynamics obtained for colloidal Si NPs (a) pure Si NPs in acetone (b) Si/SiO_2 NPs in water (c) Si-C NPs in DCM and (d) Si-C NPs in chloroform using degenerate pump-probe technique at 600 nm with ~70 fs pulses. Typically, pump and probe intensities used were ~200 GW/cm^2 and ~5 GW/cm^2, respectively. It can be noticed that the differential probe transmission was photo induced absorption (negative transmission) for pure Si NPs in acetone data shown in figure 6.12(a). Here the excitation wave length is nearly half of sample absorption band (~328 nm) and other three samples showed photo bleaching curves in figure 6.12(b)-(d) since the excitation wavelength is more towards the broad absorption band than other peaks (no peak for Si/SiO_2, 282 nm for Si-C in DCM and 274 nm for Si-C NPs in chloroform). Single exponential was used to fit the photo induced absorption curve in figure 6.12(a). Double exponential equation was utilized to fit the experimental data and two life times were acquired from fits for all the other samples. The obtained lifetimes were τ_1 = 145 ps for pure Si NPs in acetone, τ_1 = 850 fs and τ_2 = 122 ps for Si/SiO_2 NPs in water, τ_1 = 2.5 ps and τ_2 = 20 ps for Si-C NPs in DCM and τ_1 = 700 fs and τ_2 = 1.1 ps for Si-C NPs in chloroform. The single decay τ_1 = 145 ps demonstrated by pure Si NPs in acetone [figure 6.12(a)] was assigned as phonon-phonon relaxations. The first life times of τ_1 = 850 fs [figure 6.12(b)] and τ_1 = 700 fs [figure 6.12(d)] are assigned to the electron-electron relaxations and, τ_1 = 2.5 ps [figure 6.12(c)] is attributed to the electron-phonon relaxations time. These decays could have possibly occurred due to the radiative transitions since Si NPs are highly fluorescent samples. Whereas the second decay, τ_2 = 122 ps [figure 6.12(b)] obtained

could be due to phonon-phonon relaxation (the possibility of non-radiative transitions). Moreover, τ_2 = 20 ps [figure 6.12(c)] and τ_2 = 1.1 ps [figure 6.12(d)] are assigned to the electron-phonon relaxation and electron-electron interaction, respectively. Si NPs demonstrated higher lifetimes, which are influenced by the size of NPs.[83]

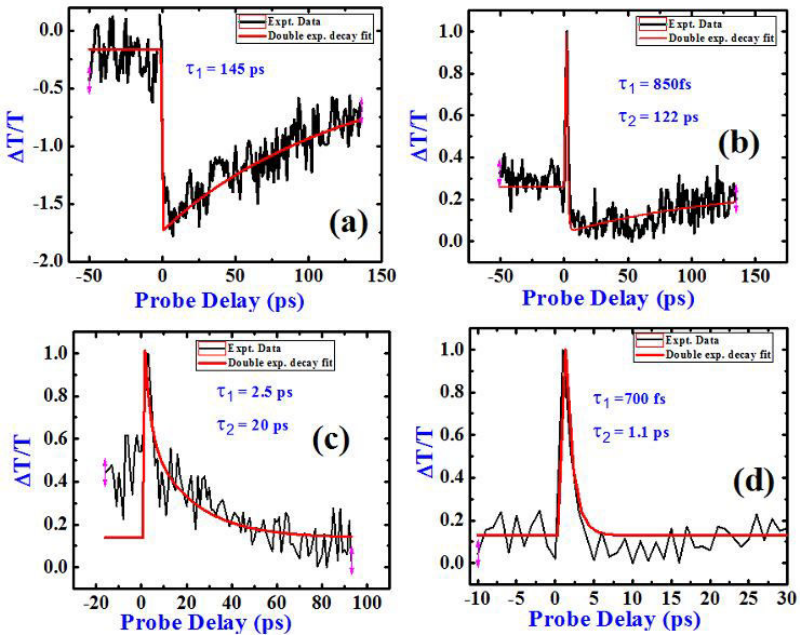

Figure 6.12 Electron transient dynamics of (a) Si NPs in acetone, (b) Si/SiO_2 NPs in water, (c) Si-C NPs in DCM and (d) Si-C NPs in chloroform were recorded at excitation of 600 nm wavelength with 70 fs pulses using Degenerate Pump-Probe spectroscopy technique.

6.6. Four wave mixing

6.6.1. Experiment

The studies on $\chi^{(3)}$ of Cu colloidal solutions in fs time scale have been performed using degenerate four wave mixing (DFWM) technique[90-94] at 800 nm wavelength with ~40 fs pulses. Detailed experimental specifications and setup were discussed in chapter 2. The optimization of DFWM experimental setup was achieved through generating SHG in a crystal (BBO, type-I) where the three fundamental beams were aligned separately (two beams at a time).[95, 96]

6.6.2. Cubic nonlinearity and temporal response of Cu Colloids

Cu colloidal solutions were utilized to record temporal data of DFWM signal with the help of a photo diode (SM1PD2A) by delaying the probe beam and measuring the power of DFWM signal. Figure 6.13 illustrates the temporal traces of different composite based Cu colloids (a) pure Cu NPs in acetone (SCuNP1) (b) CuCl NPs in DCM (SCuNP2) (c) CuO NPs in ACN (SCuNP3) and (d) $CuCl_2$ NPs in chloroform (SCuNP4).

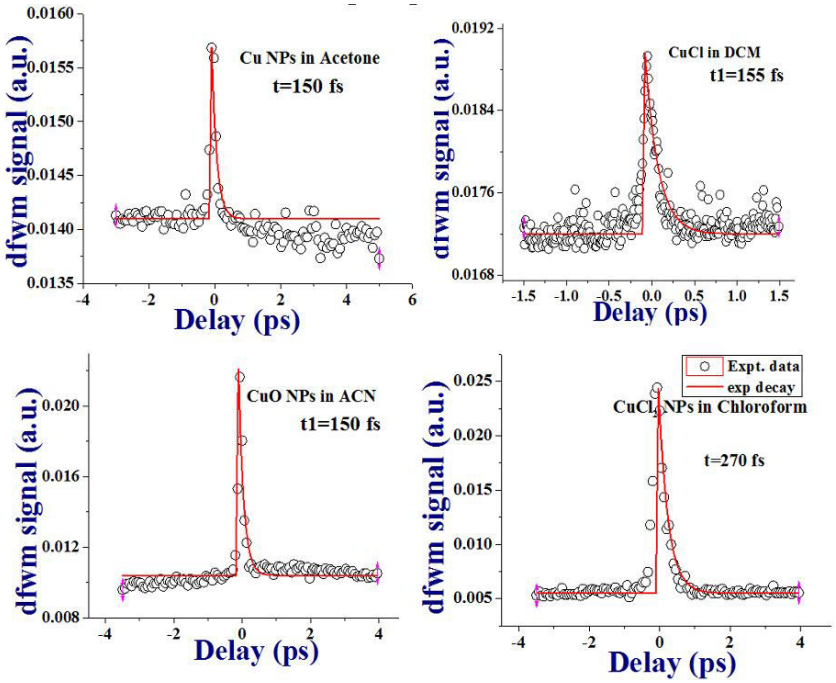

Figure 6.13 The temporal evolution of DFWM signal for (a) Cu NPs in acetone (b) CuCl NPs in DCM (c) CuO NPs in ACN and (d) $CuCl_2$ NPs in chloroform were recorded at excitation of 800 nm wavelength with 70 fs pulses using Degenerate four wave mixing technique.

The values of third order nonlinear susceptibility for all Cu colloids ($[\chi^{(3)}]_{Cu}$) were obtained by taking $\chi^{(3)}$ of carbon tetra chloride (CCl_4) as reference ($[\chi^{(3)}]_{CCl4}$ = 4.4 $\times 10^{-14}$ e.s.u.) since CCl_4 solvent mostly provides nonlinear susceptibility in fs domain which is due to the electronic contribution[97] and the trace of the reference sample was also recorded along with samples at same conditions. After estimating the intensities of DFWM signals for sample and reference sample with fs pulses and using the relation between $[\chi^{(3)}]_{Cu}$ and $[\chi^{(3)}]_{CCl4}$ [given by Sutherland et al.[98]] the $\chi^{(3)}$ of samples were evaluated as

$$\chi_S^{(3)} = \sqrt{\frac{I_S}{I_R}}\left(\frac{n_S}{n_R}\right)^2\left(\frac{L_R}{L_S}\right)\left(\frac{\alpha L}{e^{\frac{-\alpha L}{2}}(1-e^{-\alpha L})}\right)\chi_R^{(3)} \qquad (6.21)$$

Where 'n' is the linear refractive index, I is the intensity of DFWM signal, and L is the length of the sample (5 mm). Here suffice Cu refers to Cu colloidal solutions and suffice CCl_4 refers to CCl_4 as reference sample. α is the linear absorption coefficient of Cu colloids. The estimated α values were 0.091/cm (0.90), 0.141/cm (0.85), 0.053/cm (0.94) and 0.193/cm (0.8) for Cu NPs in acetone, CuCl NPs in DCM, CuO NPs in ACN and $CuCl_2$ NPs in chloroform, respectively. Estimated $[\chi^{(3)}]_{Cu}$ from equation 6.21 were ~1.5×10^{-14} e.s.u., ~1.84×10^{-14} e.s.u., ~3.5×10^{-14} e.s.u., ~5.8×10^{-14} e.s.u. for Cu NPs, CuCl NPs, CuO NPs and $CuCl_2$ NPs, respectively, for the input peak intensity was ~2.1×10^{11} W/cm^2. The solvent refractive indices considered were n=1.358 for acetone, n=1.424 for DCM, n=1.344 for ACN, and n=1.446 for chloroform where the refractive index of the reference sample (CCl_4) was 1.450. We measured the intensity of DFWM signal of all four samples for different input intensities of ~1.6×10^{11} W/cm^2, ~1.9×10^{11} W/cm^2, ~2.1×10^{11} W/cm^2 and ~2.4×10^{11} W/cm^2 at the position of zero delay. The data is which were plotted logarithmically in figure 6.14 and it was fitted with straight line. The estimated slopes from the fitting were ~2.81, ~ 2.95, ~2.84 and ~3.01 for Cu NPs, CuCl NPs, CuO NPs and $CuCl_2$ NPs, respectively. The slope values close to 3 confirmed that it was a cubic nonlinearity[99] and there were no higher order nonlinearities involved.

Santhosh et al.[100] demonstrated that the DFWM signal carries information about cubic nonlinearity when the input peak intensity ≤ 220 GW/cm^2. Moreover, the contribution of solvents in the cubic nonlinearity which could be due to the pure electronic transisitions,[101] though present, were small is magnitude compared to the contribution of Cu colloids. We have also evaluated the $[\chi^{(3)}]$ of solvents from the temporal evolution of DFWM signal and measured the signals intensities at zero delay. We extracted the pure contribution of Cu colloids, by removing the solvent contribution from the total cubic susceptibility and the resultant $[\chi^{(3)}]$ values of pure Cu colloids were ~1.4×10^{-14} e.s.u., ~1.8×10^{-14} e.s.u., ~3.3×10^{-14} e.s.u., ~5.6×10^{-14} e.s.u. for Cu NPs, CuCl NPs, CuO NPs and $CuCl_2$ NPs, respectively. The $\chi^{(3)}$ component measured with our polarization conditions is $\chi^{(3)}_{1111}$ (all polarizations

are parallel) for an isotropic media. In that media, the value of $\chi^{(3)}_{1111}$ is three times of $\chi^{(3)}_{1212}$ and $\chi^{(3)}_{1122}$ due to non resonant electronic nonlinear contribution.

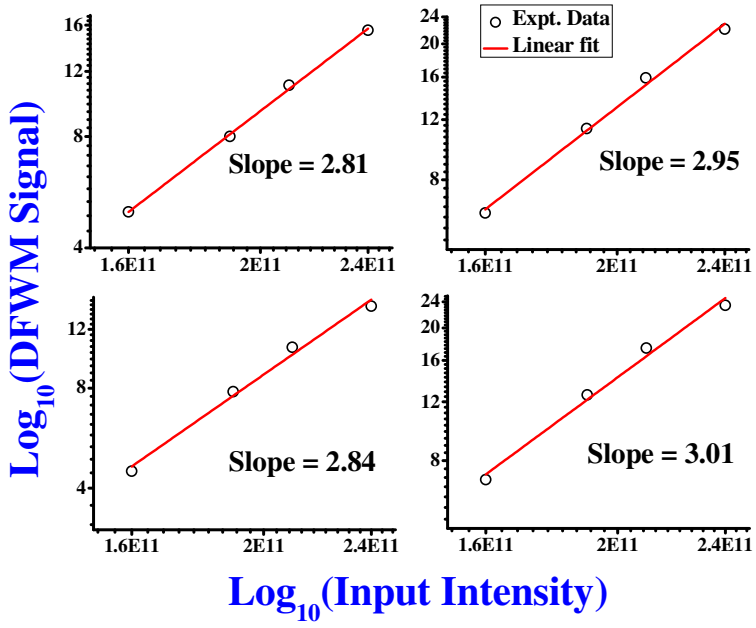

Figure 6.14 logarithmic plot of input intensity versus DFWM signal for (a) Cu NPs (b) CuCl NPs (c) CuO NPs and (d) $CuCl_2$ NPs

Generally, the NLO properties of metal NPs arise due to the excitation of LSPR. The $\chi^{(3)}$ of chemically synthesized Au nanoprisms ~170 nm using DFWM technique in ultrafast domain was ~10^{-14} e.s.u.[100] In our earlier section, we have presented the NLO properties of Cu colloids and measured $\chi^{(3)}$ with Z-scan technique in ps domain. However, ultrafast time response was also evaluated from the temporal data of DFWM signal along with cubic nonlinearity. The data was fitted with single exponential curve theoretically in figure 6.13 and the approximated time responses of the Cu colloids are ~150 fs, ~155 fs, ~150 fs and ~270 fs for Cu NPs, CuCl NPs, CuO NPs and $CuCl_2$ NPs, respectively. This time response could be the dephasing time.

6.6.3. Cubic nonlinearity and temporal response of Cu colloids generated in Corrole solutions

Figure 6.15 demonstrates the DFWM temporal evolution of Cu colloids generated in (a) TTC (TTC-Cu-Cl colloids) and (b) TPC (TPC-Cu-Cl colloids) in fs domain. Along with colloids, time evolution of DFWM signals for the organic molecules such as TTC and TPC (25 μM) were also recorded to determine the $\chi^{(3)}$ values. In our experiments, an average of 200 pulses was used for recording temporal evolution of DFWM signal. To determine the $\chi^{(3)}$ values of colloidal NPs, the known $\chi^{(3)}$ value of sample (CCl_4) was taken as reference sample.[97]

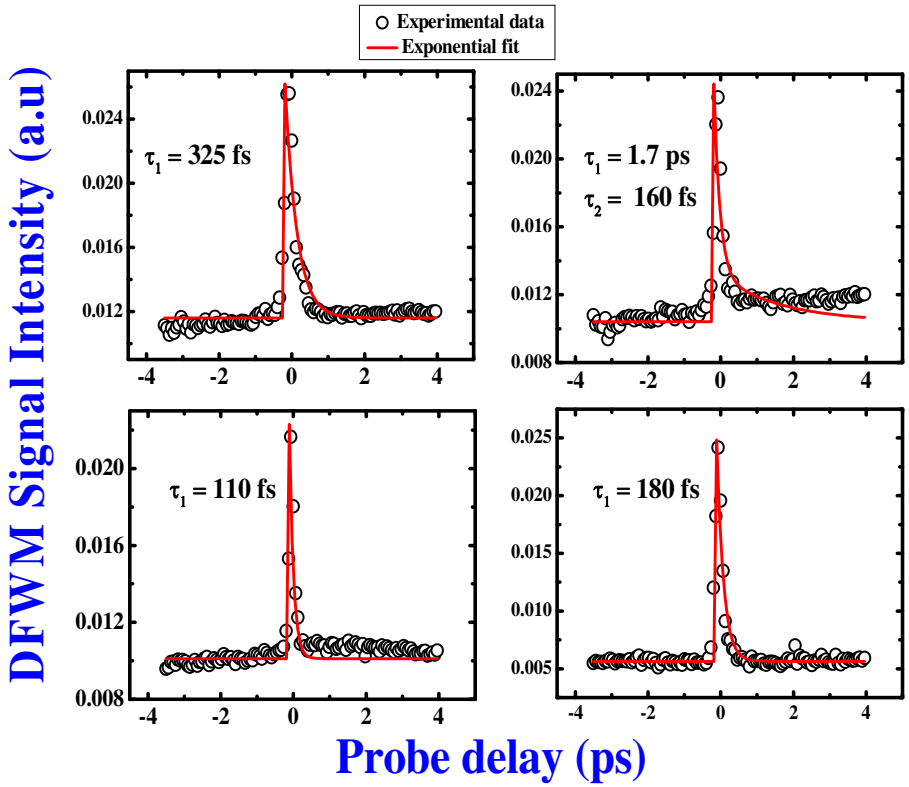

Figure 6.15 The temporal evolution of DFWM signal for (a) TTC-Cu-Cl colloids, (b) TTC, (c) TPC-Cu-Cl and (d) TPC were recorded at excitation of 800 nm wavelength with 70 fs pulses using Degenerate four wave mixing technique.

All the experiments were performed at similar experimental conditions. The time evolution data of samples involve electronic information like the data of CCl_4.[97] As observed from in figures 6.15, every time evolution data contains a coherent spike at zero delay. The beam in the probe path gets diffracted from interference pattern

produced by the interaction of two pump beams[100] and at this position, the maximum contribution from electronic transitions than vibrational one are provided by DFWM signal[101] The $\chi^{(3)}$ values were estimated using equation 6.21 and the values obtained were ~7×10^{-14} e.s.u., ~1×10^{-13} e.s.u., ~1.1×10^{-13} e.s.u., ~1.4×10^{-13} e.s.u. for TTC-Cu-Cl colloids, TTC, TPC-Cu-Cl colloids and TPC, respectively, at an input peak intensity of ~2×10^{11} W/cm^2.

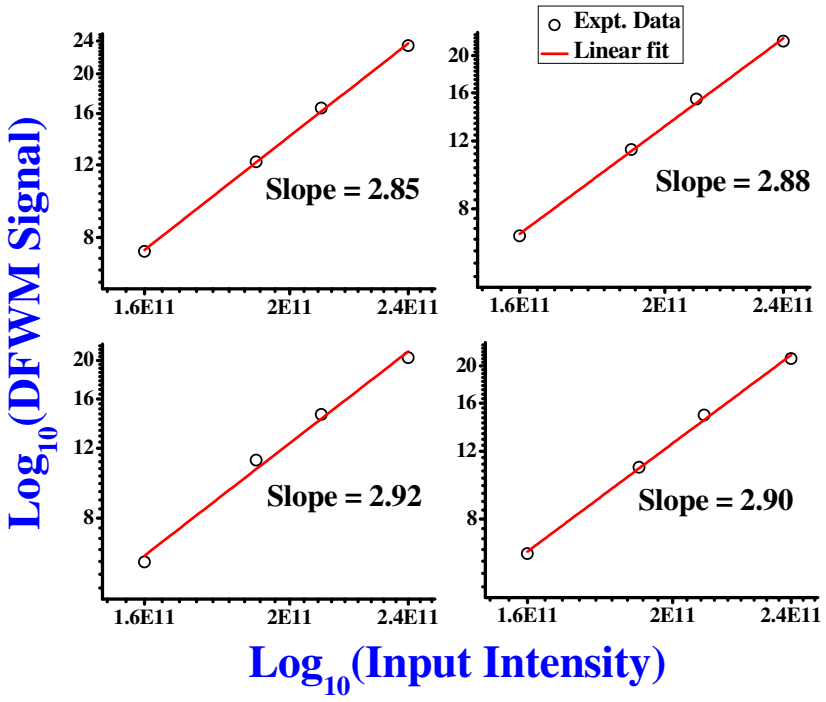

Figure 6.16 Logarithmic plot of input intensity versus DFWM signal for (a) Si NPs, (b) SiO_2 NPs, (c) Si-C NPs and (d) Si-C NPs

To confirm the third order susceptibility of all samples, we have recorded intensity dependent DFWM signal at zero delay and plot the data in logarithmic scales which was fitted with straight line. From the plot in figure 6.16 demonstrated the slope was ~3 which clearly indicates the nonlinearity was purely third order. The time evolution data in figure 6.15 was fitted with single exponential decay and the acquired lifetimes of all samples were ~325 fs; ~1.7 ps and ~160 fs; ~110 fs and ~180 fs for TTC-Cu-Cl colloids, TTC, TPC-Cu-Cl colloids and TPC, respectively.

6.5. Summary

- Investigation of ps NLO studies of colloidal Cu NPs using Z-scan technique revealed that colloids prepared through the multiple line ablation exhibited strong third order nonlinearities compared to the counterparts of single line ablation since the yield was higher in the multiple line ablation than in single line ablation. This could be probably due to the agglomeration effects which resulted in the formation of hot spots.
- ULA produced corrole conjugate Cu colloids prepared were investigated through ps Z-scan experiment demonstrated that extracted $\chi^{(3)}$ magnitude was of similar order for corresponding corrole solutions.
- Fs Z-scan studies of Si colloids fabricated through ULA have been performed which illustrated the strong 2PA coefficients and n_2 values and, consequently larger $\chi^{(3)}$ due to size and composition of colloids.
- $\chi^{(3)}$ values of colloidal Cu NPs and corrole conjugate Cu colloids were also investigated through fs DFWM.
- Fs pump-probe experiments were attempted to retrieve the information on plasmon absorption recovery for Cu/Si colloids in different liquid media.

References

1. W. Kaiser, A. Laubereau: In Nonlinear Optics, ed. by P. Harper, B. Wherrett (Academic, New York **1977**)
2. P.N. Prasad, D.J. Williams: Introduction to Nonlinear Optical Effects in Molecules and Polymers (Wiley, New York, **1990**)
3. W. Koechner: Solid-State, Laser Engineering, 3rd, edn., Springer Ser. Opt. Sci., Vol. 1 (Springer, Berlin, Heildelberg, **1992**)
4. G.I. Stegeman, A. Miller: InPhotonic Switching, Vol. 1, ed. J. Michninter (Academic, Orlando **1992**) pp. 81-146
5. R. W. Boyed, Nonlinear Optics, Third Edition, 2008, Elsevier Inc.
6. S. Hamad, S. P. Tewari, L. Giribabu and S. Venugopal Rao, J. Porphy. Phth. **16**, 140 (2012)
7. Y. Gao, X. Zhang, Y. Li, H. Liu, Y. Wang, Q. Chang, W. Jiao and Y. Song, Opt. Commun.; **251**, 429 (2005).
8. M. Samoc, A. Samoc, B. L. Davies, H. Reisch, and U. Scherf, Opt. Lett. **23**, 1295 (1998)
9. D. K. Serkland, M. M. Fejer, R. L. Byer and Y. Yamamoto, Opt. Lett. **20**, 1649 (1995).
10. D.K. Serkland, P. Kumar, M.A. Arbore and M.M. Fejer, Opt. Lett. **22**, 1497 (1997).
11. Y. Guanjun, Z. Peng, Z. Dong, C. Zhang, C. Liangyao and S. Qian, Physica.B.**393**,188 (2007).
12. H. Inouye, K. Tanaka, J. Tanahashi, T. Hattori and H. Nakatsuka, J. Appl. Phys. **39**, 5132 (2000).
13. J.F. Reintjes, Nonlinear Optical Parametric Processes in Liquids and Gases, Academic Press, New York, **1984**.
14. L. Francois, M. Mostafavi, J. Belloni and J. A. Delaire, Phys. Chem. Chem. Phys. **3**, 4965 (2001)
15. S. Qu, C. Du, Y. Song, Y. Wang, Y. Gao, S. Liu, Y. Li and D. Zhu Chem. Phys. Lett. **356**, 403 (2002)
16. M. Anija, J. Thomas, N. Singh, A. Nair, R. T. Tom, T. Pradeep and R. Philip Chem. Phys. Lett. **380**, 223 (2003)
17. Y. Deng, Y. Sun, P. Wang, D. Zhang, X. Jiao, H. Ming, Q. Zhang, Y. Jiao and X. Sun, Curr. Appl. Phys. **8**, 13 (2008)
18. C. Torres-Torres, J.A. Reyes-Esqueda, J.C. Cheang-Wong, A. Crespo-Sosa, Rodríguez- L. Fernández and A. Oliver J. Appl. Phys.**104,** 014306 (2008).
19. A. G. Luis, F. E. dos Santos, A. S. Gomes, C. B. de Araújo, P. L. R. Kassab and G. H. Windson, Appl. Phys. Lett. **92**, 141916 (2008)
20. R. Aleksandr, P. Bruno, S. Debrus, G. Rashid, A. Stepanov, C. Nurdogan, C. Buchal and U. Sibel, Appl. Opt. **44,** 2839 (2005)
21. J. M. Ballesteros, R. Serna, J. Solis, C. N. Afonso, A. K. Petford-Long, D. H. Osborne, and R. F. Haglund Jr, Appl. Phys. Lett. **71**, 2445 (1997).
22. R. Del Coso and J. Solis, J. Opt. Soc. Am. B **21**, 640 (2004).
23. R. A. Ganeev, A. I. Ryasnyansky, Sh. R. Kamalov, M. K. Kodirov and T. Usmanov, J. Phys. D: Appl. Phys. **34** 1602 (2001).
24. S. Venugopal Rao, J. Mod. Opt., **58**, 1024 (2011).
25. Y. Guillet, M. Rashidi-Huyeh and B. Palpant, Phys. Rev. B. **79**, 045410(2009).
26. U. Kreibig and M. Vollmer, Optical Properties of Metal Clusters (Springer-Verlag, **1995**).

27. K. Imakita, M. Ito, M. Fujii, and S. Hayashi, J. Appl. Phys.**105**, 093531 (2009); S. Minissale, S. Yerci, and L. D. Negro, Appl. Phys. Lett., 100, 021109 (2012); A. J. Lu, R. Q. Zhang, and S. T. Lee, Appl. Phys. Lett. 91, 263107 (2007); S. Dhara, K. Imakita, P. K. Giri, and M. Fujii, Opt. Lett., **39**, 3833 (2014); P. R. Watekar, S. Moon, A. Lin, S. Ju, and H. Won –Taek, J. Light Wave Tech. 27, 568 (2009); L. Chen, X. –f. Jiang, Z. Guo, H. Zhu, T. -S. Kao, Q. –h. Xu, G. W. Ho, and M. Hong, J. Nano Mater. **2014**, 1 (2014).
28. G. Ma, W. Sun, S. H. Tang, H. Zhang, Z, Shen and S. Qian, Opt. Lett. **27**, 1043 (2002); Y. Guillet, M. Rashidi-Huyeh, D. Prota and B. Palpant, Gold Bulletin **41**, 341 (2008).
29. A. Nag, A. Kumar, P. P. Kiran, S. Chakraborty, G.R. Kumar, and D.D. Sarma, J. Phys. Chem. C **112**, 8229 (2008)
30. R. Philip, G.R. Kumar, N. Sandhyarani, and T. Pradeep, Phys. Rev. B **62,** 13160 (2000).
31. P. Prem Kiran, B. N. S. Bhaktha and D. Narayana Rao, J. Appl. Phys. **96**, 6717 (2004)
32. R. Sreeja, R. Reshmi, P.M. Aneesh, and M.K. Jayaraj, Sci. Adv. Mat. **4**, 439 (2012)
33. B. Gu, W. Ji, Opt. Exp. **16**, 10208 (2008)
34. K.V. Saravanan, K. C. James Raju, M. G. Krishna, S. P. Tewari and S. Venugopal Rao Appl. Phys. Lett. **96**, 232905 (2010)
35. D. S. Correˆa, L. D. Boni, L. Misoguti, I. Cohanoschi, F. E. Hernandez, and C. R. Mendonca, Opt. Commu. **277,** 440 (2007)
36. J. He, Y. Qu, H. Li, J. Mi, and W. Ji, Opt. Express, **13**, 9235 (2005)
37. A. Nag, A. Kumar, P. P. Kiran ,S .Chakraborty, G.R. Kumar and D.D. Sarma, J. Phys. Chem. C **112**, 8229 (2008)
38. P.P. Kiran, B .N .S Bhaktha D .Narayana Rao and G .De, J. Appl. Phys. **96**, 6717 (2004)
39. S .Venugopal Rao, T. S. Prashant, T .Sarma, P.K. Panda, D .Swain, and S.P. Tewari, Chem. Phys. Lett. **514**, 98 (2011)
40. N.K.M. Naga Srinivas, S .Venugopal Rao, and D .Narayana Rao, J. Opt. Soc. Am. B, **20**, 2470 (2003)
41. N. Venkatram, D. Narayana Rao, L. Giribabu, and S .Venugopal Rao, Chem. Phys. Lett, **464**, 211 (2008)
42. M .Sheik-Bahae, A.A. Said, T .H .Wei and D .J .Hagan, IEEE J. Quantum Electron. **26**,760 (1999)
43. F. Hiroaki, S .Yanagida and V. K. Prashant, J. Phys. Chem. C. **103**, 2589 (1999); S. Link, C. Burda, M.B. Mohamed, B. Nikoobakht and M.A. El-Sayed, J. Phys. Chem. A, **103**, 1165 (1999); S. Besner, A.V. Kabashin and M .Meunier, **89**, 233122 (2006)
44. V. Amendola, D. Dini, S. Polizzi, J. Shen, K.M. Kadish, J.F.C. Mario, M. Hanack and M . Meneghetti ,**113**, 8688 (2009)
45. C. Torres-Torres, J.A. Reyes-Esqueda, J.C. Cheang-Wong, A. Crespo-Sosa, L.Rodríguez-Fernández and A .Oliver , J. Appl. Phys..**104**, 014306 (2008)
46. A.G. Luis, F.E.dos Santos, A.S. Gomes, C.B.de Araújo, L .R .P Kassab and G .H .Windson Appl. Phys. Lett . **92**,141916 (2008)
47. Y .Takeda, O.A. Plaksin, K .Kono and N .Kishimoto Surface & Coatings Technology, **196**, 30 (2005)
48. Y. H. Wang, Y. M. Wang, J. D. Lu, L. L. Ji, R. G. Zang and R. W. Wang Opt. Commun **283,** 486 (2010).

49. I. Tanahashi, I. Hideyuki , T. Koichiro and A. Mito Jpn. J. Appl. Phys. **38**, 5079 (1999)
50. R. Aleksandr, P. Bruno, S. Debrus, G. Rashid, A. Stepanov, C. Nurdogan, C. Buchal and U . Sibel, Appl. Opt. **44**, 2839 (2005)
51. R. A. Ganeev, A. I. Ryasnyanskii, A.L. Stepanov, M.K. Kondirov and T. Usmanov, Optics and Spectroscopy **95**, 967 (2003)
52. Y. Guanjun, Z. Peng, Z. Dong, C. Zhang, C. Liangyao and S. Qian, Physica B **393**, 188 (2007)
53. R. Serna, J.M. Ballesteros, J. Solis, C.N. Afonso, D.H. Osborne, R.F. Haglund Jr and R .F. Petford-Long ,Thin Solid films **318**, 96 (1998)
54. J. M. Ballesteros, R. Serna, J. Solis, C.N. Afonso, A.K. Petford-Long, D.H. Osborne, and R. F. Haglund Jr, Appl. Phys. Lett. **71** ,2445 (1997)
55. R. Del Coso and J. Solis , J. Opt. Soc. Am. B **21**, 64 (2004)
56. R. A. Ganeev, A.I. Ryasnyansky, Sh. R. Kamalov, M.K. Kodirov and T. Usmanov, J. Phys. D: Appl. Phys. **34**,1602 (2001)
57. G. Schmid, Clusters and Colloids: From Theory to Application; VCH: Weinheim, 1994
58. P. V. Kamat, D. Meisel, Semiconductor Nanoclusters - Physical, Chemical, and Catalytic Aspects; P.V. Kamat, D. Meisel, Eds.; Studies in Surface Science and Catalysis **103**; Elsevier: Amsterdam, 1997
59. A. S Edelstein; R. C. Cammarata, Nanoparticles: Synthesis, Properties and Applications; Institute of Physics Publishing: Bristol, 1996.
60. B. A. Smith, D. M.Waters, A. E. Faulhaber, M. A. Kreger, T. W. Roberti and J. Z.Zhang ,J. Sol-Gel Sci. Technol. **9**, 125 (1997)
61. A. E. Faulhaber; B. A Smith; J. K.Andersen and J. Z. Zhang, Mol. Cryst. Liq. Cryst. **25**, 283, 1996
62. B. A. Smith, J. Z. Zhang, U.Giebel and G. Schmid, Chem. Phys. Lett. **139**, 270 (1997)
63. R. H. M. Groeneveld, R. Sprik, and A. Lagendijk, Phys. Rev. B **45**, 5079 (1992)
64. R. H. M. Groeneveld, R. Sprik and A. Lagendijk, Phys. Rev. B **51**, 11433 (1995)
65. G. L. Esley, Phys. Rev. Lett. **51**, 2140 (1983)
66. G. L. Esley, Phys. Rev. B **33**, 2144 (1986)
67. R. W. Schoenlein, W. Z. Lin, J. G.Fujimoto and G. L. Eesley, Phys. Rev. Lett. **58**, 1680 (1987)
68. S. D. Brorson, J. G. Fujimoto, E. P. Ippen, Phys. Rev. Lett. **59**, 1962(1987).
69. C.-K Sun, F.Vallee, L. H. Acioli, E.P .Ippen and J. G. Fujimoto, Phys. Rev. B **48**, 12365 (1993)
70. C.-K.Sun, F. Vallee, L. H. Acioli, E. P. Ippen,; J. G. Fujimoto, Phys. Rev.B **50**, 15337 (1994)
71. H. E. Elsayed-Ali; T. Juhasz, G. O. Smith, W.E Bron, Phys. Rev. B **43**, 4488 (1991)
72. T. Juhasz, H. E. Elsayed-Ali, H. Hu, W. E. Bron, Phys. Rev. B **45**, 13819 (1992)
73. T. Juhasz, H. E. Elsayed-Ali, G.O. Smith, C. Suarez and W. E. Bron, Phys. Rev. B **48**, 15488 (1993)
74. W. S. Fann, R .Storz, H. W. K Tom, and J. Boker, Phys. Rev. B **46**, 13592 (1992)
75. S. Link , M. A. El-Sayed, J. Phys. Chem. B **103**, 8410 (1999)

76. T. S. Ahmadi, S. L. Logunov and M. A. El-Sayed, J. Phys. Chem. **100**, 8053 (1996)
77. T. S. Ahmadi, S. L. Logunov,.; M. A.El-Sayed, J. T.Khoury and R. L.Whetten, J. Phys. Chem. B **101**, 3713 (1997)
78. T. W. Roberti, B. A.Smith and J. Z. Zhang ,J. Chem. Phys. **102**, 3860 (1995).
79. J. K. Hodak, I. Martini and G. V.Hartland, J. Phys. Chem. B **102**, 6958 (1998)
80. T. Tokizaki, A. Nakamura, S. Kaneko, K. Uchida, S. Omi, H. Tanji and Y. Asahara, Appl. Phys. Lett. **65**, 941 (1994)
81. J. Z. Zhang, Acc. Chem. Res. **30**, 423 (1997)
82. N. J. Cherepy, D. B. Liston, J. A. Lovejoy, H. Deng and J. Z. Zhang, J. Phys. Chem. B **102**, 770 (1998)
83. B. Bescos, R. Hoch, H.-J. Schmidtke, and G. Gerbe, Appl. Phys. B **71**, 373 (2000)
84. P.T. Anusha, Debasis Swain, T. Shuvan Prashant, L. Giribabu, Surya P. Tewari and S. Venugopal Rao, J. Phys. Chem. C. **116**, 17828 (2012)
85. D. Swain, P.T. Anusha, T. Shuvan Prashant, S. P. Tewari, T. Sarma, P. K. Panda and S. Venugopal Rao, Appl. Phys. Lett. **100** , 141109 (2012)
86. D. Swain, R. Singh, V.K. Singh, N.V. Krishna, L. Giribabu and S. Venugopal Rao , J. Mater. Chem. C. **2**, 1711 (2014).
87. N. Del Fatti, F. Vallée, and C. Flytzanis, Y. Hamanaka and A. Nakamura, Chem. Phys. **251,** 215 (2000)
88. S. Link, C. Burda, Z.L. Wang and M. A. El-Sayed, J. Chem. Phys. **111**, 1255 (1999)
89. L. Anisimov, Kapeliovich, B. L.T. L. Perel'man, Sov. Phys. JETP **39,** 375 (1975)
90. S. Mukamel, Nonlinear Optical Spectroscopy, Oxford University Press, New York, vol. 561, 1995.
91. Hofer, P. Cruck, W. Kaiser, Chem. Phys. Lett. **224**, 411 (1994)
92. V. Namboodiri, M. Namboodiri, G. Flachenecker, and A. Materny, J. Chem. Phys. **133**, 054503 (2010)
93. H. Skendarovic, Phys. Scr. T. **135**,014037 (2009)
94. G. Boudebs, K. Fedus, C. Cassagne and H. Leblond, Appl. Phys. Lett., **93**, 021118 (2008)
95. P. N. Prasad and D. J. Williams, Introduction to Nonlinear Optical Effects in Molecules and Polymers (Wiley, New York, 1991).
96. S. Rozouvan, J. Opt. Soc. Am. B. **16**, 768 (1999)
97. K. Kamada, M. Ueda, T. Sakaguchi, K. Ohta and T. Fukumi, Chem. Phys. Lett. **263,** 215 (1996).
98. R. L. Sutherland, Handbook of Nonlinear Optics, 2nd ed. (Marcel Dekker, New York, 2003).
99. M. Samoc, A. Samoc, B. Luther-Davies, Z. Bao, L. Yu, B. Hsieh and U. Scherf, J. Opt. Soc. Am. B **15**, 817 (1998); M. Zhao, Y. Cui, M. Samoc, P.N. Prasad, M.R. Unroe and B.A. Reinhardt, J. Chem. Phys. **95**, 3991(1991)
100. R. S. Santosh Kumar, S. Venugopal Rao, L. Giribabu, and D. Narayana Rao, Optical Materials 3, 1042 (2009); M. Motzkus, S. Pedersen and A.H. Zewail, J. Phys. Chem. **100**, 5620 (1996)
101. E.J. Brown, Q. Zhang and M. Dantus, J. Chem. Phys. **110**, 5772 (1999)

7

Conclusions and Future Scope

7.1. Conclusion

Ultrafast laser ablation in liquid media (ULAL), wherein ps or fs pulses are utilized, is attractive technique, free from multistep processes lasting for long periods of time. ULAL significantly moderates oxidation effects to produce pure Cu/Si materials. Moreover, ULAL provides an environment (oxygen free, polar, poor capability of air dissolution) to minimize the effect of oxidation in the process of NM fabrication. Furthermore, ULAL of bulk metal target in suitable aqueous media produced colloidal NPs in liquid and periodic (submicron dimensions) surface NSs on the substrate simultaneously. ULAL has attracted a lot of attention as a unique material processing technique that provides distinct advantages in applications over the ns laser ablation. In the ultrafast regime (typically <5 ps), ablation threshold is not overtly dependent of the pulse duration and is free of transient interference when compared to the ns regime. Besides, ultrashort laser pulses permit less thermal damage and a nearly melt free ablation, if carried out close to ablation threshold. Owing to the large peak intensities associated with ps and fs laser pulses, absorption involves multi-photon processes. Moreover, within ps and fs time scales the energy cannot be transferred from electron to the lattice instantly. Thermal descriptions maintain individuality between electron and lattice temperature. Therefore, two-temperature model becomes necessary in order to describe thermal phenomena rather than one temperature model used in the ns regime. Consequently, material transits to a super critical fluid state and vaporization occurs to interact with surrounding liquid media creating multifaceted NMs.

Additionally, LIPSS [which can be expected due to the interference of incoming electric filed with the surface electromagnetic wave (SEW)] in metals/semiconductors have also been investigated using ps and fs pulses. In this regime, LIPSS (spikes or ripples) can be produced when the laser fluence is approximately equal to the threshold fluence of the material. In addition to the specific liquid environments, effect of pulse energy, different writing conditions were employed to enhance the probability of LSFL/HSFL formation. We observed laser induced periodic surface structures orient either parallel or perpendicular to input beam polarization. These ablated plasmonic metal (LIPSS) surfaces have been utilized for trace level detection of organic molecules (R6G) and explosive materials [ANTA, TNT, FOX-7 and CL-20] using the SERS technique. Especially, periodic

surface structures on metals exploiting significant Raman enhancements [via localized surface plasmon resonances (LSPR) and surface plasmon Polaritons (SPP)] have been demonstrated. We had also successfully recorded the SERS spectra (using nanostructured Cu substrate) of three different analytes after careful cleaning of the substrates clearly demonstrating the ability to recycle them. Along with SERS studies, metal and semiconductor NPs were utilized in SEF, Z-scan, pump-probe and DFWM studies for photonics applications.

The thesis inspected in detail the following aspects: (i) feasibility of ultrafast laser (ps and fs) ablation of metal (Cu) and semiconductor (Si) materials for efficient fabrication of NPs and NSs. The basic physics and advantages of ps/fs ablation was explored (ii) the effects of input pulse energy, scanning speeds, different surrounding liquids etc. on ablation mechanisms and the fabricated products (iii) a thorough analysis/characterization, including linear and nonlinear spectroscopy, of the generated NPs and NSs (iv) demonstration of applications of the generated Cu and Si NPs in photonics, and produced Cu NSs and Ag coated Si NSs for explosives detection.

- An extensive study pertaining fabrication of Cu NPs and NSs via ps laser multiple/single line ablation was carried out in organic liquids. Combined effect of (a) scan separation with respect to the beam diameter ($2\omega_0$) at the focus resulted in different writing conditions namely multiple [line separation (5 μm) < spot diameter (50 μm)] and single [line separation (60 μm) > spot diameter (50 μm)] ablation (b) different organic liquid media which led to differences in the yield and sizes of the NPs.
- The interaction of transient metallic/plasma plume with the constituents of surrounding liquid and its dependence on the intrinsic nature of the liquid media led to the fabrication of (a) pure Cu NPs in acetone, CuCl NPs in DCM, CuO NPs in ACN and $CuCl_2$ NPs in chloroform (b) pure Si NPs in acetone, Si/SiO_2 NPs in water, Si-C NPs in DCM and Si-C NPs in chloroform.
- Formation and collapse of the cavitation bubbles resulting the fabrication of NPs and NSs was understood from the numerically calculated cavitation bubble dynamics. In our cases, the construction of big bubble provided the micro voids which were observed on Cu materials in DCM and Chloroform.

Whereas small bubble offered nano-voids observed on Cu substrates in acetone. Similarly, random roughness and nano cavities were also obtained on Cu substrates under the effect of different pulse numbers which could be due to collapse of the cavitation bubble.

- Dependence of yield of the CuO NPs and Si on the input laser energy in the process of double/multiple line ablation in acetone and ACN, respectively was investigated systematically through the estimation of effective spot size on the target and corresponding fluences. Size dependent tunability of the PL peak position of the Si NPs was discussed. Present set of experiments revealed that the size of NPs is high for lower (10 μJ) and high (500 μJ) pulse energies and, the intermediate energies (~50 μJ) showed lower size of Si NPs and 100 μJ illustrated lower size of Cu NPs which depend exclusively on the formation of cavitation bubble on target.
- Additionally, production of laser induced periodic surface structures (LIPSS) on Cu substrate with periodicity of ~2λ/3-λ/3 was confirmed by surface morphology studies. Non-uniform energy distribution plays a significant role for the formation of LIPSS and it depends on the electron-phonon coupling coefficient (γ) which could increase with increasing number of shots at same place
- The periodicity of the produced HSFLIPSS on (a) the input laser energy the process of double/multiple line ablation and (b) on different pulse number in acetone was also studied. Complex refractive index and electron density in conduction band were estimated from the effective fluence and absorbance at same fluence for effect of pulse energy and effect of pulse number, respectively. Finally, theoretically estimated period of gratings were well agreed with the experimentally observed periodicity for the substrates were discussed.
- Ps multiple/single line technique fabricated Cu substrates utilized exultantly to investigate the surface plasmon (localized and propagating) mediated enhancements of different analytes using SERS studies. The reproducibility of the Cu targets for trace level detection of explosive molecules was dealt with a simple cleaning procedure. Trace level detection of explosive compounds such as ANTA, TNT was performed along with R6G individually after subjecting

surfaces to appropriate cleaning procedures and obtained enhancement factors of $>10^5$.

- The ps laser fabricated Cu NSs on the effects of pulse energies demonstrate the similar SERS enhancement factor ($>10^5$) for FOX-7 molecule for all the substrates since they could have generated similar local fields even the excitation of surface Plasmons. Cu-200 has been chosen for further SERS investigation of ANTA and CL-20 explosive molecules of 1 μM concentration and estimated E.F were ~10^8 and ~10^4, respectively.
- Pulse number influenced Cu NSs in fs regime and these were utilized to detect the R6G (5×10^{-6} M) and FOX-7 (25×10^{-6} M) with E.Fs of ~10^5 and ~10^6, respectively.
- TTC-Cu-Cl, TPC-Cu-Cl colloidal solutions in TTC, TPC and Cu/CuCl nanocomposites in chloroform were prepared by means of ps laser ablation of bulk Cu target. Significant enhancements (~10^5) in the fluorescence were obtained for TTC/TPC placed on Cu/CuCl nanocomposites compared to the case wherein fluorophores were directly adsorbed (E.F. ~333) on the substrates (TTC-Cu-Cl, TPC-Cu-Cl colloids). The possible reasons behind the enhancement are deliberated in detail. The enhancement in fluorescence is attributed to the generated localized electromagnetic field of Cu NPs.
- The fabrication of Ag plating on the fabricated Si NSs under the influence of pulse energies using ion beam deposition has been studied and these structures have been used for SERS studies of ANTA (1 μM) explosive molecule. Ag coated SiS-100 demonstrated 2 times more enhancement than other substrates.
- The colloidal Cu NPs and Si NPs demonstrated large third order nonlinearities in ps and fs domains, respectively. Moreover, Initial investigation on excited state dynamics of both colloids of Cu NPs and Si NPs were studied using fs Pump-probe technique. The Cu/Si NPs demonstrated both electron-electron relaxations and electron-phonon relations.
- Preliminary studies on DFWM of colloidal NPs and corrole conjugated Cu NPs have been studied and the data has confirmed that both colloids illustrated third order NLO behavior.

7.2. Future scope

- Detailed experimental investigations are essential on the dynamics of multiple cavitation bubbles produced by fs/ps laser ablation of metals/semiconductor targets immersed in liquid media for correlating the surface morphology of generated NPs and NSs with respect to input laser parameters.
- Combining both plasmonic (Ag/Au/Cu) NSs and NPs could improve individual enhancements and the detection limit in SERS and SEF studies.
- Plasmonic material plating on Si nanostructured targets by simple evaporation or RF sputtering techniques to utilize them as efficient cost effective SERS active platforms to detect the trace amount of molecules will be taken up in future.
- Utilizing hybrid (metal and semiconductor) nanostructures for preparing efficient SERS substrates is another possibility which could be explored.
- The process of LIPSS on metals using fs pulses is still being debated which necessitates additional investigations to understand the mechanism involved. We can understand the mechanism through measurement of electron-phonon coupling coefficient by in situ pump-probe technique at time of ablation.

8. Appendix

8.1. Curriculum vitae

Communicate Address

Syed Hamad
Research Scholar
Reg. No. 09PHPH09
School of Physics, Science Complex
University of Hyderabad
Gachhi Bowli, Hyderabad-500046,
India

Email: siddu.hamad@gmail.com
Mobile: +91-9676528880

Current area of research: Ultrashort pulse interaction of materials in aqueous media for the fabrication of nanoparticles and nanostructures: Linear and nonlinear Raman scattering for Photonic and biomedical applications

Objective: Seeking a suitable ***post doctoral position*** to utilize my skills and abilities in well reputed groups that offers opportunities to contribute towards scientific excellence.

Research Interests

- Metal/metal alloys/semiconductor NPs/NSs fabrication by ultrashort pulse laser ablation in liquids
- Surface enhanced Raman spectroscopy (detection of trace level of organic molecules such as Rodhamine 6G, crystal violet, ANTA (5-amino-3-nitro-l,2,4-triazole), Fox-7(1,1-diamino-2,2-dinitroethene); biological compounds etc. using SERS active metal and metal/semiconductor NSs.
- Nonlinear Optics: Degenerate four wave mixing, autocorrelation, 3^{rd} order and 2^{nd} order nonlinearities, SHG and Z-scan.
- Ultrafast degenerate Pump-probe spectroscopy, ultrafast non-degenerate (two colors) pump-probe spectroscopy, Ultrafast coherent anti-stokes Raman spectroscopy (UF-CARS) and Femtosecond stimulated Raman spectroscopy (FSRS).
- Experimental investigations on the dynamics of multiple cavitation bubbles produced by fs/ps laser ablation of metals/semiconductor targets immersed in liquid media for estimating the size of the generated NPs.

Academic Qualifications

2009-2014	Ph.D. (Thesis submitted on 31st December 2014) School of Physics, University of Hyderabad, Hyderabad (INDIA).
Thesis Title	"Ultrafast laser fabricated nanoparticles and nanostructures: Characterization, Spectroscopy and Applications"
Supervisors	Dr. S. Venugopal Rao (Associate Professor - ACRHEM) and Dr. Ashoka VS (Assistant Professor) at University of Hyderabad, Hyderabad.
2005-2007	M.Sc. Physics with specialization in "Condensed matter Physics" Nagarjuna University, Guntur (INDIA) Percentage: 70.5 % in aggregate - May 2007
2002-2005	B.Sc with subjects Mathematics, Physics and Chemistry. Sri Venkateshwara University, Thirupathi (INDIA) Percentage: 64.5 % in aggregate - May 2005
2000-2002	Intermediate with subjects Mathematics, Physics, Chemistry, English and Hindi. Board of Intermediate Education, Hyderabad, Andhra Pradesh (INDIA). Percentage: 71.2 % in aggregate - May 2002
1999-2000	High school, Mathematics, Science, Social, Telugu, English and Hindi. Board of Secondary Education, Andhra Pradesh (INDIA) Percentage: 69.7 % in aggregate - March 2000

Awards/Fellowships/Teaching skills

- Participated in XXIV International Conference on Raman spectroscopy (ICORS-2014) held at Jena, Germany in Aug 2014, to present a paper on laser ablation based SERS active substrates and their utility for High energy materials
- Received travel grant as award under category of Young Scientist to attend the international conference from University with Potential for Excellence (UPE, Phase-II)
- Won '*First Best Poster Award*' at 8th International High Energy Materials Conference and Exhibit (HEMCE 2011), 10-12 November, Terminal Ballistics Research Laboratory, Chandigarh, India. Poster entitled "Synthesis and characterization of Aluminum nanoparticles obtained using femtosecond laser ablation",
- Awarded as a Senior Research fellow (SRF), the interview conducted by **Council of Industrial Scientific Research (CSIR), New Delhi, India in 2013.**
- Awarded as a Junior Research Fellow (JRF), the interview conducted by University Grant Commission- Basic Scientific Research (UGC-BSR), India in 2012.
- Qualified Joint Entrance Screening Test (JEST) conducted by JEST institutes for PhD program and secured with percentile of 96 in 2010.

- Tutorial Quantum mechanics classes of M. Sc I Year and II year, Thermodynamics and Electronics classes for Integrated M. Sc III Year in University of Hyderabad, India

Research Experience

- Broad knowledge and experience in executing the multi-step fabrication of plasmonic and semiconductor nanomaterials through laser ablation using ultrafast laser pulses.
- Expertise in setting up time resolved studies such as degenerate four wave mixing (DFWM) and Pump-probe experiments to investigate excited state dynamics.
- Experience in the up gradation of DFWM experiment to coherent anti-Stokes Raman scattering experiment to enhance the signal to noise ratio. In this experiment we generated white light continuum (WLC) in one of the three paths.
- Extraction of nonlinear optical properties of plasmonic nano-colloids and organic molecules by an experimental technique "Z-Scan".

Hands-on-experience in the following Instruments

- MICRA femtosecond oscillator (tunable around 800 nm; 15-150 fsec pulses), Legend, Ultrafast amplifiers (2 ps and 40 fs), Light Conversion Optical Parametric Amplifier (2 ps and 40 fs) tunable from 230 nm to 2 microns and Single short Auto-correlator.
- Innolas Nd:YAG + Radiant Dye laser (tunable from 300 nm to 3.0 microns).
- Chameleon Femtosecond Oscillator (Tunable from 680 nm to 1060 nm; 150 fs pulses)
- Automation of Newport ESP-200 controller and X-Y-Z translation stage using Labview and Matlab.
- *Signal recovery 7265 lock-in –amplifier* was utilized to record auto-correlation traces, DFWM traces and nonlinear absorption and refraction processes in Z-scan.
- *Perkin Elmer UV-Vis absorption spectrometer* was utilized extensively for characterizing the prepared plasmonic nanomaterials.

Research Landmarks

- Investigation of solvent effects on the fabrication of Cu nanoparticles sizes and material compositions by laser ablation and their photonic applications (Journal of Physics D. Applied Physics, 2013)
- Influence of the pulse energy on the fabrication of Si nanoparticles and periodic nanostructures and estimated the periodicity of periodic surface

structures using theory and experiment (Journal of Physical Chemistry C, 2014)

- Investigation on the fabrication of solvent influenced copper nanostructures and there were utilized for cost effective SERS active substrates to the detection of high energy material and organic molecules (Applied Physics Letter, 2014) and surface enhanced fluorescence from organic molecules (Chemical Physics Letters, 2015)
- A review was written to explain extensive investigation of laser ablation and the applications of nanomaterials such as surface enhanced Raman spectroscopy (SERS), nonlinear optical instrumentation, and anti-bacterial agents. (J. Nanosci. Nanotech, 2014)

8.2. Publications

List of Publications included in Thesis: In Refereed Journals

1. **S. Hamad**, G. Krishna Podagatlapalli, M. A. Mohiddon and S. Venugopal Rao, "Surface Enhanced Fluorescence from Corroles and SERS Studies of Explosives Using Copper Nanostructures" Chem. Phys. Lett. **621**, 171 (2015). [Impact factor – 1.99]
2. **S. Hamad**, G. Krishna Podagatlapalli, M. A. Mohiddon and S. Venugopal Rao, "Cost effective nanostructured copper substrates prepared by ultrafast laser pulses for explosives detection using surface enhanced Raman scattering", Appl. Phys. Lett. **104,** 263104 (2014). [Impact factor – 3.52]
3. **S. Hamad**, G. Krishna Podagatlapalli, V.S. Vendamani, S.V.S. Nageswara Rao, A.P. Pathak, Surya P. Tewari, and S. Venugopal Ra**o**, "Femtosecond Ablation of Silicon in Acetone: Tunable Photoluminescence from Generated Nanoparticles and Fabrication of Surface Nanostructures" J. Phys. Chem. **C 118** , 7139 (2014) [Impact factor – 4.84]
4. S. Venugopal Rao, G. Krishna Podagatlapalli, **S. Hamad**, "Ultrafast Laser Ablation in Liquids for Nanomaterials and Applications," J. Nanosci. Nanotech. **14,** 1364 (2014) **(Review Article).** [Impact factor – 1.34]
5. **S. Hamad**, G. Krishna Podagatlapalli, Surya P. Tewari, and S. Venugopal Rao, "Synthesis of Cu_2O, CuCl, and Cu_2OCl_2 nanoparticles by ultrafast laser ablation of copper in liquid media," Pramana-J. Phys. **82,** 331 (2014). [Impact factor – 0.72]
6. **S. Hamad**, G. Krishna Podagatlapalli, S. P. Tewari, and S. Venugopal Rao, "Influence of picosecond multiple/single line ablation on Copper nanoparticles and nanostructures fabricated for surface enhanced Raman spectroscopy and photonics applications," J. Phys. D: Appl. Phys. **46,** 485501 (2013). [Impact factor – 2.52]

7. **S. Hamad**, Surya P. Tewari, L. Giribabu, S. Venugopal Rao**,** "Picosecond and Femtosecond Optical Nonlinearities of Novel Corroles," J. Porphy. Phth. **16,** 140 (2012). [Impact factor – 1.36]
8. **S. Hamad**, G. Krishna Podagatlapalli, Md. Ahamad Mohiddon, and S. Venugopal Rao, "SERS Studies of Explosive Molecules with Copper Nanostructures Fabricated using Ultrafast Laser Ablation" Submitted to RSC Advances (2015).

Conference Papers included in Thesis

9. **S. Hamad**, G. Krishna Podagatlapalli and S Venugopal Rao, "Explosives Detection with Copper Nanostructures Fabricated using Ultrafast Laser Ablation in Acetonitrile", DOI: 10.1364/E2.2014.EF4A.5 Conference: Light, Energy and the Environment, OSA, December 02-05, 2014. At Australian National University, Canberra.
10. **S. Hamad**, G. Krishna Podagatlapalli, S.V.S Nageswara Rao, A P Pathak, S Venugopal Rao, "Excited state dynamics of silicon nanocrystals fabricated using ultrafast laser ablation in liquids" Photonics 2014: 12th International Conference on Fiber Optics and Photonics © OSA 2014, T3A.4
11. **S. Hamad**, G. K. Podagatlapalli, A. Hussain, N. Ahmed, S. Sreedhar, and S. P. Tewari, S. Venugopal Rao, "Fabrication of Metal Nano-entities Using Ultrafast Ablation for SERS, Photonics, and Biomedical Applications," in ***International Conference on Fibre Optics and Photonics*****,** OSA Technical Digest (online) (Optical Society of America, 2012), paper MPo.31.
12. **S. Hamad**, G. Krishna Podagatlapalli, and S. Venugopal Rao, "Surface enhanced fluorescence of corroles using copper nanoparticles" accepted in IEEE CONFERENCE PUBLICATIONS, DOI: 10.1109/WRAP.2013.6917707

Other Publications: In Refereed Journals

13. G. Krishna Podagatlapalli, **S. Hamad**, Md. Ahamad Mohiddon, and **S. Venugopal Rao** , "Fabrication of Nanoparticles and Nanostructures using Ultrafast Laser Ablation of Silver with Bessel Beams" Las. Phys. Lett. **Accepted** (2015) [Impact factor – 2.96]
14. N. Sudharsana, **S. Hamad**, S. Venugopal Rao, V. Krishnakumar, R. Nagalakshmi, "Hydroxyethylammonium maleate (HEAM) single crystal for optical limiting applications" Appl. Phys. A **118**, 171 (2015) [Impact factor – 1.69]
15. V.S. Vendamani, **S. Hamad**, V. Saikiran, A.P. Pathak, S. Venugopal Rao, V. V. Ravi Kanth Kumar and S.V.S. Nageshwara Rao "Generation of Silicon Nanoparticles by Femtosecond Laser Ablation of Porous Silicon in Liquids and Radiation Effects," J. Mater. Sci., **50**, 1666 (2015). [Impact factor – 2.3]
16. V. Saikiran, V.S. Vendamani, **S. Hamad**, S.V.S. Nageswara Rao, S. Venugopal Rao, and A.P. Pathak, "Swift heavy ion irradiation induced modification of Si

nanoparticles prepared by laser ablation," NIMB. **333** , 99 (2014). [Impact factor – 1.27]

17. G. Krishna Podagatlapalli, **S. Hamad**, M. A. Mohiddon and S. Venugopal Rao, Effect of oblique laser incidence on the fabrication of silver nanomaterials in water using picosecond ablation technique Appl. Surf. Sci. **303,** 217 (2014). [Impact factor – 2.54]
18. G. Krishna Podagatlapalli, **S. Hamad**, Surya P. Tewari, S. Sreedhar, Muvva D. Prasad, and S. Venugopal Rao, "Silver nano-entities through ultrafast double ablation in aqueous media for SERS and photonics applications," J. Appl. Phys. **113** , 073106 (2013). [Impact factor – 2.19]
19. P.T. Anusha, D. Swain, **S. Hamad**, T. Shuvan Prashant, L. Giribabu, Surya P. Tewari, S. Venugopal Rao, "Ultrafast excited state dynamics and third order optical nonlinearities of novel Corroles," J. Phys. Chem. C **116**, 17828 (2012). [Impact factor – 4.84]
20. G. Krishna Podagatlapalli, **S. Hamad**, S. Sreedhar, Surya P. Tewari, S. Venugopal Rao, "Fabrication and characterization of aluminum nanostructures and nanoparticles obtained using femtosecond ablation technique," Chem. Phys. Lett. **530,** 93 (2012). [Impact factor – 1.99]

Total Impact points = 36.06

Full papers in conference proceedings/Online Conference publications

1. G. Krishna Podagatlapalli, **S. Hamad** and S. Venugopal Rao, "Silver Nanomaterials in Aqueous Media Fabricated with Non-diffracting Picosecond Bessel Beam and Applications" DOI: 10.1364/E2.2014.JW6A.13 Conference: OSA Light Energy Environment meeting, At Canberra Australia December 2-5, 2014, Volume: ISBN: 978-1-55752-756-1
2. G. Krishna Podagatlapalli, **S. Hamad** and S. Venugopal Rao, "Fabrication of Hybrid Ag-Au Nanomaterials for Explosives Detection" Conference: Photonics 2014 12th International Conference on Fiber Optics and Photonics, IIT Kharagpur, December 13-16, 2014. © OSA 2014, S5A.51.
3. D. Swain, P.T. Anusha, **S. Hamad**, L. Giribabu, Surya P Tewari, S. Venugopal Rao, "Femtosecond pump-probe spectroscopy of novel Corroles," AIP Conf. Proc, 1461**,** 363-366, 2012.
4. S**. Hamad**, G. Krishna Podagatlapalli, Surya P. Tewari, S. Venugopal Rao, "Femtosecond ablation of Aluminum for synthesis of nanoparticles and nanostructures and their optical characterization," Proc. SPIE, 8245, 82450L, 2012.
5. **S. Hamad**, G. Krishna Podagatlapalli, L. Giribabu, Surya P. Tewari, S. Venugopal Rao, "Femtosecond and picosecond nonlinear optical studies of Corroles," Proc. SPIE, 8258,82581C, 2012.

6. **S. Hamad**, G. Krishna Podagatlapalli, Surya P. Tewari, L. Giribabu, S. Venugopal Rao, "Femtosecond and Picosecond Optical Nonlinearities Of Corroles Studied Using Z- Scan Technique," AIP conf. Proc. 1391**,** 683-685, 2011

Book Chapters

1. G. K. Podagatlapalli, **S. Hamad**, S. Sreedhar, and Surya P. Tewari, S. Venugopal Rao, "Fabrication and Characterization of Aluminum Nanostructures Using Femtosecond Ablation Technique," in Advanced Nanomaterials and Nanotechnology, Giri, P. K.; Goswami, D. K.; Perumal, A. (Eds.) Springer Proceedings in Physics, Vol. 143, pp. 229-238, Springer-Verlag, Berlin Heidelberg, 2012. **(ISBN: 978-3-642-34215-8).**
2. S. Venugopal Rao, G. Krishna Podagatlapalli, **S. Hamad**, S. Sreedhar, Surya P. Tewari, "Ultrafast Laser Ablation: Creating Nanoparticles and Nanostructures for Applications in Photonics and Surface Enhanced Raman Scattering," Proc. Second International Conference on Advanced in Materials Processing and Characterization (AMPC2013), 317-322, Ed.'s S. Balasivanandha Prabu, S Senthil Kumaran, L. Karnamoorthy, and K.A. Padmanabhan, Allied Publishers Pvt. Ltd., 2013. **(ISBN: 978-81-8424-819-7)**

Presentations in International Conferences/Workshops

1. S. Hamad, G. Krishna Podagatlapalli, and S. Venugopal Rao, "Nanostructed Copper substrates for explosive detection using SERS" XXIV International Conference on Raman Spectroscopy (ICORS-2014), Aug 10^{th}– 15^{th} Jena, Germany (POSTER)
2. G. Krishna Podagatlapalli, S. Hamad, and S. Venugopal Rao, "Detection of secondary explosives using ultrafast laser ablated silver nanostructures through SERS", XXIV International Conference on Raman Spectroscopy (ICORS-2014), Aug 10^{th}– 15^{th} Jena, Germany (POSTER)
3. G. Krishna Podagatlapalli, S. Hamad, S. Venugopal Rao, "Near field detection of RDX,TNT, CL-20 and ANTA explosive molecules through surface enhanced Raman scattering using laser ablated silver targets in aqueous media " 9 th International High Energy Materials Conference and Exhibits (HEMCE), Feb 13-15 th 2014, Vikram Sarbhai Space Centre, Thituvananthapuram, India (ORAL)
4. G. Krishna Podagatlapalli, S. Hamad, S. Venugopal Rao, Explosive detection with plasmonic nanomaterials via surface enhanced Raman spectroscopy fabricated by ultrafast laser interaction, High Energy Density Sciences in Asia (Asia HEDS), Jan 19- 22nd Busan, South Korea (POSTER)
5. G. Krishna Podagatlapalli, S. Hamad, S. Venugopal Rao, "Fabrication of silver nanomaterials through ultrafast ablation in liquids and their applications in photonics and SERS studies of explosive molecules "Theme meeting on ultrafast science (UFS), Oct 25-26, 2013, IIT Kharagpur,West Bengal, INDIA (POSTER).
6. **S. Hamad,** V. S. Vendamani, R. Brahma, S.V.S. Nageswara Rao, Surya P. Tewari, A P Pathak, and S. Venugopal Rao, "Ultrafast Laser Generated Silicon Nanocrystals and Nanostructures," 7^{th} Internation Conference on

Materials for Advanced Technologies (ICMAT), 30 June-05 July 2013, Suntec, Singapore. (ORAL)

7. G. Krishna Podagatlapalli, **S. Hamad**, Surya P. Tewari, S. Venugopal Rao, "Nanoscale Silver and Copper Fabricated Using Ultrafast Laser Ablation in Liquids for SERS Studies of Explosives," 7th Internation Conference on Materials for Advanced Technologies (ICMAT), 30 June-05 July 2013, Suntec, Singapore. (POSTER)
8. V. Saikiran, **S. Hamad**, V S Vendamani, S.V.S. Nageswara Rao, S. Venugopal Rao, Surya P. Tewari, and A P Pathak, "Study of swift heavy ion irradiation effects on Si nanoparticles synthesisized by picosecond laser abalation in liquids," E-MRS 2013 Spring Meeting, May 27-31, 2013, Congress Center - Strasbourg, France.
9. G. Krishna Podagatlapalli, **S. Hamad**, Surya P. Tewari, S. Venugopal Rao, "Nanoscale silver and copper fabricated using ultrafast laser ablation in liquids for SERS studies of explosives," INDO-US International Workshop on Nanosensor Science & Technology (IWNST-2013) 27th February - 1st March, 2013, Berhampur, Odisha, India. (RECEIVED BEST POSTER AWARD)
10. S. Venugopal Rao, G. Krishna Podagatlapalli, **S. Hamad**, S. Sreedhar, Surya P. Tewari, "Ultrafast Laser Ablation: Creating Nanoparticles and Nanostructures for Applications in Photonics and Surface Enhanced Raman Scattering," Second International Conference on Advanced in Materials Processing and Characterization (AMPC2013), Anna University, Chennai, February 6-8, 2013. (ORAL)
11. **S. Hamad**, G. Krishna Podagatlapalli, Arif Hussain, Niyaz Ahmad, S. Sreedhar, Surya P. Tewari, S. Venugopal Rao, "Fabrication of Metal Nano-entities Using Ultrafast Ablation for SERS, Photonics, and Biomedical Applications," Photonics 2012, International Conference on Fiber Optics and Photonics, December 09-12, 2012, IIT Madras, Chennai, India. (POSTER)
12. **S. Hamad**, G. Krishna Podagatlapalli, S. Sreedhar, Surya P. Tewari, S. Venugopal Rao, "Surface enhanced Raman scattering studies from stable copper colloids fabricated by laser ablation," 23rd International Conference on Raman spectroscopy (ICORS - 2012), 12-17 August, IISc, Bangalore, INDIA. (POSTER)
13. G. Krishna Podagatlapalli, **S. Hamad**, S. Sreedhar, Surya P. Tewari, S. Venugopal Rao, "Fabrication of silver nano-entities through ultrafast laser ablation and their characterization for SERS applications," 23rd International Conference on Raman spectroscopy (ICORS - 2012), 12-17 August, IISc, Bangalore, INDIA. (POSTER)
14. **S. Hamad**, G. Krishna Podagatlapalli, Surya P. Tewari, S. Venugopal Rao, "Femtosecond ablation of Aluminum for synthesis of nanoparticles and nanostructures and their optical characterization," SPIE Photonics West, 21-26 January 2012, San Francisco, California, USA. (POSTER)
15. **S. Hamad**, G. Krishna Podagatlapalli, L. Giribabu, Surya P. Tewari, S. Venugopal Rao, "Femtosecond and picosecond nonlinear optical studies of Corroles," SPIE Photonics West, 21-26 January 2012, San Francisco, California, USA. (POSTER)
16. D. Swain, P.T. Anusha, **S. Hamad**, L. Giribabu, Surya P Tewari, S. Venugopal Rao, "Femtosecond pump-probe spectroscopy of novel Corroles," International Workshop on Functional Materials (IWFM-2011), NIST, Berhampur, Odisha, December 20-22, 2011. (POSTER)

17. G. Krishna Podagatlapalli, **S. Hamad**, Surya P. Tewari, S. Venugopal Rao, "Fabrication and characterization of aluminum nanostructures using femtosecond ablation technique," International conference on advanced nanomaterials and nanotechnology (ICANN 2011), IIT Guwahati, December 8-10, 2011. (POSTER)
18. **S. Hamad**, S. Sreedhar, G. Krishna Podagatlapalli, Surya P. Tewari, G. Manoj Kumar, S. Venugopal Rao, "Synthesis and characterization of Aluminum nanoparticles obtained using femtosecond laser ablation," 8th International High Energy Materials Conference and Exhibit (HEMCE 2011), 10-12 November, Terminal Ballistics Research Laboratory, Chandigarh, India. (POSTER) **(RECEIVED BEST FIRST POSTER AWARD)**
19. **S. Hamad**, G. Krishna Podagatlapalli, L. Giribabu, Surya P. Tewari, S. Venugopal Rao, "Femtosecond and Picosecond Optical Nonlinearities of Corroles Studied using Z- Scan Technique," Optics'11-A conference on light, May 23-25, 2011, Calicut, Kerala, India. (ORAL)

Presentations in **National Conferences**

20. **S. Hamad**, G Krishna Podagatlapalli, V. S. Vendamani, R. Brahma, S.V.S. Nageswara Rao, Surya P. Tewari, A P Pathak, and S. Venugopal Rao, "Femtosecond ablation of Silicon in acetone: Tunable photoluminescence from generated nanoparticles and fabrication of surface nanostructures." NLS-22, DAE-BRNS National Laser Symposium, January 08-11, 2014, Manipal institute of technology, Manipal University, Manipal, India. (POSTER)
21. G Krishna Podagatlapalli, **S. Hamad**, and S. Venugopal Rao, "Effect of non-zero angle of incidence on the fabrication of silver nanomaterials through picosecond laser ablation in water." NLS-22, DAE-BRNS National Laser Symposium, January 08-11, 2014, Manipal institute of technology, Manipal University, Manipal, India. (POSTER)
22. **S. Hamad**, G. Krishna Podagatlapalli, Surya P. Tewari, S. Venugopal Rao, "Surface enhanced Raman scattering by multiple Ultrashort pulses created metallic nanostructures in liquid media." annual Conference Frontiers in Physics (FIP-2013) during September 19-21, 2013, University of Hyderabad, Hyderabad. (POSTER)
23. G. Krishna Podagatlapalli, **S. Hamad**, Surya P. Tewari, S. Venugopal Rao, "Fabrication of periodic surface structures through ultrafast laser ablation of metals,," NLS-21, DAE-BRNS National Laser Symposium, February 06-09, 2013, BARC, Mumbai, India. (POSTER) ISBN Number 978-81-903321-3-2
24. **S. Hamad**, G. Krishna Podagatlapalli, Surya P. Tewari, S. Venugopal Rao, "Synthesis, characterization and nonlinear optical properties of copper complex nanoparticles using picosecond laser ablation," NLS-21, DAE-BRNS National Laser Symposium, February 06-09, 2013, BARC, Mumbai, India. (POSTER) ISBN Number 978-81-903321-3-2
25. **S. Hamad**, R. Bramha, S.V.S. Nageswara Rao, A.P. Pathak, Surya P. Tewari, S. Venugopal Rao, "Ultrafast laser generated silicon nanocrystals

and nanostructures," XXXVII National Symposium of Optical Society of India, Pondicherry University, Puducherry, 23-25 January 2013. (ORAL)

26. G. Krishna Podagatlapalli, **S. Hamad**, Arif Hussain, Niyaz Ahmad, S. Sreedhar, Surya P. Tewari, S. Venugopal Rao, "Anti-bacterial studies of ultrafast laser generated Copper and Silver nanoparticles," XXXVII National Symposium of Optical Society of India, Pondicherry University, Puducherry, 23-25 January 2013. (ORAL)
27. R. Bramha, **S. Hamad**, S.V.S. Nageswara Rao, A.P. Pathak, Surya P. Tewari, S. Venugopal Rao, "Fabrication of Si Nanocrystals by Ultrafast Laser Ablation of Si in Liquid Media," Frontiers in Physics 2012, September 26-28, 2012, University of Hyderabad, Hyderabad. (POSTER)
28. **S. Hamad**, G. Krishna Podagatlapalli, Arif Hussain, Niyaz Ahmad, S. Sreedhar, Surya P. Tewari, S. Venugopal Rao, "Ultrashort pulse laser generated copper nanoparticles for applications in Biomedicine, Photonics, and SERS," Frontiers in Physics 2012, September 26-28, 2012, University of Hyderabad, Hyderabad. (POSTER)
29. G. Krishna Podagatlapalli, **S. Hamad**, S. Sreedhar, Surya P. Tewari, Muvva D. Prasad, S. Venugopal Rao, "Ultrafast laser double ablation of silver nanoparticles and nanostructures," Frontiers in Physics 2012, September 26-28, 2012, University of Hyderabad, Hyderabad. (POSTER) (Received BEST POSTER AWARD)
30. R. Bramha, **S. Hamad**, V. Saikiran, A.P. Pathak, Surya P. Tewari, S.V.S. Nageswara Rao, S. Venugopal Rao, "Synthesis of Si Nanocrystals by Ultrafast Laser Ablation of Si wafers in Liquid Media," 57^{th} DAE Solid State Physics Symposium, 03-07 December 2012, IIT Bombay, Mumbai, India. (POSTER)
31. P.T. Anusha, Debasis Swain, **S. Hamad**, L. Giribabu, Surya P. Tewari, S. Venugopal Rao, "Ultrafast excited state dynamics and third order nonlinearity of novel corroles," DAE-BRNS National Laser Symposium, Anna University, Chennai, January 09-12, 2012. (POSTER)
32. **S. Hamad**, G. Krishna Podagatlapalli, Surya P. Tewari, S. Venugopal Rao, "Femtosecond ablation of Aluminum for synthesis of nanoparticles and nanostructures and their optical characterization," UH-TIFR meeting at University of Hyderabad, August 1-3, 2011. (POSTER)
33. G. Krishna Podagatlapalli, **S. Hamad**, M. Venkatesh, S. Bagchi, Surya P. Tewari, S. Venugopal Rao, "Measurement of femtosecond pulse duration using a simple web camera," DAE-BRNS National Laser Symposium, RRCAT Indore, December 1-4, 2010. (POSTER).

References

Dr. S. Venugopal Rao,
Associate Professor
Advanced Centre of Research in High Energy Materials (ACRHEM)
University of Hyderabad,
Prof. C.R. Road, Gachhi bowli
Hyderabad-500046
Email:soma.venu@yahoo.com
Phone: +91 040 2313 4406/07
Fax: +91 040 2301 2800

Dr. Ashok VS
Assistant Professor
School of Physics, Science Complex
University of Hyderabad,
Prof. C.R. Road, Gachhi bowli
Hyderabad-500046
Email: ashoksp@uohyd.ac.in

Prof. Surya P. Tewari
Former Director
(ACRHEM)
University of Hyderabad,
Prof. C.R. Road, Gachhi bowli
Hyderabad-500046
Email:suryam.tewari@gmail.com

Prof. A. P. Pathak
Eminent Scientist
School of Physics, Science Complex
University of Hyderabad,
Prof. C.R. Road, Gachhi bowli
Hyderabad-500046
Email: appsp@uohyd.ac.in

Errata

(1) Section 1.4.1, Page 5, line no.1 "Raman signature enhancement" has been changed to "Raman signal enhancement".

(2) Section 1.4.2, Page 6, line no.1 "The power of the normal Raman signal P_{NR} scattered from the analyte, depending on the scattering cross-section (σ_{NR}) and number of molecules (N_{NR}) participated in this study" has been changed to "The power of normal Raman signal (P_{NR}) scattered from the analyte depends on the scattering cross-section (σ_{NR}) and number of molecules (N_{NR}) involved"

(3) Section 1.4.2, Page 7, line no.14 "SERS enhancement factor is dependent on fourth power of local electromagnetic field" has been changed to "SERS enhancement factor depends on fourth power of local electromagnetic field".

(4) Section 1.4.2, Page 7, in eq. 1.10 there is no term with "fourth power of local electromagnetic field"

Comment: SERS signal is particularly strong when both laser and scattered fields are in resonance with the surface plasmons. The frequency shift between the laser and scattered fields is usually small compared with the width of the plasmon resonance. Therefore the laser (A_L) and the Raman scattered fields (A_S) increase by same amount, and the signal power ranges approximately with the fourth power of the local electromagnetic field enhancement.

In the eq. 1.10, $G_{EM} = |A_L|^2|A_S|^2 \approx \left|\frac{\epsilon_{inL}-\epsilon_{out}}{\epsilon_{inL}+2\epsilon_{out}}\right|^2 \left|\frac{\epsilon_{in}-\epsilon_{out}}{\epsilon_{in}+2\epsilon_{out}}\right|^2 \left(\frac{a}{a+d}\right)^{12}$

The powers of A_L and A_S fields are 2 and 2, and total power of the electric field is (2+2=) 4.

(5) (a) Section 1.5, Page 8, line 14, The Keldysh parameter is not defined and what it physically signifies?

Comment: The Keldysh parameter (γ) which provides information about the dominant mechanism, is defined as

$$\gamma = \frac{\omega}{e}\left(\frac{mc\varepsilon_0 E_g}{I}\right)^{1/2}$$

Where m, e are reduced mass and charge of the electron, I is the intensity, ω is the laser frequency, ε_0 is the permittivity of free space, E_g is the band gap of

the material, n is the refractive index of the material, and c is the velocity of light. Generally, Keldysh parameter plays a significant role in understanding the ionization process of the dielectric and semiconductor materials. For example, when $\gamma < 0.5$ the system follows tunneling process. On the other hand, multi-photon ionization process leads to generation of free carriers when $\gamma > 1$. We can also observe free electrons in the conduction band due to the dominant effect of combination of tunneling and multi-photon ionization processes when the condition $0.5 < \gamma > 1$ is fulfilled.

(b) Figures 1.2 and 1.3 no mentioned about the lines and what they represents

Comment: Red arrow - photons, black circles – electrons and open circles – holes. Moreover, the curvy lines represent the potential wells.

(6) Section 1.5, Page 8, line no.18 "multi-photon ionization process leads to generation of density of free carriers where $\gamma > 1$" has been changed to "On the other hand, multi-photon ionization process leads to generation of free carriers where $\gamma > 1$".

(7) Section 1.5, Page 9, line no.1 "This avalanche ionization process [illustrated in figure 1.3] occurs where the free electron gets excited by absorbing the incident photon energy which impacts with bound state electron to produce two free electrons at low energies and this process repeats many times" has been changed to "this avalanche ionization process (illustrated in figure 1.3) occurs when the excited free electron impacts bound state electron resulting in production of two free electrons and this process repeats many times".

(8) Section 1.5.3, Page 9, line no.7 "Some of the authors simulated data the following equations since which cannot be solved analytically" has been changed to "Some authors have simulated the above equations since these cannot be solved analytically"

(9) Page 36: What is Verdi laser? It is better to mention the manufacturer's name and some special feature of Verdi laser.

Comment: Verdi laser head (pump laser to femtosecond oscillator) was launched by M/s Coherent with typical and innovative performance which contains a green continuous laser with little noise, fine line width and the higher quality of diffraction limited mode. This continuous beam is the ideal source for pumping to the Ti: sapphire laser systems. The coherent Verdi head contains gain medium of Neodymium Yttrium ortho vanadate (Nd: YVO_4)

which is pumped by diode lasers and produces fundamental wavelength of 1064 nm.

(10) Section 2.2.1, Page No. 37, caption of Figure **2.1** "Interior parts of Micra which comprise (a) VERDI (b) folded short and long cavities (adopted from Micra manual)[1]" has been changed to "Interior parts of Micra which comprise VERDI (upper part) and folded short and long cavities (lower part) (adopted from Micra manual)[1]"

(11) Page 37, figure 2.1 caption: O.C. represents "output coupler" and H.R. represents "high reflector"

(12) Page 45, Please explain what is the meaning of "GVM and GVD are elevated from the dispersion effects"

Comment: The group velocity mismatch (GVM) and group velocity dispersion (GVD) are determined from the dispersion effects, generated in the media and these dispersion effects are explained by phase vector. The phase term can be expanded using Taylor's series

$$k(\omega) = k(\omega_0)L + k'(\omega_0)(\omega-\omega_0)L + \frac{1}{2}k''(\omega_0)(\omega-\omega_0)^2 L ------$$

Where first two terms refer to reciprocal of phase velocity and group velocity (related to GVM), and third term related to variation of group velocity (related to GVD) with respect to the frequency.

$$\beta = \sqrt{\left\{1 + \left[4ln2\left(D_2 \times \frac{L}{\tau_{in}^2}\right)^2\right]\right\}}$$

where β is GVD. D_2, L and τ_{in} refer to second order differentiation term, crystal length and pulse width, respectively.

$$GVM = \frac{1}{V_g(\lambda_1)} - \frac{1}{V_g(\lambda_2)}$$

(13) Section 2.4, Page 50, line no. 11 "The increase in size beam waist diameter on the target in liquid media" has been changed to "The increase of beam waist (diameter) on the target in liquid media"

(14) Section 2.5.1, Page 51, line no. 8 "Transmission Electron Microscopy (TEM) is one of the important techniques in the field of nanotechnology to image the

nanoparticles with resolution of ~10 nm" has been changed to "Transmission Electron Microscopy (TEM) is one of the important techniques in the field of nanotechnology to image nanoparticles with resolution of ~1 nm".

(15) I liked reading Chapter 3 and Chapter 4. It was not clear to me how many images (particles) have been analyzed to construct the histograms presented in figures 3.2, 3.3, 3.4, 3.5 and 3.11 & 4.1, 4.2 and 4.8

Comment: We have considered and analyzed more than **300 particles** to construct the histograms in all the cases.

(16) Page 88: Discrepancy in Cu NPs LSPR peak 600 nm (experimental) vs 580 nm from Mie theory. The discrepancy was attributed to the formation of oxide layer around the particles. If so, why was it is not seen in EDAX data or SAED spectra?

Comment: The EDAX and SEAD spectra/data also confirmed the oxygen presence in Cu colloids. EDAX: Oxygen peaks are present in the EDAX spectra. [Insets of figures 3.4(b), (d)]. SAED: The lattice planes in SAED confirmed the presence of Oxygen. [Figures 3.4 (b), (d)]

(17) Page 106: what is the meaning of "Zero-phonon optical transitions"

Comment: Due to the indirect band-gap nature of bulk crystalline silicon, it is not naturally capable of accomplishing efficient radiative recombination. Free electrons tend to exist in the X valley of the conduction band, which is not aligned with free holes in the valence band. Therefore, if electron–hole (e–h) carrier recombination has to lead to emission of a photon, a phonon must be involved in conserving the crystal momentum. Canham discovered in 1991 efficient light emission from porous silicon which was attributed to the quantum confinement effect. Due to geometrical confinement in the nanoscale, uncertainty in *k*-space results in delocalization of carriers in *k*-space thus allowing zero phonon optical transitions and significantly enhancing the oscillator strength of the zero phonon transitions in small silicon nanocrystals

(18) Missing sentence in Section 3.2.2, page no 72, line 3.

Comment: Insets of Figures 3.4(b), 3.4(d) demonstrate the EDAX spectra which emphasize the contribution from Cu and oxygen signatures in the NPs.